Global Translational Medicine

ACCSCIENCE PUBLISHING

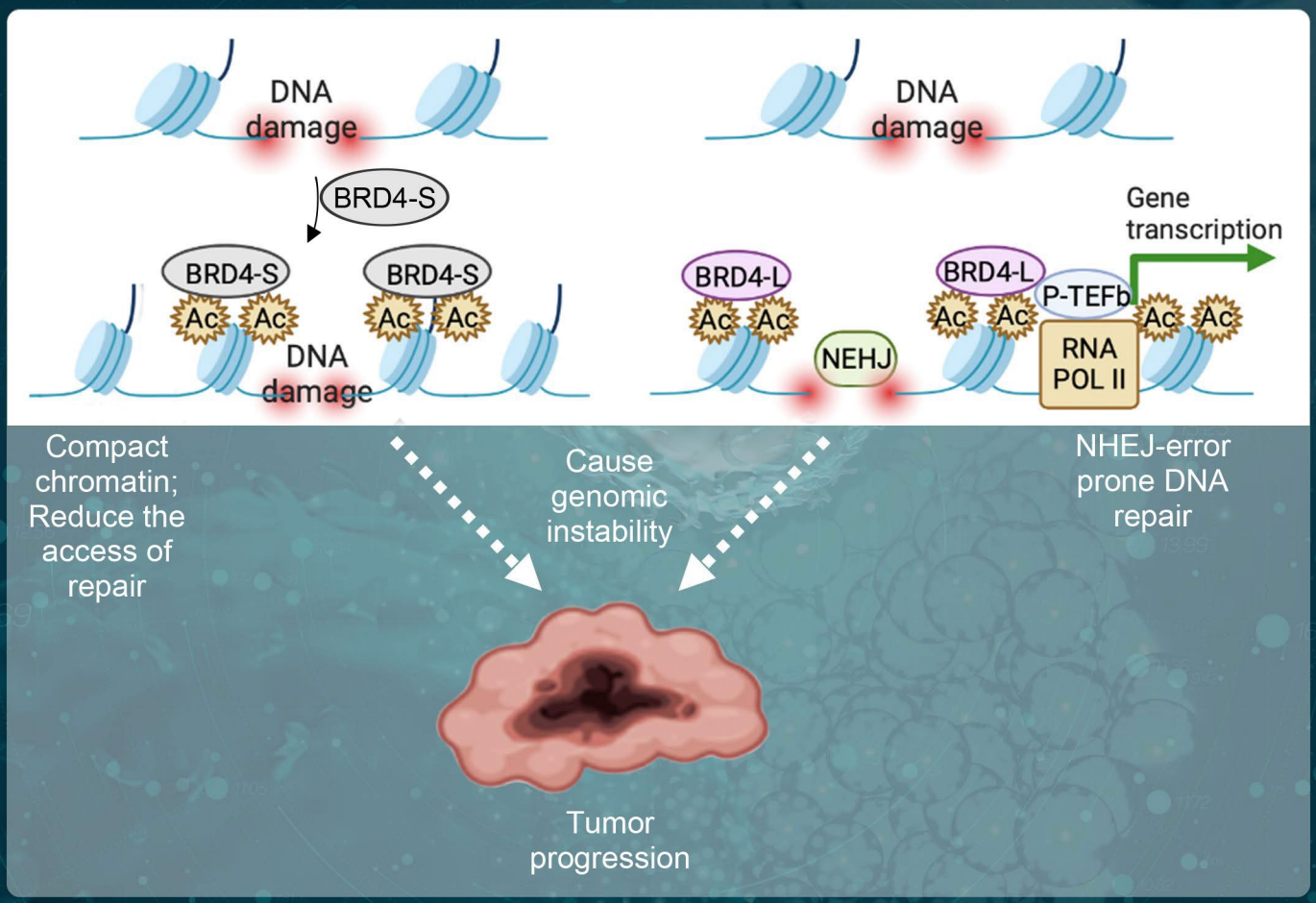

Essential roles of BRD4 in cancer: DNA damage, transcription regulation, and signal transduction

ISSN: 3060-8600 (Print)
ISSN: 2811-0021 (Online)
Volume 2 · Issue 3
September 2023

ACCSCIENCE PUBLISHING

Global Translational Medicine

Print ISSN: 3060-8600
Online ISSN: 2811-0021

Global Translational Medicine is a quarterly journal that focuses on medicine, biological sciences, and biomaterials engineering. *Global Translational Medicine* provides a platform to fill the gaps in preclinical and inter-disciplinary research, to promote clinical translation of scientific research results, and to contribute to the conception of new and improved preventive measures as well as diagnostic and therapeutic techniques of diseases.

About the Publisher

AccScience Publishing is a publishing company based in Singapore. We publish a range of high-quality, open-access, peer-reviewed journals and books from a broad spectrum of disciplines.

Contact Us

Managing Editor
gtm.office@accscience.sg

AccScience Publishing
8 Burn Road, #15-03 Trivex, Singapore 369977.

Volume 2 • Issue 3 • September 2023
ISSN 3060-8600 (print) ISSN 2811-0021 (online)

GLOBAL TRANSLATIONAL MEDICINE

ACCSCIENCE PUBLISHING

Access Science Without Barriers

GLOBAL TRANSLATIONAL MEDICINE

ISSN: 3060-8600 (print)
ISSN: 2811-0021 (online)

Editorial and Production Credits

Publisher: AccScience Publishing
Managing Editor: Lucille You
Production Editor : Sharmila Velapasamy
Article Layout and Typeset: Sinjore Technologies (India)
Cover Design: ProPub (China)

For all advertising queries, contact gtm.office@accscience.sg.

Supplementary file

Supplementary files of articles can be obtained at https://accscience.com/journal/GTM/2/3.

About the Cover

An abstract illustration of human brain

Disclaimer

AccScience Publishing is not liable to the statements, perspectives, and opinions contained in the publications. The appearance of advertisements in the journal shall not be construed as a warranty, endorsement, or approval of the products or services advertised and/or the safety thereof. AccScience Publishing disclaims responsibility for any injury to persons or property resulting from any ideas or products referred to in the publications or advertisements. AccScience Publishing remains neutral with regard to jurisdictional claims in published maps and institutional affiliations.

Global Translational Medicine

Editorial Board

ACCSCIENCE PUBLISHING

Volume 2 | Issue 3 | September 2023 |

Global Translational Medicine

https://accscience.com/journal/gtm

CONTENTS

REVIEW ARTICLES

1 **Inhibiting oxidative stress and inflammation in acute lung injury using hydrogen: A preclinical systematic review and meta-analysis**
Guoshen Zhong, Yanhua Shi, Lingyu Kong, Kaixuan Lv, Lichun Zhang, Mei Yang, Na Tian, Nana Yang

2 **Essential roles of BRD4 in cancer: DNA damage, transcription regulation, and signal transduction**
Sylvia Y. Sun

PERSPECTIVE ARTICLE

3 **Nuclear magnetic resonance-biochemical correlation toward deep learning of theranosis and precision medicine**
Rakesh Sharma, Arvind Trivedi

ORIGINAL RESEARCH ARTICLES

4 **Demystifying the influence of ferroptosis on Alzheimer's and Parkinson's diseases: A network and systems biology approach**
Deepyaman Das, Chayan Munshi, Kalpesh Jas, Sourish Pramanik

5 **Thromboembolism risk in patients diagnosed with EGFR- and ALK-mutant lung adenocarcinoma**
Suna Kavurgacı, Yasemin Söyler, Pınar Akın Kabalak, Derya Kızılgöz, Ülkü Yılmaz

6 **A simple, fast, and cost-effective high-performance liquid chromatography-ultraviolet validated method to quantify lacosamide in therapeutic drug monitoring**
Ángeles Gloria Rodríguez-Basso, María Cecilia Kravetz, María Sylvia Viola, Florencia Ayelén Fernández, Nicolás Martín Barrionuevo, Damián Consalvo, Mariano Núñez, Guillermo Federico Bramuglia

7 **Immediate onset signatures of autoimmune diseases after vaccination**
Darrell O. Ricke

8 **Genome-wide analysis identifies non-reference transposable element polymorphisms associated with Parkinson's disease**
Hao Wu, Junfeng Luo, Ganqiang Liu

ACCSCIENCE PUBLISHING

Global Translational Medicine

REVIEW ARTICLE

Inhibiting oxidative stress and inflammation in acute lung injury using hydrogen: A preclinical systematic review and meta-analysis

Guoshen Zhong[1†], Yanhua Shi[1], Lingyu Kong[2†], Kaixuan Lv[3], Lichun Zhang[1], Mei Yang[1], Na Tian[4*], and Nana Yang[1*]

[1]School of Life Science and Technology, Weifang Medical University, Weifang, 261053, China

[2]Physical Education and Sports School, Soochow University, Suzhou, 215021, China

[3]State Key Laboratory of Primate Biomedical Research, Institute of Primate Translational Medicine, Kunming University of Science and Technology, Kunming, 650032, China

[4]School of Public Health, Weifang Medical University, Weifang, 261053, China

Abstract

Acute lung injury (ALI) results from excessive inflammation and disruption of the alveolar-capillary barrier, leading to acute respiratory distress syndrome. Hydrogen, known as a reducing substance, has been commonly used in preclinical trials of ALI. The present paper aims to summarize the effects of hydrogen on animal models of ALI and the possible antioxidant and anti-inflammation mechanisms of hydrogen. We conducted a thorough search of the relevant literature on PubMed, EMBASE, Web of Science, and CNKI. Data retrieved from 20 studies were analyzed to assess the beneficial effects of hydrogen therapy on ALI animal models. To evaluate the effects of hydrogen, commonly assessed outcome indicators include wet-to-dry ratio (W/D), arterial oxygen partial pressure (PaO_2), malondialdehyde (MDA), superoxide dismutase (SOD), and tumor necrosis factor-alpha (TNF-α). The results demonstrate that hydrogen reduces pulmonary edema (W/D: 95% CI = −0.98 – −0.85, $P < 0.001$), mitigates hypoxia (PaO_2: 95% CI = 6.08 – 22.30, $P < 0.001$), represses lipid peroxidation (MDA: 95% CI = −2.12 – −1.06, $P < 0.001$), scavenges free radicals (SOD: 95% CI = 10.12 – 30.07, $P < 0.001$), and inhibits inflammatory response (TNF-α: 95% CI = −5.52 – −1.72, $P < 0.001$). The subgroup analysis showed significant differences between interventions (MDA: $P < 0.05$; TNF-α: $P < 0.05$; SOD: $P < 0.001$). The meta-regression suggests that species may cause heterogeneity ($P < 0.05$). These results suggest the potential of using hydrogen in clinical trials. Different interventions with hydrogen can affect metabolic transport and distribution *in vivo*. Further studies should be conducted to validate and confirm these findings.

Keywords: Pharmacology; Inflammation; Acute lung injury; Preclinical study; Meta-analysis

[†]These authors contributed equally to this work.

***Corresponding authors:**
Na Tian
(tina_t123@163.com)
Nana Yang
(benben1980@126.com)

Citation: Zhong G, Shi Y, Kong L, *et al*., 2023, Inhibiting oxidative stress and inflammation in acute lung injury using hydrogen: A preclinical systematic review and meta-analysis. *Global Transl Med,* 2(3): 0379.
https://doi.org/10.36922/gtm.0379

Received: March 30, 2023

Accepted: July 12, 2023

Published Online: August 11, 2023

1. Introduction

Acute lung injury (ALI) is an acute pneumonia disease caused by various factors[1]. Impairment of epithelial and endothelial barrier is a pathology hallmark of ALI, and it can progress into acute respiratory distress syndrome, resulting in diffuse pulmonary

interstitial and alveolar edema, with a mortality rate of 30 – 40%[1,2]. Injured lung tissues experience the destruction of the alveolar epithelial and endothelial barriers, causing the deactivation of the alveolar surfactant layer and an increase in lung interstitium permeability[3]. This allows the transfer of tissue fluid and hemoglobin into the pulmonary interstitium and alveoli, resulting in a reduction of lung compliance and obstruction of gas exchange[4]. In addition, various factors that cause injuries, such as bacterial toxins and mechanical stress, can induce inflammation, impairing the epithelium and endothelium, promoting the migration of neutrophils, and releasing inflammatory factors[2,4,5]. At present, a wide range of treatment strategies has been developed to address ALI, including glucocorticoid therapy, extracorporeal membrane oxygenation (ECMO), and various supportive interventions and drug therapies[6,7]. These interventions prevent further deterioration of ALI and play a therapeutic role. However, due to the heterogeneity of ALI, definitive conclusions regarding the clinical application and mechanism of these therapies are still lacking[6-8].

As a small molecule, hydrogen has a simple structure, low molecular weight, and easy diffusion characteristics, which enable it to easily access lung tissues[9]. Recent studies have highlighted its potential as a therapeutic measure for ALI, attributed to its anti-inflammatory and antioxidant effects[10,11]. So far, hydrogen therapy for ALI includes two methods: inhalation of hydrogen gas and injection of hydrogen saline[11]. Inhaling hydrogen gas has been shown to improve respiratory function and repair the lung barrier in C57BL/6 mice[12]. Similarly, injecting hydrogen saline has been found to exert protective effects on the alveolar epithelium and prevent surfactant deactivation in Sprague-Dawley (SD) rats by inhibiting excessive autophagy[13]. Moreover, hydrogen has been shown to inhibit the release of adhesion molecules and inflammatory factors, thereby reducing endothelial damage, excessive endothelial permeability, and restoring lung tension to facilitate improved gas exchange after neutrophil migration following alveolar damage[14]. Despite the promising results, hydrogen therapy is still in the preclinical trial stage, and a comparative study of the therapeutic effects between the two methods has not been conducted. Exploring the differences in intervention measures can provide valuable insights into their impact on the treatment of ALI.

The purpose of this systematic review and meta-analysis is to provide a comprehensive summary of the key findings on the effectiveness and mechanisms of hydrogen therapy in animal models of ALI, particularly focusing on the relationship between ALI and hydrogen under oxidative stress and inflammation. The review also aims to investigate the differences in treatment between 2% H_2 and hydrogen saline, aiming to guide future ALI clinical trials and clinical practice. We hypothesize that hydrogen therapy may play a role in repairing the alveolar barrier, eliminating excessive oxygen free radicals, and reducing the release of anti-inflammatory factors in ALI.

2. Materials and methods

2.1. Protocol registration

The Preferred Reporting Items for Systematic Reviews and Meta-analysis (PRISMA) 2020 reporting guidelines were used for this preclinical systematic review and meta-analysis[15]. We have preregistered a protocol on the International Prospective Register of Systematic Reviews (PROSPERO) website. (https://www.crd.york.ac.uk/PROSPERO/, Registration number: CRD42021247370).

In response to the question, "Whether treatment effects between 2% H_2 and hydrogen saline differ significantly in animal models of ALI?" we employed the sub-group analysis method to analyze the five relevant indicators within the groups of 2% H_2 and hydrogen saline.

To address the regional and national database limitations, the present paper used Fisher's exact test to analyze the association between the language of the included studies (Chinese and English) and their respective results.

2.2. Search strategy and study selection

We conducted a comprehensive search for preclinical trials investigating the effect of hydrogen on ALI in various electric databases, including PubMed, EMBASE, CNKI, and Web of Science. The search encompassed studies published through March 28, 2021. We used the PubMed search strategy to ensure that all relevant studies were included. Furthermore, the reference lists of the selected papers were manually screened to identify any additional eligible studies.

2.2.1. Inclusion criteria

The inclusion criteria are as follows:

(i) Types: Studies involved animals with induced ALI.
(ii) Intervention: 2% H_2 inhalation or injection of hydrogen saline, and unlimited treatment times.
(iii) Control: Group(s) given placebo or no treatment.
(iv) Outcomes:
  (a) Primary outcomes: W/D ratio and arterial oxygen partial pressure (PaO_2).
  (b) Secondary outcomes: Malondialdehyde (MDA), superoxide dismutase (SOD), and tumor necrosis factor-alpha (TNF-α).

(v) Other:
  (a) Experimental studies.
  (b) Published between 2010 and 2021,
  (c) Published in any publication language,
  (d) The cited literature sources should be retrievable.

2.2.2. Exclusion criteria

The exclusion criteria are as follows:

(i) Types:
  (a) Studies of non-animal experiments about ALI,
  (b) Publications that did not comply with or adequately describe standard laboratory animal rules.
(ii) Intervention: Did not use 2% H_2 or hydrogen saline but used other therapy to treat ALI animals.
(iii) Control: Group(s) given placebo or no treatment.
(iv) Other:
  (a) The same author published the same articles at different times,
  (b) Unclear literature sources,
  (c) Data are only displayed in figures and unable to contact the author to obtain original data.

After defining our strategy, each study was randomly given to two independent authors (LYK and MY) and was selected by studies of title and abstract. Disagreements between the two reviewers were solved by discussing with the third author (GSZ).

2.3. Study selection and data extraction

The information of the included studies, including authors, year of publication, species of animal subjects, and language, were recorded and considered in the study selection based on the inclusion and exclusion criteria. In addition, we extracted data, including the number of animals in the experimental and control groups, types of ALI animal models, interventions, and outcomes. Data extraction followed predefined rules, with one author (LYK) responsible for study data collection. In case of uncertainty, the chief author (GSZ) was consulted, and the final decision was reached collaboratively by all reviewers.

2.4. Assessment of Methodological Quality

In the present paper, we evaluated the research quality of included studies using the CAMARADES checklist, which covered 10 items related to a series of animal experiment designs[16]. Due to differences in the research, three evaluation indicators were modified as follows:

(i) Item no. 4: Blinded induction of model,
(ii) Item no. 6: Use of anesthetic agents without significant intrinsic neuroprotective activity,
(iii) Item no. 7: Approval of animal ethics for creating the ALI model.

Two evaluators (LYK and MY) independently extracted the data and evaluated the quality scores of each study. Any disagreements were resolved by the chief reviewer (GSZ).

2.5. Data synthesis and statistics analysis

The meta-analysis was performed using Stata software (version 14.0) and GraphPad Prism (version 9.4). The outcomes of W/D and PaO_2 were evaluated using the weighted mean difference (WMD) model to assess the improvement in lung function. For MDA and SOD, the same model was used to evaluate the antioxidant effect of hydrogen, while TNF-α was assessed using the standardized mean difference (SMD) model to analyze hydrogen's anti-inflammatory effects. In cases where studies reported standard error (SE) instead of standard difference (SD), Equation I was used to convert the values:

$$SD = SE \times \sqrt{N} \quad (I)$$

2.6. Statistical heterogeneity test and exploration

Study heterogeneity was assessed using the Q statistic and I^2 statistic[17]. Significant heterogeneity was considered present if the I^2 value exceeded 50% or if the *P*-value was less than the predefined significance level ($\alpha = 0.05$). Conversely, non-significant heterogeneity was indicated when the I^2 value was 50% or below, and $P \geq \alpha = 0.05$. Considering the possible high heterogeneity due to the differences between interventions, we used subgroup analysis to explore the heterogeneity[18]. Moreover, the diversity of species may affect the heterogeneity of the meta-analysis results. Therefore, meta-regression was used to explore the heterogeneity attributable to species. Meta-regression required a minimum of ten studies to examine one characteristic[19]. Consequently, the present paper included studies using W/D and species as the covariate to explore the sources of heterogeneity ($n = 12 > 10$). Publication bias was assessed using Egger's test, and the stability of the results from the included studies was analyzed through the trim and fill funnel plot and sensitivity analysis[18].

2.7. Grade evidence assessment

We followed the PRISMA checklists and used the GRADE profiler (version 3.6) to evaluate the grade evidence of included indicators. All the included studies were animal experiments, and their grades were downgraded by 5 impact factors. The grade evidence for these included indicators was divided into 4 levels: (i) High quality, indicating high confidence in results; (ii) moderate quality, indicating general confidence in results; (iii) low quality, indicating limited confidence in certain areas; and (iv) very low quality, indicating the confidence could not be promised or predicted. The work was completed by GSZ, LYK, and MY.

3. Results

3.1. Study retrieval and selection

In the present paper, we identified 390 potentially relevant studies using the search protocol described above. After applying the inclusion and exclusion criteria, 50 studies were selected based on their titles and abstracts. Subsequently, 30 articles lacking the necessary data were excluded, resulting in a final set of 20 studies used for this meta-analysis. The selection diagram is shown in Figure 1.

3.2. Characteristics of the included study

The main characteristics of these 20 studies are presented in Table 1. These studies were published between 2010 and 2021, encompassing a total of 406 subjects, with 203 in the experimental group and 203 in the control group. The species studied in the included studies can be classified into five categories: (i) C57BL/6 mice[20-22]; (ii) ICR mice[23,24]; (iii) Kunming (KM) mice[25]; (iv) SD rats[26-37]; and (v) Wistar rats[38,39]. These studies covered 7 types of ALI animal models: (i) Smoke inhalation[39]; (ii) cecal ligation and puncture[20-22,27,32]; (iii) lipopolysaccharide (LPS)[25,30-32,39]; (iv) oleic acid (OA)[33,34]; (v) burnt injury[26]; (vi) ischemia/reperfusion (I/R)[28,29,37]; (vii) paraquat (PQ)[24,26,35]. Regarding interventions, hydrogen saline was used in 12 studies[26-35], and 2% H_2 was used in eight studies[20-23,25,36-38]. Two studies used standard error to represent the effect size, which needed to be calculated using Equation I[22,37], while other studies used standard differences[20,21,23-36,38].

3.3. Assessment of the risk of publication bias

All included studies were checked and scored through the CAMARADES checklist to evaluate their methodological quality. The scores ranged from three to seven, with an average score of 4.75. A detailed summary of methodological quality results is provided in Table 2. Moreover, all included studies passed the peer-review process[20-38]. Out of 20 studies, 10 studies implemented temperature control during the experimental sta ges[21-24,26,28-30,33,37,38]. However, two studies did not provide random allocation[20,27]. In addition, only seven studies conformed to the use of anesthetic without significant intrinsic neuroprotective activity[22,24,26-29,34]. Three studies were found to have non-compliance with animal welfare regulations[24,26,35]. Regarding the disclosure of potential conflicts of interest, only four studies provided and declared such statements in their research[28,33,35,38].

3.4. Outcome indicators of the included studies

3.4.1. W/D ratio

The W/D ratio was used as an outcome index in 12 studies. All these studies provided complete data and showed positive effects of 2% H_2 and hydrogen saline in reducing the W/D ratio. The findings revealed

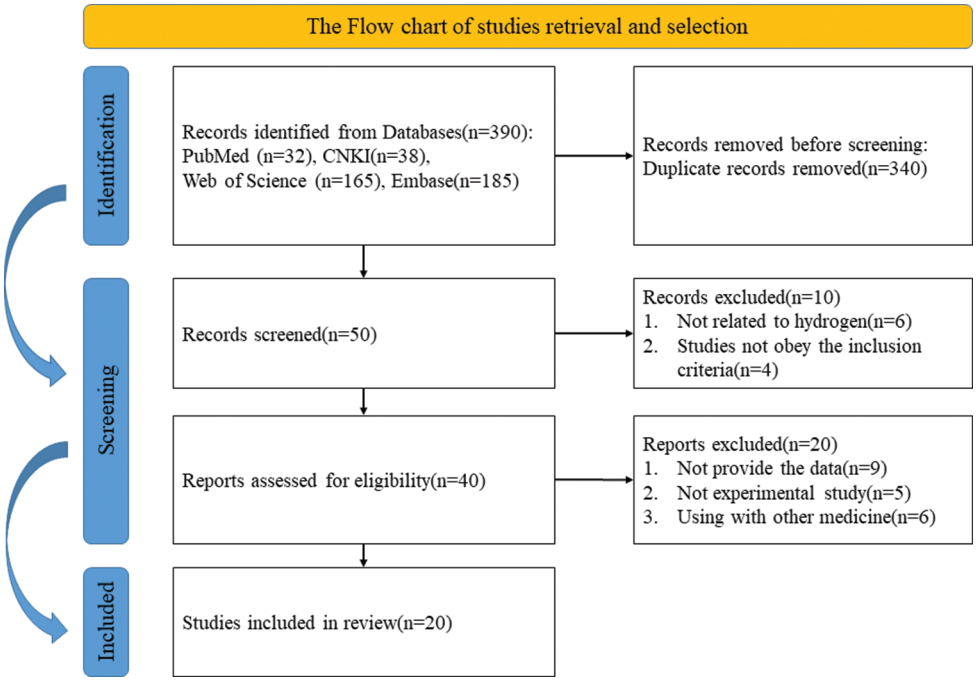

Figure 1. Study flow chart of studies retrieval and selection. The inclusion and screening were conducted by two reviewers. The first stage was filtered by the title and abstract. In the second stage, screening was conducted again based on the full text of the remaining studies after screening. Finally, studies of hydrogen therapy-treated ALI animal models were selected.

Table 1. Summary of study characteristics

Author	Species	Type & modeling process	Treatment	Indicator
Fang *et al*., 2011[21] [English]	SD rats (Male, 8/8)	BI Process: Immersed in boiling water (98ºC) for 12 seconds	Hydrogen saline (5ml/kg, ip)	Artery blood: PaO_2↑
Tian *et al*., 2012[22] [Chinese]	SD rats (Male, 8/8)	CLP Process: Use a 4-0 line to ligate the distal cecum and then 18G syringe to perforate the ligation of the cecum	Hydrogen saline (0.6 mmol/L,5 ml/kg, ip)	Lung tissue: W/D↓, SOD↑, MDA↓, TNF-α↓
Chen *et al*., 2012[23] [Chinese]	C57BL/6 (Male, 8/8)	CLP Process: Ligating the quarter of the proximal cecum (nearby the ileocecal valve)→perforating ligation at the head and tail of the cecum→ squeezing out 0.3 ml substances	2% H_2 (Nasal inhalation 2 hours)	Lung tissue: W/D↓, SOD↑
Li *et al*., 2014[24] [Chinese]	ICR mice (Male, 6/6)	CLP Process: Ligating the quarter of the proximal cecum(nearby the ileocecal valve)→20G syringe to perforate ligation at the head and tail of the cecum→ squeezing out 0.3 ml substances	2% H_2 (Nasal inhalation 2 hours)	Lung tissue: W/D↓
Zhang *et al*., 2016[25] [Chinese]	C57BL/6 mice (Male, 10/10)	CLP Process: Ligating the half of the distal cecum→ using a 21G syringe to perforate the ligation of the cecum→ using NaCl liquid (1 ml, IH) for mice recovery	2% H_2 (Nasal inhalation 2 hours)	Lung tissue: W/D↓ , SOD↑, MDA↓, TNF-α↓
Xie *et al*., 2010[26] [English]	C57BL/6 mice (Male, 30/30)	CLP Process: Ligating the half of distal cecum→ using 21G syringe to perforate the ligation of the cecum→ using NaCl liquid (1 ml, IH) for mice recovery	2% H_2 (Nasal inhalation 2 hours)	Artery blood: PaO_2-
Bu *et al*., 2015[27] [Chinese]	SD rats (Male, 8/8)	I/R Process: Dividing artery and vein of right groin (keeping shocked for 1 hour)→reinfusion blood (1 hour)	2%H_2 (Nasal inhalation 2 hours)	Lung tissue: W/D↓
Shi *et al*., 2013[28] [Chinese]	SD rats (Male, 8/8)	I/R Process: Dividing artery and vein of right groin (keeping shocked for 1 hour)→reinfusion blood (lasting 2 hours)	2% H_2 (Nasal inhalation 10 minutes)	Artery blood: PaO_2↑ Lung tissue: MDA↓, SOD↑, W/D↓, TNF-α↓
Zou *et al*., 2018[29] [English]	Wistar rats (Male, 8/8)	I/R Process: Occluding the bilateral femoral arteries (lasting 3 hours) and then reinfusion blood (lasting 2 hours)	Hydrogen saline (0.6 mmol/L, 10 ml/kg, ip)	Artery blood: PaO_2↑
Liu *et al*., 2013[30] [English]	Wistar rats (Male, 8/8)	LPS Process: LPS from Escherichia coli 055:B5 (15 mg/kg, ip)	2% H_2 (Nasal inhalation 30 minutes)	Lung tissue: PaO_2↑, W/D↓ , SOD↑, MDA↓, TNF-α↓
Mao *et al*., 2015[31] [Chinese]	KM mice (Male, 6/6)	LPS Process: LPS from Escherichia coli O127:B8 (20 mg/kg, ip)	Hydrogen saline (15 ml/L, 10 ml/kg, ip)	Lung tissue: W/D↓
Xu *et al*., 2019[32] [Chinese]	SD rats (Male, 15/15)	LPS Process: ip, 10 mg/kg	Hydrogen saline 2.2 mg/L, 5 ml/kg, ip)	Lung tissue: W/D↓, SOD↑, MDA↓
Liang *et al*., 2012[33] [Chinese]	SD rats (Male, 8/8)	LPS Process: LPS from Escherichia coli 055:B5 (15 mg/kg, ip)	2%H_2 (Nasal inhalation 6 hours)	Lung tissue: TNF-α↓
Song *et al*., 2016[34] [Chinese]	SD rats (Male, 10/10)	LPS Process: LPS from Escherichia coli 055:B5 (5 mg/kg, ip)	Hydrogen saline (0.6 mmol/l, 10 ml/kg, ip)	Lung tissue: W/D↓ , TNF-α↓
Ying *et al*., 2017[35] [English]	SD rats (Male, 10/10)	OA Process: Caudal vein injection (0.1 ml/kg)	Hydrogen saline (0.4 mg/L, 5 ml/kg, ip)	Artery blood: PaO_2↑
Ying and He, 2011[36] [Chinese]	SD rats (Male, 10/10)	OA Process: Caudal vein injection (0.1 ml/kg)	Hydrogen saline (0.4 mg/L, 5 ml/kg, ip)	Artery blood: PaO_2↑ Lung tissue: TNF-α↓
Fang *et al*., 2012[37] [Chinese]	SD rats (Male, 8/8)	PQ Process: Injecting paraquat (35 mg/kg, ip)	2% H_2 (Nasal lasting 72 hours)	Artery blood: PaO_2↑ Lung tissue: W/D↓, MDA↓
Liu *et al*., 2015[38] [Chinese]	ICR mice (Male, 8/8)	PQ Process: Gavage 20% paraquat (50 mg/kg)	Hydrogen saline (0.4 mg/L, 5 ml/kg, ip)	Lung tissue: MDA↓
Zhang *et al*., 2011[39] [English]	SD rats (Male, 10/10)	PQ Process: Gavage 20% paraquat (50 mg/kg)	Hydrogen saline (0.4 mg/L, 5 ml/kg, ip)	Artery blood: PaO_2↑ Lung tissue: W/D↓, MDA↓

(Cont'd...)

Table 1. ***(Continued)***

Author	Species	Type & modeling process	Treatment	Indicator
Liu *et al.*, 2013[40] [Chinese]	SD rats (Male, 6/6)	SI Process: Smoke inhalation	Hydrogen saline (10 ml/kg, ip)	Artery blood: TNF-α↓ Lung tissue: MDA↓

Notes: Author: First author or corresponding author; Language: The language used for the publication; Species: Including sex, numbers of experiment group, and control group; Type and modeling process: The types of acute lung injury and modeling process in animal models; Treatment: The use of intervention and lasting times; Indicator: Indicators of included study that can be used for this meta-analysis.
Abbreviations: BI: Burn injury; CLP: Cecal ligation and puncture; ip: Intraperitoneal; IH: Intraperitoneal hydration; I/R: Ischemia/reperfusion; LPS: Lipopolysaccharide; MDA: Malondialdehyde; OA: Oleic acid; PaO_2: Arterial oxygen partial pressure; PQ: Paraquat; SI: Smoke inhalation; SOD: Superoxide dismutase; TNF-α: Tumor necrosis factor-alpha; W/D: Wet-to-dry ratio.

Table 2. Risk of bias assessment for included studies

Study	1	2	3	4	5	6	7	8	9	10	Score
Fang *et al.*, 2011[26]	√	√	√	-	-	√	√	-	√	-	6
Tian *et al.*, 2012[27]	√	-	-	-	-	√	√	-	√	-	4
Chen *et al.*, 2012[20]	√	-	-	-	-	-	√	-	√	-	3
Li *et al.*, 2014[23]	√	√	√	-	-	-	√	-	√	-	5
Zhang *et al.*, 2016[21]	√	√	√	-	-	-	√	-	√	-	5
Xie *et al.*, 2010[22]	√	√	√	-	-	√	√	-	√	-	6
Bu *et al.*, 2015[28]	√	-	√	-	-	√	√	-	√	-	5
Shi *et al.*, 2013[29]	√	√	√	-	-	√	√	-	√	-	6
Zhou *et al.*, 2018[37]	√	√	√	-	-	-	√	-	√	√	6
Liu *et al.*, 2013[38]	√	√	√	-	-	-	√	-	√	√	6
Mao *et al.*, 2015[25]	√	-	√	-	-	-	√	-	√	-	4
Xu *et al.*, 2019[30]	√	√	√	-	-	-	√	-	√	-	5
Liang *et al.*, 2012[31]	√	-	√	-	-	-	√	-	√	-	4
Song *et al.*, 2016[32]	√	-	√	-	-	-	√	-	√	-	4
Ying *et al.*, 2017[33]	√	√	√	-	-	√	√	-	√	√	7
Ying and He, 2011[34]	√	-	√	-	-	-	√	-	√	-	4
Fang *et al.*, 2012[26]	√	-	√	-	-	-	√	-	-	-	3
Liu *et al.*, 2015[24]	√	√	√	-	-	-	√	-	-	-	4
Zhang *et al.*, 2011[35]	√	-	√	-	-	-	√	-	-	√	4
Liu *et al.*, 2013[36]	√	-	√	-	-	-	√	-	√	-	4

Notes: 1. Peer-review publication; 2. Control of temperature; 3. Random allocation to treatment or control; 4. Blinded induction of model (group randomly after modeling); 5. Blinded assessment of outcome (s); 6. Use of anesthetic without significant intrinsic neuroprotective activity; 7. Appropriate animal model (s) (conform to the types of participants); 8. Sample size calculation; 9. Compliance with animal welfare regulations; 10. Statement of potential conflict of interests.

that hydrogen therapy has a significant treatment effect in ALI-induced pulmonary edema (effect size: WMD = −0.91, 95% CI = −0.98 – −0.85, $P < 0.001$; heterogeneity: $I^2 = 98.5\%$, $P < 0.001$, $tau^2=0.9132$; random-effects model; Figure 2).

3.4.2. PaO_2

Nine studies demonstrated the influence of hydrogen therapy on improving PaO_2 when compared to the control group. All studies provided complete data and reported positive results. This indicator also revealed that hydrogen therapy could significantly improve the situation of hypoxia in ALI animals to a certain degree (effect size: WMD = 14.19, 95% CI = 6.08 – 22.30, $P < 0.001$; heterogeneity: $I^2 = 95.7\%$, $P < 0.001$; random-effects model; Figure 3).

3.4.3. MDA

Nine studies provided complete data for both the experimental group and the control group. The results demonstrated a significant difference in MDA levels when hydrogen therapy was used to treat ALI animal models compared to control groups. It revealed that hydrogen therapy could repress lipid peroxidation (effect size: WMD = −1.59, 95% CI = −2.12 – −1.06, $P < 0.001$; heterogeneity: $I^2 = 97.3\%$, $P < 0.001$; random-effects model; Figure 4).

3.4.4. SOD

Six studies reported that both 2% H_2 and hydrogen saline improved SOD levels in lung tissues. The findings suggested that hydrogen may scavenge superoxide free radicals in the lung by promoting the expression of SOD in ALI animal models (effect size: WMD = 20.09, 95% CI = 10.12 – 30.07, $P < 0.001$; heterogeneity: $I^2 = 98.7\%$, $P < 0.001$; random-effects model; Figure 5).

3.4.5. TNF-α

Eight studies were included in the analysis, and the results demonstrated that the experimental groups showed significantly lower TNF-α levels compared to the control group. The findings confirmed that hydrogen has an inhibitory effect on inflammatory factors (effect size: SMD = −3.62, 95% CI = −5.52 – −1.72; heterogeneity: $I^2 = 93.8\%$, $P < 0.001$; random-effects model; Figure 6).

3.6. Subgroup analysis

According to the heterogeneity values of W/D, PaO_2, MDA, SOD, and TNF-α, we performed a subgroup analysis, dividing the treatments into 2% H_2 and hydrogen saline. The analysis aimed to explore whether different

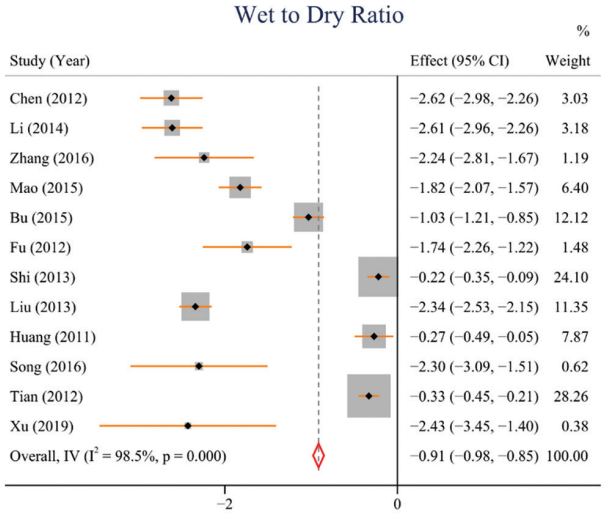

Figure 2. Effect of hydrogen for wet-to-dry ratio. Weighted means difference was used to analyze data. 95% confidence interval was use as effect sizes. The random-effects model was used to pool data.

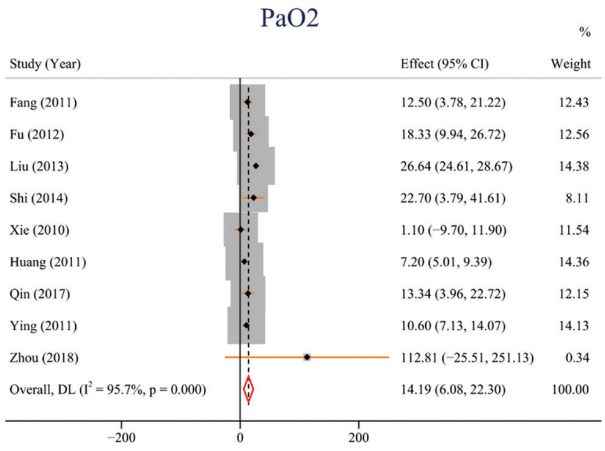

Figure 3. Effect of hydrogen for arterial oxygen pressure. Weighted means difference was used to analyze data. 95% confidence interval was used as effect sizes. The random-effects model was used to pool data.

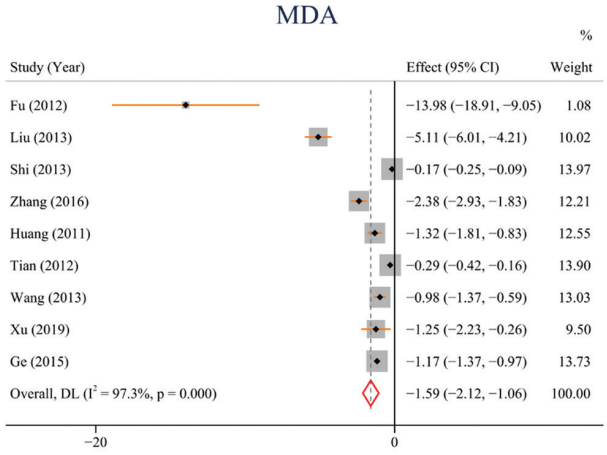

Figure 4. Effect of hydrogen for malondialdehyde. Weighted means difference was used to analyze data. 95% confidence interval was used as effect sizes. The random-effects model was used to pool data.

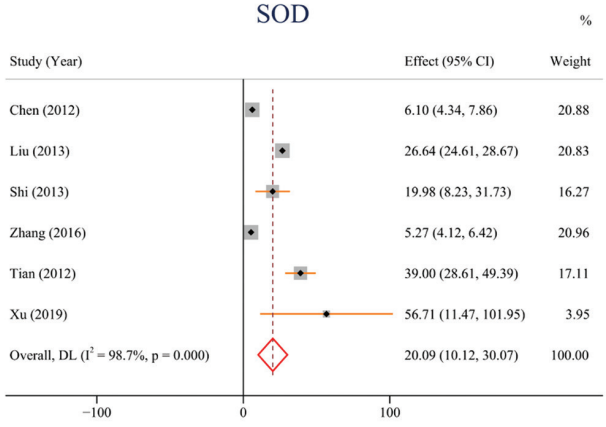

Figure 5. Effect of hydrogen for superoxide dismutase. Weighted means difference was used to analyze data. 95% confidence interval was used as effect sizes. The random-effects model was used to pool data.

interventions could affect the effects of hydrogen in the preclinical trials of ALI. The results indicated that there were no significant differences in W/D and PaO_2 ($P > 0.05$) between the two groups. However, significant differences were observed in MDA, SOD, and TNF-α ($P < 0.05$). Compared with the group receiving hydrogen saline, the group receiving 2% H_2 showed significantly lower levels of MDA (2% H_2 = −4.12 [95% CI = −6.67 – −1.57] vs. hydrogen saline = −0.96 [95% CI = −1.50 – −0.43]; $P = 0.02 < 0.05$) and TNF-α (2% H_2 = 6.54 [95% CI = −10.99 – −2.10] vs. hydrogen saline = −1.67 [95% CI = −3.14 – −0.21); $P = 0.04 < 0.05$). The results reflected the degrees of lipid peroxidation and inflammation. On the other hand, the group receiving hydrogen saline had higher SOD levels than the 2% H_2 group, reflecting the ability of SOD in scavenging free radicals *in vivo* (2% H_2 = 14.14 [95% CI = 3.31 – 24.97]) vs. hydrogen saline = 39.89 [95% CI = 29.76 – 50.02]); $P < 0.001$; Figure 7).

3.7. Meta-regression

We classified the species used in the W/D-included studies into two groups: Seven studies used SD rats, and four studies used other species, including C57BL/6J mice, ICR mice, KM mice, and Wistar rats. Since the number of studies with other species is relatively small, and we can only select one covariate for meta-regression analysis, we chose to classify the studies based on whether they used SD rats or other

species. We assigned the number "1" to represent SD rats and the number "0" to represent other species. For the meta-analysis, we used restricted maximum likelihood estimation (REML) to estimate heterogeneity and used tau^2 statistics to explain the heterogeneity between studies using Equation II.

$$\Delta = \frac{tau_0^2 - tau_1^2}{tau_0^2} \quad \text{(II)}$$

Where tau_0^2 represents the result before meta-regression, tau_0^2 represents the result after meta-regression, and Δ represents heterogeneity between studies.

The results of the meta-analysis revealed that species variations could explain 50% of heterogeneity between studies of W/D, suggesting that the choice of species can cause observed heterogeneity, particularly in the case SD rats (P = 0.015 < 0.05, tau_1^2 = 0.4579, tau_0^2 = 0.9132; Figure 8). These findings emphasize the importance of carefully selecting the appropriate ALI animal model that best aligns with the research hypothesis. Researchers should be mindful of the potential differences in ALI symptoms between animals and humans.

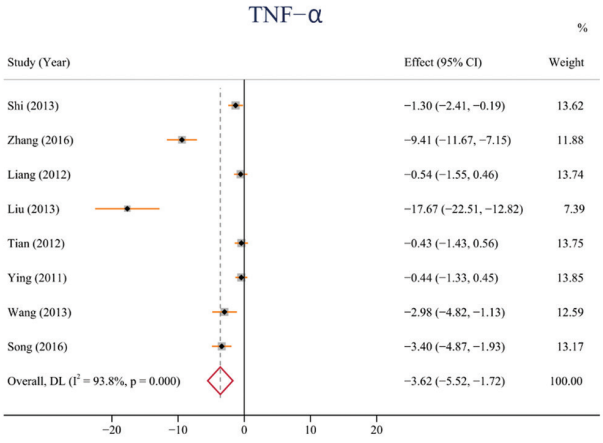

Figure 6. Effect of hydrogen for tumor necrosis factor-alpha. Weighted means difference was used to analyze data. 95% confidence interval (95% CI) was used as effect sizes. The random-effects model was used to pool data.

3.8. Influence of language

As reported by Song *et al.*[39], excluding non-English literature may introduce a specific bias. To address this concern, our study applied Fisher's exact test to compare the included studies in different publication languages, aiming to assess the impact of language on the results of the meta-analysis[40]. The result revealed that there was no significant difference between the studies published in different languages (P = 0.30 > 0.05, Table 3). This finding implied that language is not a likely factor influencing the results of our meta-analysis and indicates that the publication bias related to language was not a concern in the present paper.

3.9. Publication bias

Egger's test was used to analyze the publication bias in the present paper. As recommended by Sterne *et al.*[41], the number of included studies for tests of funnel plot asymmetry should be more than 10. Therefore, the studies related to W/D were used to evaluate the publication bias. The results of Egger's regression plot indicated the presence of significant differences between the studies (P = 0.039 < 0.05, Figure 9). This finding suggests that further analysis is necessary to assess the robustness of the results.

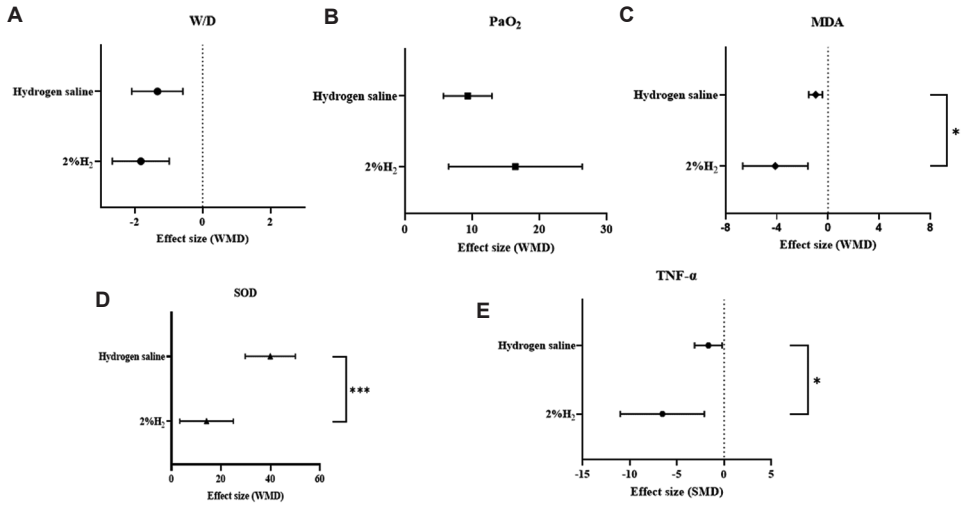

Figure 7. Subgroup analysis of interventions. The interventions were analyzed using five indicators: (A) Wet-to-dry ratio; (B) arterial oxygen pressure; (C) malondialdehyde; (D) superoxide dismutase; (E) tumor necrosis factor-alpha.

3.10. Sensitivity analysis

The stability and reliability of this meta-analysis were assessed using the trim and fill plot and sensitivity analysis. In the sensitivity analysis, we systematically omitted one study at a time and recalculated the effects of the remaining studies to assess the potential impact of individual studies on the overall results. In addition, we examined whether there were additional virtual studies in the trim and fill plot. The results showed that no significant differences were observed after the removal of any single study. Furthermore, the results of the trim and fill plot indicated that there were no omissions of included studies, further supporting the reliability of the results obtained from this meta-analysis (Figure 10).

3.11. Grade evidence assessment

As for the grade evidence of the included indicators, W/D, MDA, and SOD have moderate-quality evidence, indicating that there is moderate confidence in the conclusion that the real value is close to the estimated value. PaO_2 has a low quality, and TNF-α has a very low quality, suggesting that the present paper has reservations about the credibility of the results for PaO_2 and TNF-α. More detailed information regarding these indicators can be found in Table 4.

4. Discussion

In the present paper, we performed a meta-analysis and systematic review of 20 preclinical studies on ALI. Our findings revealed that both 2% H_2 and hydrogen saline demonstrated effects of significantly reducing the volume of pulmonary edema, improving hypoxia, repressing lipid peroxidation, scavenging oxygen free radicals, and inhibiting expressions of inflammatory factors. Moreover, we also found that 2% H_2 exhibited superior effects in reducing MDA and TNF-α compared to hydrogen saline. However, hydrogen saline outperformed 2% H_2 in terms of SOD levels. The findings suggest that hydrogen and hydrogen saline can be chosen or combined to optimize treatment efficacy for different degrees of ALI (shown in Figure 11)

Table 3. Fisher's exact test

(a)

Language	Effects		Total
	No	Yes	
English	1	5	6
Chinese	0	14	14
Total	1	19	20

(b)

	Value	DF	Asymptotic significance (2-sided)	Exact significance (2-sided)	Exact significance (1-sided)
Pearson Chi-square	2.456	1	0.117	-	-
Fisher's exact test	-	-	-	0.300	0.300
N of valid cases	20	-	-	-	-

4.1. Interventions that affect the distribution of hydrogen

The distribution and concentration of molecular hydrogen in various organs have been investigated by different researchers. Sun *et al.*[42] reported that the molecular hydrogen concentration reached its peak approximately 5 min after injecting hydrogen saline into the liver and kidneys. In contrast, Liu *et al.*[43] demonstrated that inhaling 2% H_2 gas resulted in maximum gas levels in the

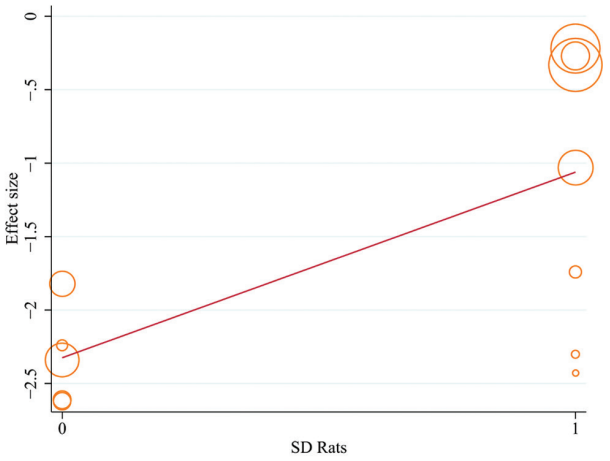

Figure 8. Meta-regression of Sprague-Dawley (SD) rats. The number "0" represents non-SD rats, and the number "1" represents SD rats.

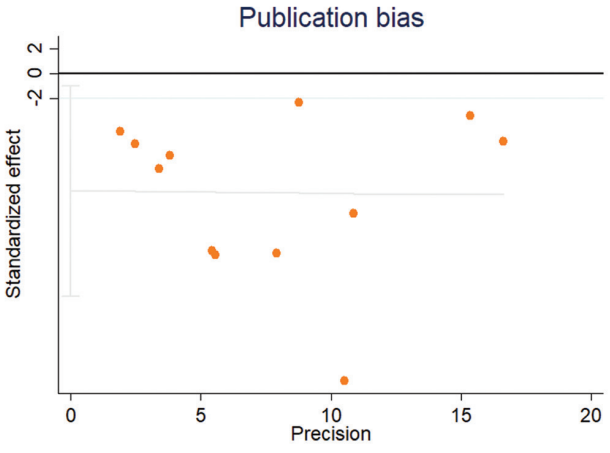

Figure 9. Egger's test of wet-to-dry ratio.

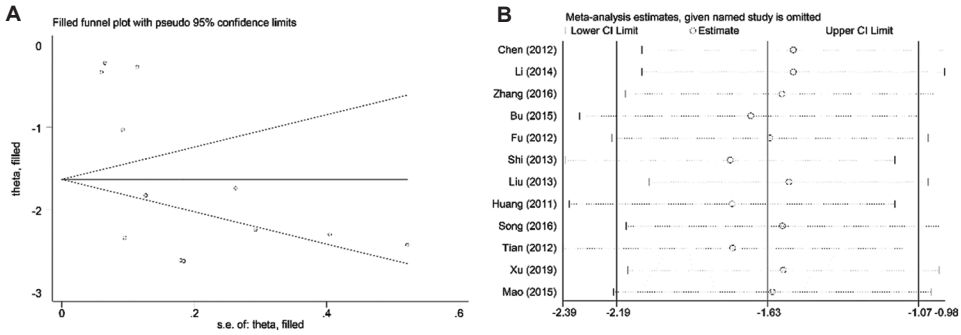

Figure 10. (A) Trim and fill plot of wet-to-dry ratio; (B) sensitivity analysis of wet-to-dry ratio.

Table 4. Grade evidence for assessment

Participants (number of studies)	Risk of bias	Inconsistency	Indirectness	Imprecision	Publication bias	Overall quality of evidence
200 (W/D) (12 studies)	Serious[1]	No serious inconsistency	No serious indirectness	No serious imprecision	Reporting bias strongly suspected[2]	⊕⊕⊕⊖ MODERATE[1,2,] due to risk of bias, publication bias
214 (PaO_2) (9 studies)	Serious[1]	No serious inconsistency	No serious indirectness	No serious imprecision	Reporting bias strongly suspected[2]	⊕⊕⊖⊖ LOW[1,2] due to risk of bias, publication bias
176 (MDA) (9 studies)	Serious[1]	No serious inconsistency	No serious indirectness	No serious imprecision	Undetected	⊕⊕⊕⊖ MODERATE[1] due to risk of bias
128 (SOD) (6 studies)	Serious[1]	No serious inconsistency	No serious indirectness	No serious imprecision	Undetected	⊕⊕⊕⊖ MODERATE[1] due to risk of bias
170 (TNF-α) (8 studies)	Serious[1]	No serious inconsistency	No serious indirectness	Serious[3]	Reporting bias strongly suspected[2]	⊕⊖⊖⊖ VERY LOW[1,2,3] Due to risk of bias, imprecision, publication bias

Notes: [1]These included studies have not obeyed some items of the CAMARADES checklists. [2]Use the egger's test to verify that the results have significant differences. [3]The units of these included studies could not be unified that used standard mean difference (SMD) to remove the influence of units.

liver and kidneys for up to 30 min, with retention in organs for at least 60 min after inhalation. Besides, Yamamoto *et al.*[44] reported that the concentration and distribution of hydrogen gas in different organs depend on gas diffusion and blood supply. Similarly, Watanabe *et al.*[45] revealed that continuous inhalation of hydrogen gas could maintain the hydrogen concentration for a longer duration compared to the injection of hydrogen saline. These studies suggest that the effects of 2% H_2 differ from hydrogen saline in the treatment of ALI animals[43-45]. However, it is essential to acknowledge the limitations. At present, no study has explored the difference between hydrogen gas and hydrogen saline in the treatment of ALI simultaneously. Therefore, researchers are encouraged to further explore this difference by comparing the therapeutic effects of both interventions concurrently. Moreover, Sano *et al.*[46] confirmed that inhaled H_2 treatment could be detected by instruments in pigs, and the concentration of H_2 can also be artificially controlled. Most importantly, the present paper suggests that priority should be given to H_2 gas inhalation in the treatment of ALI, or a combination treatment can be performed by inhaling hydrogen first and then administering hydrogen saline when ALI worsens.

4.2. Factors contributing to heterogeneity

According to the result of the meta-regression, we identified that species differences, particularly in SD rats, may contribute to heterogeneity. This finding can help researchers choose appropriate species and models for testing their hypotheses. In addition, it aids in extrapolating animal study findings into

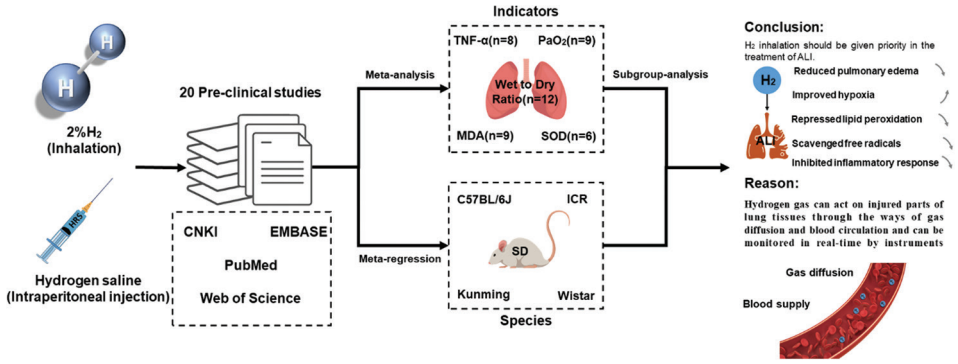

Figure 11. The summary of the meta-analysis.

clinical trials, thereby improving the feasibility of translating preclinical research. However, it is important to note that the results of this meta-regression are limited to rats and mice, and their applicability to other animal species remains uncertain. Furthermore, the GRADE assessment revealed that 40% of the indicators in the included studies had low or very low quality, which showed that most of the investigators did not adhere to relevant animal experiment guidelines, causing certain biases in the experiments. Therefore, it is essential for researchers to systematically search for all relevant experimental animal studies before designing or initiating new animal experiments or clinical trials[47].

4.3. Anti-inflammation mechanisms of hydrogen

Alveolar edema and pulmonary interstitial edema are hallmarks of ALI[48]. These symptoms are often the result of changes in the permeability of alveolar-capillary barriers. Neutrophils play a key role in the progression of ALI as they are the first cells recruited to the inflammatory site[49]. Orfanos *et al.*[50] reported that neutrophil infiltration in ALI can be divided into three stages: (i) Neutrophil capture and rolling; (ii) neutrophil adhesion; and (iii) neutrophil transmigration. In the first stage, endothelial cells are affected by cytokines like TNF-α, interleukin-1 (IL-1), or LPS and then release abundant adhesion molecules of the selectin family such as E-selectin and P-selectin to capture activated-neutrophils[51]. In the next stage, cytokines continue to be released, prompting the endothelium to release reactive oxygen species (ROS) and intercellular adhesion molecule-1, facilitating cell adhesion[52]. Finally, neutrophils transmigrate through the endothelium and cause infiltration. Myeloperoxidase, the main component of neutrophil activation and secretion, serves as an indicator of the degree of neutrophil infiltration in the alveolar cavity[53,54]. Several included studies used MPO from bronchoalveolar lavage fluid as the indicator to reflect neutrophil infiltration[20,22,26,27,29,33,34,37,38]. All these studies have demonstrated that molecular hydrogen can inhibit the expression level of MPO, reducing neutrophil infiltration and suppressing the release of inflammatory cytokines such as IL-1, IL-6, IL-8, and TNF-α cytokines in lung tissues. Ying and He[34] found that molecular hydrogen could ameliorate OA-induced ALI symptoms and inhibit the expression of NF-κB p65 proteins. Similarly, Liang *et al.*[31] showed that molecular hydrogen could inhibit p38MAPK protein activation, reduce downstream TNF-α expression, and attenuate inflammatory cell infiltration. Most importantly, these studies revealed that hydrogen not only inhibits the secretion of inflammatory cells such as neutrophils but also ameliorates ALI symptoms, modulates the expression of p38MAPK and NF-κB proteins, and blocks the release of cytokines. However, further studies are needed to identify the molecular mechanism of hydrogen in alleviating ALI.

Furthermore, several studies have shown that hydrogen can inhibit pulmonary fibrosis by regulating macrophage polarization. Macrophages can exhibit two phenotypes, M1 and M2[55]. Under normal physiological conditions, alveolar macrophages are predominantly of the M2 phenotype. However, during infection or injury, M2 macrophages can polarize into the M1 phenotype and release a large number of inflammatory mediators, inducing ALI to enter the exudation phase[56]. If injury and inflammation continue to occur, alveolar macrophages polarize will toward the M2 phenotype and release IL-6, TGF-β, IL-4, and other cytokines, leading to ALI entering the fibrosis stage[56,57]. Audi *et al.*[10] demonstrated that repeated inhalation of hydrogen could reduce persistent inflammation and prevent irreversible alveolar fibrosis.

4.4. Antioxidant mechanisms of hydrogen

The excessive production of ROS is the cause of damage to pulmonary vascular endothelial cells and dysfunction of alveolar epithelial cells[58]. Li *et al.*[23] demonstrated that hydrogen can eliminate ROS and enhance the expression of Nrf2 molecule. Under physiological conditions, Nrf2 molecule is localized in the cytoplasm and forms a complex with the

cytoplasmic protein chaperone Keap1, which inhibits Nrf2 activity. However, under the influence of oxidative stress, Nrf2 and Keap1 proteins dissociate and translocate into the nucleus. There, they bind to the GCTGAGTCA site of antioxidant response element (ARE) sequence proteins, inducing the expression of antioxidant proteins (SOD, CAT, etc.) and phase II detoxification enzymes, such as heme-oxygenase-1 (HO-1) to make the effect of anti-oxidative stress[59,60].

4.5. Limitations

This meta-analysis has several limitations. First, the number of studies available for inclusion in this meta-analysis is limited, although this meta-analysis is, to the best of our knowledge, the first to discuss how different administration methods of hydrogen affect the treatment effects of ALI animal models. Second, there is significant heterogeneity among the included studies, and the average quality scores of the studies are relatively low, indicating a potential publication bias. Third, there is a lack of research on the direct comparison between the effects of inhaling H_2 and injecting hydrogen saline. This limitation makes it difficult to further explore the effects and the relationship between treatment times for H_2 and hydrogen saline. Finally, the grade evidence indicates that the results of some included indicators may not be reliable, suggesting that there are certain issues with the experimental designs of the ALI animal models. Although the trim and fill funnel plot and sensitivity analysis provide some reassurance regarding the reliability of the meta-analysis results, it also underscores the needs for improving the design of animal experiments in future studies.

5. Conclusion

This meta-analysis provides evidence that the therapeutic potential of hydrogen in ALI is mediated through the inhibition of the relevant molecules and proteins related to the NF-κB and p38MAPK signaling pathways, which reduces inflammation. In addition, hydrogen plays a role in antioxidant stress by stimulating the expression of antioxidant proteins through the Nrf2/ARE signaling pathway. Furthermore, hydrogen can regulate neutrophil adhesion and macrophage polarization, suggesting its potential to inhibit idiopathic pulmonary fibrosis.

Acknowledgments

The authors would like to acknowledge the support provided by the Experimental Animal Center of Weifang Medical University.

Funding

This research was supported by the National Natural Science Foundation of China (No. 81600360), the Province Natural Science Foundation of Shandong (No. ZR2020KH008 and No. ZR2012HL18), the Province Science and Technology Development Foundation of Shandong (2014GSF118105), the Introduction Plan of Young Creative Talents in Colleges and Universities of Shandong Province (No. 205), and Shandong Province Technology Contract (2022370702103646).

Conflict of interest

The authors declare that there is no conflict of interest regarding the publication of this article.

Author contributions

Conceptualization: Guoshen Zhong, Nana Yang, Na Tian
Formal analysis: Guoshen Zhong, Lingyu Kong, Mei Yang
Investigation: Mei Yang
Methodology: Kaixuan Lv, Lichun Zhang
Writing – original draft: Guoshen Zhong
Writing – review & editing: Nana Yang, Yanhua Shi

Ethics approval and consent to participate

Not applicable.

Consent for publication

Not applicable.

Availability of data

All data used in the present paper can be obtained from the corresponding authors.

References

1. Butt Y, Kurdowska A, Allen TC, 2016, Acute lung injury: A clinical and molecular review. *Arch Pathol Lab Med*, 140: 345–350.

   https://doi.org/10.5858/arpa.2015-0519-RA

2. Matthay MA, Zemans RL, Zimmerman GA, *et al.*, 2019, Acute respiratory distress syndrome. *Nat Rev Dis Primers*, 5: 18.

   https://doi.org/10.1038/s41572-019-0069-0

3. Cardinal-Fernández P, Lorente JA, Ballén-Barragán A, *et al.*, 2017, Acute respiratory distress syndrome and diffuse alveolar damage. New insights on a complex relationship. *Ann Am Thorac Soc*, 14: 844–850.

   https://doi.org/10.1513/AnnalsATS.201609-728PS

4. Matthay MA, Ware LB, Zimmerman GA, 2012, The acute respiratory distress syndrome. *J Clin Invest*, 122: 2731–2740.

   https://doi.org/10.1172/JCI60331

5. Williams AE, José RJ, Mercer PF, *et al.*, 2017, Evidence for chemokine synergy during neutrophil migration in ARDS.

Thorax, 72: 66–73.

https://doi.org/10.1136/thoraxjnl-2016-208597

6. Mi MY, Matthay MA, Morris AH, 2018, Extracorporeal membrane oxygenation for severe acute respiratory distress syndrome. *N Engl J Med*, 379:884-887.

7. Steinberg KP, Hudson LD, Goodman RB, *et al.*, 2006, Efficacy and safety of corticosteroids for persistent acute respiratory distress syndrome. *N Engl J Med*, 354: 1671–1684.

https://doi.org/10.1056/NEJMoa051693

8. Villar J, Zhang H, Slutsky AS, 2019, Lung repair and regeneration in ARDS: Role of PECAM1 and Wnt signaling. *Chest*, 155:587-594.

9. Hu Q, Zhou Y, Wu S, *et al.*, 2020, Molecular hydrogen: A potential radioprotective agent. *Biomed Pharmacother*, 130: 110589.

https://doi.org/10.1016/j.biopha.2020.110589

10. Audi SH, Jacobs ER, Zhang X, *et al.*, 2017, Protection by inhaled hydrogen therapy in a rat model of acute lung injury can be tracked *in vivo* using molecular imaging. *Shock*, 48: 467–476.

https://doi.org/10.1097/SHK.0000000000000872

11. Zheng Y, Zhu D, 2016, Molecular hydrogen therapy ameliorates organ damage induced by sepsis. *Oxid Med Cell Longev*, 2016: 5806057.

https://doi.org/10.1155/2016/5806057

12. Aokage T, Seya M, Hirayama T, *et al.*, 2021, The effects of inhaling hydrogen gas on macrophage polarization, fibrosis, and lung function in mice with bleomycin-induced lung injury. *BMC Pulm Med*, 21: 339.

13. Zhang Y, Liu Y, Zhang J, 2015, Saturated hydrogen saline attenuates endotoxin-induced lung dysfunction. *J Surg Res*, 198: 41–49.

https://doi.org/10.1016/j.jss.2015.04.055

14. Zhang Y, Zhang J, Fu Z, 2022, Molecular hydrogen is a potential protective agent in the management of acute lung injury. *Mol Med*, 28: 27.

https://doi.org/10.1186/s10020-022-00455-y

15. Liberati A, Altman DG, Tetzlaff J, *et al.*, 2009, The PRISMA statement for reporting systematic reviews and meta-analyses of studies that evaluate healthcare interventions: Explanation and elaboration. *BMJ*, 339: b2700.

https://doi.org/10.1136/bmj.b2700

16. Macleod MR, O'Collins T, Howells DW, *et al.*, 2004, Pooling of animal experimental data reveals influence of study design and publication bias. *Stroke*, 35: 1203–1208.

https://doi.org/10.1161/01.STR.0000125719.25853.20

17. Higgins JP, Thompson SG, Deeks JJ, *et al.*, 2003, Measuring inconsistency in meta-analyses. *BMJ*, 327: 557–560.

https://doi.org/10.1136/bmj.327.7414.557

18. Deeks JJ, Higgins JPT, Altman DG, 2022, Analysing data and undertaking meta-analyses. In: Higgins JPT, Thomas J, Chandler J, *et al.*, editors. Cochrane Handbook for Systematic Reviews of Interventions Version 6.3. Ch. 10. United Kingdom: Cochrane.

19. Andrade C, 2020, Understanding the basics of meta-analysis and how to read a forest plot: As simple as it gets. *J Clin Psychiatry*, 81: 20f13698.

https://doi.org/10.4088/JCP.20f13698

20. Chen H, Xie K, Han H, *et al.*, 2012, Effect of hydrogen on acute lung injury in septic mice. *Chin J Anesthesiol*, 32: 195–197. (in Chinese)

21. Zhang H, Liu L, Yu Y, *et al.*, 2016, Role of Rho/ROCK signaling pathway in the protective effects of hydrogen against acute lung injury in septic mice. *Zhonghua Wei Zhong Bing Ji Jiu Yi Xue*, 28: 401–406. (in Chinese)

22. Xie K, Yu Y, Pei Y, *et al.*, 2010, Protective effects of hydrogen gas on murine polymicrobial sepsis via reducing oxidative stress and HMGB1 release. *Shock*, 34: 90–97.

https://doi.org/10.1097/SHK.0b013e3181cdc4ae

23. Li Y, Xie K, Chen H, *et al.*, 2014, Effects of hydrogen on nuclear factorE2-related factor 2/antioxidant response element pathway in lung tissues in septic mice. *Chin J Anesthesiol*, 34: 852–855. (in Chinese)

24. Liu G, Song D, Jiang Y, *et al.*, 2015, Effect of hydrogen-saline on lung injury and heme oxygenase-1 expression in the lung tissue of acute paraquat-intoxicated mice. *Zhonghua Lao Dong Wei Sheng Zhi Ye Bing Za Zhi*, 33: 337–341.

25. Mao L, Luo X, Luo Z, 2015, Early protective effect of hydrogen-saturated saline on lipopolysaccharide induced acute lung injury in mice. *J Pract Med*, 31: 14–16. (in Chinese)

26. Fang Y, Fu XJ, Gu C, *et al.*, 2011, Hydrogen-rich saline protects against acute lung injury induced by extensive burn in rat model. *J Burn Care Res*, 32: e82–e91.

https://doi.org/10.1097/BCR.0b013e318217f84f

27. Tian G, Liu F, Ji M, *et al.*, 2012, Effect of hydrogen-rich saline on sepsis induced acute lung injury in a rat model of sepsis. *Prog Mod Biomed*, 12: 6225–6227+6224. (in Chinese)

28. Bu Q, Yan Z, Li H, *et al.*, 2015, Effect of hydrogen inhalation on aquaporin expression in lung tissue of rats with hemorrhagic shock. *Shandong Med J*, 55: 25–27. (in Chinese)

29. Shi H, Zhou H, Jia Y, *et al.*, 2013, The effect of hydrogen on hemorrhagic shock induced acute lung injury in rats. *Zhonghua Wei Zhong Bing Ji Jiu Yi Xue*, 25: 6347–6350. (in Chinese)

30. Xu H, Qi Q, Wang B, *et al.*, 2019, Effects of high concentration hydrogen rich saline on lipopolysaccharide-induced acute lung injury in rats. *J Hebei Med Univ*, 40: 1372–1376.

31. Liang C, Liu X, Liu L, *et al.*, 2012, Effect of hydrogen inhalation on p38 MAPK activation in rats with lipopolysaccharide-induced acute lung injury. *Nan Fang Yi Ke Da Xue Xue Bao*, 32: 1211–1213.

32. Song X, Wang K, Wang L, *et al.*, 2016, Effect of hydrogen-rich saline on TLR4/MyD88 signaling pathway in rats with endotoxin-induced acute lung injury. *Chin J Anesthesiol*, 36: 120–122.

33. Ying Y, Xu H, Yao M, *et al.*, 2017, Protective effect of hydrogen-saturated saline on acute lung injury induced by oleic acid in rats. *J Orthop Surg Res*, 12: 134.

34. Ying Y, He J, 2011, Protective effect of hydrogen-rich saline on lung injury induced by oleic acids. *Chin J Crit Care Med*, 31: 426–429. (in Chinese)

35. Zhang HL, Liu YF, Luo XR, *et al.*, 2011, Saturated hydrogen saline protects rats from acute lung injury induced by paraquat. *World J Emerg Med*, 2: 149–153.

https://doi.org/10.5847/wjem.j.1920-8642.2011.02.013

36. Liu Q, Wang DW, Chen X, *et al.*, 2013, Protective effects of hydrogen gas on acute lung injury induced by smoke inhalation in rats and its dose-effect relationship. *J Tianjin Med Univ*, 19: 445–448. (in Chinese)

37. Zou R, Wang MH, Chen Y, *et al.*, 2019, Hydrogen-rich saline attenuates acute lung injury induced by limb ischemia/reperfusion via down-regulating Chemerin and NLRP3 in rats. *Shock*, 52: 134–141.

https://doi.org/10.1097/SHK.0000000000001194

38. Liu W, Shan LP, Dong XS, *et al.*, 2013, Combined early fluid resuscitation and hydrogen inhalation attenuates lung and intestine injury. *World J Gastroenterol*, 19: 492–502.

https://doi.org/10.3748/wjg.v19.i4.492

39. Song F, Parekh S, Hooper L, *et al.*, 2010, Dissemination and publication of research findings: An updated review of related biases. *Health Technol Assess*, 14: iii, ix–xi, 1–220.

https://doi.org/10.3310/hta14080

40. Moher D, Pham B, Lawson ML, *et al.*, 2003, The inclusion of reports of randomised trials published in languages other than English in systematic reviews. *Health Technol Assess*, 7: 1–90.

https://doi.org/10.3310/hta7410

41. Sterne JA, Sutton AJ, Ioannidis JP, *et al.*, 2011, Recommendations for examining and interpreting funnel plot asymmetry in meta-analyses of randomised controlled trials. *BMJ*, 343: d4002.

https://doi.org/10.1136/bmj.d4002

42. Sun H, Chen L, Zhou W, *et al.*, 2011, The protective role of hydrogen-rich saline in experimental liver injury in mice. *J Hepatol*, 54: 471–480.

https://doi.org/10.1016/j.jhep.2010.08.011

43. Liu C, Kurokawa R, Fujino M, *et al.*, 2014, Estimation of the hydrogen concentration in rat tissue using an airtight tube following the administration of hydrogen via various routes. *Sci Rep*, 4: 5485.

https://doi.org/10.1038/srep05485

44. Yamamoto R, Homma K, Suzuki S, *et al.*, 2019, Hydrogen gas distribution in organs after inhalation: Real-time monitoring of tissue hydrogen concentration in rat. *Sci Rep*, 9: 1255.

https://doi: 10.1038/s41598-018-38180-4

45. Watanabe M, Kamimura N, Iuchi K, *et al.*, 2017, Protective effect of hydrogen gas inhalation on muscular damage using a mouse hindlimb ischemia-reperfusion injury model. *Plast Reconstr Surg*, 140: 1195–1206.

46. Sano M, Ichihara G, Katsumata Y, *et al.*, 2020, Pharmacokinetics of a single inhalation of hydrogen gas in pigs. *PLoS One*, 15: e0234626.

https://doi.org/10.1371/journal.pone.0234626

47. Hooijmans CR, Ritskes-Hoitinga M, 2013, Progress in using systematic reviews of animal studies to improve translational research. *PLoS Med*, 10: e1001482.

https://doi.org/10.1371/journal.pmed.1001482

48. Pittet JF, Mackersie RC, Martin TR, *et al.*, 1997, Biological markers of acute lung injury: Prognostic and pathogenetic significance. *Am J Respir Crit Care Med*, 155: 1187–1205.

https://doi.org/10.1164/ajrccm.155.4.9105054

49. Grommes J, Soehnlein O, 2011, Contribution of neutrophils to acute lung injury. *Mol Med*, 17: 293–307.

https://doi.org/10.2119/molmed.2010.00138

50. Orfanos SE, Mavrommati I, Korovesi I, *et al.*, 2004, Pulmonary endothelium in acute lung injury: From basic science to the critically ill. *Intensive Care Med*, 30: 1702–1714.

51. Albelda SM, Smith CW, Ward PA, 1994, Adhesion molecules and inflammatory injury. *FASEB J*, 8: 504–512.

52. Lum H, Roebuck KA, 2001, Oxidant stress and endothelial cell dysfunction. *Am J Physiol Cell Physiol*, 280: C719–C741.

https://doi.org/10.1152/ajpcell.2001.280.4.C719

53. Perkins GD, Nathani N, McAuley DF, *et al.*, 2007, *In vitro* and *in vivo* effects of salbutamol on neutrophil function in acute lung injury. *Thorax*, 62: 36–42.

https://doi.org/10.1136/thx.2006.059410

54. Arnhold J, 2020, The dual role of myeloperoxidase in immune response. *Int J Mol Sci*, 21: 8057.

https://doi.org/10.3390/ijms21218057

55. Schultze JL, Schmidt SV, 2015, Molecular features of macrophage activation. *Semin Immunol*, 27: 416–423.

https://doi.org/10.1016/j.smim.2016.03.009

56. Huang X, Xiu H, Zhang S, *et al.*, 2018, The role of

macrophages in the pathogenesis of ALI/ARDS. *Mediators Inflamm*, 2018: 1264913.

https://doi.org/10.1155/2018/1264913

57. Chen X, Tang J, Shuai W, *et al.*, 2020, Macrophage polarization and its role in the pathogenesis of acute lung injury/acute respiratory distress syndrome. *Inflamm Res*, 69: 883–895.

https://doi.org/10.1007/s00011-020-01378-2

58. Liu Y, Zhou S, Xiang D, *et al*, 2021, Friend or foe? The roles of antioxidants in acute lung injury. *Antioxidants* (*Basel*), 10: 1956.

https://doi.org/10.3390/antiox10121956

59. Kensler TW, Wakabayashi N, Biswal S, 2007, Cell survival responses to environmental stresses via the Keap1-Nrf2-ARE pathway. *Annu Rev Pharmacol Toxicol*, 47: 89–116.

https://doi.org/10.1146/annurev.pharmtox.46.120604.141046

60. Kim JH, Choi YK, Lee KS, *et al.*, 2012, Functional dissection of Nrf2-dependent phase II genes in vascular inflammation and endotoxic injury using Keap1 siRNA. *Free Radic Biol Med*, 53: 629–640.

https://doi.org/10.1016/j.freeradbiomed.2012.04.019

ACCSCIENCE PUBLISHING

Global Translational Medicine

REVIEW ARTICLE

Essential roles of BRD4 in cancer: DNA damage, transcription regulation, and signal transduction

Sylvia Y. Sun[1,2]*

[1]Mortimer B. Zuckerman Research Center - Sloan Kettering Institute, 417 E 68th Street, New York, United States of America

[2]Department of Dental, New York University, 345 E. 24th Street, New York, United States of America

Abstract

During cancer progression, bromodomain and extra-terminal (BET) families regulate chromatin and recruit enzymes that are associated with chromatin regulation to control gene expression. The bromodomain-containing protein 4 (*BRD4*) plays an important role in DNA damage repair, nuclear factor kappa B (NFκB) signaling, interaction with c-Myc, and transcription regulation of genes essential in carcinogenesis, as well as links transcription at enhancers and genes to regulate enhancer transcription. The colocalization of BRD4 with enhancer and promoter-proximal gene regions enables the elongation activation at enhancer genes. The inactivation of BRD4 has been demonstrated to inhibit cancer development, corroborating BRD4 as a promising therapeutic target. In addition, small-molecule inhibitors targetting functional domains of BRD4 are under investigation for their potential therapeutic applications in cancer and other diseases. This review presents an overview of BRD4 function and its dysfunction in cancer progression, as well as discusses how the potential of BRD4 as a therapeutic target.

***Keywords*:** BRD4 signaling; Therapy; Cancer

***Corresponding author:**
Sylvia Y. Sun
(sys9221058@gmail.com)

Citation: Sun SY, 2023, Essential roles of BRD4 in cancer: DNA damage, transcription regulation, and signal transduction. *Global Transl Med*, 2(3): 1442. https://doi.org/10.36922/gtm.1442

Received: August 2, 2023
Accepted: September 22, 2023
Published Online: September 29, 2023

1. Introduction

Although initially recognized as epigenetic regulators in inflammation and inflammatory diseases, bromodomain and extra-terminal (BET) proteins, consisting of bromodomain-containing protein (BRD)2, BRD3, BRD4, and bromodomain testis-specific protein (BRDT) (Figure 1), are frequently deregulated in cancer, playing a significant role in tumorigenesis through the promotion of aberrant chromatin modeling and gene transcription[1,2]. BET families, including BRD4, share two N-terminus domains (N-terminal bromodomain, BD1 and N-terminal bromodomain, BD2) and a C-terminal domain (extra-terminal, ET domain). A high level of conservation exists among the bromodomains of different species, and the sequences of different BET family members are highly similar. The BD domains bind to acetylated lysine residues on histones, while the ET domain mediates protein-protein interactions and regulates transcriptional activity[3,4].

The bromodomains are conserved protein modules which share a high degree of sequence similarity in amino acid; however, each BET protein recruits a distinct set of transcriptional regulatory complexes. Through their unique protein domains outside

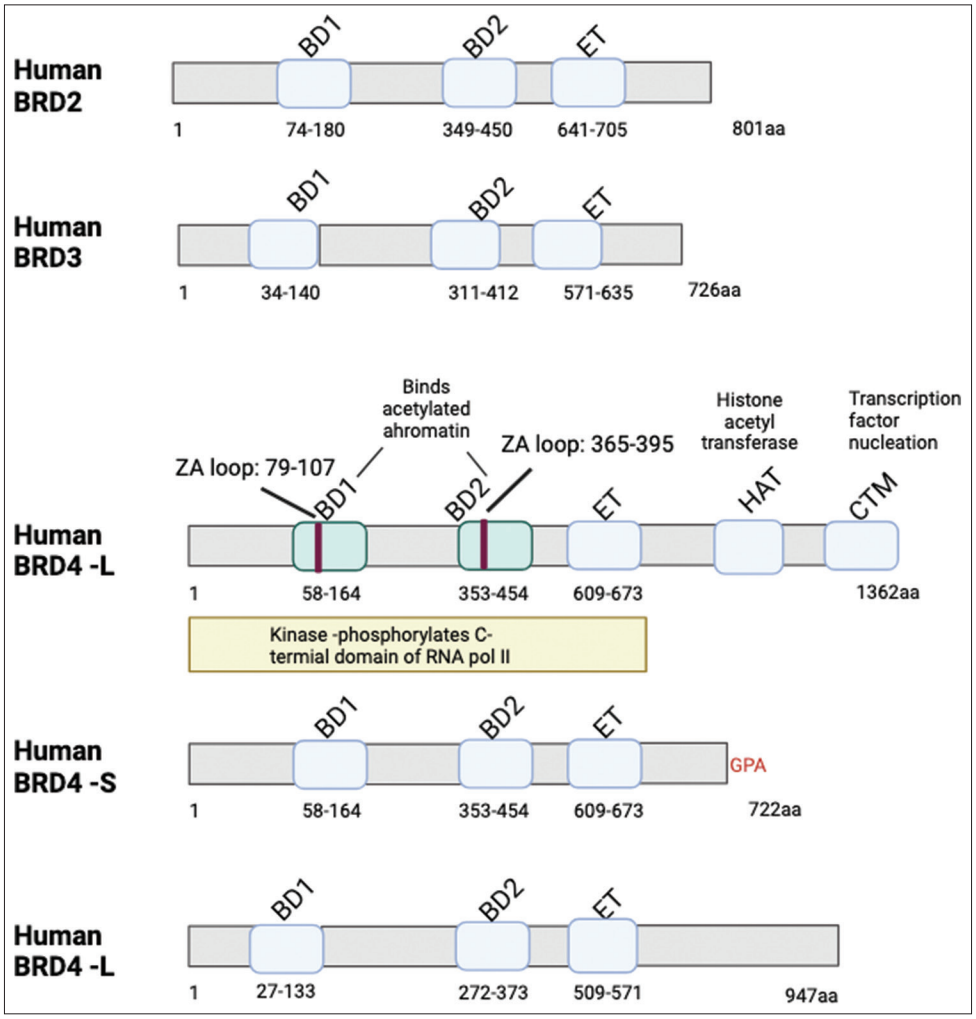

Figure 1. BRD4 and BET family isoform structure. Human BRD2, BRD3, BRD4, and BRDT isoforms are presented. There are two tandem bromodomains in BRD4 long isoforms (BRD4-L) that are incorporated into a protein with 200 kDa, one extra-terminal (ET) domain, histone acetyltransferase (HAT) activity, and a C-terminal domain (CTM). BD1 and BD2 domains are present in the BRD4 short isoform (BRD4-S), along with an ET domain and one C-terminal domain. As an additional protein-protein interaction domain, the ET domain is characteristic of members of the BET family.

their bromodomains, BET proteins, including BRD2, BRD3, BRD4, and BRDT, can recruit a distinct set of transcriptional regulatory complexes, thereby altering gene expression and cellular processes. For example, C terminus of BRD4 contains a conserved motif known as the P-TEFb interacting domain (PID), which interacts with the positive transcription elongation factor b (P-TEFb) and facilitates the recruitment of P-TEFb-containing complexes to chromatin. This results in the activation of RNA polymerase II and transcriptional elongation[5,6]. The ET domain of BRD4 plays a role in the recruitment of transcription modifiers, such as NSD3 histone methyltransferase and independently of the bromodomains[7]. In summary, the diverse functions of BET proteins and their recruitment of distinct transcriptional regulatory complexes stem from the interplay of different functional domains within their molecular structure.

Genetic events affecting *BRD4* may affect tumor initiation, progression, and metastasis. Genetic changes to *BRD4*, including gene rearrangements and mutations such as missense substitutions, in various human cancers have been reported[8]. *BRD4* gene rearrangements have been identified in hematological malignancies, such as NUT midline carcinoma (NMC), acute myeloid leukemia (AML), and multiple myeloma (MM). In NMC, *BRD4* is fused with the nuclear protein in testis (*NUT*) gene, giving rise to, if expressed, a chimeric protein that is thought to regulate pathogenesis of this aggressive and often lethal cancer. In AML, *BRD4* gene rearrangements result in *BRD4* overexpression, which promotes cancer cell proliferation and survival[6]. The oncogenic potential of mutated BRD4 has been found to be enhanced through several missense mutations resulting in amino acid substitutions in the two

terminal helices of BRD4 and in the region proximal to its acetyl-lysine docking site[9]. Bromodomains recognize acetylated histones and other proteins through these two helices, along with the ZA loop (Figure 1). Amino acid substitutions in these regions can alter the specificity and affinity of the acetyl-lysine binding pocket, leading to aberrant recruitment of transcriptional regulators and gene expression dysregulation. Several studies have identified specific amino acid substitutions in BRD4 that are associated with oncogenesis. For example, G485D in the αB helix has been shown to increase BRD4 interaction with acetylated histones and to promote cancer survival. Other substitutions in the αB and αC helices, such as E429V and P593L, have also been shown to promote oncogenic properties in various cancer types[9]. Overall, these findings underscore the importance of BRD4 as a transcriptional regulator in both normal cellular processes and carcinogenesis. In view of its dysregulation in cancer, BRD4 might serve as a prime candidate for therapeutic targeting, and more detailed studies are required to provide valuable insights into the molecular mechanisms driving tumorigenesis.

2. BRD4 enzymatic activities

BRD4 has two isoforms. BRD4 long isoform (BRD4-L) is a protein of 152 kDa that contains BD1 and BD2 domains, an ET domain, and a C-terminal domain, whereas BRD4 short isoform (BRD4-S), originally called HUNK1[10], is approximately 81 kDa and consists of BD1 and BD2 domains, an ET domain, and a C-terminal domain (Figure 1). Unless otherwise stated, the BRD4 mentioned in this review refers to BRD4-L only.

The enzymatic activities of BRD4 are distinctly different from those of other BET family proteins. Kinase and histone acetyltransferase (HAT) activity are enzyme functions intrinsic to BRD4, enabling the dynamic regulation of its interacting partners. Through its kinase activity, BRD4 phosphorylates many of its interacting partners, including c-Myc, TATA-box binding protein associated factor 7 (TAF7), P-TEFb, and most importantly, the C-terminal domain of RNA polymerase II[11], thereby directly controlling their transcription. BRD4 contains an HAT domain, which acetylates histone proteins in the nucleosome[12]. Following the histone acetylation by BRD4, the chromatin structure is loosened to enable DNA-histone interactions, increasing the access of transcription factors and regulatory proteins to DNA and then altering the cell behavior.

Other domains and motifs in BRD4 assist with the enzymatic activities or interact with multiple factors in a positive manner. On structural binding with N-terminus and C-terminus, the BRD4 complex can facilitate recruitment and interaction with other factors in a bigger extent[13]. The A motif is critical for its binding to the C-terminal domain of RNA polymerase II. The C-terminus of BRD4 binds to c-Myc and inhibits its HAT activity[12,14]. Taken together, the distinct enzyme domains of BRD4 contribute to transcriptional regulation by increasing the access of transcriptional regulators to chromatin.

3. BRD4 and transcriptional regulation

BRD4 has been shown to regulate transcription in both *in vivo* and *in vitro* models. The interaction between *BRD4* and chromosomes during mitosis could identify the genes whose transcription has already begun in G1 phase, which are required to ensure cell cycle progression[15-18]. Apart from that, BRD4 also helps to maintain embryonic stem cell characteristics, and it is essential during embryogenesis[19-21] and cell identity determination during both early phases and development. During early phases of embryogenesis, BRD4 regulates the self-renewal and pluripotency of embryonic stem cells by controlling Nanog[20] and OCT4[21]. *In vivo*, BRD4-deficient embryos, which lack sufficient BRD4 function, exhibit developmental defects, particularly during the early stages of development, which can lead to embryo lethality shortly after implantation[22]. The unfavorable outcome can be justified by its inability to maintain the inner cell mass, which is crucial for proper embryo development. BRD4 plays a crucial role in cell identity determination during development by selectively regulating lineage-specific genes. During embryonic development, pluripotent stem cells develop into various differentiated cell types through a process known as differentiation. This process is tightly controlled by transcriptional factors and epigenetic regulators, such as BRD4, which help establish and maintain cell identity[23]. In addition to its role in development, dysregulation of BRD4 activity has been implicated in the progression of various diseases.

BRD4 also serves as a transcriptional activator and a histone code reader (Figure 2)[24]. BRD4 is a recognized as transcription activator, even though it can also act as a transcriptional repressor[25,26]. In addition, BRD4 accumulates in hyperacetylated and transcriptionally-prone chromatin regions where it reads the histone code, where it acts as a nucleation center for large protein complexes whose function is to stimulate transcription initiation and elongation, leading to RNA polymerase II activity. Transcription factors transmit signals between enhancers and their target genes[27]. This function largely relies on BRD4 with its colocalization with genes and enhancer regions[28,29], as well as its BD domains and their ability to recognize acetyl proteins[10,11]. Bressin *et al.*

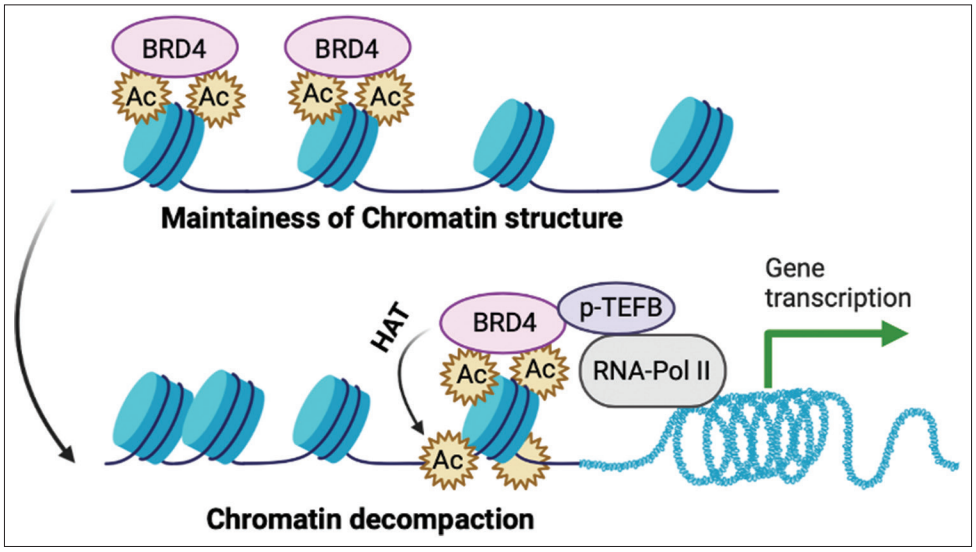

Figure 2. BRD4 is involved in the organization of chromatin and the transcription of genes. Through BRD4-L, histone acetylation is promoted, leading to the recruitment of more BRD4-L molecules. Subsequently, positive transcription elongation factor b (P-TEFb) binds to BRD4-L. Together, P-TEFb and BRD4-L reactivate gene transcription with the aid of RNA polymerase II in a pause-release manner. This figure is adapted and modified from Drumond-Bock and Bieniasz[24].

have recently shown, by means of high-sensitive nascent transcript sequencing, that BRD4 specifically controls enhancers and the target gene transcription, correlating the transcription of enhancers and genes[30]. Overall, BRD4 plays a critical role in transcription regulation, and its transcriptional activity has a bearing on cell development.

4. BRD4 and DNA damage repair

As a reader of the chromatin state, BRD4 is a major player in DNA damage repair. In general, genomic instability and cancer development induce DNA double-strand break (DSB) repair[31], and DNA damage response is thought to be regulated by histone modifications mediated by post-translational modifications[32]. BRD4 plays a role in transcriptionally independent DNA damage repair and acts as a master regulator of numerous genes. It is a core component of the DNA repair system and an activator of DNA damage checkpoints.

There BRD4 transcriptional activity depends on its ability to link histone modifications to DNA repair machinery, instead of DNA repair. In B lymphocytes, Stanlie *et al.* found that BRD4 is required for the activation-induced cytidine deaminase (AID) to complete class switch recombination following DSBs[33]. The study also demonstrated that BRD4 facilitates gene rearrangements in prostate cancer when induced by ionizing radiation to repair DNA DSBs. Using BET inhibitor or specific silencer to inhibit BRD4 causes increased phosphorylated H2AX and persistent DNA damage, leading to genomic catastrophe and eventual cell death[34]. BRD4 contributes to DNA repair by modifying histones and DNA repair machinery. As these modifications accumulate at both ends of the breaks, BRD4 is recruited, which serves as docking sites for DNA repair enzymes.

The p53 binding protein (53BP1), a major binding partner of BRD4, is among the DNA repair components that coimmunoprecipitate with BRD4[33,34]. As a molecular scaffold[35,36] and recruiter of DSB-responsive proteins, 53BP1 is recruited by DSB-specific histone to damage chromatin. 53BP1 recruitment to ionizing radiation-induced DSB is abrogated when BRD4 is inhibited, as demonstrated by Li *et al.*[34]. Similarly, BRD4, which functions upstream of 53BP1, guides it to DSBs since silencing of 53BP1 does not affect BRD4 binding (Figure 3)[35], and 53BP1 binding to DNA repair complexes on site is likely to be stabilized by interaction with BRD4 at DSBs[37].

The inhibition of BRD4 results in a decreased expression of genes in non-homologous end joining (NHEJ) pathway. In addition, BRD4 promotes NHEJ activity, as well as DNA damage checkpoint activation[38,39]. Replication stress is a complex phenomenon induced by, among others, oncogenes that increase DNA transcription and replication[40]. Activation of ATR and CHK1 kinase axes occurs when the replication fork structure exposes single-stranded DNA[41]. When the DNA damage checkpoint malfunctions, the replication fork collapses and DNA DSBs occur, followed by chromosome rearrangements[42]. Chromatin associated with BRD4 is known to be associated with replication forks. DNA replication initiation is licensed by CDC6, and BRD4 is involved in this process. When

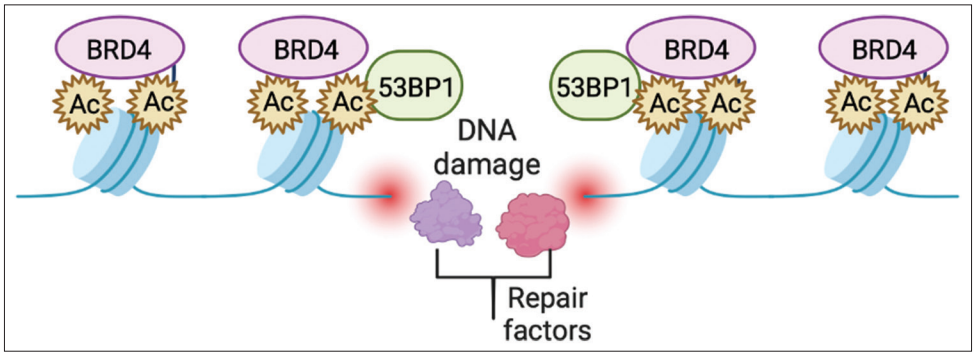

Figure 3. An illustration of how BRD4 participates in double-strand break (DSB) repair. H4Ac and γH2AX accumulate at DSBs, triggering BRD4 recruitment. Assembly and activation of DNA repair machinery are facilitated and stabilized by BRD4, which facilitates and stabilizes 53BP1. This figure is adapted from Drumond-Bock and Bieniasz[24].

BRD4 is inhibited, cells can be exposed to stress-inducing agents due to a defective DNA damage checkpoint[39]. Thus, in view of the above, targeting the DNA damage repair pathway (DDR) in the treatment of cancers whose DNA damage repair components are defective could be a promising therapeutic approach[43-47].

5. The opposite roles of BRD4-L and BRD4-S

BRD4 plays a crucial role in DDR[34,48,49]. The BRD4-L isoform regulates the transcription of genes involved in DNA repair and NHEJ genes[33,48]. It also binds and modulates NHEJ protein complexes. In contrast, BRD4-S isoform has been reported to act as an endogenous inhibitor of DNA repair complexes in the DDR (Figure 4)[38,48] and protect chromatin from the DDR machinery in the presence of DNA damage[48,50,51] by stably binding to DNA molecules. Further, BRD4-S recruits condensation II complex components, preventing DDR propagation by inducing chromatin condensation. BRD4-L promotes NHEJ DNA repair, which is however inhibited by BRD4-S, pointing to the opposite roles of BRD4-L and BRD4-S in DNA repair machinery.

6. Functions of BRD4 in cancer

6.1. Expression of BRD4 in cancers

Enhanced BRD4 activity in cancer patients leads to increased expression of MYC, NOTCH3, and NRG1. In addition to a high proliferation rate and genetic instability, cancer cells expressing BRD4 are capable of epithelial-mesenchymal transition and metastasis, as well as exhibit chemotherapy resistance[24].

Aberrant promoter hypermethylation often causes BRD4 downregulation in primary colon cancer tumors and cell lines. It is suggested that BRD4 plays a role in human colon cancer by inducing ectopic re-expression in these colon cancer cell lines; however, more studies are warranted to determine whether BRD4 plays a role in this cancer type[52].

6.2. BRD4 and NFκB signaling

BRD4 is involved in NFκB-dependent promoter and super-enhancer modulation, while NFκB signaling blocks cognate transcriptional elements and activates cognate promoters. P-TEFb can be recruited by BRD4 to NFκB-dependent acetylated histones through caspase-3 to achieve primary response gene transcription[53]. It is also possible that NFκB-dependent signaling in cancer cells may enhance orphan disease pathology[52].

BRD4 also modulates non-histone proteins, such as coactivator RELA. Acetylated RELA binds to BRD4, increasing its transactivation activity in the nucleus. The previous studies have shown that RELA/p65 is phosphorylated at serine 276 and 536, thereby facilitating the recruitment of p300/CBP histone acetyl-transferase in the RELA/BRD4 interaction[54]. STAT3-dependent phosphorylation of RELA increases RELA acetylation by p300/CBP, contributing to constitutive NFκB activity in tumors[55,56]. It is noteworthy that SETD6 monomethylates lysine 310 in RELA and has been demonstrated to interact with EHMT1/GLP histone methyltransferase at chromatin, helping contribute to the control of NFκB signaling at target promoters[57]. Activation-dependent phosphorylation of serine 311 blocks monomethylation of RELA/p65 lysine 310. Taken together, these findings corroborate a close connection between NFκB and BET protein family signaling through BRD4.

6.3. BRD4 and c-Myc as a couple

Several cancer types have shown that the oncogene *MYC* is regulated by super-enhancer elements[58-61]. c-Myc oncoprotein is a central regulator of gene expression that exerts a profound influence on various cellular processes. It has been estimated that a substantial portion of human

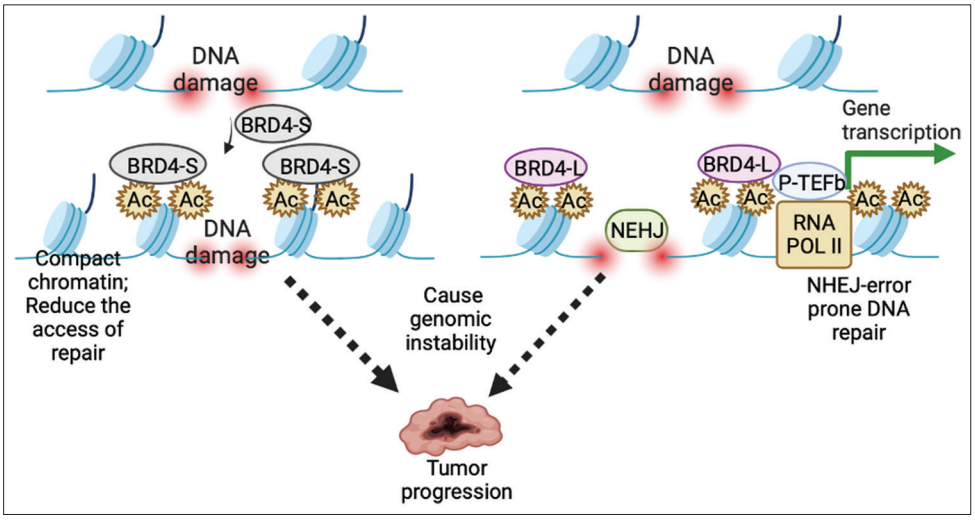

Figure 4. Molecular mechanisms of DNA damage response mediated by BRD4 isoforms. DNA damage repair machinery (DDR) is prevented from repairing damaged DNA due to the BRD4-S protein stably bound to the DNA molecules. BRD4-S promotes chromatin compaction by binding lysine-acetylated histones (Ac). NHEJ DNA repair is facilitated by BRD4-L. BRD4-L isoform activates the transcription of NHEJ genes and stabilizes NHEJ protein complexes in DNA damage site. By decreasing DDR and promoting error-prone NHEJ, increased activity of either or both isoforms can cause genomic instability. This figure is adapted from Drumond-Bock and Bieniasz[24].

genome-wide genes are under the control of the MYC protein[62]. c-Myc and BRD4 together play a crucial role in cell biology and diseases. They act as transcription and chromatin regulators for a wide array of genes. Evidence suggests that transcriptional and post-transcriptional regulation of MYC is tightly intertwined with BRD4. It has been found that BET inhibitors[63,64] regulate c-Myc levels through BRD4. Mechanistically, the acetyl lysine-binding pockets of BET proteins are occluded by these inhibitors, which mimicking the acetyl moiety and inhibiting tumor growth by reducing oncogene expression[65]. Most of these inhibitors are currently evaluated for their therapeutic efficacy in hematological and solid cancers under early-phase clinical trials.

6.4. BRD4 and retinoblastoma protein

Ding *et al.* (2022) demonstrated that retinoblastoma (RB)-inhibited cancers possess an increased resistance to BET inhibitors[66]. As an inhibitor of cancer-promoting activities, RB protein interacts with E2F family proteins to inhibit accelerated cell cycle progression[67]. Researchers have shown that the RB amino-terminal region interacts with the FXXXV motif of client proteins, such as EP300 interacting inhibitor of differentiation 1 (EID1) and p65, to regulate cancers[68,69]. The levels of GNBIL protein in prostate cancer are positively correlated with the levels of S249/T252-phosphorylated RB. Genes enriched in pathways such as the GPCR/GNBIL/CREB signaling are enriched in BRD4 proteins upon RB knockdown. Thus, BRD4 can be intrinsically inhibited by RB protein, and the inactivation of RB protein confers resistance to small-molecule inhibitors of BET.

7. Post-translational modifications of BRD4

Post-translational modifications are critical to the role of BRD4 in tumors. At present, ubiquitination and phosphorylation are the primary post-translational modifications of BRD4[70]. BRD4 protein structure, stability, and biological function are impacted by the diversity, complexity, and reversibility of post-translational modifications, which also play a role in tumor progression and development by regulating the expression of tumor-related genes.

7.1. Ubiquitination

The accumulation of BRD4 protein is the key determinant of the development of BET inhibitor resistance as well as the requisite for tumor development, which has been demonstrated to be associated with E3 ubiquitin ligase adaptor Speckle-type POZ protein (SPOP). SPOP facilitates proteasome degradation by ubiquitinating and degrading BRD4, which is a polyubiquitination target[71-73]. By increasing the level of BRD4 protein, SPOP-mediated BRD4 protein degradation disorder contributes to prostate cancer formation[74]. SPOP mutations in endometrial cancer drive more rapid degradation of BRD4 protein, making the cancer cells susceptible to BET inhibitors. There is currently no clear mechanism as to how the SPOP mutation leads to BRD4 protein degradation; however, how BRD4 protein accumulation facilitates BET

Table 1. Examples of BET inhibitors

BET inhibitors	Functions
JQ1	Inhibition of tumor cell proliferation and promotion of tumor cell apoptosis are achieved through JQ1 suppressing the target genes of BRD4[63,77].
Molibresib (GSK525762)	GSK525762 has antitumor activity in preclinical models of carcinoma and non-small cell lung cancer[78,79].
OTX-015 (MK-8628)	NSCLC cell lines translocated with or without EML4-ALK undergo reduced proliferation and are arrested in the cell cycle when treated with OTX015[80].
I-BET151(GSK1210151A)	BET151 inhibits BET selectively and functions similarly to temozolomide. I-BET151 decreases cell percentage in S/G2 phase and increases cell apoptosis in a dose-dependent manner in six myeloma cell lines[78].
BI894999	BRD-NUT is rapidly dislodged from chromatin following BI894999 treatment[81].

BET: Bromodomain and extra-terminal

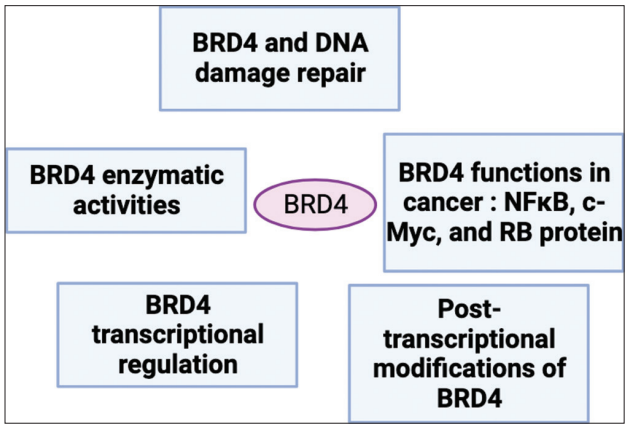

Figure 5. A summary of bromodomain-containing protein 4 (BRD4) functions. BRD4 is involved in DNA repair, transcriptional regulation, and post-translational modifications, as well as regulation of cancer progression.

inhibitor resistance and tumor development has been mechanistically deciphered.

7.2. Phosphorylation

It has been demonstrated that phosphorylating BRD4 at the tyrosine 97/98 (Y97/98) site could improve the binding of BRD4 to chromatin but decrease binding to BET inhibitor, which gives rise to BET inhibitor resistance. BRD4 is phosphorylated at Y97/98 by the matrix signal IL-6/8 (IL-6/8-JAK2) in colorectal cancer[75]. Further experiments showed that BRD4 phosphorylation at Y97/98 promotes interaction with STAT3 in the tumor microenvironment and promotes the transcriptional program through chromatin remodeling and activation of carcinogenic enhancers, such as MYC, CXCL1, and CXCL2. This study provides insights into a more effective cancer treatment that emphasized on the inhibition of IL6/IL8-JAK2 signaling to reduce phosphorylation of BRD4 and sensitize the cancer cells to BET inhibitors.

8. BET inhibitors

The BET inhibitor prevents protein-protein interactions between acetylated histones and transcription factors by binding reversibly to the bromodomains of the BRD2 and BRD3 proteins[25,76]. Some noteworthy BET inhibitors are listed in Table 1.

9. Conclusion

BRD4 and BET family members are epigenetic readers, writers, and erasers, which are implicated in cancer development. BRD4 and its BET family protein play essential roles in DNA damage repair, NFκB signaling, interaction with c-Myc, and transcription regulation of essential in cancers, as well as link transcription at enhancers and genes to regulate enhancer transcription. In addition, post-translational modifications also play critical roles in BRD4-mediated tumorigenesis (Figure 5). Colocalization of BRD4 to enhancer and promoter-proximal gene regions enables elongation activation at enhancer genes. As BRD4 inactivation could inhibit cancer development, BRD4 is now recognized as a promising therapeutic target. Meanwhile, by regulating tumor-related gene expressions, post-translational modification functions of BRD4 contribute to the development of tumors. Apart from that, BRD4 inhibition induces chromatin remodeling and leads to the regulation of oncogenes responsible for tumor progression. To address the BRD4-mediated carcinogenesis, small-molecule inhibitors targeting functional domains of BRD4 and BET family proteins are currently under investigation.

Acknowledgments

None.

Funding

None.

Conflict of interest

The author declares no conflicts of interest.

Author contributions

This is a single-authored paper.

Ethics approval and consent to participate

Not applicable.

Consent for publication

Not applicable.

Availability of data

Not applicable.

References

1. Deeney JT, Belkina AC, Shirihai OS, *et al*., 2016, BET bromodomain proteins Brd2, Brd3 and Brd4 selectively regulate metabolic pathways in the pancreatic β-cell. *PLoS One*, 11: e0151329.

   https://doi.org/10.1371/journal.pone.0151329

2. Marazzi I, Greenbaum BD, Low DH, *et al*., 2018, Chromatin dependencies in cancer and inflammation. *Nat Rev Mol Cell Biol*, 19: 245–261.

   https://doi.org/10.1038/nrm.2017.11

3. Jones MH, Numata M, Shimane M, 1997, Identification and characterization of BRDT: A testis-specific gene related to the bromodomain genes RING3 and *Drosophila* fsh. *Genomics*, 45: 529–534.

   https://doi.org/10.1006/geno.1997.5000

4. Shang E, Nickerson HD, Wen D, *et al*., 2007, The first bromodomain of Brdt, a testis-specific member of the BET sub-family of double-bromodomain-containing proteins, is essential for male germ cell differentiation. *Development*, 134: 3507–3515.

   https://doi.org/10.1242/dev.004481

5. Zhou Q, Li T, Price DH, 2012, RNA polymerase II elongation control. *Annu Rev Biochem*, 81: 119–143.

   https://doi.org/10.1146/annurev-biochem-052610-095910

6. French CA, 2016, Small-molecule targeting of BET proteins in cancer. *Adv Cancer Res*, 131: 21–58.

   https://doi.org/10.1016/bs.acr.2016.04.001

7. Liu Z, Wang P, Chen H, *et al*., 2017, Drug discovery targeting bromodomain-containing protein 4. *J Med Chem*, 60: 4533–4558.

   https://doi.org/10.1021/acs.jmedchem.6b01761

8. Bradner JE, Hnisz D, Young RA, 2017, Transcriptional addiction in cancer. *Cell*, 168: 629–643.

   https://doi.org/10.1016/j.cell.2016.12.013

9. Lori L, Pasquo A, Lori C, *et al*., 2016, Effect of BET missense mutations on bromodomain function, inhibitor binding and stability. *PLoS One*, 11: e0159180.

   https://doi.org/10.1371/journal.pone.0159180

10. Wu SY, Chiang CM, 2007, The double bromodomain-containing chromatin adaptor Brd4 and transcriptional regulation. *J Biol Chem*, 282: 13141–13145.

    https://doi.org/10.1074/jbc.R700001200

11. Devaiah BN, Gegonne A, Singer DS, 2016, Bromodomain 4: A cellular Swiss army knife. *J Leukoc Biol*, 100: 679–686.

    https://doi.org/10.1189/jlb.2RI0616-250R

12. Devaiah BN, Case-Borden C, Gegonne A, *et al*., 2016, BRD4 is a histone acetyltransferase that evicts nucleosomes from chromatin. *Nat Struct Mol Biol*, 23: 540–548.

    https://doi.org/10.1038/nsmb.3228

13. Malvezzi F, Stubbs CJ, Jowitt TA, *et al*., 2021, Phosphorylation-dependent BRD4 dimerization and implications for therapeutic inhibition of BET family proteins. *Commun Biol*, 4: 1273.

    https://doi.org/10.1038/s42003-021-02750-6

14. Devaiah BN, Mu J, Akman B, *et al*., 2020, MYC protein stability is negatively regulated by BRD4. *Proc Natl Acad Sci U S A*, 117: 13457–13467.

    https://doi.org/10.1073/pnas.1919507117

15. Dey A, Ellenberg J, Farina A, *et al*., 2000, A bromodomain protein, MCAP, associates with mitotic chromosomes and affects G(2)-to-M transition. *Mol Cell Biol*, 20: 6537–6549.

    https://doi.org/10.1128/MCB.20.17.6537-6549.2000

16. Dey A, Nishiyama A, Karpova T, *et al*., 2009, Brd4 Marks select genes on mitotic chromatin and directs Postmitotic transcription. *Mol Biol Cell*, 20: 4899–4909.

    https://doi.org/10.1091/mbc.e09-05-0380

17. Mochizuki K, Nishiyama A, Jang MK, *et al*., 2008, The bromodomain protein Brd4 stimulates G1 gene transcription and promotes progression to S phase. *J Biol Chem*, 283: 9040–9048.

    https://doi.org/10.1074/jbc.M707603200

18. Yang ZY, He N, Zhou Q, 2008, Brd4 recruits P-TEFb to chromosomes at late mitosis to promote G1 gene expression and cell cycle progression. *Mol Cell Biol*, 28: 967–976.

    https://doi.org/10.1128/MCB.01020-07

19. Di Micco R, Fontanals-Cirera B, Low V, *et al*., 2014, Control of embryonic stem cell identity by BRD4-dependent transcriptional elongation of super-enhancer-associated pluripotency genes. *Cell Rep*, 9: 234–247.

    https://doi.org/10.1016/j.celrep.2014.08.055

20. Liu W, Stein P, Cheng X, *et al*., 2014, BRD4 regulates Nanog expression in mouse embryonic stem cells and preimplantation embryos. *Cell Death Differ*, 21: 1950–1660.

    https://doi.org/10.1038/cdd.2014.124

21. Wu T, Pinto HB, Kamikawa YF, *et al*., 2015, The BET

family member BRD4 interacts with OCT4 and regulates pluripotency gene expression. *Stem Cell Reports*, 4: 390–403.

https://doi.org/10.1016/j.stemcr.2015.01.012

22. Houzelstein D, Bullock SL, Lynch DE, *et al*., 2002, Growth and early postimplantation defects in mice deficient for the bromodomain-containing protein Brd4. *Mol Cell Biol*, 22: 3794–3802.

https://doi.org/10.1128/MCB.22.11.3794-3802.2002

23. Lee JE, Park YK, Park S, *et al*., 2017, Brd4 binds to active enhancers to control cell identity gene induction in adipogenesis and myogenesis. *Nat Commun*, 8: 2217.

https://doi.org/10.1038/s41467-017-02403-5

24. Drumond-Bock AL, Bieniasz M, 2021, The role of distinct BRD4 isoforms and their contribution to high-grade serous ovarian carcinoma pathogenesis. *Mol Cancer*, 20: 145.

https://doi.org/10.1186/s12943-021-01424-5

25. Shi J, Vakoc CR, 2014, The mechanisms behind the therapeutic activity of BET bromodomain inhibition. *Mol Cell*, 54: 728–736.

https://doi.org/10.1016/j.molcel.2014.05.016

26. Wu SY, Lee AY, Hou SY, *et al*, 2006, Brd4 links chromatin targeting to HPV transcriptional silencing. *Genes Dev*, 20: 2383–2396.

https://doi.org/10.1101/gad.1448206

27. Karr JP, Ferrie JJ, Tjian R, *et al*., 2021, The transcription factor activity gradient (TAG) model: Contemplating a contact-independent mechanism for enhancer-promoter communication. *Gene Dev*, 36: 7–16.

https://doi.org/10.1101/gad.349160.121

28. Winter GE, Mayer A, Buckley DL, *et al*., 2017, BET bromodomain proteins function as master transcription elongation factors independent of CDK9 recruitment. *Mol Cell*, 67: 5–18.e19.

https://doi.org/10.1016/j.molcel.2017.06.00

29. Rahnamoun H, Lee J, Sun Z, *et al*., 2018, RNAs interact with BRD4 to promote enhanced chromatin engagement and transcription activation. *Nat Struct Mol Biol*, 25: 687–697. https://doi.org/10.1038/s41594-018-0102-0

30. Bressin A, Jasnovidova O, Arnold M, *et al*., 2023, High-sensitive nascent transcript sequencing reveals BRD4-specific control of widespread enhancer and target gene transcription. *Nat Commun*, 14: 4971.

https://doi.org/10.1038/s41467-023-40633-y

31. Mani RS, Chinnaiyan AM, 2010, Triggers for genomic rearrangements: Insights into genomic, cellular and environmental influences. *Nat Rev Genet*, 11: 819–829.

https://doi.org/10.1038/nrg2883

32. Misteli T, Soutoglou E, 2009, The emerging role of nuclear architecture in DNA repair and genome maintenance. *Nat Rev Mol Cell Biol*, 10: 243–254.

https://doi.org/10.1038/nrm2651

33. Stanlie A, Yousif AS, Akiyama H, *et al*., 2014, Chromatin reader Brd4 functions in Ig class switching as a repair complex adaptor of nonhomologous end-joining. *Mol Cell*, 55: 97–110.

https://doi.org/10.1016/j.molcel.2014.05.018

34. Li X, Baek G, Ramanand SG, *et al*., 2018, BRD4 promotes DNA repair and mediates the formation of TMPRSS2-ERG gene rearrangements in prostate cancer. *Cell Rep*, 22: 796–808.

https://doi.org/10.1016/j.celrep.2017.12.078

35. Schultz LB, Chehab NH, Malikzay A, *et al*., 2000, p53 binding protein 1 (53BP1) is an early participant in the cellular response to DNA double-strand breaks. *J Cell Biol*, 151: 1381–1390.

https://doi.org/10.1083/jcb.151.7.1381

36. Wang B, Matsuoka S, Carpenter PB, *et al*., 2002, 53BP1, a mediator of the DNA damage checkpoint. *Science*, 298: 1435–1438.

https://doi.org/10.1126/science.1076182

37. Sabari BR, Dall'Agnese A, Boija A, *et al*., 2018, Coactivator condensation at super-enhancers links phase separation and gene control. *Science*, 361: eaar3958.

https://doi.org/10.1126/science.aar3958

38. Floyd SR, Pacold ME, Huang Q, *et al*., 2013, The bromodomain protein Brd4 insulates chromatin from DNA damage signalling. *Nature*, 498: 246–225.

https://doi.org/10.1038/nature12147

39. Zhang J, Dulak AM, Hattersley MM, *et al*., 2018, BRD4 facilitates replication stress-induced DNA damage response. *Oncogene*, 37: 3763–3777.

https://doi.org/10.1038/s41388-018-0194-3

40. Zeman MK, Cimprich KA, 2014, Causes and consequences of replication stress. *Nat Cell Biol*, 16: 2–9.

https://doi.org/10.1038/ncb2897

41. Zhou BB, Bartek J, 2004, Targeting the checkpoint kinases: Chemosensitization versus chemoprotection. *Nat Rev Cancer*, 4: 216–225.

https://doi.org/10.1038/nrc1296

42. Gelot C, Magdalou I, Lopez BS, 2015, Replication stress in mammalian cells and its consequences for mitosis. *Genes* (*Basel*), 6: 267–298.

https://doi.org/10.3390/genes6020267

43. Cheung-Ong K, Giaever G, Nislow C, 2013, DNA-damaging agents in cancer chemotherapy: Serendipity and chemical biology. *Chem Biol*, 20: 648–659.

https://doi.org/10.1016/j.chembiol.2013.04.007

44. Ledermann JA, Harter P, Gourley C, *et al*., 2016, Overall survival in patients with platinum-sensitive recurrent serous ovarian cancer receiving olaparib maintenance monotherapy: An updated analysis from a randomised, placebo-controlled, double-blind, phase 2 trial. *Lancet Oncol*, 17: 1579–1589.

https://doi.org/10.1016/S1470-2045(16)30376-X

45. Ledermann JA, Harter P, Gourley C, *et al*., 2016, Overall survival (OS) in patients (pts) with platinum-sensitive relapsed serous ovarian cancer (PSR SOC) receiving olaparib maintenance monotherapy: An interim analysis. *J Clin Oncol*, 34: 5501.

https://doi.org/10.1200/JCO.2016.34.15_suppl.5501

46. Zimmer AS, Gillard M, Lipkowitz S, *et al*., 2018, Update on PARP inhibitors in breast cancer. *Curr Treat Options Oncol*, 19: 21.

https://doi.org/10.1007/s11864-018-0540-2

47. Sun CY, Yin J, Fang Y, *et al*., 2018, BRD4 inhibition is synthetic lethal with PARP inhibitors through the induction of homologous recombination deficiency. *Cancer Cell*, 33: 401–416.e8.

https://doi.org/10.1016/j.ccell.2018.01.019

48. Donati B, Lorenzini E, Ciarrocchi A, 2018, BRD4 and cancer: Going beyond transcriptional regulation. *Mol Cancer*, 17: 164.

https://doi.org/10.1186/s12943-018-0915-9

49. Gee ME, Faraahi Z, McCormick A, *et al*., 2018, DNA damage repair in ovarian cancer: Unlocking the heterogeneity. *J Ovarian Res*, 11: 50.

https://doi.org/10.1186/s13048-018-0424-x

50. Dey A, Chitsaz F, Abbasi A, *et al*., 2003, The double bromodomain protein Brd4 binds to acetylated chromatin during interphase and mitosis. *Proc Natl Acad Sci U S A*, 100: 8758–8763.

https://doi.org/10.1073/pnas.1433065100

51. Choi S, Bakkenist CJ, 2013, Brd4 shields chromatin from ATM kinase signaling storms. *Sci Signal*, 6: pe30.

https://doi.org/10.1126/scisignal.2004622

52. Rodriguez RM, Huidobro C, Urdinguio RG, *et al*., 2012, Aberrant epigenetic regulation of bromodomain BRD4 in human colon cancer. *J Mol Med* (*Berl*), 90: 587–595.

https://doi.org/10.1007/s00109-011-0837-0

53. Filippakopoulos P, Knapp S, 2014, Targeting bromodomains: Epigenetic readers of lysine acetylation. *Nat Rev Drug Discov*, 13: 337–356.

https://doi.org/10.1038/nrd4286

54. Brasier AR, Tian B, Jamaluddin M, *et al*., 2011, RelA Ser276 phosphorylation-coupled Lys310 acetylation controls transcriptional elongation of inflammatory cytokines in respiratory syncytial virus infection. *J Virol*, 85: 11752–11769.

https://doi.org/10.1128/JVI.05360-11

55. Zou Z, Huang B, Wu X, *et al*., 2014, Brd4 maintains constitutively active NF-κB in cancer cells by binding to acetylated RelA. *Oncogene*, 33: 2395–2404.

https://doi.org/10.1038/onc.2013.179

56. Lee H, Herrmann A, Deng JH, *et al*., 2009, Persistently activated Stat3 maintains constitutive NF-kappaB activity in tumors. *Cancer Cell*, 15: 283–293.

https://doi.org/10.1016/j.ccr.2009.02.015

57. Levy D, Kuo AJ, Chang Y, *et al*., 2011, Lysine methylation of the NF-κB subunit RelA by SETD6 couples activity of the histone methyltransferase GLP at chromatin to tonic repression of NF-κB signaling. *Nat Immunol*, 12: 29–36.

https://doi.org/10.1038/ni.1968

58. Chapuy B, McKeown MR, Lin CY, *et al*., 2013, Discovery and characterization of super-enhancer-associated dependencies in diffuse large B cell lymphoma. *Cancer Cell*, 24: 777–790.

https://doi.org/10.1016/j.ccr.2013.11.003

59. Delmore JE, Issa GC, Lemieux ME, *et al*., 2011, BET bromodomain inhibition as a therapeutic strategy to target c-Myc. *Cell*, 146: 904–917.

https://doi.org/10.1016/j.cell.2011.08.017

60. Gröschel S, Sanders MA, Hoogenboezem R, *et al*., 2014, A single oncogenic enhancer rearrangement causes concomitant EVI1 and GATA2 deregulation in leukemia. *Cell*, 157: 369–381.

https://doi.org/10.1016/j.cell.2014.02.019

61. Glodzik D, Morganella S, Davies H, *et al*., 2017, A somatic-mutational process recurrently duplicates germline susceptibility loci and tissue-specific super-enhancers in breast cancers. *Nat Genet*, 49: 341–348.

https://doi.org/10.1038/ng.3771

62. Dang CV, O'Donnell KA, Zeller KI, *et al*., 2006, The c-Myc target gene network. *Semin Cancer Biol*, 16: 253–264.

https://doi.org/10.1016/j.semcancer.2006.07.014

63. Filippakopoulos P, Qi J, Picaud S, *et al*., 2010, Selective inhibition of BET bromodomains. *Nature*, 468: 1067–1073.

https://doi.org/10.1038/nature09504

64. Nicodeme E, Jeffrey KL, Schaefer U, *et al*., 2010, Suppression of inflammation by a synthetic histone mimic. *Nature*, 468: 1119–1123.

https://doi.org/10.1038/nature09589

65. Mertz JA, Conery AR, Bryant BM, *et al*., 2011, Targeting MYC dependence in cancer by inhibiting BET bromodomains.

Proc Natl Acad Sci U S A, 108: 16669–16674.

https://doi.org/10.1073/pnas.1108190108

66. Ding D, Zheng R, Tian Y, *et al*., 2022, Retinoblastoma protein as an intrinsic BRD4 inhibitor modulates small molecule BET inhibitor sensitivity in cancer. *Nat Commun*, 13: 6311.

https://doi.org/10.1038/s41467-022-34024-y

67. Weintraub SJ, Prater CA, Dean DC, 1992, Retinoblastoma protein switches the E2F site from positive to negative element. *Nature*, 358: 259–261.

https://doi.org/10.1038/358259a0

68. Jin X, Ding D, Yan Y, *et al*., 2019, Phosphorylated RB promotes cancer immunity by inhibiting NF-κB activation and PD-L1 expression. *Mol Cell*, 73: 22–35.e6.

https://doi.org/10.1016/j.molcel.2018.10.034

69. Hassler M, Singh S, Yue WW, *et al*., 2007, Crystal structure of the retinoblastoma protein N domain provides insight into tumor suppression, ligand interaction, and holoprotein architecture. *Mol Cell*, 28: 371–385.

https://doi.org/10.1016/j.molcel.2007.08.023

70. Liu, N, Ling R, Tang X, *et al*., 2022, Post-translational modifications of BRD4: Therapeutic targets for tumor. *Front Oncol*, 12: 847701.

https://doi.org/10.3389/fonc.2022.847701

71. Dai X, Gan W, Li X, *et al*., 2017, Prostate cancer-associated SPOP mutations confer resistance to BET inhibitors through stabilization of BRD4. *Nat Med*, 23: 1063–1071.

https://doi.org/10.1038/nm.4378

72. Janouskova H, El Tekle G, Bellini E, *et al*., 2017, Opposing effects of cancer-type-specific SPOP mutants on BET protein degradation and sensitivity to BET inhibitors. *Nat Med*, 23: 1046–1054.

https://doi.org/10.1038/nm.4372

73. Jin X, Yan Y, Wang D, *et al*., 2018, DUB3 promotes BET inhibitor resistance and cancer progression by deubiquitinating Brd4. *Mol Cell*, 71: 592–605.e4.

https://doi.org/10.1016/j.molcel.2018.06.036

74. Zhang P, Wang D, Zhao Y, *et al*., 2017, Intrinsic BET inhibitor resistance in SPOP-mutated prostate cancer is mediated by BET protein stabilization and AKT-mTORC1 activation. *Nat Med*, 23: 1055–1062.

https://doi.org/10.1038/nm.4379

75. Wang W, Tang Y, Xiao Q, *et al*., 2021, Stromal induction of BRD4 phosphorylation results in chromatin remodeling and BET inhibitor resistance in colorectal cancer. *Nat Commun*, 12: 4441.

https://doi.org/10.1038/s41467-021-24687-4

76. Garnier JM, Sharp PP, Burns CJ, 2014, BET bromodomain inhibitors: A patent review. *Expert Opin Ther Pat*, 24: 185–199.

https://doi.org/10.1517/13543776.2014.859244

77. Rahman S, Sowa ME, Ottinger M, *et al*., 2011, The Brd4 extraterminal domain confers transcription activation independent of pTEFb by recruiting multiple proteins, including NSD3. *Mol Cell Biol*, 31: 2641–2652.

https://doi.org/10.1128/MCB.01341

78. Chaidos A, Caputo V, Gouvedenou K, *et al*., 2014, Potent antimyeloma activity of the novel bromodomain inhibitors I-BET151 and I-BET762. *Blood*, 123: 697–705.

https://doi.org/10.1182/blood-2013-01-478420

79. Wyce A, Degenhardt Y, Bai Y, *et al*., 2013, Inhibition of BET bromodomain proteins as a therapeutic approach in prostate cancer. *Oncotarget*, 4: 2419–2429.

https://doi.org/10.18632/oncotarget.1572

80. Riveiro ME, Astorgues-Xerri L, Vazquez R, *et al*., 2016, OTX015 (MK-8628), a novel BET inhibitor, exhibits antitumor activity in non-small cell and small cell lung cancer models harboring different oncogenic mutations. *Oncotarget*, 7: 84675–84687.

https://doi.org/10.18632/oncotarget.13181

81. Tontsch-Grunt U, Traexler PE, Baum A, *et al*., 2022, Therapeutic impact of BET inhibitor BI 894999 treatment: Backtranslation from the clinic. *Br J Cancer*, 127: 577–586.

https://doi.org/10.1038/s41416-022-01815-5

ACCSCIENCE PUBLISHING

Global Translational Medicine

PERSPECTIVE ARTICLE

Nuclear magnetic resonance-biochemical correlation toward deep learning of theranosis and precision medicine

Rakesh Sharma[1]* and Arvind Trivedi[2]

[1]Plastic Surgery Scholar, Surgery NMR Lab, Shriners Children Hospital, Massachusetts General Hospital, Harvard Medical School, Boston, MA, USA

[2]Department of Medicine, Government Medical College, Saharanpur, Uttar Pradesh, India

Abstract

Efforts have been made to employ the nuclear magnetic resonance (NMR)-biochemical correlation concept or a combination of MR imaging (MRI) and MR spectroscopy (MRS) as an established diagnostic tool for medical practice in clinical settings. Recent reviews and meta-analyses indicate the great possibility of using integrated multimodal multiparametric MRI and MRS for deep learning (DL) of soft-tissue pathophysiology, enabling improved decision-making and disease progression monitoring in precision medicine. Recent guidelines and clinical trials suggest the need for DL of the biophysical and biochemical nature of the brain, breast, prostate, liver, and heart tissue from digital spectromics analysis, along with other molecular imaging modalities. The current opinions, based on recent recommendations, available literature on evidence-based MR spectromics, clinical trials, and meta-analyses on high-resolution MRI and MRS suggest that utilizing MRI and MRS signals as theranostic biomarkers for various soft tissues can demonstrate NMR-biochemical correlation and employ MRI with MRS as adjunct real-time tools, generating robust, and fast tissue digital images with metabolic screening. The integration of DL features can aid in evaluating patient disease diagnosis and therapy within a clinical setting, considering the available medical practices and their limitations.

Keywords: Nuclear magnetic resonance-biochemical correlation; Magnetic resonance imaging; Magnetic resonance spectroscopy; Deep learning of disease nature; Clinical trials; Magnetic resonance meta-analysis

***Corresponding author:**
Rakesh Sharma
(rksz2009@gmail.com)

Citation: Sharma R, Trivedi A, 2023, Nuclear magnetic resonance-biochemical correlation toward deep learning of theranosis and precision medicine. *Global Transl Med,* 2(3): 337.
https://doi.org/10.36922/gtm.337

Received: January 23, 2023
Accepted: June 7, 2023
Published Online: August 16, 2023

1. Introduction

The concept of "nuclear magnetic resonance (NMR)-biochemical correlation" was proposed by researchers in the 90s as a non-invasive diagnostic monitoring tool[1]. Initially, the correlation of longitudinal T1 and transverse T2* with *ex vivo* NMR and *in vivo* MR spectroscopy (MRS) data, along with serum analytes and tissue histology, were integrated as established NMR relaxation-biochemical biomarkers, as shown in Figure 1 and Table 1[1,2]. Over years of continued efforts, NMR has shown great potential in deep learning (DL) features by integrating multimodal T1-, T2-molecular images, 2D/3D spectra generating regression, convolutional neural network (CNN) framework, trained dataset for decision-making, and measurements of metabolite concentrations at

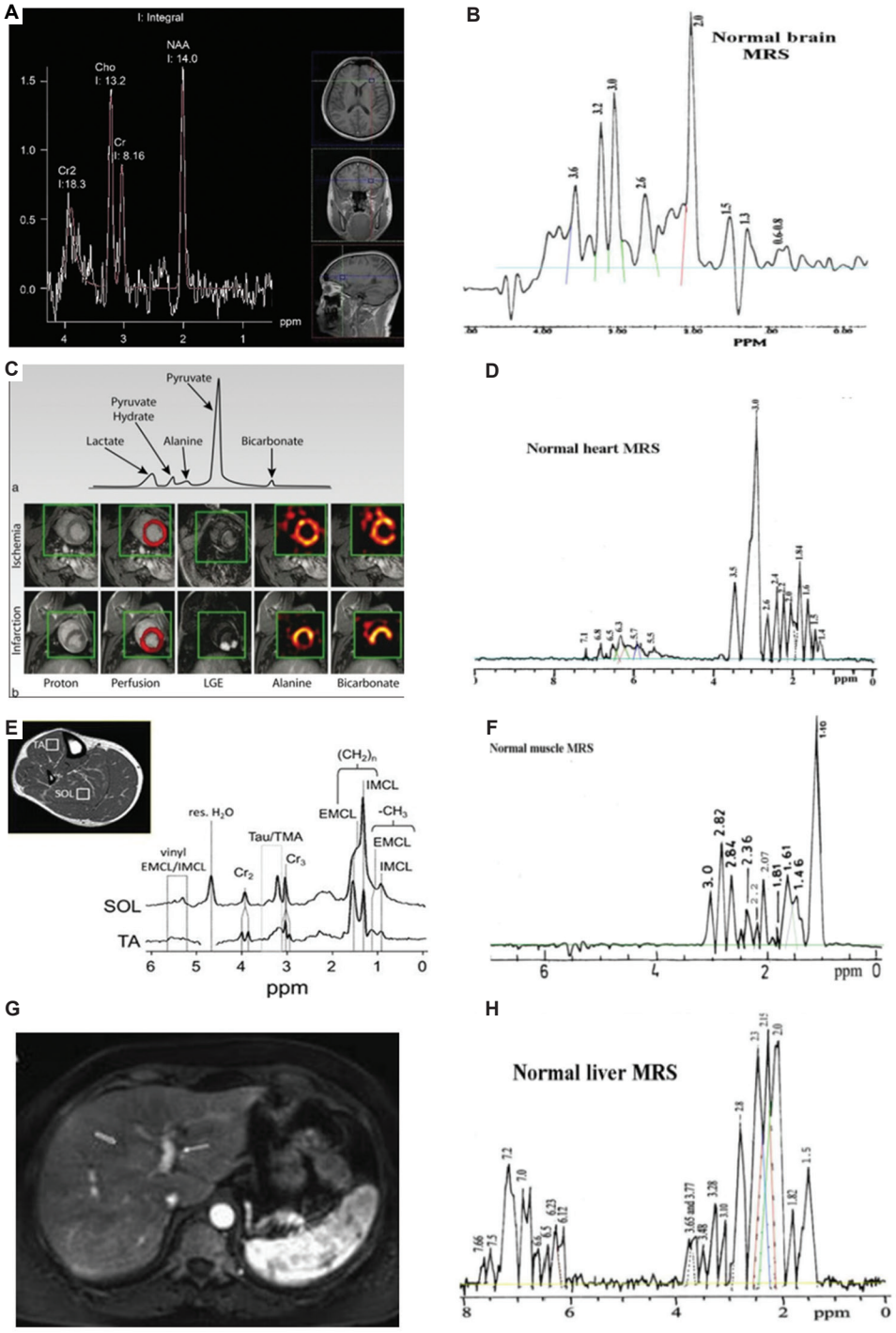

Figure 1. Representative nuclear magnetic resonance (NMR) peaks are used in magnetic resonance spectroscopic (MRS) imaging methods and biochemical tests by assessing metabolite concentrations in tissue and serum to interpret the disease burden in normal brain, breast, myocardium, prostate, and liver. (A-D) are NMR of the brain, heart, muscle, and liver, respectively, and (E-H) are the MRS results of the respective organs. Images are reproduced from a dissertation submitted at IIT Delhi in 1995[1].

different locations in human tissues for physiological and functional metabolic screening with parallel development in ultrahigh-resolution NMR imagers[2]. Simultaneously, robust automated MRS imaging (MRSI) segmentation and registration processing have been routinely used for extracting focal lesion features (size, chemical composition,

Table 1. Established NMR relaxation-biochemical biomarkers as measured metabolite concentrations in normal brain, heart, muscle, and liver tissues

NMR parameters	Brain	Heart	Muscle	Liver
T1	774±23 ms	946±30 ms	600±20 ms	448±20 ms
T2	145±81 ms	68±9 ms	65±9 ms	88±7 ms
Metabolite Peaks	• NAA 18 mM • Glx 7.2 mM • Aspartate 2.3 mM • Creatine 7.3 mM	• Cholesterol 13.5 mM • Creatine 24 mM	• Fatty Acids 29 mM • Phospholipids 26 mM	• Glutamine 36.1 mM • Aspartate 6.27 mM
Tissue metabolites	• Lactate 146.6±8.8 µg% • Pyruvate 98.8±3.5 µg% • Acetoacetate 36.6±2.1 µg%	• Cholesterol 175±5.8 mg% • Triglycerides 106±8.1 mg% • Lactate 89.4±4.8 µg%	• Triglycerides 30.2±8 mg% • Phospholipids 139.7±12.4 mg%	• Triglycerides 89.7±4.8 mg% • Phospholipids 113.8±3.9 mg%
Serum metabolites	• Lactate 24.8 µg% • Pyruvate 95.6 µg% • SGOT 23.4 IU	• CK-MB 19.5±2.4 IU • SGOT 23.4±2.9 IU • Lactate 24.8±7.9 µg%	• Creatine Kinase 21.1±2.9 IU • SGPT 13.6±1.4 IU	• SGPT 18.5±1.9 IU • Alkaline Pase 39.5±7.8 IU • Bilirubin 1.5±0.2 mg%

Abbreviations: CK-MB: Creatine kinase-myocardial band; Glx: Glutamine+glutamate, NAA: *N*-acetylaspartate; SGOT: Serum glutamic-oxaloacetic transaminase, SGPT: Serum glutamic-pyruvic transaminase.

and disease-specific metabolism) as trained non-invasive MR imaging (MRI) and spectroscopy supervised dataset (biosignals), along with tissue-specific neuropsychological tests and organ function laboratory tests to define the structure and physiochemical or behavioral nature of diseased soft tissues such as heart, muscle, kidney, breast, prostate, liver, and brain for confirming disease behavior, differential diagnosis, and monitoring purposes. The author shares his opinion that T1 and T2 relaxation constants, MRS peaks, and MRSI-produced NMR spectral diagnostic peaks and metabolite maps can be used to monitor the metabolite distribution in tissues based on spectromics peak ratio, features of peak area at full-width half-maximum half, peak relaxivities, peak shape, peak cross-connectivity, and peak dynamics[2,3]. Over the years, clinicians have routinely used integrated *in vivo* MR imaging and spectroscopy to define quantitative changes in *in vivo* organ anatomy, tissue histology, digital histochemistry, perfusion, and metabolism for theranostic physiochemical specificity to improve clinical efficacy[4-6]. Due to the time-consuming data analysis, some research centers have adopted DL (integrating extracted and calculated biosignal changes as the footprint of specific disease status) data processing methods using 3D metabolic peaks/maps to reveal metabolite concentration profiles or metabolomics as disease-specific fingerprints of focal lesions in human heart, muscle, kidney, breast, prostate, liver, and brain diseases[2-7]. The disease burden as spatially and temporarily averaged metabolite information is measured by 3D- and 4D-tissue metabolite concentrations distributed in human brain tumors, muscle, bone, and glands[8,9]. Despite all, low NMR-visible metabolite concentrations in *in vivo* NMR spectra and poor metabolic maps of tissues still show limited clinical value in federal guidelines. In this case, DL features may enhance the theranostic accuracy in disease diagnosis and treatment, moving toward precision medicine.

The current perspective article aims to construe the interpretation of MRSI and hybrid imaging features in physiochemical imaging and spectroscopy as a means of "DL" in clinical trials on theranosis in light of meta-analyses and previous clinical trials, if suitable, for precision medicine.

The MRSI signal extracts the metabolic information from large areas of spatial MRI maps by optimization process to select diseased tissue volume with no external artifacts. The chemical shift encoding and readout methods generate metabolite signals by suppressing water and lipids signals by fat saturation bands [11,12]. Fast Fourier transformation and fast pace transform signal processing visualize chemical shift data from non-zero gyromagnetic ratio nuclei of scarce metabolites, temperature, pH, and tissue oxygenation[12]. Now, high-speed localized 2D NMR-total correlation spectroscopy, localized-correlation spectroscopy (COSY), and high-resolution magic angle spinning (HRMAS) acquisition with added second spectroscopic dimension can generate greater spectral peak discrimination and separated overlapping resonances at ultrahigh NMR spectrometers for DL, as shown in Figure 2[13].

Using DL, MRI processing, robust MRSI coregistration, atlas matching, and tissue segmentation methods improve diagnostic sensitivity by detecting a spatial transformation of diseased tissue normalized MRSI data coordinates relative to normal or control tissue metabolite concentrations in the matched region. Atlas matching identifies brain regions for analysis of matching MRSI

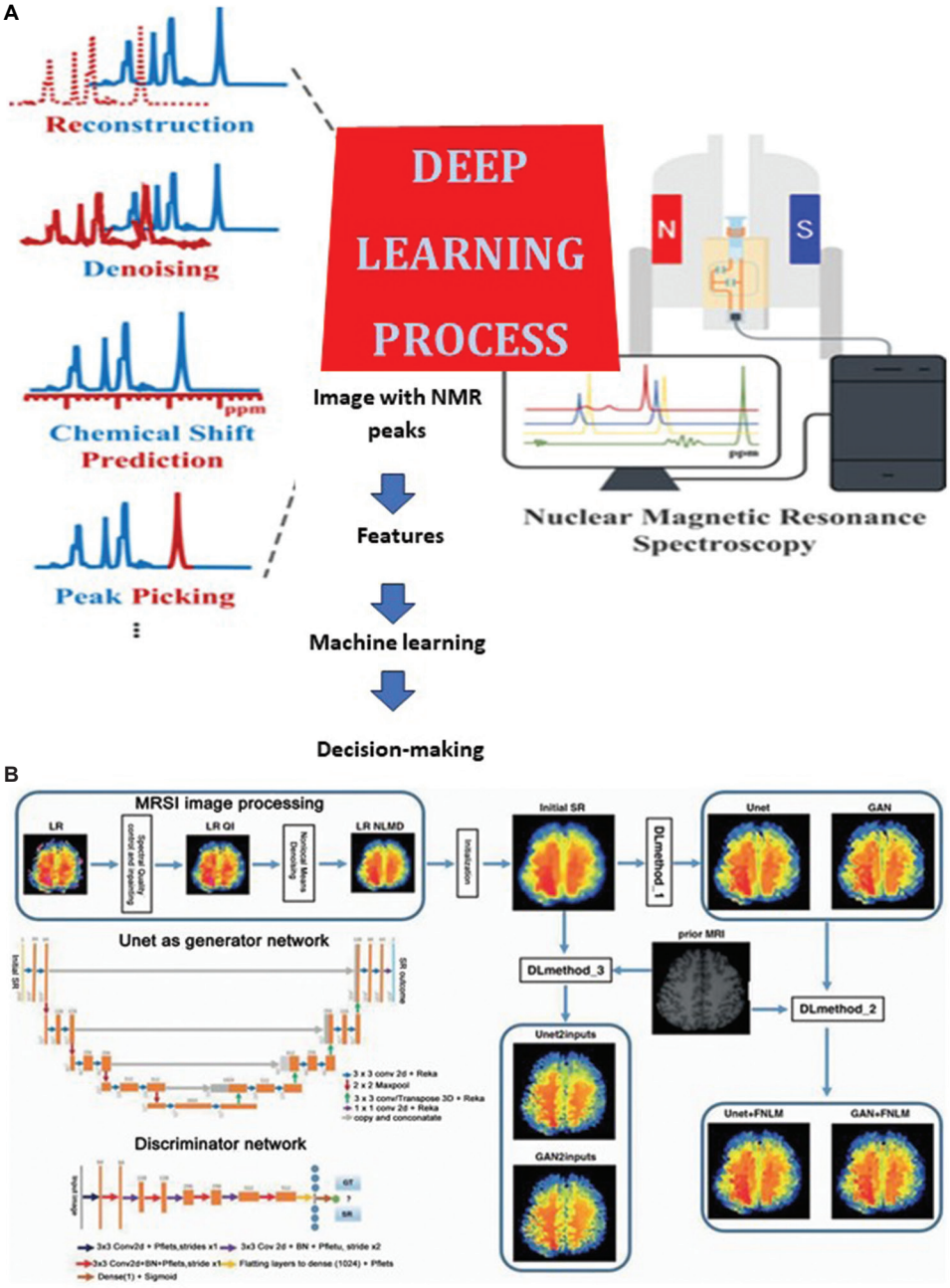

Figure 2. A flowchart diagram of deep learning for magnetic resonance spectroscopy imaging (MRSI), showing three blocks: (i) filtered low-resolution metabolite maps using denoising, painting, and spectrum quality criteria; (ii) interpolation of denoised maps to make super-resolution (SR) maps; and (iii) implementing a deep neural network (Unet or GAN) to produce the final SR image. Use of SR images in the last block to run three deep learning methods, which are: (i) deep neural network applied to initial MRSI data; (ii) feature nonlocal means (FNLM) with prior magnetic resonance imaging (MRI) input applied to results of deep learning method I; and (iii) deep neural network applied to both initial MRSI and prior MRI inputs. The sketch of the generator network (Unet) and discriminator GAN network is shown in the bottom-left[19]. Courtesy: Dr Migdadi.

voxels with a database of normal metabolite values[14]. The segmentation delineates the disease-specific tissue pixel areas with a change in metabolites using boundary-based, thresholding, feature plots, subtle points, volume rendering, filtering, and interpolation methods[15]. The registration permits connected disease-specific pixels across tissue slices (coordinates) to extract the disease volume based on edge detection and morphometry matching validated segmented-out trained data sets of disease burden by the observer[16]. In the brain, DL is now

done by trained operators on selected brain tissue voxels or brain regions[17].

2. Clinical disorders and MRSI applications toward DL

The MRSI is now used in the clinic to help diagnose, treat, and follow cancer and lesion progression in patients. DL of MRSI data visualizes metabolite peaks as spectromics fingerprints (relaxation constants+metabolite ratio or concentrations) from different diseased brain regions, as shown in Figures 1 and 2.

2.1. Segmentation, coregistration, validation, and feature analysis by artificial intelligence

Artificial intelligence-related entities, such as Kernel Null Foley-Sammon transform (KNFST), support vector machines, third (PC3) and fourth (PC4) degree polynomial, fuzzy c-means (FCM) clustering algorithm, K-nearest neighbors, CNN, regression, the pattern of the trained segmentation data set, image registration, pixel coordinates, delineation, and localized NMR peak characteristics, can be used to extract the tissue pathology or disease burden or tumor stage using color-coding and biophysical signal measurements[18]. However, all these methods need optimization or trimming of the input data by one or other methods. Thus, the maximum outcome of tissue disease burden close to real disease-specific etiology or pathology obtained from biopsies can be measured by combining artificial intelligence outcomes from multimodal signal processing methods.

2.2. Spectromics fingerprints in precision medicine by multimodal MRSI with physiological screening

DL by integrating MRI with multiparametric modalities answers metabolic spectral distribution. The author proposes spectromics fingerprint to define tissue metabolite distribution as the fingerprint of disease burden by DL. Spectromics is an integration of multiple clinical patient data, molecular imaging, and genomics modalities toward the "Precision Medicine Initiative," as shown in Table 2. It is a precise interpretation to decide on a patient-care management plan specific to the individual patients, as shown in Figures 2-4.

Now, image analysis by computer-aided diagnosis (CAD) using quantitative breast tumor metabolites and NMR relaxation constants and MRI image analysis can reflect the associations of clinical, pathologic, and genomic data (genomic measurements) in tumor phenotypes. For example, brain tumors, multiple sclerosis (MS) lesions, Alzheimer's disease, epilepsy episodes, and effective cancer theranosis rely on the combined information from multiple patient tests, including molecular, clinical, imaging, and genomic data, toward patient-specific outcomes for precision medicine. Adapting the "Precision Medicine Initiative" includes current radiological interpretation from "average patient" to interpret the precise patient-care management decision specific to an individual patient.

3. Examples of MRI- and MRS-based DL

Three examples of breast tumor, glioblastoma (GBM), and MS lesions are illustrated toward understanding the value of DL as a potential "Precision Medicine Initiative" to evaluate disease progression, correlation with a disability, prognosis in occult diseases, correlation with fatigue, and *in vivo* theranostic effect of therapies.

3.1. Classification of breast tumors to determine reoccurrence and future risk

The breast image analysis using CAD predicts the breast lesion characteristics on clinical images. The CAD is useful in performing clinical tasks, such as risk assessment, detection, screening, diagnosis, theranostic response, recurrence, and others, using "virtual digital biopsies," as shown in Figures 4 and 5[18].

The DL of MRSI interpretation explores digital metabolic lesion segmentation-based features of lesion volume, sphericity, texture and uptake, maximum enhancement variance (dynamic contract-enhanced [DCE]), margin sharpness on ImageNet and texture analysis T2-weighted [T2wt] MRI and apparent diffusion coefficient (diffusion-weighted imaging [DWI])] with minimum computer data processing, as shown in Figures 6 and 7.

The DL feature extraction on CADx tasks minimizes extensive computing, as shown in Figure 8.

The artificial intelligence neural network-analyzed CNNs-based breast image features classify the malignant and benign breast tumors using mammography, ultrasound, and DCE-MRI methods as visual likelihoods of malignant lesions with DL performance, as shown in Figure 9.

3.1.1. Computerized image-based breast cancer recurrence risk measurement

Breast cancer risk or density measurement assessed by DCE-MRI and mammography screen out high-risk women. Cancer-risk spectromic features on DCE-MRI are breast metabolite density, parenchyma texture pattern on digital mammograms, and background parenchymal enhancement (BPE) signal. The MRI-visible breast volume-growing algorithm classifies the fibroglandular and MRS-visible fat depots. Enhanced breast fibroglandular kinetic curves in breast regions categorize the BPE signal using FCM clustering. The mammogram images show a

Table 2. Clinical trials on NMR-biochemical correlation (MRI+MRS and other biomarkers) using deep learning

Clinical trial	Outcomes of MRS in the clinical trials and reviews	References
Sleep apnea	Echo-planar J-resolved spectroscopic imaging and compressed sensing validation study in obstructive sleep apnea.	[20]
Multiple sclerosis	Brain MRS of secondary progressive multiple sclerosis: MRSI study	[21]
Multiple sclerosis	i. Clinical trials and clinical practice in multiple sclerosis. ii. High-field MR imaging and ^{1}H-MR spectroscopy in multiple sclerosis: diagnostic MR imaging criteria. iii. The role of MRS and fMRI in monitoring the treatment of multiple sclerosis: US National MS Society guidelines	[22] [23] [24] [25]
Brain tumor	Reproducibility of localized 2D correlated MR spectroscopy.	[26]
Prostate cancer	Standard evaluation system in prostate endorectal MRSI.	[27]
SCA2/MSA-C	Proton MRSI in differentiation of SCA2 from MSA-C	[28]
Obesity	Effect of low-fat diets on intramyocellular and hepatocellular lipids: a randomized clinical trial	[29]
Brain tumor	MRI biomarkers in neuro-oncology	[30]
Prion disease	Combined diffusion imaging and MR spectroscopy in human prion diseases	[31]
Glioblastoma	Impact of MRSI on response assessment: glioblastoma clinical trials.	[32]
Neurodegeneration	*In vivo* imaging markers of neurodegeneration in substantia nigra	[33]
Glioblastoma	The theranostic ability of temozolomide follow-up MRI+MRS and apparent diffusion coefficient mapping.	[34]
Amyotrophic lateral sclerosis	Diffusion tensor MRI and MRS in the upper motor neuron in amyotrophic lateral sclerosis.	[35]
Non-Hodgkin's lymphoma	MRS in multi-center trials and early results in non-Hodgkin's lymphoma	[36]
Breast cancer	i. Hybrid multiparametric MRI-MRS-sodium MRI monitoring of breast cancers ii. 7 Tesla breast proton MRI-MRS, diffusion-weighted imaging for intrinsic sensitivity in breast cancer patients receiving non-adjuvant therapy	[37] [38]
Low back pain	*In vivo* MRS and T1ρ imaging: discography and Oswestry Disability Index questionnaires: SF-36 Health survey.	[39]
Ischemia syndrome	MRSI study on woman ischemia: Woman Ischemia syndrome evaluation WISE study	[40]
Neurofibromatosis	Randomized controlled trial for autism neurofibromatosis type 1 (SANTA)	[41]
Aorta coarctation	Perfusion imaging of surgical repair of coarctation of aorta study	[42]
Brain pH	Detecting activity-evoked pH changes in the human brain	[43]
Thalamic GABA	GABA levels in depressive disorder	[44]
Glioma	i. Volumetric and metabolic evolution in diffused intrinsic pontine gliomas. ii. Use of multiparametric MRI-FDG PET screening in diffused brain glioma: A prospective phase II study iii. Dynamic susceptibility-weighted and spectroscopic MRI monitoring.	[45] [46] [47]
Coronary plaque	Multi-modality intra-coronary plaque characterization: a pilot study.	[48]
HIV and dementia	An *in vivo* proton MRS of HIV-associated dementia and its relationship to age.	[49]
Renal disease	MRS to predict radiofrequency-ablated renal tissue: phase 1 trial.	[50]
Brain fMRI	An evidence based analysis by functional MRI and MRS	[51]
Soft-tissue tumor	A prospective study by ^{31}Phosphorus MRS and histology on tumor response after perfusion in soft tumors	[52]
Cerebral astrocytoma	i. Short TE multi-voxel spectroscopy for choline/N-acetyl aspartate ratio in grading of cerebral astrocytomas ii. Chemotherapy monitoring of high-grade malignant astrocytoma: comparison by ^{201}Thallium SPECT and proton MRI/MRS	[53] [54]
Colorectal liver metastasis	Pre-operative MRS of steatohepatitis in patients with colorectal liver metastasis	[55]
Alzheimer's disease	Proton-MRS of Alzheimer's disease and Binswanger's disease	[56]
Prostate cancer	i. Prostate cancer MRI screening: Göteborg prostate cancer screening 2 trial ii. Dynamic MRI and choline MRS in prostate cancer: Metabolites versus CAD	[57] [58]
Bone metastasis	3T-MR-HIFU for bone metastases of solid tumors.	[59]
Serotonin reuptake syndrome	Selective serotonin reuptake inhibitor in rostral anterior cingulate choline metabolite decrease.	[60]
Depressive disorder	A 31P MRS study on creatine in female adolescents with SSRI-resistant major depressive disorder	[61]

Abbreviations: CAD Computer-aided diagnosis, FDG-PET: Fluorodeoxyglucose-positron emission tomography, fMRI: Functional magnetic resonance imaging, HIV: Human immunodeficiency virus, MR: Magnetic resonance, MRI: Magnetic resonance imaging, MRS: Magnetic resonance spectroscopy, MRSI: Magnetic resonance spectroscopic imaging, MSA-C: Multiple system atrophy-cerebellar subtype, SCA2; Spinocerebellar ataxia type 2, SPECT: Single-photon emission computerized tomography, TE: Echo time, GABA: Gamma-aminobutyric acid, 3T-MR-HIFU: 3T MRI-guided high-intensity focused ultrasound.

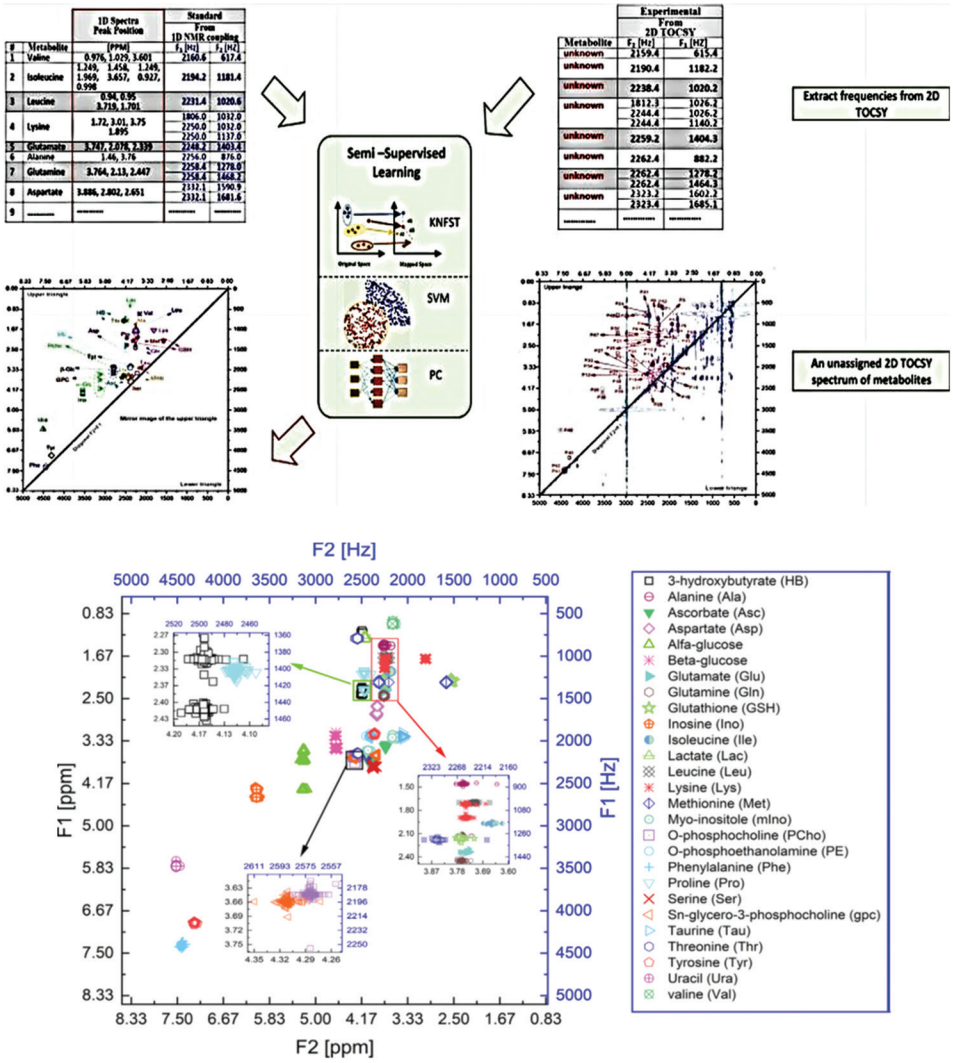

Figure 3. An illustration of deep learning (DL). DL extracts digital features using artificial intelligence or computation algorithms to analyze the pathology in voxels on images to process the magnetic resonance spectroscopy data with demonstrated results in computer metabolomic datasets, medical images, natural language processing, and so forth (upper panels). Applications of deep learning in 2D nuclear magnetic resonance spectroscopy are shown as feature space of 27 metabolite-trained datasets derived from the total correlation spectroscopy spectrum of breast cancer tissue. The insets are the selected enlarged peaks overlapped in (F2, F1) dimensions (lower panel). https://radiologykey.com/13-future-applications-radiomics-and-deep-learning-on-breast-mri/.

texture and metabolite density correlation. Dense breast tissues show higher citrate (Cit) and choline (Cho) peak enhancement than fatty breast tissues.

3.1.2. Breast tumor MRI phenotyping relative to molecular subtyping for diagnosis and prognosis

The spectromics needs extensive data analysis to transform the breast 4D DCE-MR images and molecular spectrum features into phenotypic descriptors at the breast MRI workstation. One spectromic feature represents only one clinical task. A breast biopsy confirms the tumor's pathologic stage after *in vivo* MRI imaging of breast cancer, allowing for further discussion of the treatment plan. Recently, the MRSI phenotyping resource the cancer genome atlas/the cancer imaging archive (TCGA/TCIA) set up by the national cancer institute advocates spectromic biomarkers to predict the pathological stage and allow quick patient management/treatment by neoadjuvant chemotherapy and/or radiation therapy and surgery[18]. The TCGA/TCIA cancer research group established the relationships between computer-extracted quantitative MRSI spectromics with prognostic markers and clinical, molecular, and genomics gene expression profiles[18]. The biopsy-proven invasive breast

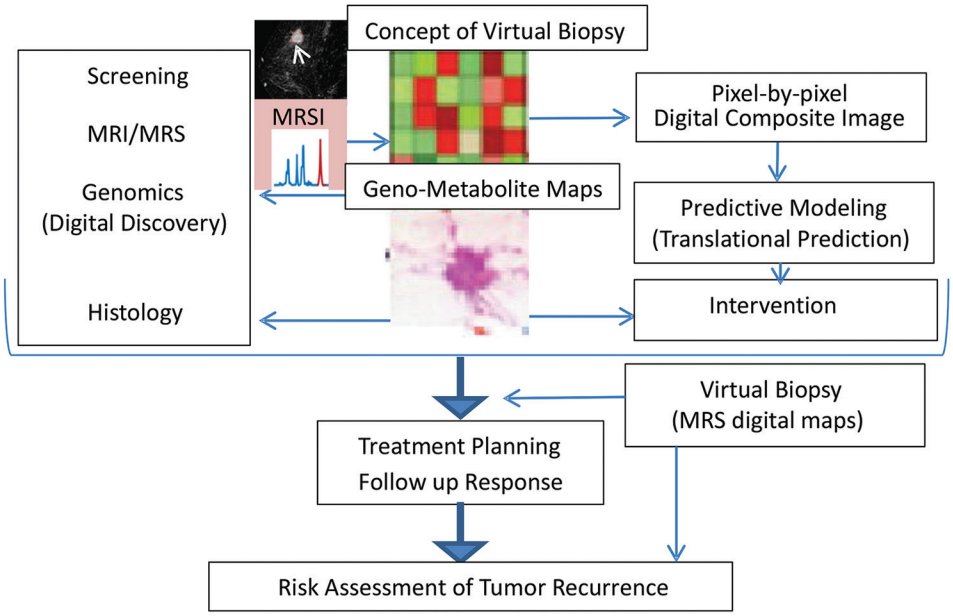

Figure 4. An illustration of multiple-stage spectromics discovery, process, and translation for validation of quantitative imaging features based on the discovery of new relationships to other "omics" and translation into clinical predictive models as reference "virtual digital biopsies," similar to actual biopsies to screen and assess therapeutic response. https://radiologykey.com/13-future-applications-radiomics-and-deep-learning-on-breast-mri/.

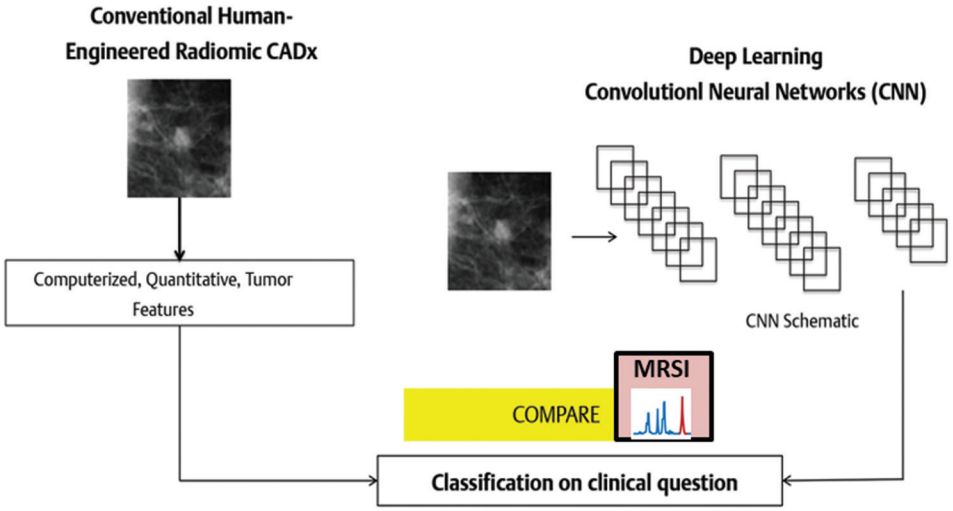

Figure 5. A scheme of computer-aided diagnosis (on the left) and deep learning (on the right) shows the approach of quantitative spectromics using segmentation features of dynamic contrast-enhanced magnetic resonance spectroscopy of tumors. https://radiologykey.com/13-future-applications-radiomics-and-deep-learning-on-breast-mri/.

cancer tissue cross-checks with DCE-MRI image archive and genomic data (Figure 10), predicting the power of spectromic MRS features versus pathological stage and cancer subtypes.

3.1.3. A physician's guide

DL characterizes the breast tumors based on MRI radiomics for (i) radiologist-measured tumor size, (ii) computer-extracted quantitative spectromic features or models, and (iii) computer-extracted MRI tumor phenotype for lymph node damage and pathological stage. Today, the estimation of tumor size is the best predictor of the pathologic stage. Moreover, the spectromic feature clearly predicts the metabolic role in tumor stage I (benign) and II (premalignant) versus stage III (malignant). Breast tumor receptor status (human epidermal growth factor receptor 2

[HER2], estrogen receptor [ER], and progesterone receptor [PR]) further classifies tumors into subtypes. The profiles of breast cancer gene expression categorize tumors into molecular subtypes of basal-like, normal-like luminal A, luminal B, and HER2-enriched tumors. Different breast cancer subtypes have different MRI radiomic features serving as prognostic indicators called PR+ versus PR-, ER+ versus ER-, HER2+ versus HER2-, and triple-negative tumors or cancers. All these respond differently to different therapies and are used in DL.

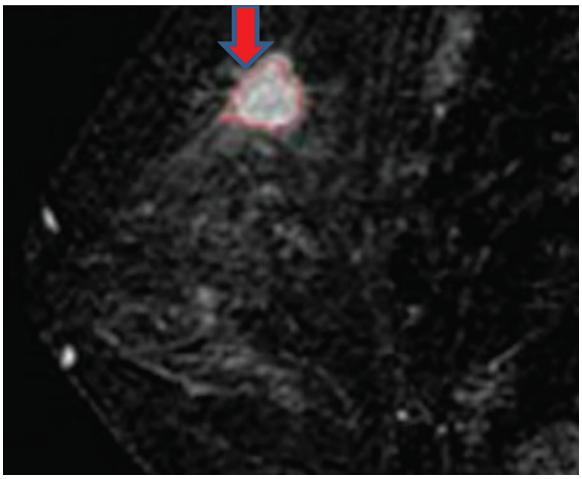

Figure 6. A case of luminal A estrogen receptor (ER)-positive, progesterone receptor-positive, and progesterone receptor (HER2)-negative tumor stage II (see arrow) with negative lymph nodes shows the segmented tumor outline by 4D automatic computer segmentation algorithm. Computer analysis of the magnetic resonance spectroscopy imaging spectromics measured the tumor size of 13.6 mm with spectromics irregularity shape of 0.49 and the spectromics enhancement texture energy of 0.00185. https://radiologykey.com/13-future-applications-radiomics-and-deep-learning-on-breast-mri/.

In short, DL information from computer-extracted MRI-visible soft-tissue tumor features with metabolite phenotypes distinguish breast cancer subtypes by quantitative signatures to predict prognosis for precision medicine.

3.2. Classification of brain GBM tumors

In GBM tumor cells, cell membrane show increased Cho-containing phospholipids concentration in proliferating cells, while *N*-acetylaspartate (NAA) compounds in neurons diminish in GBM tissue samples after local neuronal destruction in the neuronal milieu. The neurochemical Cho to NAA Cho/NAA ratio is elevated in GBM tumors. The T1-weighted contrast-enhanced (T1wt-CE) and fluid-attenuated inversion recovery (FLAIR) pulse sequences generate distinct MRI scans. The echo-planar MRI pulse sequence with the generalized

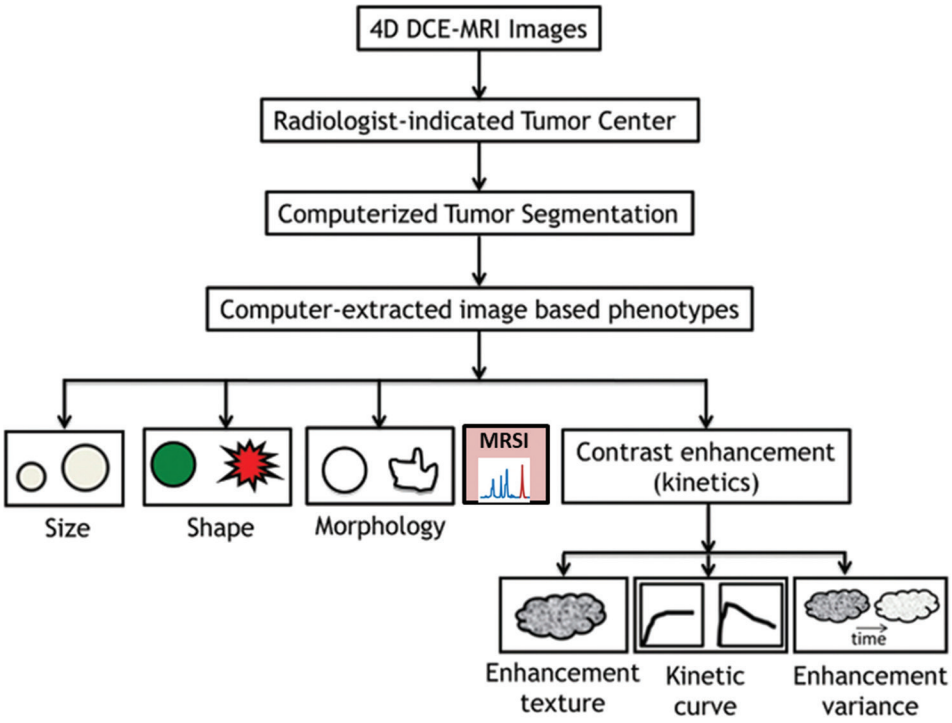

Figure 7. Schematic diagram illustrates the steps of establishing computer-extracted magnetic resonance spectroscopy imaging-based tumor phenotypes. Multiple mathematical descriptors calculate these phenotype features for specific clinical tasks. https://radiologykey.com/13-future-applications-radiomics-and-deep-learning-on-breast-mri/.
Abbreviation: DCE-MRI: Dynamic contrast-enhanced magnetic resonance imaging.

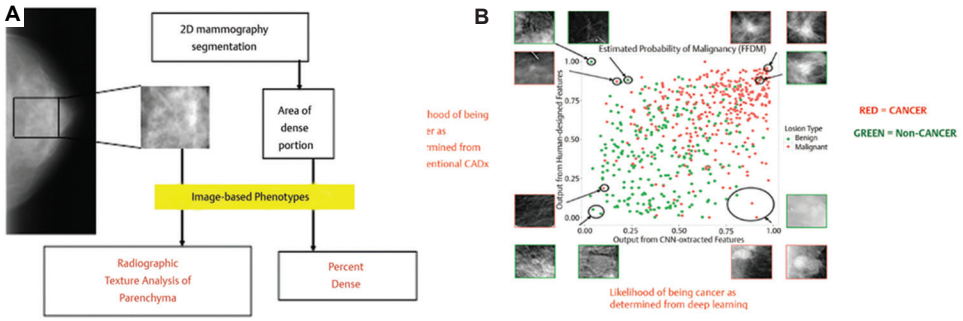

Figure 8. (A) Image-based extracted phenotypes on digital mammograms of breast parenchyma show the risk of breast cancer reoccurrence[18]. (B) Distinct cancer and non-cancer features show the likelihood of malignancy by deep learning. https://radiologykey.com/13-future-applications-radiomics-and-deep-learning-on-breast-mri/.

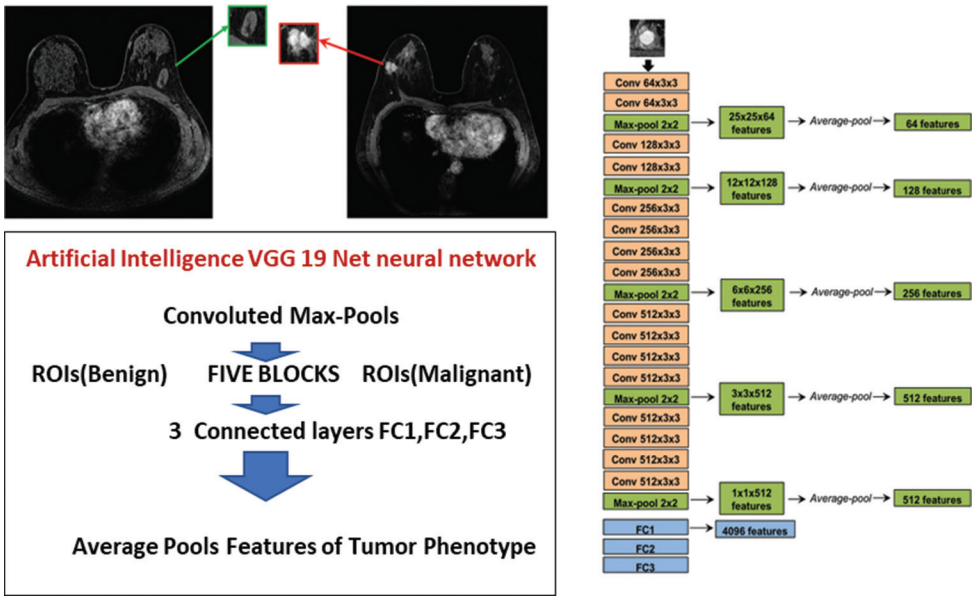

Figure 9. The region of interest taken from a malignant (green arrow) and a benign (Red arrow) breast tumor as input show convolution on VGGNet Neural Network. The VGG19 model is shown in 5 blocks. Each block has two or more convolution layers and a max-pooling layer. These five blocks have three connected layers. From five max-pooling layers, features are extracted as average-pooled across the channel in the third dimension and normalized with the L2 norm. Extracted normalized features are shown to generate a convolutional neural network feature vector. https://radiologykey.com/13-future-applications-radiomics-and-deep-learning-on-breast-mri/.

autocalibrating partially parallel acquisition (GRAPPA) parallel scans on 3T scanner with 32-channel or 20-channel head and neck coil covering 314 MRI pulse sequences with GRAPPA parallel scans on Siemens 3T scanner with a 32-channel or 20-channel head and neck coil covered a voxel size of 314 µL (voxel size µL) over the field of view of 280 mm × 280 mm × 180 mm, and matrix 50 cubic units × 50 cubic units × 18 cubic units, generated resolution of 4.5 mm × 4.5 mm × 5.6 mm. The T1wt images with 1 mm isotropic voxels are converted into coregistered spatial-spectral spectromic data using MRIAP or MIDAS software. All imaging data in the DICOM format are processed by MIDAS on a custom-built Brain-Imaging-Collaboration-Suite platform (BrICS) to coregister all images. The abnormal Cho/NAA ratio in a normal-appearing white matter (NAWM) voxel versus contralateral NAWM on the BrICS platform identifies the contour region showing an elevated ratio of Cho/NAA≥2 × normal (Figure 10).

The GBMs brain tumors remain aggressive and hidden even after 60 Gy radiation therapy and temozolomide. MRSI seems to highlight a high-risk metabolite pattern of GBM recurrence; otherwise, it remains non-visible on contrast-enhanced (CE) MRI. Recently, a randomized phase II clinical trial reported the efficacy, safety, and feasibility of MRSI-guided escalated radiation therapy (60 Gy → 75 Gy) to manage newly diagnosed GBMs as shown in Figure 11. The outcome of MRSI-guided escalated radiation therapy, however, warrants additional testing[62].

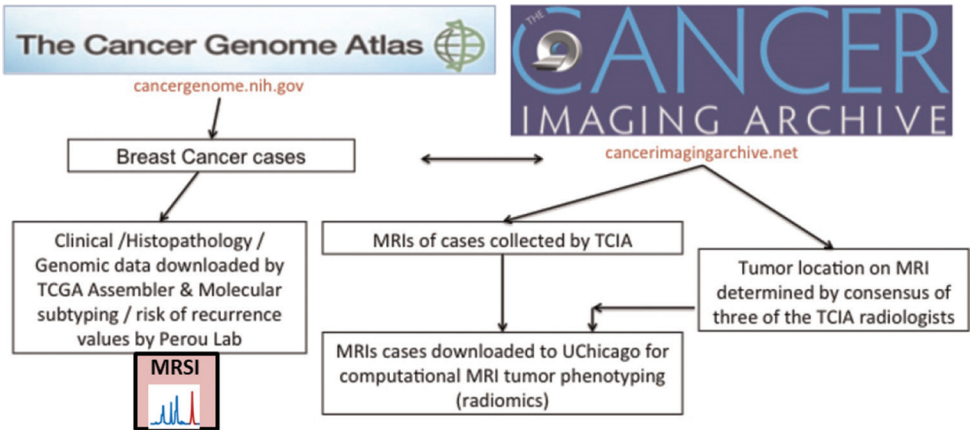

Figure 10. (A) The cancer genome atlas/the cancer imaging archive genomic atlas and imaging scheme illustrates the datasets and lesion features with molecular magnetic resonance spectroscopy imaging, clinical, and genomic gene expression markers show the likelihood of new carcinoma re-occurrence. Reproduced with permission https://radiologykey.com/13-future-applications-radiomics-and-deep-learning-on-breast-mri/.

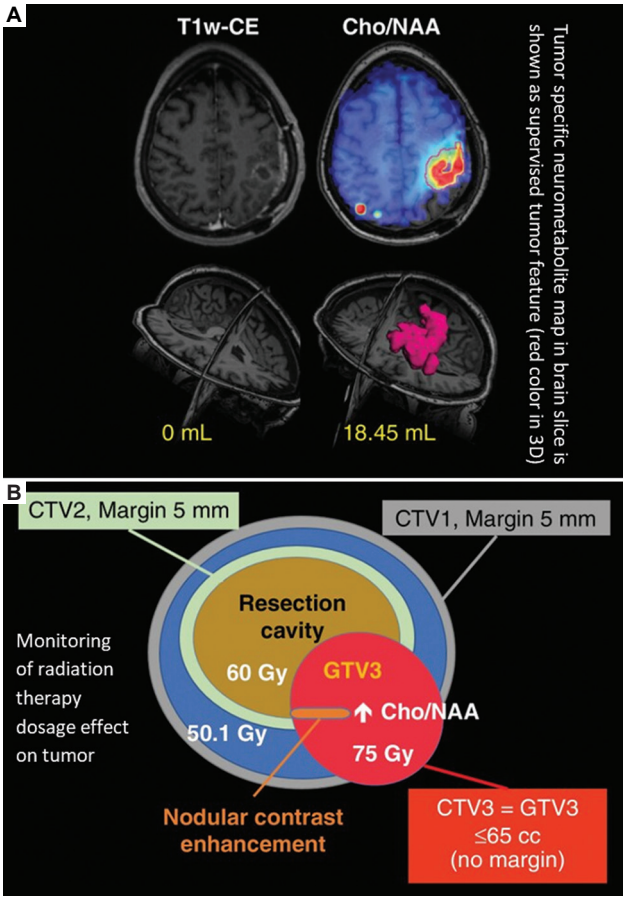

Figure 11. (A) A post-operative glioblastoma subject shows nodular resection cavity high contrast on T1-weighted contrast-enhanced magnetic resonance imaging on the BrICS platform showing normal spectromic (Cho/NAA≥2 × normal) data in GTV3 tumor size 19 mL (right). Deep learning shows contours in GTV3 after radiation 75 Gy. (B) Radiation therapy target volumes at different doses show 30 dose fractions (concurrent dose-painted intensity-modulated radiation). Illustration Modified from references[18].

The author presents the value of MRSI in brain cancer patients with hypothalamic-chiasmatic gliomas (HCG) (GBM multiforme [GBM] and anaplastic astrocytoma), low-grade gliomas (LGG) (oligodendrogliomas and astrocytomas), and metastatic brain tumors. MRS-visible spectromic high ratio of neurochemicals confirms specific tumor core and peritumoral edema by elevated Cho/NAA, Cho/Cr (choline-containing compounds/creatine-phosphocreatine complex) with low NAA/creatine (Cr) ratio. NMR-visible lipids/lactate ratio in the peritumoral and tumoral regions combined with high Cho/Cr, Cho/NAA ratio, and low NAA/Cr ratio discriminate different HGG, LGG, gliomas, and metastases[63].

3.3. Classification of MS lesions

Using DL method, accelerated MRI analysis package (MRIAP) and automated proton spectroscopic image processing (APSIP) postprocessing software provide a reproducible and efficient assessment of white matter MS lesion volumes, white matter-gray matter-cerebrospinal fluid (WM-GM-CSF) composition, and metabolites using T1, T2* parametric, and probability maps as spectromic fingerprints[64,65]. The author believes that metabolite changes of neurochemicals in the MR spectrum as low NAA peak (a marker of neuronal and axonal integrity), high Cho peak (a marker of cell membrane metabolism), and high myo-inositol (MI) peak (a marker of gliosis) can be biochemical-NMR fingerprints. A diminished NAA peak represents neuronal/axonal dysfunction or loss. The elevated Cho peak represents heightened cell-membrane turnover during demyelination, remyelination, inflammation, or gliosis. Thus, the combination of MRI+MRS measures the lesion evolution, correlates the disability with a lesion, and assesses occult disease. MRS

establishes a prognosis, correlates with fatigue, and monitors the effectiveness of drug therapies[66]. At our laboratory, a training model in a semi-supervised KNFST algorithm showed an optimized projection matrix, confidence band values, and class-wise MS lesion training data projections into the null space. Semi-supervised KNFST algorithm iteratively selected samples in the learning phase from data. The classifier predicted new labels to accepted lesion data samples, as shown in Figure 12[64,67].

4. New developments in MRSI multimodal approach and limitations

The potentials of 4D localized *in vivo* NMR image spectroscopy, slice selective N MRS, biopsy HRMAS spectroscopy, and multimodal, multinuclear, and water-fat suppression NMR techniques have emerged for better tissue contrast with metabolomics on high magnetic fields of up to 11.4 tesla in whole human body imagers, as well as an ultrahigh resolution at 21- and 36-tesla microimagers. The localized tissue metabolism in selected diseased body parts or biopsies was studied using modified surface coils, multiple contrast media, modified radiofrequency pulses with high resolutions, and dynamic gradient fields for localized 2D spectral characterization or metabolic screening for spectrally resolved metabolomics imaging applications[20]. Due to being non-invasive and non-radioactive, NMR techniques have been proven safe, with no biological hazards associated with the current level of SAR energy exposures. In the next few years, NMR methods will emerge as a safer, cheaper, and cost-effective alternative modality compared to other diagnostic or therapeutic techniques using ionized radiation.

MRI-digital histochemical correlation is now established to exhibit malignancy-associated changes due to NMR T1 variations where T1 relaxivities depend on visible water contents, proton densities, environments in tissue, and pathology[1].

MRI and biochemical correlation initially proposed in the nineties[1] has been established in routine clinical assessment trials for tissue content chemical analysis, *in vivo* MRS, *ex vivo* MRS, and relaxivities using artificial metabolite solutions and MR database. MRI and 2D-spectral characterization of small-size metabolites in diseased tissues is reported with correlated spectroscopy COSY-MRI, nuclear Overhauser effect spectroscopy (NOESY)-MRI, and high-pressure liquid chromatography (HPLC)-MRI with little success but greater potentials in non-invasive molecular details in undefined molecular etiology of poorly understood diseases. The final outcome depends on significant information and cost-effective constraints[20-61].

The implementation of MRS in clinical use has been slow and remains unclear due to the high technical demands of spectroscopic methods and difficult interpretations in the brain. However, MRI with MRS using ^{1}H and ^{31}P spectroscopic imaging provides information on demyelination, neuron loss, glial tissue formation, changes in glycogenolysis and lactate accumulation, energy metabolism and pH imbalance in brain diseases, and inborn errors of metabolism. In the skeletal muscles, dynamic ^{31}P MRS is used to detect metabolic disorders, while ^{1}H MRI/MRS evaluates muscle degeneration with fat accumulation. ^{31}P MRS is inconclusive for liver metabolic function, but ^{1}H-MRS/MRI indicates metabolites, mobile lipids, and bone marrow characteristics. In the heart, MRSI provides *in vivo* metabolites with global cardiomyopathy. The role of MRI/MRS in cancer differential diagnosis and treatment is still unclear due to the lack of preclinical investigations on physiological and metabolic events on NMR spectra and minimal clinical trials.

From the technical point of view, coil sensitivity with a higher signal-to-noise ratio is crucial in enhanced metabolite quantification.

5. MRSI diagnostic use in clinical trials and healthcare: A physician's guide

The author considers MRS an evidence and fact-finding method for following diseases with metabolite indications (shown in brackets) collected over three decades: i. focal brain tissues for maturating brains in gestation (elevated NAA, glutamine + glutamate [Glx] peaks, low Cho, taurine [Tau] peaks), recurrent brain tumor distinction from radiation-induced necrosis (low NAA, Cr with high Cho peaks), assessment of prognosis in hypoxic-ischemic encephalopathy (low NAA, low NAA/Cho), grading the low-grade and high-grade glioma (change in MI, gamma-aminobutyric acid [GABA] peaks), and evaluation of indeterminate brain lesion to postpone resection/biopsy (low NAA, low Cr, high Cho, lactate [Lac] peaks); ii. diagnosis and monitoring of metabolic diseases, such as cerebral ischemia (high Lac peak), creatine deficiency (Cr peak missing), Canavan disease (increased NAA/tCr ratio), non-ketotic hyperglycinemia (DWI, DTI [diffusion tensor imaging]) and tractography, fractional anisotropy [FA], and diffusivity), maple syrup urine disease (edema, high Glx, tau, and alanine [Ala] peaks), MS periventricular and parahippocampus hypointense lesions (low NAA/total creatine [tCr] and Cho/tCr ratios), metachromatic leukodystrophy (low NAA peak and high NAA in urine), Parkinson's disease substantia nigra (low NAA and GABA peaks, high Lac/tCr ratio), Pelizaeus-Merzbacher disease (high NAA+NAAG peaks and low Cho peaks),

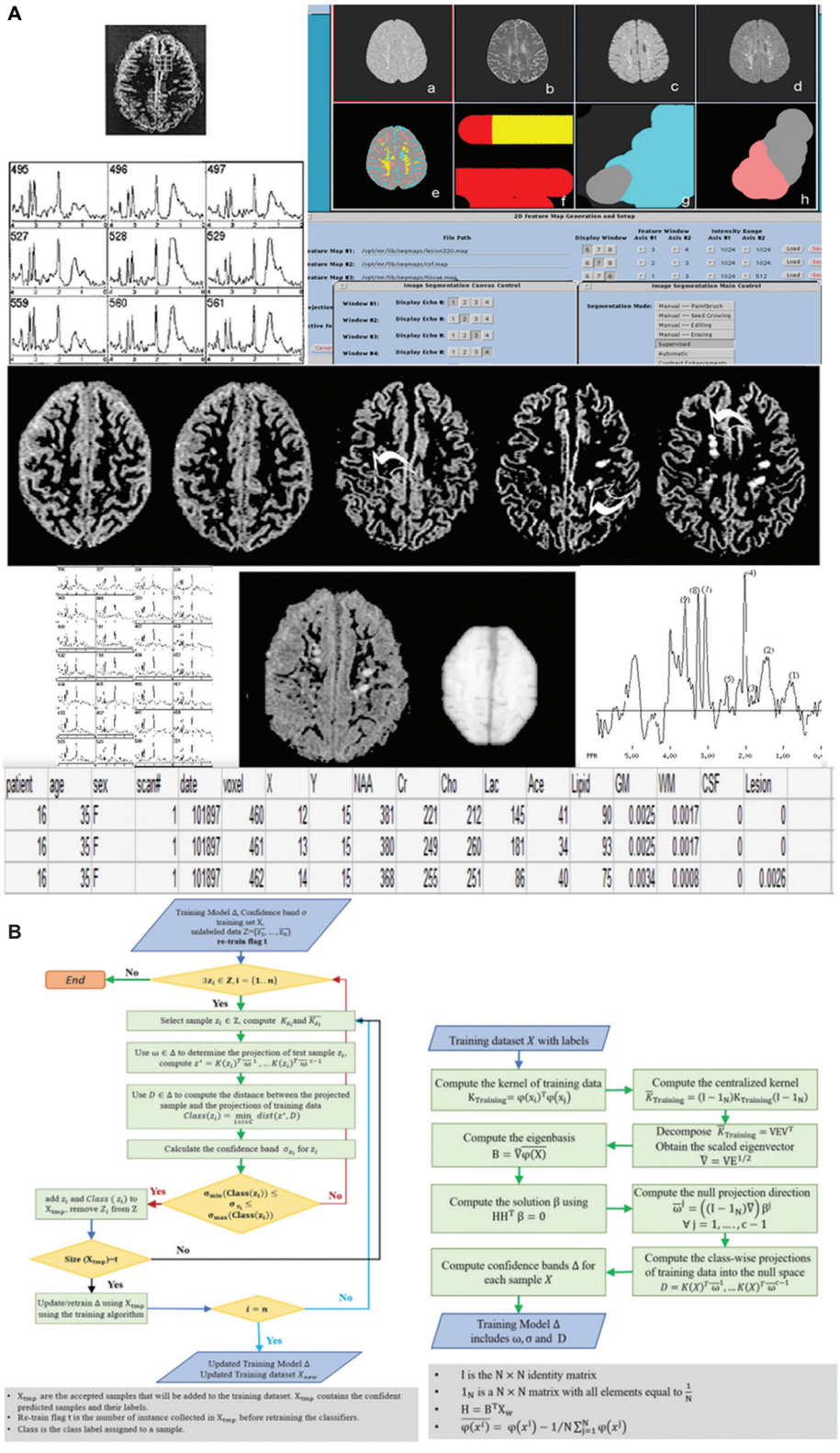

Figure 12. (A) Segmentation of multiple sclerosis lesions is shown as trained data set with yellow color coding and magnetic resonance spectroscopy peaks. (B) The semi-supervised KNFST algorithm procedure is shown to select data samples (on the left panel) and accept the unlabeled data match with confidence band conditions until all processed data are predicted (on the right panel). Modified from references[19].

hypomyelination and congenital cataract (high glucose peak, low valine, lysine, and tyrosine peaks), Krabbe disease (globoid cell leukodystrophy) (low NAA peak), X-linked adrenoleukodystrophy (X-ALD) and cerebral X-linked adrenoleukodystrophy (cALD) (low NAA/Cr and Glx/Cr, high MI/Cr and Cho/Cr ratio), mitochondrial disorders (Kearns-Sayre syndrome, Leigh's syndrome, mitochondrial encephalomyopathy, lactic acidosis, and stroke-like episodes [MELAS]) (low Cr peak), Alexander disease (ALX, AxD, and demyelinogenic leukodystrophy) (elevated Glx/tCr ratios), megalencephalic leukoencephalopathy with subcortical cysts (low NAA, low Cr peaks), wasted white matter disease (leukoencephalopathy childhood ataxia with central hypomyelination [CACH]/vanishing white matter [VWM] syndrome) (low NAA peak), and neuroborreliosis (low NAA peak, high mI/Cr, Lipid/Cr and Cho/Cr ratios, and normal NAA/Cr and Lac/Cr ratios).

While MRI findings are inconclusive in deciding the change in treatment, MRS becomes mandatory in disease monitoring and evaluation by MRS-based spectromics in the following diseases: (i) cancers of breast, prostate, colon, esophagus, liver, brain, and bone tissues; (ii) coma and cerebrovascular diseases/injuries and disorders; (iii) cognitive disorders, movement disorders, and dementia (frontotemporal dementia, vascular dementia, Alzheimer's disease with Lewy bodies, motor neuron disease, Huntington's disease (HD), motor neuron disease, and Parkinson's disease/Parkinsonian syndromes); (iv) psychiatric disorders (autism disorder, attention-deficit/hyperactivity disorder, bipolar disorder, schizophrenia, emotional dysregulation, depression, and obsessive-compulsive disorder); (v) MS; (vi) dermatomyositis; (vii) hepatic steatosis in liver donor survivors; (viii) central nervous system with autoimmune rheumatic diseases; (ix) esophagus squamous cell carcinoma; (x) mesial temporal sclerosis; (xi) primary central nervous system (CNS) lymphoma lesions; (xii) epilepsy juvenile myoclonic epilepsy, mesial lobe epilepsy, and temporal lobe epilepsy; (xiii) hepatic encephalopathy; (xiv) migraine pathophysiology; (xv) head trauma; (xvi) low back pain; (xvii) hepatic carcinoma; (xviii) liver cirrhosis; (xix) Lyme neuroborreliosis; (xx) mucopolysaccharidosis; (xxi) radiation encephalopathy; (xxii) polymyositis; (xxiii) sport injuries; (xxiv) substance abuse disorders; and (xxv) brain trauma injury.

All these diseases need evidence of MRS metabolite specificity and accuracy, as reported in recent years and summarized below.

Now, MRS is an established as non-invasive analytical technique to study metabolite changes in depression, Alzheimer's disease, stroke, seizures, brain tumors, and other diseases affecting the brain. MRS also examines the metabolism of other human organs. The role of MRS in medical diagnosis and therapeutic planning is not yet established for clinical trials or clinical practice. Now, advanced techniques of high-resolution MRI and MRSI favor routine clinical practice with the following evidence in the literature. Still, MRI with MRSI use remains inconclusive as per new guidelines.

i. At Massachusetts, Tuft's Agency on Healthcare Research and Quality (AHRQ) indicated concern about diagnostic thinking and therapeutic decision-making in light of the paucity of high-quality evidence. Still, MRS spectra interpretation is not standardized. MRS technical feasibility, study plan flaws of inadequate sample size, retrospective design, and other limitations bias the results and decision-making. A review of MRS of brain tumors by Blue Cross Blue Shield Association Technology Evaluation Center (2003) indicated that weak evidence is insufficient to draw conclusions on MRSI use on health outcomes[67]. Centers for Medicare and Medicaid Services (CMS) has concluded that there is insufficient support to deem MRS reasonable and necessary for diagnosing brain lesions. As a result, CMS maintained its decision of the non-coverage of MRS-based diagnosis of brain lesions on the national scale[67].
ii. Patients with neuroborreliosis disease showed non-specific MRS changes in assessing central nervous system tissue damage. In ^{1}H-MRS, a point-resolved spectroscopic sequence (PRESS) was used by placing an 8 cm^3 voxel box on the NAWM region of the frontal lobe[68].
iii. The ^{1}H-MRS was described for epilepsy surgery as a research tool with a correlation of ipsilateral MRS abnormality as a good outcome. However, prospective studies on both localized and non-localized ictal scalp electroencephalopathy in MRI-negative patients need validation. Furthermore, ^{1}H-MRS is an adjunct to MRI characterization of brain tumors to convince policymakers[69].
iv. Male fragile X syndrome (FRAX) patients are at risk of significant cognitive and behavioral deficits, specifically those that impact executive prefrontal systems. The cholinergic system damage secondary to FRAX mental retardation shows protein deficiency and contributes to cognitive behavior impairments. The ^{1}H-MRS showed a low choline/Cr ratio in the right dorsolateral prefrontal cortex in male FRAX versus controls, with a negative correlation to intelligence and age in the left cortex. The donepezil improved cognitive-behavioral function[70]. The author believes that biochemical-MRI neuroimaging approach has

the potential to design treatment for FRAX and other genetic disorders based on neurometabolite intervention for treatment efficacy.

v. Proton endorectal MRI with ^{1}H-MRSI of prostate cancer lesions showed a high Gleason score toward an increased (Cho+Cr)/Cit ratio and large tumor volume. For detecting prostate cancer, proton-MRS-visible Cit peak and citrate concentration in semen or prostatic secretions showed better results over prostate-specific antigen testing[71]. The 3D chemical-shift imaging (CSI) spin-echo sequence with MRS of biopsy from proven prostate carcinoma was used for DL, along with tumor volume and voxels per slice counts. The MRS differentiated marginally T2 and T3 tumor stages. MRI with MRS slightly improved the tumor staging with no advantage in diagnosis and tumor staging over MRI alone[72].

vi. MRS is a technique for diagnosis and monitoring cancer of the prostate, colon, breast, cervix, pancreas, and esophagus organs. The 3D MRS has emerged as a new and sensitive tool in metabolic evaluation, specifically for assessing the loss of Cit and elevated ratio of Cho/Cit of prostate cancer[73]. American College of Radiology Imaging Network (ACRIN) considers MRSI a routine diagnostic technique. MRS has high diagnostic accuracy. However, randomized controlled large-scale trial studies are needed[73].

vii. Mucopolysaccharidosis (MPS) patients show a poor correlation between enzyme levels, urine mucopolysaccharides (GAG), and neuroimaging findings. The semi-automated and automated segmentation techniques analyzed the T2-FLAIR brain images for several MRI variables of normalized cerebral volume (NCV), normalized cerebrospinal fluid volume (NCSFV), normalized ventricular volume (NVV), and normalized lesion load (NLL). The point-resolved MRS annotation positioned at white and gray matter showed a positive correlation to age, enzyme levels, urinary GAG, and neuroimaging. However, metabolite ratios by MRS, MRI-visible NCV, NCSFV, NVV, and enzyme activity or GAG levels were poorly correlated to disease duration or the age of patients. Patients with MPS II showed aggressive white matter lesion increases that remain non-visible by MRI and MRS findings, which neither correlated to enzymatic nor glycosaminoglycan levels[74]. The MRI protocol of a sagittal T1-weighted 3D fast low-angle shot (3D FLASH) sequence and transverse T2- and spin-density-weighted turbo spin-echo sequences with ^{1}H-MR 2D CSI sequence at short and long echo time (TE) MRSI images showed low Cho/Cr, NAA/Cr ratios in multiple system atrophy-cerebellar subtypes (MSA-C) and spinocerebellar ataxia type 2 (SCA2) with no difference from normal controls. The cerebellar lactate peak in SCA-2 patients was distinct due to cerebellar degeneration, while no Lac peak was evident in MSA-C or control subjects[75].

viii. The 3T MRI with ^{1}H-MRSI measured the increased Cho, Lac, and NAA/tCr ratio and decreased NAA and choline/NAA ratio at peritumoral tissues in GBM to assess the post-resection response in the contralateral brain at 3 – 5 weeks of post-Gliadel therapy and surgery plan before radiation therapy[76]. The ^{1}H-MRSI localizes different regions showing heterogeneous responses after being given Gliadel treatment. The author suggests that MRS metabolic indicators can monitor pre-surgery and postsurgery resection after Gliadel implantation to assess the tumor regression and gauze the chemotherapy efficacy.

ix. Clinical MRS in MS showed metabolic changes at MS lesion sites, and multi-centered clinical trials of MS incorporated MRS into their MRI imaging diffusion tensor DTI protocols to quantify the effect of therapeutic intervention on MS tissue damage[77,78].

x. Biomarkers of disc degeneration and discogenic back pain are not available. In frozen discectomy disc samples, quantitative *ex vivo* ^{1}H HRMAS MRS measured low proteoglycan/collagen and proteoglycan/lactate ratios and high lactate/collagen ratio as biochemical markers associated with discogenic back pain versus scoliosis conditions. Several MRS-visible metabolites, such as proteoglycan, collagen, and lactate, may serve as metabolic markers of disc degeneration-associated back pain[79].

xi. MRS-visible biomarkers distinguished the painful discs (PD) and quantified the severity of disc degeneration to predict the surgical outcomes in chronic low back pain (CLBP) patients. MRS showed disc proteins (proteoglycan and collagen) and acidic metabolites (lactate, alanine, propionate) as pain MRS biomarkers in CLBP versus PD Pfirrmann grade or ratios of acidity metabolites to proteins. MRS correlation with PD may improve surgical outcomes in CLBP patients. *In vivo* MRS may define mechanisms of pain metabolites to design therapies[80,81]. The author believes that MRS-derived pain analysis is the first-line method.

xii. American College of Radiology (ACR) Guidelines on bone tumor musculoskeletal imaging indicate that MRS may differentiate benign and malignant lesions. Still, more efforts are needed[82].

xiii. With ultrahigh MRS availability and access, MRS is a clinical tool in the oncologic management of patients[83]. MRS is still an experimental investigation tool in

suspected breast cancer due to limited peer-reviewed clinical literature on cancer MRS use in theranosis.

The diagnostic value of ^{1}H-MRS in cancer is based on the detection of elevated choline levels as a marker of active tumors. The ^{1}H-MRS with breast MRI improves the specificity to distinguish benign from malignant lesions and monitors to predict the neoadjuvant chemotherapy response to treat patients. Integrating MRI with ^{1}H-MRS evaluation cuts down the need for multiple benign biopsies, and MRS may predict response within 24 h after the first dose of neoadjuvant chemotherapy given[84].

The non-invasive *in vivo* ^{1}H-MRS differentiated the benign and malignant breast lesions as different increased levels of choline (Cho) compounds and increased Cho metabolism in breast pre-cancer cells showing infiltrating ductal carcinoma, infiltrating medullary, mucinous, and lobular adenoid cystic carcinoma as active lesions by ^{1}H-MRS. However, ^{1}H-MRS showed no change or normal metabolites in benign breast lesions, including cysts, galactoceles, ductal carcinoma, papilloma, fibroadenoma, fibrocystic changes, tubular adenoma, and phyllodes tumors[85]. The author suggests stronger ultrahigh field MR imagers with advanced coils will increase the ^{1}H-MRS sensitivity. Ultrahigh field ^{1}H-MRS will detect the smallest malignant lesions to characterize the malignant lesions into non-invasive or invasive disease progression monitoring.

The clinical evidence is insufficient for MRS in the evaluation of leukoencephalopathy and childhood white matter diseases because both disorders show similar MRI signal intensity changes despite different pathologies. The ^{1}H-MRSI distinguished three conditions of white matter rarefaction, hypomyelination, and demyelination. Neurochemicals from six white matter rarefaction and intra-intervoxel (relative to gray matter) neurochemical ratios showed significant pathophysiological differences in high Cho/NAA, Cho/Cr, and low NAA/Cr ratios. These measurements serve as accurate linear discriminant parameters for classifying hypomyelinating conditions[86]. Combined MRI/MRS explored risk profiles in prostate cancer and can be a promising cost-effective screening test for low-risk patients[87].

In a prospective, multicenter trial on patients undergoing radical prostatectomy and visualized with endorectal 1.5 tesla MRI and MRS reported an accurate sextant localization of peripheral zone (PZ) in prostate cancer tissue matched with biopsy-confirmed prostate adenocarcinoma to schedule the removal of prostate or radical prostatectomy[88]. T1-weighted, T2wt, and 1.5 tesla MRS with pelvic-phased array coil in combination with an endorectal coil improved the diagnostic accuracy of MRI-MRS over MRI alone.

xiii. The ^{19}F MRS used SR4554 (fluorinated 2-nitroimidazole) as a hypoxia intra-tumoral marker in the phase I trial. The ^{1}H/^{19}F surface coils and localized ^{19}F MRS acquisition spectra showed different signals in post-SR4554 infusion (MRS no.1) after 16 h (MRS no. 2) and 20 h (MRS no. 3) in both unlocalized and localized MRS indicating different grades of hypoxia[89].

6. Clinical trial reports on MRSI in the years 2010 – 2022

The present consensus on clinical MRS acceptance was focused on new guidelines and meta-analyses. MRI generates an image, while MRS generates a graph or peak "spectrum" array of metabolite types to quantify them in the brain or other organs. The present consensus on MRS metabolite interpretation is in favor of theranosis and treatment planning in neurological and other human diseases. Documented meta-analysis and review studies in recent years (2010 – 2022) recommend the need for investigative and reproducible multicentric cost-effective clinical trials on large patient numbers with diagnostic accuracy and validation before clinical practice. Still, MRS evaluation in primary brain tumors or metastases remains investigational/experimental due to the lack of peer-reviewed clinical literature on the effectiveness of MRS.

The Food and Drug Administration (FDA) granted 510 (k) clearance to prescribe MRS to cancer patients. However, MRI and MRS use different postprocessing software to acquire data, integrate, and manipulate the spectroscopic image signal.

6.1. Malignancy and tumors in human

6.1.1. The clinical evidence is inconclusive on the MRS of prostate cancer

MRS offers prostate gland choline and citrate metabolic information as prognostic information that is useful for treatment planning. Combined proton MRSI with T2wt MRI to T2wt MRI improves tumor localization, volume estimation, tumor staging, tissue characterization, and identification of recurrent disease after therapy. The American College of Radiology Imaging Network showed that the combined ^{1}H-MRSI and T2wt MR images do not improve tumor detection in patients with low-grade, low-volume diseases selected to undergo radical prostatectomy. Thus positive ^{1}H-MRSI reflects only higher tumor grade and/or volume. In a retrospective trial, MRI and MRS predicted the normal prostate or suggestive of progressive prostate cancer malignancy risk of the Gleason score and subsequent biopsy. MRSI did not predict cancer progression[89].

A retrospective MRSI study with T2wt MRI images showed recurrent prostate cancer after androgen therapy

and definite external beam radiation therapy. A_Z analysis of T2wt MRI+MRSI improved the diagnostic accuracy and detection of locally recurrent prostate cancer[90].

The MRS-guided radiation administration of higher dose delivery is precise to treat metabolically active prostate tumor areas. MRS-compatible implants are available to deliver high radiation doses in metabolically active regions of tumors.

The diagnostic accuracy of MRS, DCE-MRI, and DWI localizes malignancy and prostate abnormalities in negative prostate biopsies. Multiparametric T2wt MRI+MRS, transrectal ultrasound-guided biopsy T2wt MRI, with DCE/DW-MRI images, and histopathological assessment of prostate biopsy tissue showed high sensitivity and specificity of MRS than T2wt MRI to detect moderate or high-risk cancer[91]. A few multi-parametric MRS, DCE-MRI/DW-MRI imaging approaches with MR-guided biopsy, and extended 14-core ultrasound-guided biopsy showed better diagnostic accuracy against a reference biopsy obtained by histopathology biopsy, template biopsy, or prostatectomy specimens. MRS is useful in the differential diagnosis of dermatomyositis and polymyositis.

6.1.2. The clinical evidence is inconclusive on the MRS of CNS cancer

The National Comprehensive Cancer Network (NCCN, 2016) gave guidelines on CNS cancer imaging. The MRS examination may be useful to differentiate anaplastic gliomas from radiation-induced necrosis or "pseudoprogression." The MRS marginally differentiated the glioma recurrence from radiation necrosis. The MRS data statistics in glioma showed elevated Cho/Cr, Cho/NAA ratio in favor of high sensitivity, specificity, areas under receiver operative curves for heterogeneity test, and threshold effect test as moderate diagnostic value to distinguish radiation-induced necrosis from glioma recurrence[92].

Furthermore, MR perfusion and MRS successfully distinguished the primary brain tumors, radiation-induced necrosis, and brain metastasis in patients by analyzing cerebral blood volume (rCBV), the ratios of Cho/tCr, Cho/NAA, and conducting a chi-square-based heterogeneity test using Cochran's Q statistics. Among 12 patients with tumor recurrence, elevated Cho/NAA and Cho/Cr ratios were observed. Furthermore, MR perfusion and MRS successfully distinguished the primary brain tumors, radiation-induced necrosis, and brain metastasis in patients by analyzing cerebral blood volume (rCBV), the ratios of Cho/tCr, Cho/NAA, and conducting a chi-square-based heterogeneity test using Cochran's Q statistics. Among 12 patients with tumor recurrence, elevated Cho/NAA and Cho/Cr ratios were observed[93]. The MRS method shows the accuracy of assessing metabolites and rCBV in primary brain tumors or metastases and recurrent necrotic tumors in patients. The author suggests that the MRS with MRI technique will improve diagnostic accuracy using multimodal multicenter trials in the future.

In vivo single-voxel ^{1}H-MRS showed brain metabolite differences as low NAA in putamen due to loss of neuronal integrity in early HD and pre-HD against controls; high glial myo-inositol cell marker in pre-HD and early-HD against controls with Unified Huntington's Disease Rating Scale (UHDRS) motor score, tongue pressure task, and disease burden score as neuropsychological biomarkers of HD onset and progression to establish an association with motor performance in TRACK-HD study[94]. The lower putaminal tNAA and high MI in early HD compared to controls established putamen MRS as HD onset and progression biomarker in a cross-section of subjects.

The role of MRS is wide in the classification of human brain tumors, the distinction of tumors versus non-neoplastic lesions, prediction of survival, treatment planning, and monitoring of post-therapy effects in tumor diagnosis and treatment response[95].

6.1.3. Non-invasive in vivo ^{1}H-MRS in breast cancer

Breast proton 3T MRS differentiated the benign tumors from malignant lesions by 1D single-voxel spatially resolved MRS high choline peak high sensitivity and variable specificity. Details are given in Section 3.1.

MRS with breast MRI enhances the cancer diagnostic accuracy to avoid repeat benign biopsies. MRS clearly visualizes the choline peaks in the evaluation of suspicious non-cancer mass otherwise non-visible on breast MRI. MRS still remains an investigational tool due to ethical concerns, but it monitors the outcome and response of therapy.

6.1.4. Non-invasive in vivo 31-phosphorous (^{31}P)-MRS in myocardium

MRS showed the metabolic state and biochemical score of the myocardial molecular imaging in ischemic heart disease and valvular disease to assess the effectiveness of metabolic modulating agents. Limited research, low temporal and spatial resolution, poor reproducibility, and longer data collection time are the major bottlenecks[96]. The author believes that MRS will be a multi-modal non-invasive cardiac assessment in the future.

6.2. Neurophysiological diseases

Neuro-metabolic changes in glucose metabolism, ionic shifts, the release of neurotransmitters, altered cerebral

blood flow, and impaired axonal functions are associated with concussion and neuronal depolarization. ^{1}H-MRS, or MRS, measures brain metabolites and physiologic changes after sport-related concussions. MRS-visible neurochemicals monitor the altered neurophysiology and recovery of post-concussive symptoms or injury returning to normative levels in adult athletes[97]. The author suggests that large cross-sectional, prospective, and longitudinal studies will establish the high sensitivity and prognostic value of MRS in concussion. The American Medical Society for Sports Medicine advocated the use of MRS in concussion in sports as a research tool, not a management tool[98].

The "Current Lyme disease" and "Nervous system Lyme disease" guidelines mentioned the MRS as a diagnostic tool, not as a management tool[99].

The MRS studies showed high specificity and sensitivity in children at short TE-chemical shift imaging of brain tumors[100].

The American College of Radiology's Appropriateness Criteria of dementia and movement disorders favor the use of fMRI and MRS in neurodegenerative disorders but not for routine clinical practice[101]. Moreover, positron emission tomography (PET), single-photon emission computerized tomography (SPECT), fMRI, DTI, and MRS may visualize head trauma injury occult in children by standard imaging but are insufficient in routine clinical use. In young children with attention-deficit/hyperactivity disorder (ADHD), autism spectrum disorders, emotional dysregulation, and schizophrenia, ^{1}H-MRS showed increased glutamine/glutamate, related metabolites in the anterior cingulate cortex (ACC), and other regions. In major depression, bipolar disorders, and obsessive-compulsive disorder children, ^{1}H-MRS showed low glutamine/glutamate. Limited evidence showed a normal GLx level after treatment of bipolar disorder and ADHD diseases to indicate the mechanism of glutamate dysregulation in these disorders[102].

6.3. Amyloid pathology in Alzheimer's disease

^{1}H-MRS showed low NAA and low NAA/Cr ratio in posterior cingulate and bilateral left/right hippocampus regions and high MI/Cr ratio in posterior cingulate and gray matter in Alzheimer's disease patients[103]. The author suggests that NAA/Cr ratio, NAA, and MI are indicators of brain dysfunction, while MI/NAA and Cho/Cr ratios are diagnostic indicators in Alzheimer's disease subjects.

The amyloid pathology and proton MRS metabolites in non-dementia individuals show cognitive decline as changes +2.9%/year of MI/tCr ratio and −3.6%/year of NAA/MI ratio in mild cognitive impairment β-amyloid (Aβ+) patients; −0.05%/y mI/Cr and +1.2/y NAA/mI ratio in Aβ- patients, and the changes were associated with Mini-Mental State Examination (MMSE), *APOE4*, age, and sex. Low NAA/MI indicated low cognitive capacity in Aβ+ patients with a high NAA/MI baseline. The longitudinal changes in mI/Cr and NAA/mI ratios classified the amyloid pathology types due to dementia[104]. In Aβ+ individuals, NAA/mI ratio predicts a declining rate of cognition in the future. Now, a PET scan indicates the amyloid and tau deposition to screen dementia and monitors the disease progression to evaluate molecular pathology *in vivo* using MRS/PET in a clinical setting. The author suggests using multimodal large-scale hybrid MRS-PET clinical trials to measure metabolites and early β-amyloid and tau protein changes in a single MRI+MRS session in Alzheimer's disease and shows the increased MI/Cr ratio with longitudinal decline in NAA/mI ratio to track pre-dementia Alzheimer's disease progression in clinical trials.

6.4. Radiation encephalopathy

The proton MRS measured the varied metabolite concentrations of NAA/tCr ratio, Cho/Cho ratio, NAA, Cho, and Cr in healthy control and post-radiotherapy encephalopathy subjects. MRS evaluation is feasible to evaluate radiation therapy-induced encephalopathy in nasopharyngeal carcinoma. The author suggests precise subgroup analysis includes variables such as disease stage, age, and sex[105].

6.5. Theranosis of hepatic encephalopathy

MRSI visualized the altered imaging features showing stratification, the severity of the hepatic encephalopathy in non-hepatic encephalopathy (HE) cirrhosis, minimal HE, and overt HE patients by monitoring high glutamine/glutamate ratio, high choline, and high MI peaks in parietal lobe by Metafor v3.4.1 software analysis in brain regions. These MRI+MRS features showed a correlation with high homogeneity and HE grade in all brain regions. However, evaluation can be biased by HE assessment cutoff, sample size, the method used, and geographic variation. In parallel, overt HE severity and classification vary by West Haven grades[106].

6.6. Evaluation of liver steatosis in liver donors

A meta-analysis of hepatosteatosis using MRI+MRS in living liver donors showed high specificity and sensitivity of hepatosteatosis to avoid liver biopsy[107]. However, the use of MRS had several drawbacks: (i) moderate inter-study clinical or statistical heterogeneity due to diagnostic threshold variability study methodology; (ii) MRI and MRS suffer from selection and recall biases with higher sensitivity and specificity or may over-estimate in retrospective studies; and (iii) sample size, sex ratio, and mean age factors need meta-regression with these

parameters and demand large data and uniform thresholds of substantial hepatosteatosis limits.

6.7. Monitoring hepatocellular carcinoma and liver cirrhosis development

^{1}H-MRI+MRS predicted the probability by high Cho, lipid (Lip) contents, and Cho/Lip ratio on LCModel software to assess the magnitude of hepatocellular carcinoma (HCC) with secondary chronic hepatitis B and cirrhosis[108]. The author suggests that ^{1}H-MRS-visible hepatic metabolite levels may monitor both HCC and liver cirrhosis development, but more validation studies are needed.

6.8. Low back pain

In vivo MRS in low back pain subjects showed: (i) low NAA concentration in the right primary motor cortex, left anterior insula, left somatosensory cortex (SSC), anterior cingulate cortex (ACC), and dorsolateral prefrontal cortex (DLPFC) regions; (ii) low glutamate in ACC; (iii) low MI in ACC and thalamus; (iv) high choline in the right SSC; and (v) high glucose in the DLPFC locations[109]. Biochemical alteration in low back pain-brain MRS profile correlates with possible therapy response and the physiochemical functions of brain metabolites and pain receptors. The author notices concerns about the few subjects selected, confounding factors, medication effects, and unclear biochemical basis of pain-specific metabolite changes.

6.9. Juvenile myoclonic epilepsy

^{1}H-MRS showed distinct low NAA and NAA/Cr ratio, a rise in Glx/Cr ratio in the insula and striatum to indicate juvenile myoclonic epilepsy (JME) as multi-region, thalamo-frontal network epilepsy (not idiopathic general epilepsy)[110]. The frontal cortex and thalamo-cortical pathways indicated low NAA and low NAA/Cr ratio in the frontal region of JME related to memory and visual attention Stroop test; low NAA/Cr ratio in thalamic linguistic and memory regional Wisconsin card sorting test. Unaltered Glx, Glx/tCr ratio, Cho compounds, and Cho/tCr ratio in frontal and thalamic regions were associated with epileptic cortical functions, neuropsychological cognitive tests as visuospatial executive functions, linguistic, memory, and visual attention[111]. The MRS may show subclinical cognitive changes. The author suggests the need for validation studies.

6.10. Primary focal CNS lymphoma lesions

A hybrid approach of MRS with SPECT and PET distinguished the CNS lymphoma from the human immunodeficiency virus (HIV)[112]. MR perfusion, MRI APC ratio, and regional cerebral blood volume characteristics distinguish lymphoma from HIV-infected patients. The author suggests more clinical investigations to establish the diagnostic accuracy of hybrid MRI approaches.

6.11. Migraine pathophysiology and identification of neuromarkers in migraine

The ^{1}H-MRS studies suggested many inter-ictal abnormalities in migraine patients with persistent altered mitochondrial energy loss, neuronal excitability indicated by high excitatory glutamate, high inhibitory GABA neurotransmitter peaks, low NAA levels due to mitochondrial dysfunction, and abnormal energy metabolism toward excitatory stimulation or migraine attack triggers[113]. MRS can be a valuable non-invasive method to determine migraine attacks, correlate severity, and monitor medication efficacy.

6.12. Adrenoleukodystrophy

Status epilepticus or childhood cALD shows abrupt pathogenic ABCD1 mutation or transiently altered mental status neurodegeneration in autism with fever, diarrhea, seizures, coma, gross motor loss, fine motor loss, and poor speech skills. Serial brain MRI/MRS showed elevated lactate peak and CSF protein levels associated with diffused progressive cortex swelling, laminar necrosis, and restricted diffusion indicative of mitochondrial, lysosomal, and peroxisomal disorders. Moreover, MRS showed elevated very-long-chain fatty acids, lactate peaks, and high CSF proteins. The acute decline in neurologic functions with elevated CSF proteins and lactate and acute decline in neurologic NAA/Cr functions by MRS indicates MRI non-visible white matter abnormalities to predict disease progression[114].

6.13. Hypoxic-ischemic encephalopathy

Proton MRI with MRS showed elevated Lac/NAA ratio in posterior white matter areas and deep gray nuclei of putamen and thalamus areas as prognostic indicators for brain hypoxic-ischemic injury underlying neonatal hypoxic-ischemic encephalopathy (HIE)[115]. Proton MRS (^{1}H-MRS) showed high NAA/tCr in basal ganglia/thalamus(BG/T), high NAA/Cho in basal ganglia/thalamus (BG/T), and high Myo-inositol/choline in the cerebral cortex as a prognostic marker of therapeutic hypothermia (TH) with adverse outcomes of white matter and gray matter NAA in prediction for all HIE subjects. The author suggests the need for prospective multi-center studies by standardized protocol and analysis methods[116].

6.14. Traumatic brain injury

The single-voxel ^{1}H-MRS showed an altered ratio of NAA/Cr+phosphocreatine(PCr),NAA+*N*-acetylaspartylglutamate

(NAAG)/Cr+PCr relative to creatine neurometabolites in complicated and uncomplicated traumatic brain injury (TBI) patients. The NAA peaks and NAA values were lower in complicated and uncomplicated TBI groups compared to the control group. Neurometabolite alterations indicated the onset of both complicated and uncomplicated TBI with injury severity in mild TBI[117]. Furthermore, MRS is not a biomarker option in the management of TBI.

Mild TBI is a risk factor for dementia. The *in vivo* MRS detected low NAA, high glutamate, low choline, and variable Cr in frontal lobe brain white matter as membrane high turnover changes after a negative routine CCT/MRI scan of frontal lobe acute or subacute mild TBI within 3 months[118]. MRS correlated post-traumatic brain metabolism with cognitive dysfunction to detect mTBI patients at risk of post-traumatic neurodegeneration early. However, the author suggests follow-up studies are needed to correlate MRS with cognitive outcomes using different modified MRI sequences, high-field strength, accurate voxel placements, voxel sizes, and reasonable Cramér-Rao lower-bounds cutoffs.

6.15. Evaluation of prognostic consciousness recovery in wakefulness syndrome individuals

Multi-voxel MRS of the frontal cortex, temporal cortex, brain stem, fornix, internal capsule, thalamus, globus pallidus, and putamen regions in patients with vegetative state/unresponsive wakefulness syndrome (VS/UWS) showed low NAA/Cr ratio in the temporal cortex, capsula interna, and thalamus, while higher NAA/Cr ratio in these structures is indicative of recovery of consciousness[119]. The low NAA/Cr and NAA/(NAA+Ch+Cr) ratios in mid-brain regions were associated with hypoxia in patients. The MRS accurately predicted recovery of consciousness from hypoxic brain damage in unconscious VS/UWS patients with TBI to the level of emergence of a minimal conscious state (EMCS).

6.16. Substance use disorders

^{1}H-MRS is used to evaluate the effect of narcotic substances such as methamphetamine, alcohol, 3,4-methylenedioxymethamphetamine (MDMA), nicotine, marijuana, cocaine, opiate, and opioid in after-use disorders. A decrease in NAA and Cho levels in brain regions was a common feature in defining the substance-specific effect of the above-said substance use. The author recommends more MRS clinical trials to monitor novel substance abuse treatment. The ^{1}H-MRS showed low NAA and low Cho levels in the brain indicating altered neurometabolites in addicts on MDMA, cocaine, alcohol, methamphetamine, opiates/opioids, nicotine, and marijuana[120].

6.17. CNS system with rheumatic autoimmune diseases

Proton MRS measures neuronal loss or CNS damage with autoimmune rheumatic diseases. An MRS study reviewed vasculitis, Behcet's disease, Sjogren's syndrome, psoriasis, rheumatoid arthritis, juvenile idiopathic arthritis, systemic sclerosis, and systemic lupus erythematosus from November 2003 to December 2019[121]. Low NAA/Cr and high Cho/Cr ratios in different regions of the above brain diseases showed an association with various CNS disease inflammatory activities and comorbidities with diseases. The neurometabolite abnormalities with non-overt CNS manifestations suggested the association of abnormal vascular reactivity and systemic inflammation with subclinical CNS manifestations.

6.18. Diagnosis of mesial temporal lobe sclerosis

Recently, MRS metabolic features of the brain were reported to classify mesial lobe epilepsy, hippocampal sclerosis, mesial temporal sclerosis (MTS), and mesial and temporal seizures[122]. A decreased NAA, NAA/(Cho+Cr) ratio, and NAA/Cr ratio in the ipsilateral hippocampus and reduced NAA levels in extra-hippocampal regions are suggested as pre-surgical localization of epileptogenic focus.

6.19. Theranosis of mitochondrial diseases

Serial MRS visualized the response of weekly intravenous 500 mg/kg L-arginine therapy in MELAS, showing improvement clinically for the treatment of mitochondrial encephalopathy with lactic acidosis and stroke-like events. L-arginine therapy normalizes brain lactate and NAA/Cho ratio as a radiologic and clinical improvement[123]. The consensus suggests that the management of mitochondrial stroke-like episodes may be achievable through the utilization of MRS[124]. Mitochondrial myopathies in the brain, muscle, and cardiac tissue were indicated by elevated lactate levels detected by MRS[125].

7. Future directions and perspectives

In the future, clinical MRSI will be multimodal, robust, fast, equipped with new supervised segmentation, component-specific registration, and disease-specific spatio-spectral-encoded trained pixel data sets (spectromics) by super-resolution DL toward customized precision medicine[126-130]. A new perception of 3D-MRSI clinical value will certainly depend on new computer data generation and feature extraction using integrated diagnosis with high acceptance in medical practice[131,132]. Hybrid approaches of HPLC-MR, biochemical-MR, and digital histochemical-MR correlation may contribute better. It seems that quantification of metabolite

absolute concentrations may indicate actual spectral metabolic screening of inborn errors of metabolism, EEG neurophysiological properties in brain diseases, and cancer compared with test phantoms for quality assessment of clinical spectroscopy. New approaches using ^{13}C, ^{19}F, ^{7}Li, and ^{11}B spectroscopic imaging may be useful.

8. Conclusion

With minimum computation time, a DL approach is emerging with new hopes to utilize multimodal MRSI maps with concentrations, diffusion, perfusion, and flow MRI fingerprints combined with dynamic PET, CT, SPECT, and optic molecular imaging common platform screening modality. The segmentation, registration, and artificial intelligence further define disease courses and their clinical value jointly acceptable by scientists and clinician radiologists. Present opinion displays a common ground for the above. Government and academic clinical trials are quiet on this issue due to insufficient evidence.

Acknowledgments

I would like to acknowledge the recommendation of a plastic surgery research scholar fellowship in SMMH Government Medical College, Saharanpur, India, and the mentorship of Professor Aria Tzika, from Surgery NMR laboratory at Shriners Children Hospital, Massachusetts General Hospital, Harvard Medical School, Boston MA. I also acknowledge Drs PK Sharma, Arun Agarwala, NMR Laboratory, Indian Institute of Technology Delhi, New Delhi to provide ideas in NMR-biochemical correlation as radioimaging modality with artificial intelligence application in the present time.

Funding

None.

Conflict of interest

The authors declare no conflict of interest.

Author contributions

Conceptualization: Rakesh Sharma
Writing – original draft: Rakesh Sharma
Writing – review & drafting: Arvind Trivedi

Ethics approval and consent to participate

Not applicable.

Consent for publication

Not applicable.

Availability of data

Not applicable.

References

1. Sharma R, 1995, Studies on NMR Relaxation Times and NMR-Biochemical Correlation in Medicine. Ph. D Dissertation Submitted to AIIMS/Indian Institute of Technology, New Delhi.

2. Mountford CE, Doran SJ, Lean CL, *et al*., 2004, Proton MRS can determine the pathology of human cancers with a high level of accuracy. *Chem Rev*, 104: 3677–3704.

   https://doi.org/10.1021/cr030410g

3. Boada FE, Christensen JD, Huang-Hellinger FR, *et al*., 1994, Quantitative *in vivo* tissue sodium concentration maps: The effects of biexponential relaxation. *Magn Reson Med*, 32: 219–213.

   https://doi.org/10.1002/mrm.1910320210

4. Tkac I, Gruetter R, 2005, Methodology of 1H NMR spectroscopy of the human brain at very high magnetic fields. *Appl Magn Reson*, 27: 139–157.

   https://doi.org/10.1007/BF03166960

5. Geppert C, Dreher W, Leibfritz D, 2003, PRESS-based proton single-voxel spectroscopy and spectroscopic imaging with very short echo times using asymmetric RF pulses. *MAGMA*, 16: 144–148.

   https://doi.org/10.1007/s10334-003-0016-6

6. Seeger U, Klose U, Mader I, *et al*., 2003, Parameterized evaluation of macromolecules and lipids in proton MR spectroscopy of brain diseases. *Magn Reson Med*, 49: 19–28.

   https://doi.org/10.1002/mrm.10332

7. Kanowski M, Kaufmann J, Braun J, *et al*., 2004, Quantitation of simulated short echo time 1H human brain spectra by LCModel and AMARES. *Magn Reson Med*, 51: 904–912.

   https://doi.org/10.1002/mrm.20063

8. Sharma R, 2002, Serial amino-neurochemicals analysis in progressive lesion analysis of multiple sclerosis by magnetic resonance imaging and proton magnetic resonance spectroscopic imaging. *Magn Reson Med Sci*, 1: 169–173.

9. Grutter R, Rothman DL, Novotny EJ, *et al*., 1992, Detection and assignment of glucose signal in 1H NMR difference spectra of human brain. *Magn Reson Med*, 27: 183–188.

   https://doi.org/10.1002/mrm.1910270118

10. Rothman DL, Hanstock CC, Petroff OA, *et al*., 1992, Localized 1H NMR spectra of glutamate in human brain. *Magn Reson Med*, 25: 94–106.

    https://doi.org/10.1002/mrm.1910250110

11. Portais JC, Pianet J, Allard M, *et al*., 1991, Magnetic resonance spectroscopy and mretabolism. Applications

of proton and 13C NMR study of glutamate metabolism in cultured glial cells and human brain *in vivo*. *Biochemie*, 73: 93–97.

https://doi.org/10.1016/0300-9084(91)90080-k

12. Zia B, Bogia DP, 2020, Fast Fourier Transform and Convolution in Medical Image Reconstruction. Available from: https://www.intel.com/content/www/us/en/developer/articles/technical/fast-fourier-transform-and-convolution-in-medical-image-reconstruction.html [Last accessed on 2019 Nov 30].

13. Iqbal Z, Nguyen D, Thomas MA, *et al*., 2021, Deep learning can accelerate and quantify simulated localized correlated spectroscopy. *Sci Rep*, 11: 8727.

14. Yang J, Lei D, Qin K, *et al*., 2021, Using deep learning to classify pediatric posttraumatic stress disorder at the individual level. *BMC Psychiatry*, 21: 535.

https://doi.org/10.1186/s12888-021-03503-9

15. Balakrishnan R, Valdés Hernández MDC, Farrall AJ, 2021, Automatic segmentation of white matter hyperintensities from brain magnetic resonance images in the era of deep learning and big data - A systematic review. *Comput Med Imaging Graph*, 88: 101867.

https://doi.org/10.1016/j.compmedimag.2021.101867

16. Terpstra ML, Maspero M, Sbrizzi A, *et al*., 2022, A symmetric loss function for magnetic resonance imaging reconstruction and image registration with deep learning. *Med Image Anal*, 80: 102509.

https://doi.org/10.1016/j.media.2022.102509

17. Chen D, Wang Z, Guo D, 2020, Review and prospect: Deep learning in nuclear magnetic resonance spectroscopy. *Chemistry*, 26: 10391–10401.

https://doi.org/10.1002/chem.202000246

18. Li X, Strasser B, Neuberger U, *et al*., 2022, Deep learning super-resolution magnetic resonance spectroscopic imaging of brain metabolism and mutant isocitrate dehydrogenase glioma. *Neurooncol Adv*, 4: vdac071.

https://doi.org/10.1093/noajnl/vdac071

19. Migdadi L, Lambert J, Telfah A, *et al*., 2021, Automated metabolic assignment: Semi-supervised learning in metabolic analysis employing two dimensional Nuclear Magnetic Resonance (NMR). *Comput Struct Biotechnol J*, 19: 5047–5058.

20. Sarma MK, Nagarajan R, Macey PM, *et al*., 2014, Accelerated echo-planar J-resolved spectroscopic imaging in the human brain using compressed sensing: A pilot validation in obstructive sleep apnea. *AJNR Am J Neuroradiol*, 35: S81–S89.

https://doi.org/10.3174/ajnr.A3846

21. Marshall I, Thrippleton MJ, Bastin ME, *et al*., 2018, Characterisation of tissue-type metabolic content in secondary progressive multiple sclerosis: A magnetic resonance spectroscopic imaging study. *J Neurol*, 265: 1795–1802.

https://doi.org/10.1007/s00415-018-8903-y

22. Filippi M, Rocca MA, Rovaris M, 2002, Clinical trials and clinical practice in multiple sclerosis: Conventional and emerging magnetic resonance imaging technologies. *Curr Neurol Neurosci Rep*, 2: 267–276.

https://doi.org/10.1007/s11910-002-0086-2

23. Zuo J, Joseph GB, Li X, *et al*., 2012, *In vivo* intervertebral disc characterization using magnetic resonance spectroscopy and T1ρ imaging: Association with discography and Oswestry Disability Index and Short Form-36 Health Survey. *Spine (Phila Pa 1976)*, 37: 214–221.

https://doi.org/10.1097/BRS.0b013e3182294a63

24. Tartaglia MC, Arnold DL, 2006, The role of MRS and fMRI in multiple sclerosis. *Adv Neurol*, 98: 185–202.

25. Miller DH, Albert PS, Barkhof F, *et al*., 1996, Guidelines for the use of magnetic resonance techniques in monitoring the treatment of multiple sclerosis. US National MS Society Task Force. *Ann Neurol*, 39: 6–16.

https://doi.org/10.1002/ana.410390104

26. Binesh N, Yue K, Fairbanks L, *et al*., 2002, Reproducibility of localized 2D correlated MR spectroscopy. *Magn Reson Med*, 48: 942–948.

https://doi.org/10.1002/mrm.10307

27. Jung JA, Coakley FV, Vigneron DB, *et al*., 2004, Prostate depiction at endorectal MR spectroscopic imaging: Investigation of a standardized evaluation system. *Radiology*, 233: 701–708.

https://doi.org/10.1148/radiol.2333030672

28. Boesch SM, Wolf C, Seppi K, *et al*., 2007, Differentiation of SCA2 from MSA-C using proton magnetic resonance spectroscopic imaging. *J Magn Reson Imaging*, 25: 564–569.

https://doi.org/10.1002/jmri.20846

29. Kahleova H, Petersen KF, Shulman GI, *et al*., 2020, Effect of a low-fat vegan diet on body weight, insulin sensitivity, postprandial metabolism, and intramyocellular and hepatocellular lipid levels in overweight adults: A randomized clinical trial. *JAMA Netw Open*, 3: e2025454.

https://doi.org/10.1001/jamanetworkopen.2020.25454

30. Smits M, 2021, MRI biomarkers in neuro-oncology. *Nat Rev Neurol*, 17: 486–500.

https://doi.org/10.1038/s41582-021-00510-y

31. Galanaud D, Haik S, Linguraru MG, *et al*, 2010, Combined diffusion imaging and MR spectroscopy in the diagnosis of human prion diseases. *AJNR Am J Neuroradiol*, 31: 1311–1318.

https://doi.org/10.3174/ajnr.A2069

32. Reardon DA, Ballman KV, Buckner JC, *et al*., 2014, Impact of imaging measurements on response assessment in glioblastoma clinical trials. *Neuro Oncol*, 16 Suppl 7: vii24–35.

https://doi.org/10.1093/neuonc/nou286

33. Auer DP, 2009, *In vivo* imaging markers of neurodegeneration of the substantia nigra. *Exp Gerontol*, 44: 4–9.

https://doi.org/10.1016/j.exger.2008.08.051

34. Bulik M, Kazda T, Slampa P, *et al*., 2015, The diagnostic ability of follow-up imaging biomarkers after treatment of glioblastoma in the temozolomide era: Implications from proton MR spectroscopy and apparent diffusion coefficient mapping. *Biomed Res Int*, 2015: 641023.

https://doi.org/10.1155/2015/641023

35. Lombardo F, Frijia F, Bongioanni P, *et al*., 2009, Diffusion tensor MRI and MR spectroscopy in long lasting upper motor neuron involvement in amyotrophic lateral sclerosis. *Arch Ital Biol*, 147: 69–82.

36. Griffiths JR, Tate AR, Howe FA, *et al*., 2002, Magnetic Resonance Spectroscopy of cancer-practicalities of multi-centre trials and early results in non-Hodgkin's lymphoma. *Eur J Cancer*, 38: 2085–2093.

https://doi.org/10.1016/s0959-8049(02)00389-1

37. Jacobs MA, Stearns V, Wolff AC, *et al*., 2010, Multiparametric magnetic resonance imaging, spectroscopy and multinuclear (^{23}Na) imaging monitoring of preoperative chemotherapy for locally advanced breast cancer. *Acad Radiol*, 17: 1477–1485.

https://doi.org/10.1016/j.acra.2010.07.009

38. Korteweg MA, Veldhuis WB, Visser F, *et al*., 2011, Feasibility of 7 Tesla breast magnetic resonance imaging determination of intrinsic sensitivity and high-resolution magnetic resonance imaging, diffusion-weighted imaging, and (1)H-magnetic resonance spectroscopy of breast cancer patients receiving neoadjuvant therapy. *Invest Radiol*, 46: 370–376.

https://doi.org/10.1097/RLI.0b013e31820df706

39. Ashokkumar N, Meera S, Anandan P, *et al*., 2022, Deep learning mechanism for predicting the axillary lymph node metastasis in patients with primary breast cancer. *BioMed Res Int,* 2022: 8616535.

https://doi.org/10.1155/2022/8616535

40. Lewis JF, McGorray SP, Pepine CJ, 2002, Assessment of women with suspected myocardial ischemia: Review of findings of the Women's Ischemia Syndrome Evaluation (WISE) Study. *Curr Womens Health Rep*, 2: 110–114.

41. Stivaros S, Garg S, Tziraki M, *et al*., 2018, Randomised controlled trial of simvastatin treatment for autism in young children with neurofibromatosis Type 1 (SANTA). *Mol Autism*, 9: 12.

https://doi.org/10.1186/s13229-018-0190-z

42. Kulyabin YY, Bogachev-Prokophiev AV, Soynov IA, *et al*., 2020, Clinical assessment of perfusion techniques during surgical repair of coarctation of aorta with aortic arch hypoplasia in neonates: A pilot prospective randomized study. *Semin Thorac Cardiovasc Surg*, 32: 860–871.

https://doi.org/10.1053/j.semtcvs.2020.04.015

43. Magnotta VA, Heo HY, Dlouhy BJ, *et al*., 2012, Detecting activity-evoked pH changes in human brain. *Proc Natl Acad Sci U S A*, 109: 8270–8273.

https://doi.org/10.1073/pnas.1205902109

44. Streeter CC, Gerbarg PL, Brown RP, *et al*., 2020, Thalamic gamma aminobutyric acid level changes in major depressive disorder after a 12-week iyengar yoga and coherent breathing intervention. *J Altern Complement Med*, 26: 190–197.

https://doi.org/10.1089/acm.2019.0234

45. Löbel U, Hwang S, Edwards A, *et al*., 2016, Discrepant longitudinal volumetric and metabolic evolution of diffuse intrinsic Pontine gliomas during treatment: Implications for current response assessment strategies. *Neuroradiology*, 58: 1027–1034.

https://doi.org/10.1007/s00234-016-1724-8

46. Goda JS, Dutta D, Raut N, *et al*., 2014, Can multiparametric MRI and FDG-PET predict outcome in diffuse brainstem glioma? A report from a prospective phase-II study. *Pediatr Neurosurg*, 49: 274–281.

https://doi.org/10.1159/000366167

47. Vöglein J, Tüttenberg J, Weimer M, *et al*., 2011, Treatment monitoring in gliomas: Comparison of dynamic susceptibility-weighted contrast-enhanced and spectroscopic MRI techniques for identifying treatment failure. *Invest Radiol*, 46: 390–400.

https://doi.org/10.1097/RLI.0b013e31820e1511

48. Gonzalo N, Serruys PW, Barlis P, *et al*., 2010, Multi-modality intra-coronary plaque characterization: A pilot study. *Int J Cardiol*, 138: 32–39.

https://doi.org/10.1016/j.ijcard.2008.08.030

49. Chang L, Lee PL, Yiannoutsos CT, *et al*., 2004, A multicenter *in vivo* proton-MRS study of HIV-associated dementia and its relationship to age. *Neuroimage*, 23: 1336–1347.

https://doi.org/10.1016/j.neuroimage.2004.07.067

50. Stern JM, Merritt ME, Zeltser I, *et al*., 2008, Phase one pilot study using magnetic resonance spectroscopy to predict the histology of radiofrequency-ablated renal tissue. *Eur Urol*, 5: 433–438.

https://doi.org/10.1016/j.eururo.2008.03.106

51. Medical Advisory Secretariat, 2006, Functional brain

imaging: An evidence-based analysis. *Ont Health Technol Assess Ser*, 6: 1–79.

52. Kettelhack C, Wickede MV, Vogl T, *et al*., 2002, 31Phosphorus-magnetic resonance spectroscopy to assess histologic tumor response noninvasively after isolated limb perfusion for soft tissue tumors. *Cancer*, 94: 1557–1564.

https://doi.org/10.1002/cncr.10361

53. de Fátima Vasco Aragão M, Otaduy MCG, de Melo RV, *et al*., 2007, Multivoxel spectroscopy with short echo time: Choline/N-acetyl-aspartate ratio and the grading of cerebral astrocytomas. *Arq Neuropsiquiatr*, 65: 286–294.

https://doi.org/10.1590/s0004-282x2007000200019

54. Kallén K, Burtscher IM, Holtås S, 2000, 201Thallium SPECT and 1H-MRS compared with MRI in chemotherapy monitoring of high-grade malignant astrocytomas. *J Neurooncol*, 46: 173–185.

https://doi.org/10.1023/a:1006429329677

55. Urdzik J, Bjerner T, Wanders A, *et al*., 2012, The value of pre-operative magnetic resonance spectroscopy in the assessment of steatohepatitis in patients with colorectal liver metastasis. *J Hepatol*, 56: 640–646.

https://doi.org/10.1016/j.jhep.2011.10.006

56. Watanabe T, Shiino A, Akiguchi I, 2008, Absolute quantification in proton magnetic resonance spectroscopy is superior to relative ratio to discriminate Alzheimer's disease from Binswanger's disease. *Dement Geriatr Cogn Disord*, 26: 89–100.

https://doi.org/10.1159/000144044

57. Wallström J, Geterud K, Kohestani K, *et al*., 2021, Prostate cancer screening with magnetic resonance imaging: Results from the second round of the göteborg prostate cancer screening 2 trial. *Eur Urol Oncol*, 5: 54–60.

https://doi.org/10.1016/j.euo.2021.09.001

58. Schmuecking M, Boltze C, Geyer H, *et al*., 2009, Dynamic MRI and CAD vs. choline MRS: Where is the detection level for a lesion characterisation in prostate cancer? *Int J Radiat Biol*, 85: 814–824.

https://doi.org/10.1080/09553000903090027

59. Bongiovanni A, Foca F, Oboldi D, *et al*., 2022, 3-T magnetic resonance-guided high-intensity focused ultrasound (3 T-MR-HIFU) for the treatment of pain from bone metastases of solid tumors. *Support Care Cancer*, 30: 5737–5745.

https://doi.org/10.1007/s00520-022-06990-y

60. Kaufman MJ, Henry ME, Frederick BB, *et al*., 2003, Selective serotonin reuptake inhibitor discontinuation syndrome is associated with a rostral anterior cingulate choline metabolite decrease: A proton magnetic resonance spectroscopic imaging study. *Biol Psychiatry*, 54: 534–539.

https://doi.org/10.1016/s0006-3223(02)01828-0

61. Kondo DG, Sung YH, Hellem TL, *et al*., 2011, Open-label adjunctive creatine for female adolescents with SSRI-resistant major depressive disorder: A 31-phosphorus magnetic resonance spectroscopy study. *J Affect Disord*, 135: 354–361.

https://doi.org/10.1016/j.jad.2011.07.010

62. Ramesh K, Mellon EA, Gurbani SS, *et al*., 2022, A multi-institutional pilot clinical trial of spectroscopic MRI-guided radiation dose escalation for newly diagnosed glioblastoma. *Neurooncol Adv*, 4: vdac006.

https://doi.org/10.1093/noajnl/vdac006

63. Caivano R, Lotumolo A, Rabasco P, *et al*., 2013, 3 Tesla magnetic resonance spectroscopy: Cerebral gliomas vs. metastatic brain tumors. Our experience and review of the literature. *Int J Neurosci*, 123: 537–543.

https://doi.org/10.3109/00207454.2013.774395

64. Sharma R, Narayana PA, Wolinsky JS, 2001, Grey matter abnormalities in multiple sclerosis: Proton magnetic resonance spectroscopic imaging. *Mult Scler*, 7: 221–226.

https://doi.org/10.1177/135245850100700402

65. Bedell BJ, Narayana PA, Johnston DA, 1996, 3-dimensional MR image registration of the human brain. *Magn Reson Med*, 35: 384–390.

https://doi.org/10.1002/mrm.1910350317

66. Shoeibi A, Khodatars M, Jafari M, *et al*., 2021, Applications of deep learning techniques for automated multiple sclerosis detection using magnetic resonance imaging: A review. *Comput Biol Med*. 136: 104697.

https://doi.org/10.1016/j.compbiomed.2021.104697

67. Centers for Medicare & Medicaid Services (CMS), 2004, Decision Memo for Magnetic Resonance Spectroscopy for Brain Tumors (CAG-00141N). Baltimore, MD: CMS.

68. Ustymowicz A, Tarasow E, Zajkowska J, *et al*., 2004, Proton MR spectroscopy in neuroborreliosis: A preliminary study. *Neuroradiology*, 46: 26–30.

https://doi.org/10.1007/s00234-002-0851-6

69. Hollingworth W, Medina LS, Lenkinski RE, *et al*., 2006, A systematic literature review of magnetic resonance spectroscopy for the characterization of brain tumors. *AJNR Am J Neuroradiol*, 27: 1404–1411.

70. Hallahan BP, Daly EM, Simmons A, *et al*., 2012, Fragile X syndrome: A pilot proton magnetic resonance spectroscopy study in premutation carriers. *J Neurodev Disord*, 4: 23.

https://doi.org/10.1186/1866-1955-4-23

71. Zakian KL, Sircar K, Hricak H, *et al*., 2005, Correlation of proton MR spectroscopic imaging with Gleason score based on step-section pathologic analysis after radical prostatectomy. *Radiology*, 234: 804–814.

https://doi.org/10.1148/radiol.2343040363

72. Wetter A, Engl TA, Nadjmabadi D, *et al*., 2006, Combined MRI and MR spectroscopy of the prostate before radical prostatectomy. *AJR Am J Roentgenol*, 187: 724–730.

https://doi.org/10.2214/AJR.05.0642

73. Wang P, Guo YM, Liu M, *et al*., 2008, A meta-analysis of the accuracy of prostate cancer studies which use magnetic resonance spectroscopy as a diagnostic tool. *Korean J Radiol*, 9: 432–438.

https://doi.org/10.3348/kjr.2008.9.5.432

74. Vedolin L, Schwartz IV, Komlos M, *et al*., 2007, Brain MRI in mucopolysaccharidosis: Effect of aging and correlation with biochemical findings. *Neurology*, 69: 917–924.

https://doi.org/10.1212/01.wnl.0000269782.80107.fe

75. Chen HC, Lee LH, Lirng JF, *et al*., 2022, Radiological hints for differentiation of cerebellar multiple system atrophy from spinocerebellar ataxia. *Sci Rep*, 12: 10499.

https://doi.org/10.1038/s41598-022-14531-0

76. Dyke JP, Sanelli PC, Voss HU, *et al*., 2007, Monitoring the effects of BCNU chemotherapy Wafers (Gliadel) in glioblastoma multiforme with proton magnetic resonance spectroscopic imaging at 3.0 Tesla. *J Neurooncol*, 82: 103–110.

https://doi.org/10.1007/s11060-006-9254-6

77. Filippi M, Rocca MA, Arnold DL, *et al*., 2006, EFNS guidelines on the use of neuroimaging in the management of multiple sclerosis. *Eur J Neurol*, 13: 313–325.

https://doi.org/10.1111/j.1468-1331.2006.01543.x

78. De Stefano N, Filippi M, Miller D, *et al*., 2007, Guidelines for using proton MR spectroscopy in multicenter clinical MS studies. *Neurology*, 69: 1942–1952.

https://doi.org/10.1212/01.wnl.0000291557.62706.d3

79. Keshari KR, Lotz JC, Link TM, *et al*., 2008, Lactic acid and proteoglycans as metabolic markers for discogenic back pain. *Spine* (*Phila Pa 1976*), 33: 312–317.

https://doi.org/10.1097/BRS.0b013e31816201c3

80. Gornet MG, Peacock J, Claude J, *et al*., 2019, Magnetic resonance spectroscopy (MRS) can identify painful lumbar discs and may facilitate improved clinical outcomes of lumbar surgeries for discogenic pain. *Eur Spine J*, 28: 674–687.

https://doi.org/10.1007/s00586-018-05873-3

81. Benoist M, 2019, The Michel Benoist and Robert Mulholland Yearly European Spine journal review: A survey of the "medical" articles in the European Spine Journal, 2018. *Eur Spine J*, 28: 10–20.

https://doi.org/10.1007/s00586-018-5857-9

82. Morrison WB, Dalinka MK, Daffner RH, *et al*., 2005, Expert Panel on Musculoskeletal Imaging. Bone Tumors. Reston, VA: American College of Radiology (ACR).

83. Shah N, Sattar A, Benanti M, *et al*., 2006, Magnetic resonance spectroscopy as an imaging tool for cancer: A review of the literature. *J Am Osteopath Assoc*, 106: 23–27.

84. Bartella L, Huang W, 2007, Proton (1H) MR spectroscopy of the breast. *Radiographics*, 27 Suppl 1: S241–S252.

https://doi.org/10.1148/rg.27si075504

85. Tse GM, Yeung DK, King AD, *et al*., 2007, *In vivo* proton magnetic resonance spectroscopy of breast lesions: An update. *Breast Cancer Res Treat*, 104: 249–255.

https://doi.org10.1007/s10549-006-9412-8

86. Bizzi A, Castelli G, Bugiani M, *et al*., 2008, Classification of childhood white matter disorders using proton MR spectroscopic imaging. *AJNR Am J Neuroradiol*, 29: 1270–1275.

https://doi.org/10.3174/ajnr.A1106

87. Umbehr M, Bachmann LM, Held U, *et al*., 2009, Combined magnetic resonance imaging and magnetic resonance spectroscopy imaging in the diagnosis of prostate cancer: A systematic review and meta-analysis. *Eur Urol*, 55: 575–590.

https://doi.org/10.1016/j.eururo.2008.10.019.

88. Lee CP, Payne GS, Oregioni A, *et al*., 2009, A phase I study of the nitroimidazole hypoxia marker SR4554 using 19F magnetic resonance spectroscopy. *Br J Cancer*, 101: 1860–1868.

https://doi.org/10.1038/sj.bjc.6605425

89. Chuang MT, Liu YS, Tsai YS, *et al*., 2016, Differentiating radiation-induced necrosis from recurrent brain tumor using MR perfusion and spectroscopy: A meta-analysis. *PLoS One*, 11: e0141438.

https://doi.org/10.1371/journal.pone.0141438

90. National Comprehensive Cancer Network (NCCN), 2016, Central Nervous System Cancers. NCCN Clinical Practice Guidelines in Oncology, version 1.2016. Fort Washington, PA: NCCN.

91. Sturrock A, Laule C, Decolongon J, *et al*., 2010, Magnetic resonance spectroscopy biomarkers in premanifest and early Huntington disease. *Neurology*, 75: 1702–1710.

https://doi.org/10.1212/WNL.0b013e3181fc27e4

92. Beadle R, Frenneaux M, 2010, Magnetic resonance spectroscopy in myocardial disease. *Expert Rev Cardiovasc Ther*, 8: 269–277.

https://doi.org/10.1586/erc.09.169

93. Horská A, Barker C, 2010, Imaging of brain tumors: MR spectroscopy and metabolic imaging. *Neuroimaging Clin N Am*, 20: 293–310.

https://doi.org/10.1016/j.nic.2010.04.003

94. Westphalen AC, Coakley FV, Roach M 3rd *et al*., 2010, Locally recurrent prostate cancer after external beam radiation therapy: Diagnostic performance of 1.5-T endorectal MR

imaging and MR spectroscopic imaging for detection. *Radiology*, 256: 485–492.

https://doi.org/10.1148/radiol.10092314

95. Baltzer PA, Dietzel M, 2013, Breast lesions: Diagnosis by using proton MR spectroscopy at 1.5 and 3.0 T -- systematic review and meta-analysis. *Radiology*, 267: 735–746.

https://doi.org/10.1148/radiol.13121856

96. Mowatt G, Scotland G, Boachie C, *et al.*, 2013, The diagnostic accuracy and cost-effectiveness of magnetic resonance spectroscopy and enhanced magnetic resonance imaging techniques in aiding the localisation of prostate abnormalities for biopsy: A systematic review and economic evaluation. *Health Technol Assess*, 17: vii–xix, 1–281.

https://doi.org/10.3310/hta17200

97. Gardner A, Iverson GL, Stanwell P, 2014, A systematic review of proton magnetic resonance spectroscopy findings in sport-related concussion. *J Neurotrauma*, 31: 1–18.

https://doi.org/10.1089/neu.2013.3079

98. Harmon KG, Drezner JA, Gammons M, *et al.*, 2013, American Medical Society for Sports Medicine position statement: Concussion in sport. *Br J Sports Med*, 47: 15–26.

https://doi.org/10.1136/bjsports-2012-091941

99. Mygland A, Ljostad U, Fingerle V, *et al.*, 2010, European Federation of Neurological Societies. EFNS guidelines on the diagnosis and management of European Lyme neuroborreliosis. *Eur J Neurol*, 17: 8–16, e1–e4.

https://doi.org/10.1111/j.1468-1331.2009.02862.x

100. Wang W, Hu Y, Lu P, *et al.*, 2014, Evaluation of the diagnostic performance of magnetic resonance spectroscopy in brain tumors: A systematic review and meta-analysis. *PLoS One*, 9: e112577.

https://doi.org/10.1371/journal.pone.0112577

101. Wippold FJ 2nd, Brown DC, Broderick DF, *et al.*, 2014, Expert Panel on Neurologic Imaging. ACR Appropriateness Criteria® Dementia and Movement Disorders. Reston, VA: American College of Radiology (ACR).

102. Spencer AE, Uchida M, Kenworthy T, *et al.*, 2014, Glutamatergic dysregulation in pediatric psychiatric disorders: A systematic review of the magnetic resonance spectroscopy literature. *J Clin Psychiatry*, 75: 1226–1241.

103. Wang H, Tan L, Wang HF, *et al.*, 2015, Magnetic resonance spectroscopy in Alzheimer's disease: Systematic review and meta-analysis. *J Alzheimers Dis*, 46: 1049–1070.

https://doi.org/10.3233/JAD-143225

104. Voevodskaya O, Poulakis K, Sundgren P, *et al.*, 2019, Swedish BioFINDER Study Group. Brain myoinositol as a potential marker of amyloid-related pathology: A longitudinal study. *Neurology*, 92: e395–e405.

https://doi.org/10.1212/WNL.0000000000006852

105. Chen WS, Li JJ, Hong L, *et al.*, 2016, Diagnostic value of magnetic resonance spectroscopy in radiation encephalopathy induced by radiotherapy for patients with nasopharyngeal carcinoma: A meta-analysis. *Biomed Res Int*, 2016: 5126074.

https://doi.org/10.1155/2016/5126074

106. Zeng G, Penninkilampi R, Chaganti J, *et al.*, 2020, Meta-analysis of magnetic resonance spectroscopy in the diagnosis of hepatic encephalopathy. *Neurology*, 94: e1147–e1156.

https://doi.org/10.1212/WNL.0000000000008899

107. Zheng D, Guo Z, Schroder PM, *et al.*, 2017, Accuracy of MR imaging and MR spectroscopy for detection and quantification of hepatic steatosis in living liver donors: A meta-analysis. *Radiology*, 282: 92–102.

https://doi.org/10.1148/radiol.2016152571

108. Wang D, Li Y, 2015, 1H magnetic resonance spectroscopy predicts hepatocellular carcinoma in a subset of patients with liver cirrhosis: A randomized trial. *Medicine* (*Baltimore*), 94: e1066.

https://doi.org/10.1097/MD.0000000000001066

109. Zhao X, Xu M, Jorgenson K, 2016, Neurochemical changes in patients with chronic low back pain detected by proton magnetic resonance spectroscopy: A systematic review. *Neuroimage Clin*, 13: 33–38.

110. Zhang L, Li H, Hong P, 2016, Proton magnetic resonance spectroscopy in juvenile myoclonic epilepsy: A systematic review and meta-analysis. *Epilepsy Res*, 121: 33–38.

https://doi.org/10.1016/j.eplepsyres.2016.01.004

111. Cevik N, Koksal A, Dogan VB, *et al.*, 2016, Evaluation of cognitive functions of juvenile myoclonic epileptic patients by magnetic resonance spectroscopy and neuropsychiatric cognitive tests concurrently. *Neurol Sci*, 37: 623–627.

https://doi.org/10.1007/s10072-015-2425-5

112. Yang M, Sun J, Bai HX, *et al.*, 2017, Diagnostic accuracy of SPECT, PET, and MRS for primary central nervous system lymphoma in HIV patients: A systematic review and meta-analysis. *Medicine* (*Baltimore*), 96: e6676.

https://doi.org/10.1097/MD.0000000000006676

113. Younis S, Hougaard A, Vestergaard MB, *et al.*, 2017, Migraine and magnetic resonance spectroscopy: A systematic review. *Curr Opin Neurol*, 30: 246–262.

https://doi.org/10.1097/WCO.0000000000000436

114. Lai D, Sharma R, Wolinsky JS, *et al.*, 2003, A comparative study of correlation coefficients in spatially MRSI-observed neurochemicals from multiple sclerosis patients. *J Appl Stat*, 30: 1221–1229.

115. Wu Y, 2020, Clinical Features, Diagnosis, and Treatment

of Neonatal Encephalopathy. UpToDate. Waltham, MA: UpToDate.

116. Zou R, Xiong T, Zhang L, *et al*., 2018, Proton magnetic resonance spectroscopy biomarkers in neonates with hypoxic-ischemic encephalopathy: A systematic review and meta-analysis. *Front Neurol*, 9: 732.

https://doi.org/10.3389/fneur.2018.00732

117. Veeramuthu V, Seow P, Narayanan V, *et al*., 2018, Neurometabolites alteration in the acute phase of mild traumatic brain injury (mTBI): An *in vivo* proton magnetic resonance spectroscopy (1H-MRS) study. *Acad Radiol*, 25: 1167–1177.

https://doi.org/10.1016/j.acra.2018.01.005

118. Eisele A, Hill-Strathy M, Michels L, *et al*., 2020, Magnetic resonance spectroscopy following mild traumatic brain injury: A systematic review and meta-analysis on the potential to detect posttraumatic neurodegeneration. *Neurodegener Dis*, 20: 2–11.

https://doi.org/10.1159/000508098

119. Kondratyeva EA, Diment SV, Kondratyev SA, *et al*., 2019, Magnetic resonance spectroscopy data in the prognosis of consciousness recovery in patients with vegetative state. *Zh Nevrol Psikhiatr Im S S Korsakova*, 119: 7–14.

https://doi.org/10.17116/jnevro20191191017

120. Finnell DS, 2015, A clinical translation of the article titled, The utility of magnetic resonance spectroscopy for understanding substance use disorders: A systematic review of the literature. *J Am Psychiatr Nurses Assoc*, 21: 276–278.

https://doi.org/10.1177/1078390315598605

121. Frittoli RB, Pereira DR, Rittner L, *et al*., 2020, Proton magnetic resonance spectroscopy (1 H-MRS) in rheumatic autoimmune diseases: A systematic review. *Lupus*, 29: 1873–1884.

https://doi.org/10.1177/0961203320961466

122. Fernandez-Vega N, Ramos-Rodriguez JR, Alfaro F, *et al*., 2021, Usefulness of magnetic resonance spectroscopy in mesial temporal sclerosis: A systematic review. *Neuroradiology*, 63: 1395–1405.

https://doi.org/10.1007/s00234-021-02704-z

123. Hovsepian DA, Galati A, Chong RA, *et al*., 2019, MELAS: Monitoring treatment with magnetic resonance spectroscopy. *Acta Neurol Scand*, 139: 82–85.

https://doi.org/10.1111/ane.13027

124. Ng YS, Bindoff LA, Gorman GS, *et al*., 2019, Consensus-based statements for the management of mitochondrial stroke-like episodes. *Wellcome Open Res*, 4: 201.

https://doi.org/10.12688/wellcomeopenres.15599.1

125. O'Ferrall E, 2021, Mitochondrial Myopathies: Clinical Features and Diagnosis. UpToDate. Waltham, MA: UpToDate.

126. Weinreb JC, Blume JD, Coakley FV, *et al*., 2009, Prostate cancer: Sextant localization at MR imaging and MR spectroscopic imaging before prostatectomy-- results of ACRIN prospective multi-institutional clinicopathologic study. *Radiology*, 251: 122–133.

https://doi.org/10.1148/radiol.2511080409

127. Wang Z, Li Y, Lam F, 2022, High-resolution, 3D multi-TE 1 H MRSI using fast spatiospectral encoding and subspace imaging. *Magn Reson Med*, 87: 1103–1118.

128. Li Y, Wang Z, Sun R, *et al*., 2021, Separation of metabolites and macromolecules for short-TE 1H-MRSI using learned component-specific representations. *IEEE Trans Med Imaging*, 40: 1157–1167.

https://doi.org/10.1109/TMI.2020.3048933

129. Li Y, Wang Z, Lam F, 2022, SNR enhancement for multi-TE MRSI using joint low-dimensional model and spatial constraints. *IEEE Trans Biomed Eng*, 69: 3087–3097.

https://doi.org/10.1109/TBME.2022.3161417

130. Dong S, Hangel G, Chen EZ, *et al*., 2022, Flow-based visual quality enhancer for super-resolution magnetic resonance spectroscopic imaging. In: Mukhopadhyay A, Oksuz I, Engelhardt S, *et al*., (eds) Deep Generative Models. DGM4MICCAI 2022. Lecture Notes in Computer Science. Vol. 13609. Cham: Springer.

https://doi.org/10.1007/978-3-031-18576-2_1

131. Li X, Strasser B, Jafari-Khouzani K, *et al*., 2020, Super-resolution whole-brain 3D MR spectroscopic imaging for mapping D-2-hydroxyglutarate and tumor metabolism in isocitrate dehydrogenase 1-mutated human gliomas. *Radiology*, 294: 589–597.

https://doi.org/10.1148/radiol.2020191529

132. Wang L, Chen G, Dai K, 2022, Hydrogen proton magnetic resonance spectroscopy (MRS) in differential diagnosis of intracranial tumors: A systematic review. *Contrast Media Mol Imaging*, 18: 7242192.

https://doi.org/10.1155/2022/7242192

ACCSCIENCE PUBLISHING

Global Translational Medicine

ORIGINAL RESEARCH ARTICLE

Demystifying the influence of ferroptosis on Alzheimer's and Parkinson's diseases: A network and systems biology approach

Deepyaman Das[1,2]*, Chayan Munshi[2,3]*, Kalpesh Jas[2,4], and Sourish Pramanik[2,5]

[1]Department of Microbiology, Raiganj University, Raiganj, Uttar Dinajpur, 733134, West Bengal, India

[2]Ethophilia (An Autonomous Research Group), Santiniketan, 731235, West Bengal, India

[3]Berlin School of Business and Innovation GmbH, Alte Post, Karl-Marx-Straße, 97-99 12043 Berlin, Germany

[4]Department of Zoology, Visva Bharati University, Santiniketan, 731235, West Bengal, India

[5]Palli Siksha Bhavana, Institute of Agriculture, Visva Bharati University, Sriniketan, 731236, West Bengal, India

Abstract

Research into the pathophysiology of Alzheimer's disease (AD) and Parkinson's disease (PD) has spanned decades, unraveling deregulated signaling cascades in these diseases. Recently, the discovery of the link between ferroptosis and neurodegeneration has opened new avenues for neurodegenerative disease research. Despite this, the key players in the ferroptotic pathway potentially governing the progression of neurodegenerative disease remain unidentified. Thus, in the present study, we reconstructed two protein–protein interaction networks (PPINs) for AD and PD with their respective differentially expressed genes from post-mortem tissues and identified 21 highly connected clusters within the AD PPIN and 17 clusters within the PD PPIN. Then, we identified 8 ferroptotic transcription factors (FerrTFs) that regulate hub genes from the 7 deregulated clusters of AD and 6 FerrTFs from the 4 deregulated clusters of PD. Functional enrichment analysis of these clusters revealed impairment in important neurological functions. Finally, we identified 681 drugs with potential therapeutic effects against the 8 FerrTFs associated with AD and 633 drugs against the 6 FerrTFs linked to PD. In addition, 126 and 114 miRNAs might silence 7 and 5 FerrTFs against AD and PD, respectively. This exploratory study identifies potential markers of ferroptosis that could exacerbate these neurodegenerative diseases and also suggests possible therapeutic measures against them.

Keywords: Alzheimer's disease; Parkinson's disease; Ferroptosis; Transcription factors; Hub genes; Protein–protein interaction network

***Corresponding authors:**
Deepyaman Das
(deepyaman.das@gmail.com)
Chayan Munshi
(chayanbio@gmail.com)

Citation: Das D, Munshi C, Jas K, et al., 2023, Demystifying the influence of ferroptosis on Alzheimer's and Parkinson's diseases: A network and systems biology approach. *Global Transl Med*, 2(3): 0318.
https://doi.org/10.36922/gtm.0318

Received: March 9, 2023
Accepted: July 12, 2023
Published Online: August 8, 2023

1. Introduction

In recent paradigms, ferroptosis has emerged as a key driver of neurological disorders, including Alzheimer's disease (AD) and Parkinson's disease (PD). The dysregulation of iron homeostasis is the main cause of ferroptosis, eventually resulting in the progressive loss of neurons in neurodegenerative diseases. This iron-dependent mechanism of ferroptotic cell death is accompanied by the production of highly reactive free radicals

and severe peroxidation of membrane phospholipids that are rich in polyunsaturated fatty acids (primarily of arachidonic or adrenic acids from phosphatidyl ethanolamine molecules). This process contributes to the formation of extremely reactive free radicals[1,2].

Being a redox-active metal, iron plays an important role in the cellular metabolism of the central nervous system (CNS). However, the CNS is highly susceptible to oxidative damage induced by excess iron accumulation. The correlation between the accumulation of brain iron and the progression of neurological disorders along with cognitive decline substantiates ferroptosis as the main form of cell death in pathophysiological neurodegeneration. Ferroptosis is associated with the accumulation of brain iron, glutathione depletion, and lipid peroxidation, leading to functional and cognitive impairment, as well as progressive degeneration and death of nerve cells[3]. Recent studies on ferroptosis have clearly demonstrated the direct association between free iron, oxidative stress, lipid peroxidation, and neuronal cell death, suggesting a programmed cell death caused by the accumulation of iron-dependent lipid reactive oxygen species (L-ROS)[4]. Dysfunction in iron metabolism, such as impaired iron uptake by transferrin receptor (TFRC), compromised iron export by ferroportin, and disrupted iron storage in ferritin, causes L-ROS production, further resulting in ferroptosis[5].

Iron abundance, lipid peroxidation levels, and changes in glutathione peroxidase 4 activity are the most critical indicators of ferroptosis[5,6]. The modulation of ferroptosis in neurodegenerative illnesses has been linked to a number of genetic and epigenetic variables. For instance, mutations in genes encoding proteins involved in lipid peroxidation and iron metabolism have been associated with neurological disorders. This newly discovered cell death mechanism is regulated by several genes related to iron metabolism, including TFRC, divalent metal transporter 1, ferritin heavy chain 1, nuclear receptor coactivator 4, and iron response element binding protein 2[7,8]. Moreover, it can be regulated by several pathways, such as system x_c^-, voltage-dependent anion channels, p53, p62-Keap1-Nrf2, and others. Experimental use of iron chelators and several antioxidants has demonstrated their effectiveness in interrupting the process of ferroptosis and addressing neurodegenerative diseases[3]. However, further exploration of the regulatory mechanisms underlying ferroptosis is needed to advance the prevention and treatment of neurological diseases.

In the context of AD, ferroptosis has been implicated in neuronal cell death and neuroinflammation, both of which are associated with disease progression[9]. Several factors related to AD have been linked to ferroptosis. Firstly, iron dysregulation appears to play a key role. Iron is essential for normal brain function, but abnormal iron accumulation or distribution can lead to oxidative stress and neuronal damage[10]. In AD, increased iron levels have been observed in specific brain regions, and this iron dysregulation can promote the occurrence of ferroptosis[11]. Second, lipid peroxidation is also a primal factor. Ferroptosis involves the peroxidation of polyunsaturated fatty acids, leading to the production of lipid peroxides and subsequent cell membrane damage[12]. Lipid peroxidation has been detected in the brain of AD patients, suggesting a potential link between ferroptosis and neuronal damage in the disease[13]. In addition, depletion of glutathione levels has been observed in the brain of AD patients[14]. Glutathione depletion can impair the cells' ability to defend against oxidative damage, making them more susceptible to ferroptosis[15]. Finally, neuroinflammation, characterized by the activation of microglia and the release of pro-inflammatory factors, is a common feature of AD[16]. Inflammatory processes can induce ferroptosis by promoting the accumulation of iron and ROS while reducing antioxidant defenses[15].

PD is one of the most prevalent neurodegenerative conditions. It is characterized by the gradual loss of dopaminergic neurons in the substantia nigra pars compacta and the development of Lewy bodies and Lewy neurites, which are two important pathogenic features of PD. The main protein involved in Lewy disease is α-synuclein, which is misfolded and aggregated[17]. The pathogenesis of PD depends heavily on both iron dyshomeostasis and glial cell activation, which act as "partners in crime," mutually impacting each other and accelerating the degradation of dopaminergic neurons[18,19]. Activated glia promotes iron dyshomeostasis, leading to stronger microglial activation[20]. These findings suggest that the pathophysiology of PD may be related to the link between ferroptosis, glia activation, and neurodegeneration.

While these observations suggest a potential association of ferroptosis with Alzheimer's and PDs, it is important to note that the exact role and contribution of ferroptosis to the development and progression of both diseases are still areas of ongoing research. Further studies are needed to fully elucidate the complex mechanisms underlying the relationship between ferroptosis and these neurodegenerative diseases. In this study, we have unraveled the regulatory pathways that might be controlled by ferroptotic transcription factors (FerrTFs) during the progression of neurodegenerative diseases, such as AD and PD. In addition, we have devised potential therapeutic measures against them.

2. Materials and methods

2.1. Identification of differentially expressed genes (DEGs)

We used previously available microarray and RNA-seq transcriptome data deposited in NCBI (National Center for Biotechnology Information) to identify the DEGs. For AD, we used data from a previously published study by Guennewig *et al.*[21], which investigated the disease using samples from post-mortem brain tissues. We specifically focused on the genes that showed differential expression in the precuneus (AD-PREC) and primary visual cortex (VIC) of the brain. The identification of DEGs in this study was performed using "edgeR"[22]. Next, we obtained RNA-seq data from the subthalamic nucleus (STN) of post-mortem brain tissues from PD and non-PD patients, which is accessible in GSE106608. This data allowed us to determine DEGs associated with PD. Specifically, we compared the transcriptomic data of 7 PD patients against 9 healthy controls. Table S1 provides patient-specific details of the samples used in these datasets. To assess batch effects in the RNA-seq datasets, we conducted the principal component analysis (PCA). We set cutoff values of $\log_2$FC>1.0 and adjusted $P < 0.05$ across all the studies and datasets to identify significant DEGs.

2.2. Reconstruction of protein-protein interaction networks (PPINs) and identification of functional modules for AD and PD

We utilized only the physical protein–protein interactions available in the STRING v11.5 database (https://string-db.org/)[23] for network reconstruction. To screen the interactors of the DEGs, we employed the STRING application programming interface (API) in Python v3.9.2. The resulting interactors and DEGs were used to visualize their interaction network in Cytoscape 3.9.1[24]. A confidence score >0.7 was considered for both PPINs. For the detection of important modules from the PPIN in both cases, we used the MCODE v2.0.0 app in Cytoscape 3.9.1., which identifies densely connected sub-networks considering topological features of the main network[25]. Default settings were applied to find clusters within the network. For functional enrichment analysis of the modules, we used BiNGO in Cytoscape 3.9.1[26]. Subsequently, we identified hubs from the modules using Network Analyzer in Cytoscape 3.9.1 to calculate the topological features of the network. The mean degree was considered the cutoff value for identifying hubs from each module[27].

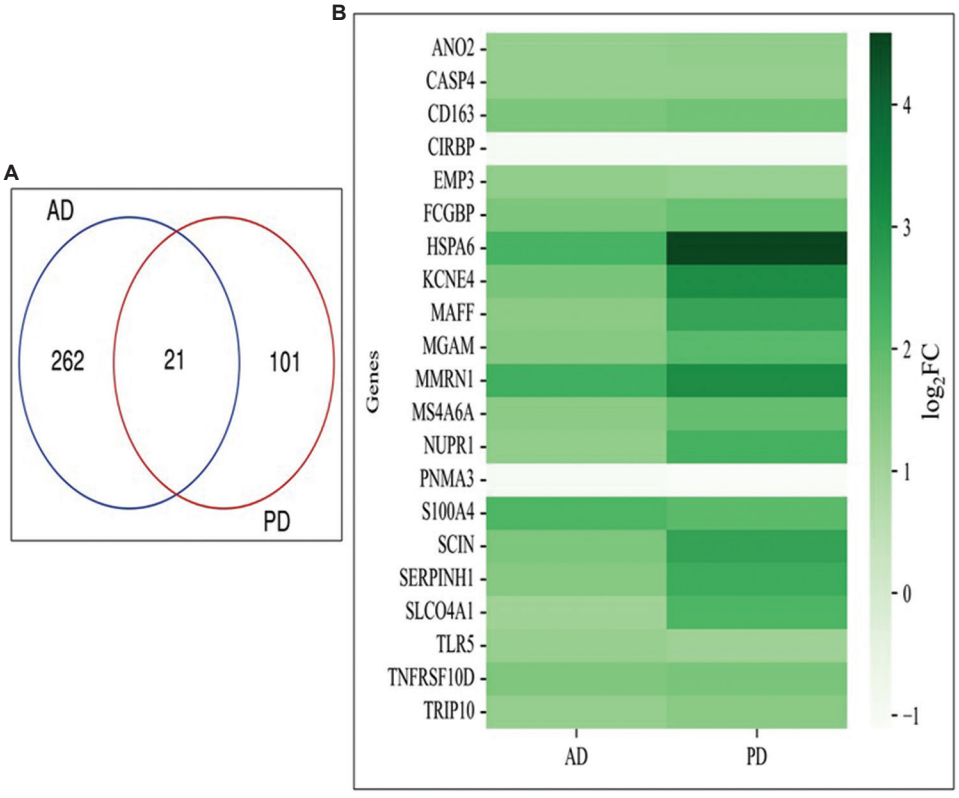

Figure 1. Common differentially expressed genes (DEGs) between Alzheimer's disease (AD) and Parkinson's disease (PD). (A) Venn diagram representing the number of DEGs common between AD and PD. (B) Log_2FC expression of common DEGs between AD and PD.

Figure 2. The protein–protein interaction network for Alzheimer's disease (AD protein–protein interaction networks) consists of 1478 nodes and 13344 edges.

2.3. Identification of FerrTFs regulating important modules in PPINs

Initially, we identified drivers and markers for ferroptosis from FerrDb[28]. Subsequently, we screened the transcription factors among these markers and drivers using the data available in TRRUST[29] and RegNetwork[30]. Using the gene regulatory data from these databases, we also identified the FerrTFs that might regulate the hubs from each module.

2.4. Identification of probable therapeutic miRNAs and drugs targeting FerrTFs

To screen drugs targeting FerrTFs, we used drug-protein interactions from Drug SIGnatures DataBase (DSigDB) [31]. For identifying therapeutic miRNAs targeting FerrTFs, we relied on miRNA-TF interactions from RegNetwork[30].

3. Results

3.1. Screening and identification of DEGs in the progression of neurodegenerative diseases

To investigate the influence of ferroptosis on neurodegeneration, we focused on two common neurodegenerative diseases: AD and PD[32]. We aimed to identify DEGs from gene expression data obtained from post-mortem brain tissues of these diseases, which could potentially serve as mediators of disease progression *in vivo*. For AD, we relied on the results from the study conducted by Guennewig *et al.*[21]. Specifically, we considered DEGs from AD-PREC and VIC of the brain. We successfully identified 283 DEGs for AD using cutoff values of $\log_2$FC > 1.0 and adjusted $P < 0.05$ (Table S2). Significant DEGs associated with AD included *CASP4, TLR9*, and *C5AR1*. *CASP4* has been associated with an increased risk of late-onset AD (LOAD)[33]. *TLR9* is implicated in neuroinflammation

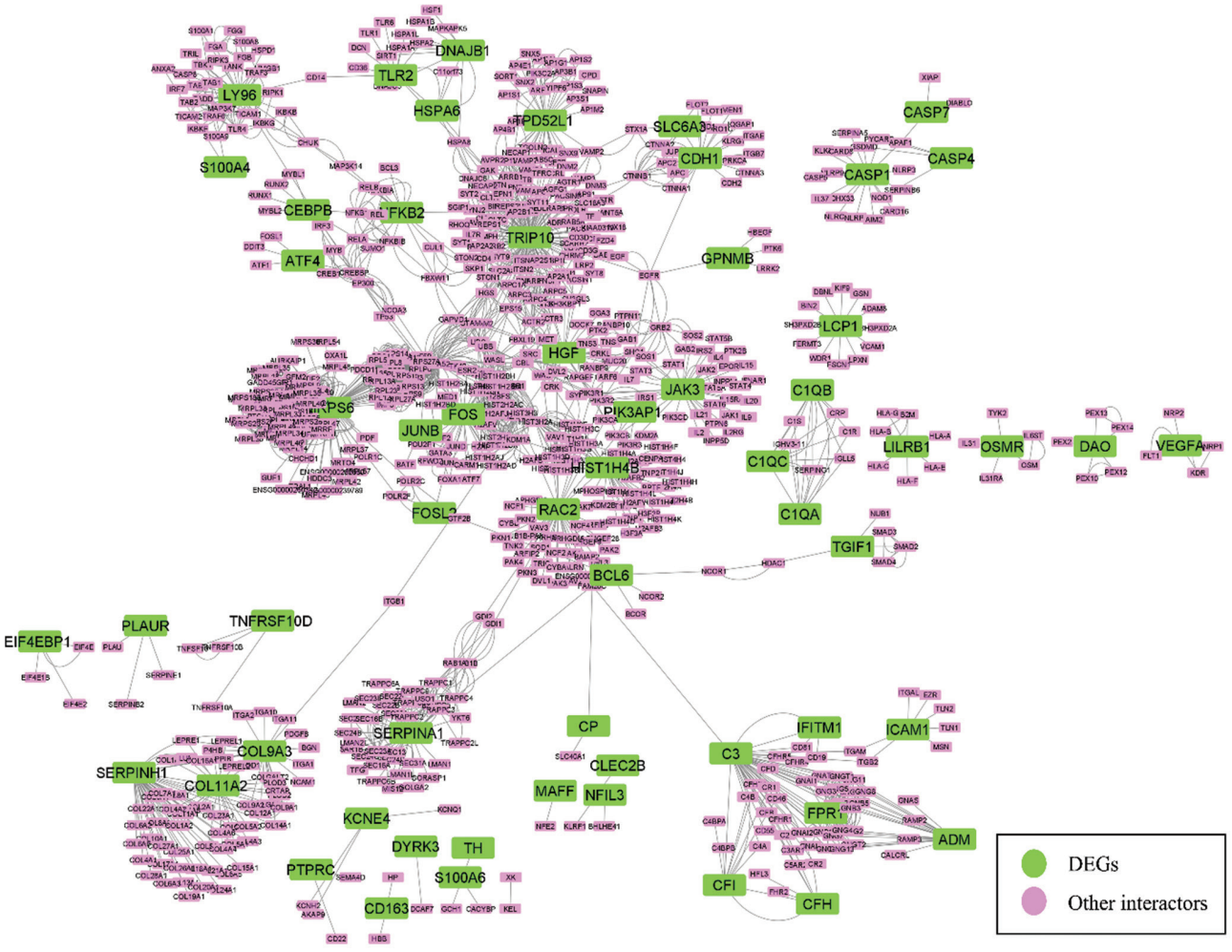

Figure 3. The protein–protein interaction network for Parkinson's disease (PD protein–protein interaction networks) consists of 819 nodes and 4766 edges.

during later stages of AD[34]. *C5AR1* encodes a proinflammatory receptor for C5a, with C5aR1 antagonists found to protect against the onset of AD[35].

To identify DEGs for PD, we analyzed gene expression data from GSE106608 and examined gene expression changes in STN from post-mortem brains of PD patients. By applying cutoff values of $\log_2$FC > 1.0 and adjusted P < 0.05 (Table S2), 122 DEGs were identified. Significant DEGs associated with PD included *NEAT1, CASP7*, and *SERPINA1. NEAT1* is known to initiate the formation of nuclear paraspeckles, which are involved in the progression of PD. It has been proposed to be a possible biomarker for PD[36]. *CASP7* encodes caspase-7, which has been found to promote the activation of microglia[37] and lead to neurotoxicity and neurodegeneration. *SERPINA1*, which encodes serpina1 protein, has modified forms associated with dementia in PD[38].

Thus, the DEGs we identified represent genes that play crucial roles in disease progression. Moreover, we found 21 DEGs that were common to both AD and PD (Figure 1).

3.2. Detection of hub genes from functional modules in AD and PD PPIN

The results indicate that ferroptosis may play a role in instigating the progression of both AD and PD. Reconstruction of PPIN with direct interactors of DEGs provides a comprehensive view of molecular signaling events and the diverse pathways involved in disease progression[39]. Thus, we initially reconstructed two separate PPINs for AD and PD using STRING v11 API in Python 3.9.2., considering only physical interactions with a confidence score >0.7[40]. The resulting networks were then visualized in Cytoscape v3.9.1[24] (Figures 2 and 3). The PPIN for AD (AD-PPIN) consists of 1478 nodes and 13344 edges (Figure 2), while the PPIN for PD (PD-PPIN) consists of 819 nodes and 4766 edges

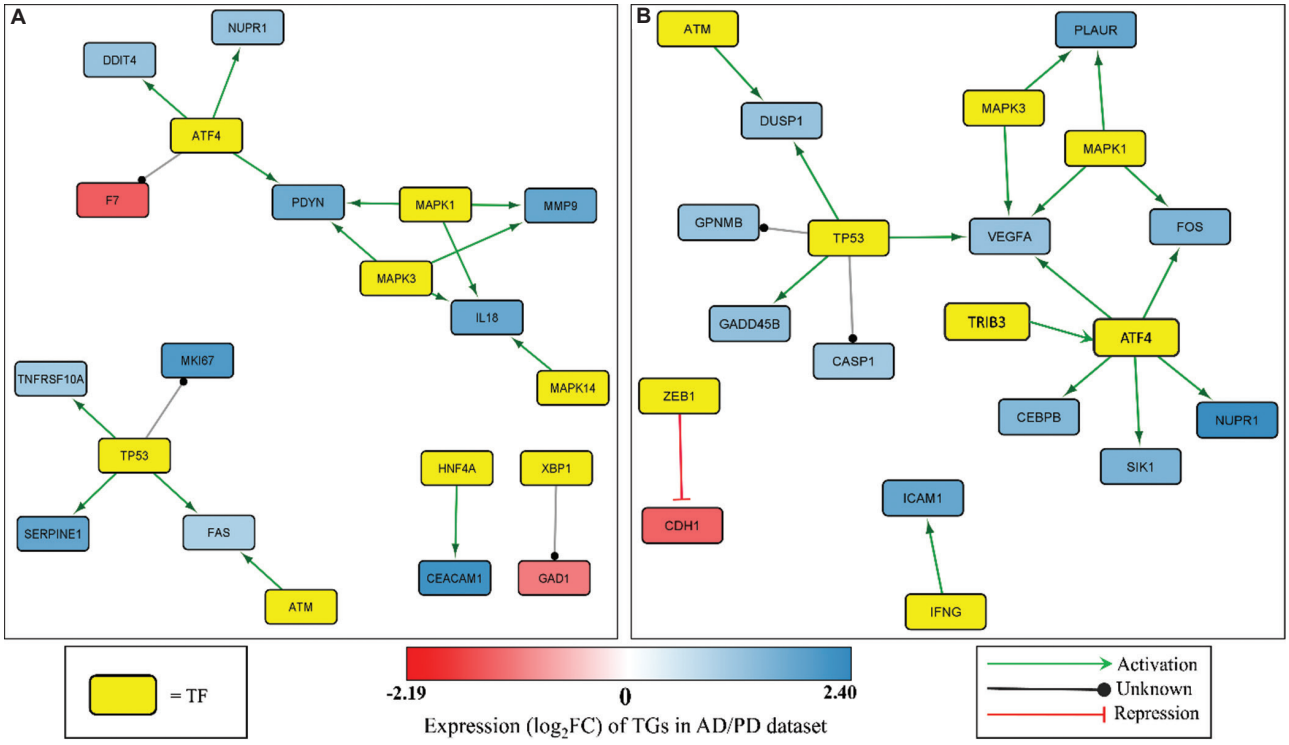

Figure 4. Differentially expressed genes (DEGs) regulated by FerrTFs. (A) Alzheimer's disease DEGs regulated by ferroptotic transcription factors (FerrTFs). (B) Parkinson's disease DEGs regulated by FerrTFs.

(Figure 3). Subsequently, we identified statistically relevant sub-networks or clusters from these PPINs using MCODE v2.0.0 app[25] in Cytoscape v3.9.1.[24]. The default settings of MCODE v2.0.0 app were used for module detection. The AD-PPIN and PD-PPIN consist of 21 and 17 clusters, respectively. Next, we performed functional enrichment analyses on each module using BiNGO in Cytoscape 3.9.1 to determine their functional roles during AD and PD.

Hub genes are the most interconnected genes within a network. Thus, in the next step, we calculated the degree centrality of each cluster using Network Analyzer in Cytoscape v3.9.1.[24,27]. The mean degree centrality for each cluster was used as the cutoff value to select hubs from the clusters (Figures S1 and S2). We aimed to decipher the influence of ferroptosis in the progression of neurodegeneration in both AD and PD. To achieve this, we initially selected probable markers and drivers of ferroptosis from FerrDb[28]. Driver genes are likely to induce ferroptosis, while marker genes indicate the occurrence of ferroptosis. We considered 162 probable ferroptotic drivers and markers for our study. We further sought to decode the influence of ferroptosis in instigating neurodegeneration in AD and PD. Using TRRUST[29] and RegNetwork[30], we identified 25 FerrTFs among the drivers and markers of ferroptosis. Initially, we identified targets of these FerrTFs among the DEGs (Figure 4). Then, we analyzed the targets of these FerrTFs within the cluster-specific hub genes to understand the role of FerrTFs in regulating functional clusters within AD- and PD-PPIN. Our analysis revealed that 8 and 6 FerrTFs regulate hub genes from the 7 and 4 deregulated clusters of AD and PD, respectively. Figures 5 and 6 illustrate the hub genes that are regulated by FerrTFs and the function of the module to which they belong (Figures S1 and S2).

3.3. Devising therapeutic miRNAs and drugs targeting FerrTFs

Finally, we were interested in identifying therapeutic miRNAs and drugs targeting FerrTFs. Thus, we retrieved miRNA-FerrTF interactions from RegNetwork[30] and drug-FerrTF interactions from Drug SIGnatures DataBase (DSigDB). Our analysis revealed 126 miRNAs that could silence 7 FerrTFs and 681 drugs that might have therapeutic effects against 8 FerrTFs in the case of AD (Figure 7; Table S3). Similarly, 114 miRNAs could have therapeutic roles against 5 FerrTFs, and 633 drugs could dampen the effects of 6 FerrTFs during PD (Figure 8; Table S3).

4. Discussion

Ferroptosis is an iron-dependent cell death process that has recently been implicated in the death of dopaminergic

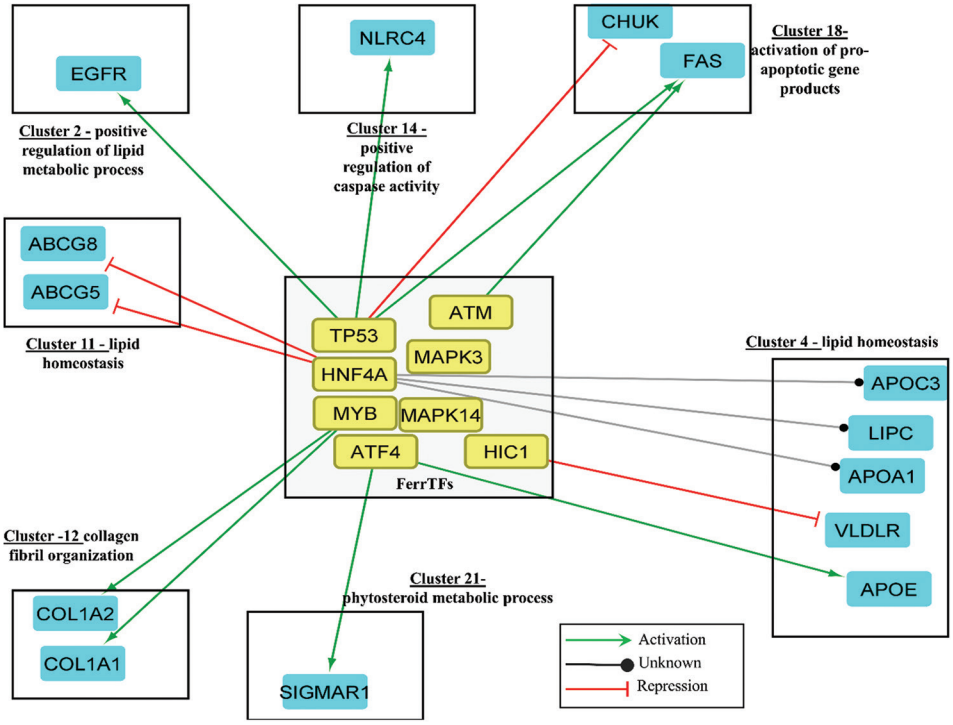

Figure 5. Hub genes from the modules of Alzheimer's disease protein–protein interaction networks (AD-PPIN) that are regulated by ferroptotic transcription factors (FerrTFs). The figure represents only the modules from AD-PPIN that contains hub genes that might be regulated by FerrTFs.

neurons in neurodegenerative diseases[41]. We were interested in investigating the role of ferroptotic pathways in the progression of neurodegenerative diseases, namely AD and PD. Among the AD DEGs, we identified two ferroptosis marker genes, namely *PLIN4* and *ANGPTL7*. *PLIN4* has been reported to store lipid droplets and thereby prevent mitophagy of neurons in neurodegenerative diseases[42]. Strikingly, it has also been linked to instigating ferroptosis in cancer tissues[43]. Similarly, *ANGPTL7* has been suggested as a marker for ferroptosis in cancer tissue[44], but recent evidence revealed an increase in its protein concentration during the pre-clinical stages of AD[45]. Thus, these ferroptotic genes may play a role in the progression of AD. For PD, we identified ferroptotic genes among the DEGs, namely *HMOX1* and *VEGFA*. Both *HMOX1* and *VEGFA* have been reported as markers of ferroptosis in different tissues[46,47]. However, *HMOX1* has been shown to promote the production of α-synuclein during PD[48], and blocking the release of *VEGFA* from astrocytes has been shown to decrease PD progression[49]. Hence, the expression of ferroptotic genes in PD and AD is evident. After identifying the DEGs, we reconstructed PPINs for AD and PD. Functional enrichment analysis of important modules from the PPINs showed that for AD, modules 2, 4, and 14 were functionally enriched with Gene Ontology biological processes (GO BP) such as "lipid homeostasis" and "positive regulation of lipid metabolic process" (Figure S1). Coincidentally, abnormal lipid homeostasis has been shown to not only drive ferroptosis but also aggravate AD[50,51]. In contrast, cluster 14 for PD was enriched with GO BP, GO:34367: "macromolecular complex remodeling" (Figure S2). Ferroptosis can lead to the accumulation of misfolded proteins due to an increase in endoplasmic reticulum stress[52], and protein misfolding and aggregation have been implicated in familial forms of PD[53]. Thus, the ferroptotic pathway significantly influences the progression of AD and PD[13].

While the coexistence of ferroptosis with the progression of both diseases is evident, we aimed to decode the specific influence of ferroptosis in instigating neurodegeneration in AD and PD. To achieve this, we used TRRUST[29] and RegNetwork[30] to identify 25 FerrTFs among the drivers and markers of ferroptosis. Among these 25 FerrTFs, 5 common FerrTFs – ATF4, ATM, MAPK1, MAPK3, and TP53 – were found to target a total of 11 DEGs in AD and 10 DEGs for PD (Figure 4). For instance, ATF4 has been shown to promote the autophagy of neuronal cells under prolonged ER stress[54], ultimately leading to neurodegeneration. In our study, ATF4 was found to increase the expression of *VEGFA* and *NUPR1* in PD and AD, respectively (Figure 4). As previously mentioned, silencing VEGFA has been linked to the prevention of PD-mediated neurodegeneration. On the other hand, *NUPR1* has been reported to induce methamphetamine

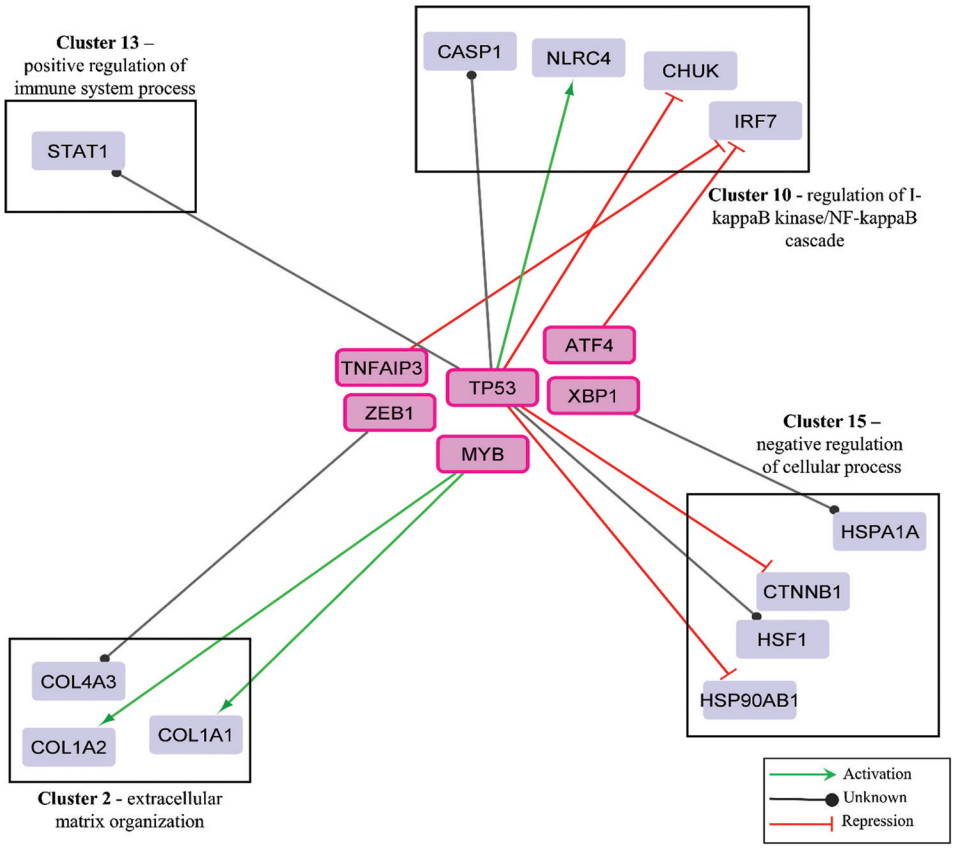

Figure 6. Hub genes from the modules of Parkinson's disease protein–protein interaction networks (PD-PPIN) that are regulated by ferroptotic transcription factors (FerrTFs). The figure represents only the modules from PD-PPIN that contains hub genes that might be regulated by FerrTFs.

(METH)-mediated neuronal apoptosis[55]. Three unique FerrTFs for AD – HNF4A, XBP1, and MAPK14 – were found to target three AD DEGs – *CEACAM1, GAD1*, and *IL18*, respectively. *HNF4A* has been identified as a blood biomarker for neurodegenerative disease[56], and in our study, it increased the expression of *CEACAM1*, which has earlier been reported to cause blood–brain barrier dysfunction[57]. We also identified three unique FerrTFs for PD – IFNG, TRIB3, and ZEB1 – that control 4 PD DEGs. ZEB1 has been linked to neuroinflammation in CNS disorders[58]. Thus, FerrTFs regulate the progression of both AD and PD by influencing the expression of several DEGs.

We also observed that the FerrTFs regulate a significant number of hub genes from clusters in both AD-PPIN and PD-PPIN. In our study, we found that ATF4 regulates the expression of *APOE* in AD (Figure 5). *APOE* has been identified as the main genetic marker for AD risk[59]. In the single-cell RNA-seq study of AD by Mathys *et al.*[60], *APOE* was significantly upregulated in excitatory neurons ($log_2FC = 0.32$). Strikingly, *APOE* has also been reported to influence iron homeostasis in the brain[61]. The upregulation of *APOE* in the brain during AD may be linked to the induction of ferroptosis, which could contribute to enhanced neurodegeneration. Further analysis of the cluster containing *APOE* [Cluster 4] (Figure 5) revealed its functional enrichment in GO BP – "lipid homeostasis." As previously mentioned, disruption of lipid homeostasis is the hallmark of AD[8]. Moreover, 3 of the 5 target genes (TGs) for the HNF4A, one of the FerrTFs, were found in this cluster. HNF4A is a well-known blood biomarker for neurodegenerative disease[56]. In the single-cell RNA-seq study of AD by Mathys *et al.*[60], HNF4A was significantly expressed in excitatory neurons ($log_2FC = 0.42$) and has been shown to induce ferroptosis in hepatocarcinoma cells by binding to histone acetyltransferases.[47]. In addition, 2 TGs of HNF4A, namely *APOE1* and *LIPC*, were found to be upregulated in excitatory neurons of the AD brain (log_2FC: 0.25 and 0.40, respectively)[60]. HNF4A also downregulates the expression of hubs *ABCG5* and *ABCG8* (log_2FC: -0.70 and -0.30, respectively)[60] from cluster 11, which is functionally enriched for lipid homeostasis. *ABCG5* and *ABCG8* are important proteins for cholesterol efflux[62]. These findings suggest a close association between lipid metabolism and ferroptosis. Existing literature also supports

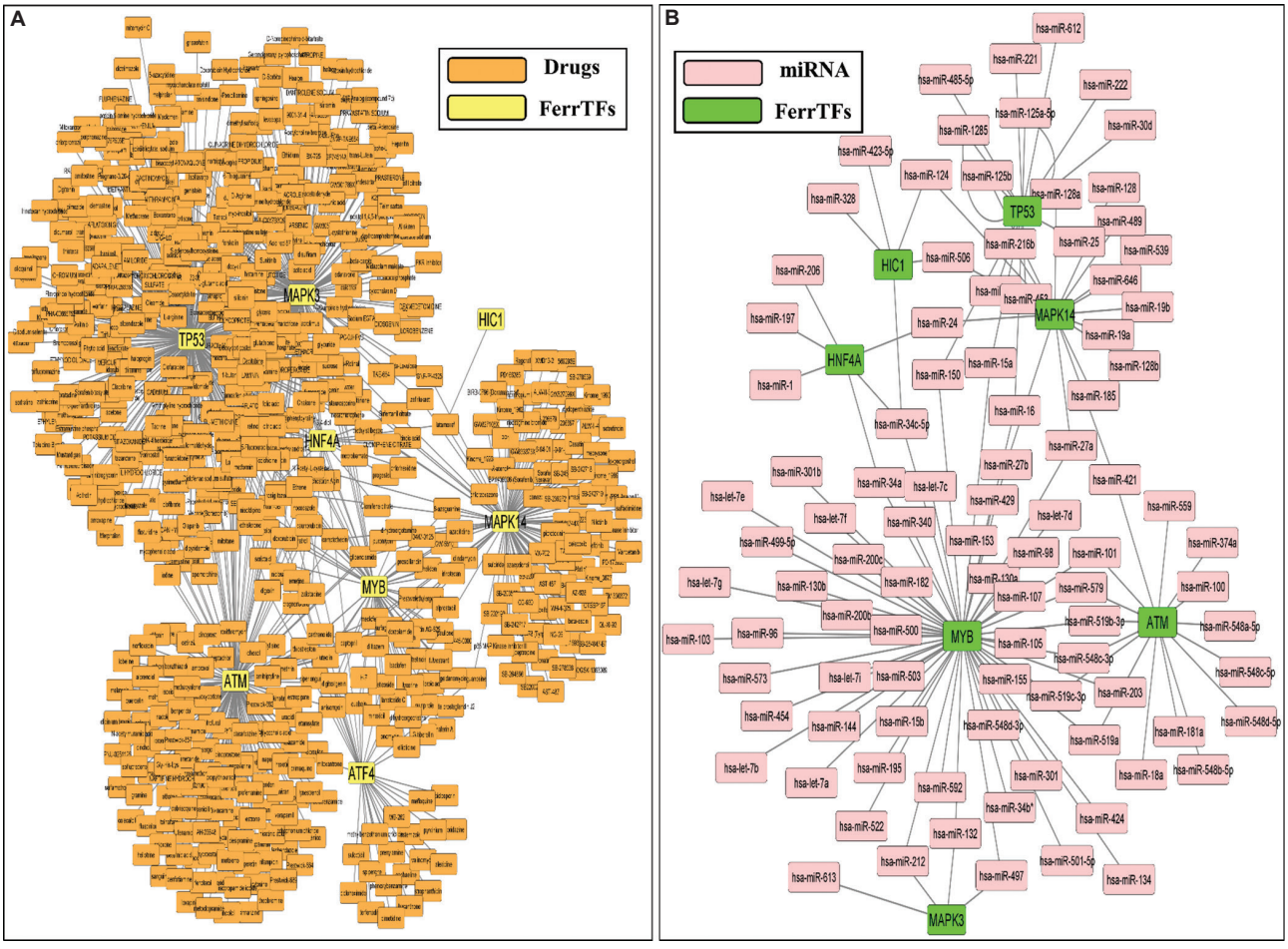

Figure 7. Therapeutic drugs and miRNA that might target ferroptotic transcription factors (FerrTFs) for Alzheimer's disease (AD). (A) 681 drugs that might be therapeutic against 8 FerrTFs for AD. (B) 126 miRNAs that might silence 7 FerrTFs against AD.

this notion, as ferroptosis has been shown to influence lipid synthesis and metabolic pathways[51]. Therefore, the disruption of lipid metabolism by ferroptosis may contribute to the progressive neurodegeneration in AD.

Existing literature suggests that dysregulation of NF-κB signaling can lead to apoptosis, inflammation, and the progression of several neurodegenerative diseases, including PD[63]. Strikingly, several components of the NF-κB signaling cascade, such as *IRF7, NLRC4, CHUK*, and *CASP1*, are regulated by FerrTFs (Figure 6). NLRC4 has been reported to cause neuroinflammation and promote PD[64]. Among the FerrTFs, *TP53* encodes tumor protein p53, which was found to be upregulated in dopaminergic neurons of the substantia nigra pars compacta in PD brains[65]. The loss of dopaminergic neurons in this brain region is a hallmark of PD progression[65]. p53, along with NF-κB, has been shown to contribute to the progressive degradation of dopaminergic neurons in the PD brain[66]. Recent research has demonstrated that both tumor-associated mutant p53 and the signaling system linked with p53 can control ferroptosis[67]. In our study, we found that p53 targets the maximum number of hubs from different clusters of the PD PPIN, and 3 out of 7 of its TGs were from cluster 10, which was functionally enriched with the GO BP – "regulation of I-κB kinase/NF-κB cascade." The targets of p53 in this cluster include *CASP1, NLRC4*, and *CHUK*. p53 aggravates the expression of *NLRC4*, and the role of *NLRC4* in PD has been elucidated earlier in this discussion. *CHUK* encodes IKKα, an important tumor suppressor for suppressing the inflammatory NF-κB pathway within the cell[68]. However, in our study, p53 was found to suppress the expression of *CHUK*, potentially exacerbating NF-κB-mediated inflammatory pathways. Moreover, TP53 was also found to regulate the expression of the hub for cluster 13, namely *STAT1*. This cluster was functionally enriched with GO BP – "Positive regulation of immune system process." It has been reported that the interaction of *STAT1* and NF-κB is responsible for bringing about inflammatory responses[69]. Strikingly, ferroptosis aggravates pro-

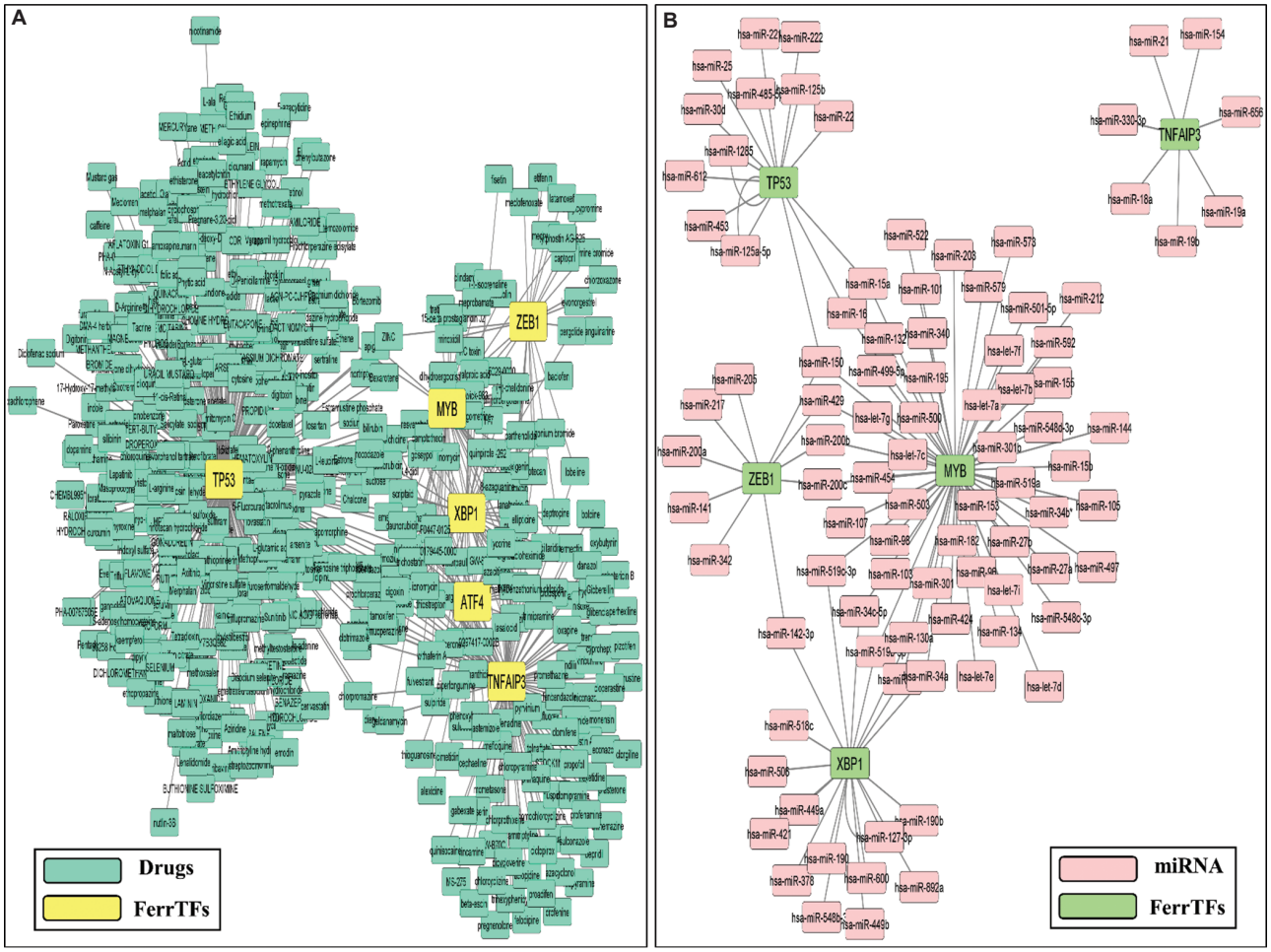

Figure 8. Therapeutic drugs and miRNA that might target ferroptotic transcription factors (FerrTFs) for Parkinson's disease (PD). (A) 633 drugs that might be therapeutic against 6 FerrTFs for PD. (B) 114 miRNAs that might silence 5 FerrTFs against PD.

inflammatory processes, which trigger neuroinflammation and neurodegeneration[70]. Our analysis suggests that FerrTFs induce inflammatory pathways through NF-κB signaling, contributing to neurodegeneration during PD.

Thus, it can be asserted that FerrTFs influence the progression of neurological disorders such as AD and PD to a greater extent, warranting the development of therapeutic measures targeting these FerrTFs. Accordingly, we have also devised therapeutic drugs and miRNAs that can be used to combat AD and PD. Among the drugs, we identified 592 drugs that commonly target FerrTFs found in both neurodegenerative diseases. Notably, most of the drugs are targeted against TP53, and the drugs citric acid and daunorubicin are commonly implicated. Citric acid has previously been shown to reduce oxidative stress in brain cells[71], and in our study, it was found to target two FerrTFs, namely TP53 and HNF4A, in both AD and PD. While there is no evidence pointing to its ability in preventing neurodegeneration, daunorubicin may act against 5 common FerrTFs, namely ATF4, MAPK3, MYB, TNFAIP3, and TP53, in AD and PD. Regarding therapeutic miRNAs, our findings suggest that hsa-miR-132 could silence three common FerrTFs for AD and PD, namely MYB, MAPK1, and MAPK3. Literature supports miR-132's multifarious neuroprotective roles, and its decreased expression has been reported in post-mortem AD brains[72]. These drugs and miRNAs represent promising candidates for future experimental testing to elucidate their potential in dampening ferroptosis during the pathogenesis of AD and PD.

5. Conclusion

In this study, we have unveiled the crosslink between ferroptosis, an iron-mediated cell death process, and two neurodegenerative diseases, AD, and PD, using a network and systems biology approach. Our analyses have demonstrated that the expression of a significant number of genes is modulated by ferroptosis-associated

transcription factors during the pathogenesis of these two neurodegenerative diseases. Thus, this study identifies potential ferroptosis markers that may play a driving role in these diseases. Finally, we have devised therapeutic measures that can be experimentally tested for their efficacy in combating ferroptosis in AD and PD. This study provides valuable insights for experimental biologists to use these ferroptosis markers and demystify their mode of action in causing neurodegeneration, thereby advancing our understanding of these diseases.

Acknowledgments

This research is an outcome of the autonomous research group "Ethophilia." We thank all the members for their constant support and enthusiasm.

Funding

This research did not receive any specific grant from funding agencies in the public, commercial, or not-for-profit sectors.

Conflict of interest

The authors declare no conflict of interest with any organization or financial entity.

Author contributions

Conceptualization: Deepyaman Das, Chayan Munshi
Formal analysis: Deepyaman Das
Investigation: Deepyaman Das, Chayan Munshi
Methodology: Deepyaman Das
Writing – original draft: Deepyaman Das, Kalpesh Jas, Sourish Pramanik
Writing – review & editing: Deepyaman Das, Chayan Munshi

Ethics approval and consent to participate

Not applicable.

Consent for publication

Not applicable.

Availability of data

All the data used in the study are publicly available.

References

1. Sun Y, Chen P, Zhai B, *et al*., 2020, The emerging role of ferroptosis in inflammation. *Biomed Pharmacother*, 127: 110108.

   https://doi.org/10.1016/j.biopha.2020.110108

2. Galaris D, Barbouti A, Pantopoulos K, 2019, Iron homeostasis and oxidative stress: An intimate relationship. *Biochim Biophys Acta Mol Cell Res*, 1866: 118535.

   https://doi.org/10.1016/j.bbamcr.2019.118535

3. Reichert CO, de Freitas FA, Sampaio-Silva J, *et al*., 2020, Ferroptosis mechanisms involved in neurodegenerative diseases. *Int J Mol Sci*, 21: 8765.

   https://doi.org/10.3390/ijms21228765

4. Xu Y, Zhao J, Zhao Y, *et al*., 2023, The role of ferroptosis in neurodegenerative diseases. *Mol Biol Rep*, 50: 1655–1661.

   https://doi.org/10.1007/s11033-022-08048-y

5. Chen X, Yu C, Kang R, *et al*., 2020, Iron metabolism in ferroptosis. *Front Cell Dev Biol*, 8: 590226.

   https://doi.org/10.3389/fcell.2020.590226

6. Munshi C, Bhattacharya S, 2022, The "irony" of ferroptosis: A review on neurological challenges. In: Xu K, editor. Cell Death and Disease. Rijeka: IntechOpen.

   https://doi.org/10.5772/intechopen.108737

7. Ou M, Jiang Y, Ji Y, *et al*., 2022, Role and mechanism of ferroptosis in neurological diseases. *Mol Metab*, 61: 101502.

   https://doi.org/10.1016/j.molmet.2022.101502

8. Yan H, Zou T, Tuo Q, *et al*., 2021, Ferroptosis: Mechanisms and links with diseases. *Signal Transduct Target Ther*, 6: 49.

   https://doi.org/10.1038/s41392-020-00428-9

9. Ma H, Dong Y, Chu Y, *et al*., 2022, The mechanisms of ferroptosis and its role in Alzheimer's disease. *Front Mol Biosci*, 9: 965064.

   https://doi.org/10.3389/fmolb.2022.965064

10. Ward RJ, Zucca FA, Duyn JH, *et al*., 2014, The role of iron in brain ageing and neurodegenerative disorders. *Lancet Neurol*, 13: 1045–1060.

    https://doi.org/10.1016/S1474-4422(14)70117-6

11. Zhang Y, Wang M, Chang W, 2022, Iron dyshomeostasis and ferroptosis in Alzheimer's disease: Molecular mechanisms of cell death and novel therapeutic drugs and targets for AD. *Front Pharmacol*, 13: 983623.

    https://doi.org/10.3389/fphar.2022.983623

12. Yang WS, Kim KJ, Gaschler MM, *et al*., 2016, Peroxidation of polyunsaturated fatty acids by lipoxygenases drives ferroptosis. *Proc Natl Acad Sci U S A*, 113: E4966–E4975.

    https://doi.org/10.1073/pnas.1603244113

13. Chen K, Jiang X, Wu M, *et al*., 2021, Ferroptosis, a potential therapeutic target in Alzheimer's disease. *Front Cell Dev Biol*, 9: 704298.

    https://doi.org/10.3389/fcell.2021.704298

14. Chen JJ, Thiyagarajah M, Song J, *et al*., 2022, Lanctôt, altered central and blood glutathione in Alzheimer's disease and

mild cognitive impairment: A meta-analysis. *Alzheimers Res Ther*, 14: 23.

https://doi.org/10.1186/s13195-022-00961-5

15. Kuang F, Liu J, Tang D, *et al*., 2020, Oxidative damage and antioxidant defense in ferroptosis. *Front Cell Dev Biol*, 8: 586578.

https://doi.org/10.3389/fcell.2020.586578

16. Guzman-Martinez L, Maccioni RB, Andrade V, *et al*., 2019, Neuroinflammation as a common feature of neurodegenerative disorders. *Front Pharmacol*, 10: 1008.

https://doi.org/10.3389/fphar.2019.01008

17. Jankovic J, Tan EK, Parkinson's disease: Etiopathogenesis and treatment. *J Neurol Neurosurg Psychiatry*, 91: 795–808.

https://doi.org/10.1136/jnnp-2019-322338

18. Fernández-Mendívil C, Luengo E, Trigo-Alonso P, *et al*., 2021, Protective role of microglial HO-1 blockade in aging: Implication of iron metabolism. *Redox Biol*, 38: 101789.

https://doi.org/10.1016/j.redox.2020.101789

19. Zhu Y, Wang B, Tao K, *et al*., 2017, Iron accumulation and microglia activation contribute to substantia nigra hyperechogenicity in the 6-OHDA-induced rat model of Parkinson's disease. *Parkinsonism Relat Disord*, 36: 76–82.

https://doi.org/10.1016/j.parkreldis.2017.01.003

20. Novgorodov SA, Voltin JR, Gooz MA, *et al*., 2018, Acid sphingomyelinase promotes mitochondrial dysfunction due to glutamate-induced regulated necrosis. *J Lipid Res*, 59: 312–329.

https://doi.org/10.1194/jlr.M080374

21. Guennewig B, Lim J, Marshall L, *et al*., 2021, Defining early changes in Alzheimer's disease from RNA sequencing of brain regions differentially affected by pathology. *Sci Rep*, 11: 4865.

https://doi.org/10.1038/s41598-021-83872-z

22. Robinson MD, McCarthy DJ, Smyth GK, 2010, edgeR: A bioconductor package for differential expression analysis of digital gene expression data. *Bioinformatics*, 26: 139–140.

https://doi.org/10.1093/bioinformatics/btp616

23. Szklarczyk D, Gable AL, Nastou KC, *et al*., 2020, The STRING database in 2021: Customizable protein-protein networks, and functional characterization of user-uploaded gene/measurement sets. *Nucleic Acids Res*, 49: D605–D612.

https://doi.org/10.1093/nar/gkaa1074

24. Shannon P, Markiel A, Ozier O, *et al*., 2003, Cytoscape: A software environment for integrated models. *Genome Res*, 13: 2498–2504.

https://doi.org/10.1101/gr.1239303.metabolite

25. Bader GD, Hogue CW, 2003, An automated method for finding molecular complexes in large protein interaction networks. *BMC Bioinformatics*, 4: 2.

https://doi.org/10.1186/1471-2105-4-2

26. Maere S, Heymans K, Kuiper M, 2005, BiNGO: A cytoscape plugin to assess overrepresentation of gene ontology categories in biological networks. *Bioinformatics*, 21: 3448–3449.

https://doi.org/10.1093/bioinformatics/bti551

27. Assenov Y, Ramírez F, Schelhorn SE, *et al*., 2008, Computing topological parameters of biological networks. *Bioinformatics*, 24: 282–284.

https://doi.org/10.1093/bioinformatics/btm554

28. Zhou N, Bao J, 2020, FerrDb: A manually curated resource for regulators and markers of ferroptosis and ferroptosis-disease associations. *Database*, 2020: baaa021.

https://doi.org/10.1093/database/baaa021

29. Han H, Cho JW, Lee S, *et al*., 2018, TRRUST v2: An expanded reference database of human and mouse transcriptional regulatory interactions. *Nucleic Acids Res*, 46: D380–D386.

https://doi.org/10.1093/nar/gkx1013

30. Liu ZP, Wu C, Miao H, *et al*., 2015, RegNetwork: An integrated database of transcriptional and post-transcriptional regulatory networks in human and mouse. *Database* (*Oxford*), 2015: bav095.

https://doi.org/10.1093/database/bav095

31. Yoo M, Shin J, Kim J, *et al*., 2015, DSigDB: Drug signatures database for gene set analysis. *Bioinformatics*, 31: 3069–3071.

https://doi.org/10.1093/bioinformatics/btv313

32. Lelos M, 2020, Chapter 2 Overview of Alzheimer's and Parkinson's diseases and the role of protein aggregation in these neurodegenerative diseases. In: Salgado AJ, editor. Handbook of Innovations in Central Nervous System Regenerative Medicine. Amsterdam: Elsevier, p29–53.

https://doi.org/10.1016/B978-0-12-818084-6.00002-7

33. Kajiwara Y, McKenzie A, Dorr N, *et al*., 2016, The human-specific CASP4 gene product contributes to Alzheimer-related synaptic and behavioural deficits. *Hum Mol Genet*, 25: 4315–4327.

https://doi.org/10.1093/hmg/ddw265

34. Gambuzza ME, Sofo V, Salmeri FM, *et al*., 2014, Toll-like receptors in Alzheimer's disease: A therapeutic perspective. *CNS Neurol Disord Drug Targets*, 13: 1542–1558.

https://doi.org/10.2174/1871527313666140806124850

35. Hernandez MX, Namiranian P, Nguyen E, *et al*., 2017, C5a increases the injury to primary neurons elicited by fibrillar amyloid beta. *ASN Neuro*, 9.

https://doi.org/10.1177/1759091416687871

36. Boros FA, Vécsei L, Klivényi P, 2021, NEAT1 on the field of Parkinson's disease: Offense, defense, or a player on the

bench? *J Parkinsons Dis*, 11: 123–138.

https://doi.org/10.3233/jpd-202374

37. Venero JL, Burguillos MA, Brundin P, *et al*., 2011, The executioners sing a new song: Killer caspases activate microglia. *Cell Death Differ*, 18: 1679–1691.

https://doi.org/10.1038/cdd.2011.107

38. Halbgebauer S, Nagl M, Klafki H, *et al*., 2016, Modified serpinA1 as risk marker for Parkinson's disease dementia: Analysis of baseline data. *Sci Rep*, 6: 26145.

https://doi.org/10.1038/srep26145

39. Peng X, Wang J, Peng W, *et al*., 2017, Protein-protein interactions: Detection, reliability assessment and applications. *Brief Bioinform*, 18: 798–819.

https://doi.org/10.1093/bib/bbw066

40. Szklarczyk D, Gable AL, Lyon D, *et al*., 2019, STRING v11: Protein-protein association networks with increased coverage, supporting functional discovery in genome-wide experimental datasets. *Nucleic Acids Res*, 47: D607–D613.

https://doi.org/10.1093/nar/gky1131

41. Do Van B, Gouel F, Jonneaux A, *et al*., 2016, Ferroptosis, a newly characterized form of cell death in Parkinson's disease that is regulated by PKC. *Neurobiol Dis*, 94: 169–178.

https://doi.org/10.1016/j.nbd.2016.05.011

42. Han X, Zhu J, Zhang X, *et al*., 2018, Plin4-dependent lipid droplets hamper neuronal mitophagy in the MPTP/p-induced mouse model of Parkinson's disease. *Front Neurosci*, 12: 397.

https://doi.org/10.3389/fnins.2018.00397

43. Zhang X, Du L, Qiao Y, *et al*., 2019, Ferroptosis is governed by differential regulation of transcription in liver cancer. *Redox Biol*, 24: 101211.

https://doi.org/10.1016/j.redox.2019.101211

44. Song J, Liu Y, Guan X, *et al*., 2021, A novel ferroptosis-related biomarker signature to predict overall survival of esophageal squamous cell carcinoma. *Front Mol Biosci*, 8: 675193.

https://doi.org/10.3389/fmolb.2021.675193

45. Visser PJ, Reus LM, Gobom J, *et al*., 2022, Cerebrospinal fluid tau levels are associated with abnormal neuronal plasticity markers in Alzheimer's disease. *Mol. Neurodegener*, 17: 27.

https://doi.org/10.1186/s13024-022-00521-3

46. Liao S, Huang M, Liao Y, *et al*., 2023, HMOX1 promotes ferroptosis induced by erastin in lens epithelial cell through modulates Fe(2+) production. *Curr Eye Res*, 48: 25–33.

https://doi.org/10.1080/02713683.2022.2138450

47. Zhou Z, Lu J, Ma J, *et al*., 2022, Identification of potential ferroptosis key genes in the pathogenesis of lumbosacral spinal root avulsion by RNA sequencing and bioinformatics analysis. *Front Mol Biosci*, 9: 902607.

https://doi.org/10.3389/fmolb.2022.902607

48. Cressatti M, Song W, Turk AZ, *et al*., 2019, Glial HMOX1 expression promotes central and peripheral α-synuclein dysregulation and pathogenicity in parkinsonian mice. *Glia*, 67: 1730–1744.

https://doi.org/10.1002/glia.23645

49. Lan G, Wang P, Chan RB, *et al*., 2022, Astrocytic VEGFA: An essential mediator in blood-brain-barrier disruption in Parkinson's disease. *Glia*, 70: 337–353.

https://doi.org/10.1002/glia.24109

50. KaoYC, Ho PC, Tu YK, *et al*., 2020, Lipids and Alzheimer's disease. *Int J Mol Sci*, 21: 1505.

https://doi.org/10.3390/ijms21041505

51. Lin Z, Liu J, Kang R, *et al*., 2021, Lipid metabolism in ferroptosis. *Adv Biol*, 5: e2100396.

https://doi.org/10.1002/adbi.202100396

52. Tang D, Chen X, Kang R, *et al*., 2021, Ferroptosis: Molecular mechanisms and health implications. *Cell Res*, 31: 107–125.

https://doi.org/10.1038/s41422-020-00441-1

53. Tan JM, Wong ES, Lim KL, 2009, Protein misfolding and aggregation in Parkinson's disease. *Antioxid Redox Signal*, 11: 2119–2134.

https://doi.org/10.1089/ars.2009.2490

54. Pitale PM, Gorbatyuk O, Gorbatyuk M, 2017, Neurodegeneration: Keeping ATF4 on a tight leash. *Front Cell Neurosci*, 11: 410.

https://doi.org/10.3389/fncel.2017.00410

55. Xu X, Huang E, Tai Y, *et al*., 2017, Nupr1 modulates methamphetamine-induced dopaminergic neuronal apoptosis and autophagy through CHOP-Trib3-mediated endoplasmic reticulum stress signaling pathway. *Front Mol Neurosci*, 10: 203.

https://doi.org/10.3389/fnmol.2017.00203

56. Santiago JA, Potashkin JA, 2015, Network-based metaanalysis identifies HNF4A and PTBP1 as longitudinally dynamic biomarkers for Parkinson's disease. *Proc Natl Acad Sci U S A*, 112: 2257–2262.

https://doi.org/10.1073/pnas.1423573112

57. Hernandes MS, Lassègue B, Yepes M, *et al*., 2016, Abstract TP110: Polymerase δ-interacting protein 2 regulates astrocyte activation in ischemic stroke. *Stroke*, 47: ATP110.

https://doi.org/10.1161/str.47.suppl_1.tp110

58. Poonaki E, Kahlert UD, Meuth SG, *et al*., 2022, The role of the ZEB1-neuroinflammation axis in CNS disorders. *J Neuroinflammation*, 19: 275.

https://doi.org/10.1186/s12974-022-02636-2

59. Liu CC, Liu CC, Kanekiyo T, *et al*., 2013, Apolipoprotein E and Alzheimer disease: Risk, mechanisms and therapy. *Nat Rev Neurol*, 9: 106–118.

https://doi.org/10.1038/nrneurol.2012.263

60. Mathys H, Davila-Velderrain J, Peng Z, *et al*., 2019, Single-cell transcriptomic analysis of Alzheimer's disease. *Nature*, 570: 332–337.

https://doi.org/10.1038/s41586-019-1195-2

61. Kahl CR, Means AR, 2003, Regulation of cell cycle progression by calcium/calmodulin-dependent pathways. *Endocr Rev*, 24: 719–736.

https://doi.org/10.1210/er.2003-0008

62. Lee SD, Tontonoz P, 2015, Liver X receptors at the intersection of lipid metabolism and atherogenesis. *Atherosclerosis*, 242: 29–36.

https://doi.org/10.1016/j.atherosclerosis.2015.06.042

63. Bellucci A, Bubacco L, Longhena F, *et al*., 2020, Nuclear factor-κB dysregulation and α-synuclein pathology: Critical interplay in the pathogenesis of Parkinson's disease. *Front Aging Neurosci*, 12: 68.

https://doi.org/10.3389/fnagi.2020.00068

64. De Rivero Vaccari J, Mejias NH, Travascio F, 2017, The NLRC4 inflammasome contributes to brain inflammaging. *Innov Aging*, 1: 978–979.

https://doi.org/10.1093/geroni/igx004.3534

65. Kamath T, Abdulraouf A, Burris SJ, *et al*., 2022, Single-cell genomic profiling of human dopamine neurons identifies a population that selectively degenerates in Parkinson's disease. *Nat Neurosci*, 25: 588–595.

https://doi.org/10.1038/s41593-022-01061-1

66. Jembrek MJ, Oršolić N, Mandić L, *et al*., 2021, Anti-oxidative, anti-inflammatory and anti-apoptotic effects of flavonols: Targeting Nrf2, NF-κB and p53 pathways in neurodegeneration. *Antioxidants* (*Basel, Switzerland*), 10: 1628.

https://doi.org/10.3390/antiox10101628

67. Liu J, Zhang C, Wang J, *et al*., 2020, The regulation of ferroptosis by tumor suppressor p53 and its pathway. *Int J Mol Sci*, 21: 8387.

https://doi.org/10.3390/ijms21218387

68. Li X, Hu Y, 2021, Attribution of NF-κB activity to CHUK/IKKα-involved carcinogenesis. *Cancers* (*Basel*), 13: 1411.

https://doi.org/10.3390/cancers13061411

69. Krämer OH, Baus D, Knauer SK, *et al*., 2006, Acetylation of Stat1 modulates NF-kappaB activity. *Genes Dev*, 20: 473–485.

https://doi.org/10.1101/gad.364306

70. Li JY, Yao YM, Tian YP, 2021, Ferroptosis: A trigger of proinflammatory state progression to immunogenicity in necroinflammatory disease. *Front Immunol*, 12: 701163.

https://doi.org/10.3389/fimmu.2021.701163

71. Abdel-Salam OM, Youness ER, Mohammed NA, *et al*., 2014, Citric acid effects on brain and liver oxidative stress in lipopolysaccharide-treated mice. *J Med Food*, 17: 588–598.

https://doi.org/10.1089/jmf.2013.0065

72. Zhang M, Bian Z, 2021, Alzheimer's disease and microRNA-132: A widespread pathological factor and potential therapeutic target. *Front Neurosci*, 15:

https://doi.org/10.3389/fnins.2021.687973

ACCSCIENCE PUBLISHING

Global Translational Medicine

ORIGINAL RESEARCH ARTICLE

Thromboembolism risk in patients diagnosed with *EGFR*- and *ALK*-mutant lung adenocarcinoma

Suna Kavurgacı*, Yasemin Söyler, Pınar Akın Kabalak, Derya Kızılgöz, and Ülkü Yılmaz

Department of Chest Disease, Atatürk Sanatorium Training and Research Hospital, Ankara, Turkey

Abstract

In this study, we investigated the incidence of venous thromboembolism (VTE), related risk factors for VTE, and the effect of VTE on overall survival in patients with non-small-cell lung cancer harboring epidermal growth factor receptor (*EGFR*) and anaplastic lymphoma kinase (*ALK*) gene mutations. The study included patients older than 18 years of age who were diagnosed with histologically proven locally advanced or advanced-stage adenocarcinoma and were followed in our center between January 2014 and December 2019. These patients were divided into two groups: one comprising mutation-positive individuals and the other mutation-negative individuals. We examined factors influencing the occurrence of VTE, assessed the incidence of VTE, and compared the differences in overall survival. Univariate Cox regression analysis revealed that the independent predictors of VTE were the number of metastases (Hazard ratio [HR]: 3.784; 95% confidence interval [CI]: 2.198 – 6.515; $P < 0.001$) and the presence of *EGFR* exon 21 mutations (HR: 2.386; 95% CI: 1.276 – 4.462; $P = 0.006$). However, in multivariate analysis, only the number of comorbidities was associated with an increased risk for VTE (HR: 3.462; 95% CI: 1.977 – 6.060; $P < 0.001$). It is essential to consider the risk of VTE development in patients with *EGFR* exon 21 mutation-positive lung adenocarcinoma. Physicians should be vigilant in terms of screening, prophylaxis, and follow-up for underlying VTE in these patients.

Keywords: Pulmonary embolism; Venous thromboembolism; Epidermal growth factor receptor; Survival

***Corresponding author:**
Suna Kavurgacı
(suna.dr01@gmail.com)

Citation: Kavurgacı S, Söyler Y, Kabalak PA, *et al.*, 2023, Thromboembolism risk in patients diagnosed with *EGFR*- and *ALK*-mutant lung adenocarcinoma. *Global Transl Med*, 2(3): 1027. https://doi.org/10.36922/gtm.1027

Received: June 1, 2023
Accepted: August 30, 2023
Published Online: September 12, 2023

1. Introduction

The incidence of venous thromboembolism (VTE) is higher among cancer patients compared to the general population[1]. Approximately 20% of all VTE cases can be attributed to cancer[2]. The highest risk of VTE is observed in patients with lung cancer, hematological malignancies, gastrointestinal cancer, or distant metastases[3]. Furthermore, studies have indicated that the presence of VTE increases the mortality risk in cancer patients by 3 – 5 times[3,4]. Despite the thrombosis prophylaxis, the risk of VTE following surgical procedures in cancer patients surpasses that in non-malignant patients[5]. Notably, the risk of fatal pulmonary embolism (PE) increases more than

3 times in cancer patients[6]. In particular, pneumonectomy has been associated with a higher risk of VTE than lobectomy for stage I and II lung cancer[7].

In comparison to other tumor types, lung cancer has been associated with a moderate risk of VTE, particularly during the 1st year following cancer diagnosis. The prevalence of VTE in lung cancer patients has been reported to range between 7% and 15%[3]. Factors such as longer life expectancy, advanced age at the time of cancer diagnosis, and utilization of thrombogenic anti-cancer agents have increased the incidence of VTE in cancer patients[4]. Although patients diagnosed with lung cancer are also predisposed to arterial thromboembolism (ATE), the effect of lung cancer on ATE development is less pronounced than its effect on VTE development[8].

Research has indicated that certain laboratory parameters can predict an elevated risk of cancer-related thrombosis. However, the identification of a standardized biomarker specific to lung cancer is still underway. Therefore, there is a growing need to uncover biomarkers that can effectively identify individuals at risk for developing thromboembolism and determine suitable candidates for thromboprophylaxis.

Lately, significant advancements have been introduced in the treatment approaches for advanced non-small-cell lung carcinoma (NSCLC). Guidelines now recommend the thorough investigation of targetable driver gene mutations in all patients with advanced NSCLC[9]. At present, lung cancer patients are categorized based on tumor histological characteristics and the presence of epidermal growth factor receptor (*EGFR*) mutations or anaplastic lymphoma kinase (*EML4-ALK*) translocations such as echinoderm microtubule-associated protein 4[9].

Studies have indicated a lack of association between increased risk of VTE and *EGFR* mutations in patients with NSCLC[10,11]. Interestingly, Zer *et al.* demonstrated that the incidence of VTE was 3 – 5 times greater in cohorts with anaplastic lymphoma kinase (*ALK*) gene mutations than in the previously reported NSCLC population[12]. Dou *et al.*'s study, further, corroborated these findings, establishing a correlation between the increased VTE risk in NSCLC patients and the presence of *ALK* gene mutation[13]. Given the heightened VTE risk in cancer patients, the new thromboprophylactic agents have garnered increasing importance[14-16].

Our study aimed to elucidate the difference in VTE occurrence between lung cancer patients with *EGFR* mutations, those with *ALK* mutations, and patients without these mutations. In addition, we evaluated the effect of VTE on overall survival (OS) within this patient cohort.

2. Materials and methods

2.1. Study population

This retrospective observational study was designed to investigate the relationship between *EGFR* and *ALK* gene mutations and the occurrence of VTE in patients with lung adenocarcinoma (LA). The study included patients older than 18 years who had received a histologically confirmed diagnosis of either locally advanced or advanced-stage adenocarcinoma and followed in our center between January 2014 and December 2019. Tumor tissue DNA analysis for gene mutations was conducted at the time of study entry.

The following inclusion criteria were defined as follows: (i) Patients with a confirmed pathological diagnosis of adenocarcinoma, (ii) patients who underwent mutation analysis, and (iii) patients with available data regarding occurrences of VTE. Exclusions encompassed patients with *ROS1* gene mutations, patients with a confirmed pathological diagnosis of small-cell lung cancer, patients who had undergone surgical intervention, patients receiving anticoagulant therapy, patients with a diagnosis of chronic embolism, and patients in the early stages of the disease.

The patients were divided into two groups: those with gene mutations (mutation [+]) and those without mutation (mutation [-]). The mutation (+) group comprised patients with *EGFR* and *ALK* gene mutations. This study sought to analyze the incidence of VTE within these groups, discern factors affecting the occurrence of VTE, and compare the OS between the mutation (+) and mutation (-) groups.

2.2. Data collection

The demographic and clinical data of the patients (age, gender, tumor histopathology, clinical stage, number of metastases, and the administration of active cancer therapy within the 4 weeks leading up to the diagnosis of VTE), laboratory parameters at the time of VTE onset, and the presence of documented VTE were recorded. Clinical staging was determined in accordance with TNM classification (8th edition)[17].

2.3. Laboratory methods

All tumor molecular tests were conducted by a pathologist at regional laboratories.

Tumor biopsy specimens were processed as formalin-fixed and paraffin-embedded samples for histological examination and mutation analysis. *EGRF* mutation analysis (covering exons 18, 19, 20, and 21) was performed using real-time PCR. *ALK* rearrangement and *ROS1* rearrangement were investigated using the FISH method, utilizing the BX51 Olympus fluorescence microscope. For *ALK* and *ROS1* results to be considered positive, a minimum of 50 scoreable tumor cells in 4 – 5 μm thick tissue sections

were required, with at least 15% of these tumor cells displaying split or monopatterned characteristics.

2.4. Diagnosis and classification of VTE

Incidentally detected VTE events identified through imaging, regardless of the presence of patient symptoms, as well as symptomatic VTE events confirmed through radiological assessment prompted by clinical suspicion, were both included as TE events.

The confirmation of deep vein thrombosis (DVT) cases involved venous ultrasound imaging. In instances of PE, confirmation was achieved through computed tomography pulmonary angiography or ventilation-perfusion scanning, chosen based on patients' history of contrast allergy or renal failure.

2.5. Statistical analysis

Categorical data were presented as percentages (%) and absolute numbers, and their comparison was carried out using Chi-square or Fisher's exact tests. The normal distribution of continuous variables was assessed using the Kolmogorov–Smirnov test. Levene's test was utilized to analyze the homogeneity of variances. Continuous data were described either as mean±standard deviation (SD) or as median (minimum–maximum), based on the normality of distribution. The differences between groups were examined using Student's *t*-test and Mann–Whitney U-tests. Univariate and multivariate Cox regression analyses were conducted to assess risk factors independently associated with VTE. The multivariate analysis was conducted for variables that demonstrated significance ($P < 0.05$) as per the univariate test. Hazard ratios (HRs) with corresponding 95% confidence intervals (CI) were calculated. The observation time was defined as the period between the date of NSCLC diagnosis and the occurrence of VTE, death, or censoring time (February 1, 2023). The median OS was determined as the duration (in days) from the date of LA diagnosis to either the date of all-cause mortality or the analysis time. The Kaplan–Meier method was employed to estimate survival curves for different molecular subtypes (mutation [-] and mutation [+]), with a log-rank test employed for comparisons. The reverse Kaplan–Meier method was used to estimate median follow-up time. All statistical analyses were performed using IBM SPSS Statistics for Windows, Version 25.0 (IBM Corp. Released 2017, Armonk, NY: IBM Corp). $P < 0.05$ was considered statistically significant.

3. Results

A total of 343 patients with locally advanced or advanced LA (97 females and 246 males, with a mean age of 61.9 ± 10.6 years) were enrolled in the study.

According to the TNM-8 staging system, 19.5% ($n = 67$) of the patients had locally advanced cancers, while 80.5% ($n = 276$) had advanced cancers. Multiple metastases (occurring on >2 sides) were present in 61.2% ($n = 210$) of patients with advanced-stage patients. The distribution of molecular mutations included 115 (33.5%) *EGFR*-mutant patients, 37 (10.8%) *ALK*-mutant patients, and 190 (55.4%) patients without any detected mutations.

Occurrences of DVT were identified in 23 patients (6.7%), and PE was observed in 31 patients (9%) within the entire study population. Among mutation (+) patients, 8 (5.2%) exhibited DVT, and 22 (14.2%) showed PE. While 30 (19.4%) of 155 patients developed VTE in the mutation (+) group, this number was 24 (12.8%) in the mutation (-) group ($P = 0.07$). The prevalence of PE was significantly higher in the mutation (+) group compared to the mutation (-) group (14.4% vs. 4.7%, $P < 0.002$). There was no statistically significant difference between the two groups in terms of DVT prevalence (5.2% vs. 7.9%, $P = 0.32$) (Table 1).

The median follow-up time for all patients was 87 months (95% CI: 75.819 – 98.181), 82 months (95% CI: 73.328 – 90.672) for mutation (+) patients, and 95 months (95% CI: 93.570 – 96.430) for mutation (-) patients.

Overall, 155 patients were administered specific tyrosine kinase inhibitors (TKI) based on their driver mutations. Among these, 148 patients initiated TKI treatment before experiencing VTE, while seven patients began TKI treatment after the development of VTE events.

Demographic and clinical characteristics were compared between the mutation (+) and mutation (-) groups (Table 1). Both groups exhibited similar age distribution, clinical stage, gender composition, and presence of multiple metastases. However, the rate of PE was significantly higher in the mutation (+) group ($P = 0.002$).

Two groups were compared based on laboratory parameters, revealing a statistically significant difference in D-dimer levels and lymphocyte counts ($P = 0.01$) (Table 2).

An analysis of the mutation (+) group failed to yield statistically significant results when *EGFR* (+) and *ALK* (+) patients were assessed in terms of VTE ($P = 0.9$). Similarly, no statistically significant results were observed in terms of pulmonary thromboembolism (PTE) ($P = 0.47$).

The rate of VTE was also investigated within the subgroups of *EGFR* exon 19 and exon 21 mutations in our study. Although statistical significance was not reached, a higher PE rate was evident in the exon 21 group ($P = 0.22$).

Table 1. The demographic and clinical characteristics of the study population.

Variables	Study population (*n*=343)	Mutation (+) (*n*=153, 44.6%)	Mutation (-) (*n*=190, 55.4%)	*P*-value
Age (mean±SD)	61.9±10.6	61.6±12.5	60.6±8.8	0.38
Age group				0.18
<65	226 (65.9%)	95 (62.1%)	131 (68.9%)	
≥65	117 (34.1%)	58 (37.9%)	59 (31.1%)	
Gender				<0.001
Female	97 (28.3%)	69 (45.1%)	28 (14.7%)	
Male	246 (71.7%)	84 (54.9%)	162 (85.3%)	
Comorbidities	90 (26.2%)	73 (47.7%)	17 (8.9%)	<0.001
TNM stage				0.05
Locally advanced	67 (19.5%)	23 (15%)	44 (23.9%)	
Advanced	276 (80.5%)	130 (85%)	146 (76.8%)	
≥2 sides of metastasis	210 (61.2%)	99 (64.7%)	111 (58.4%)	0.23
EGFR mutation (+)	115 (33.5%)	115 (74.2%)	-	
EGFR exon 19 (+)	72 (21%)	72 (47.1%)		
EGFR exon 21 (+)	43 (12.5%)	43 (28.1%)		
ALK translocation	37 (10.8%)	37 (24.2%)	-	
Overall survival (months [95% Cl])	20 (16.27 – 23.72)	37 (26.77 – 47.22)	12 (9.49 – 14.50)	<0.001
VTE	54 (15.7%)	30 (19.6%)	24 (12.6%)	0.07
Type of thrombosis				
DVT	23 (6.7%)	8 (5.2%)	15 (7.9%)	0.32
PE	31 (9%)	22 (14.4%)	9 (4.7%)	0.002*

Note: *Represents a statistically significant difference (P<0.05) between the mutation (+) and mutation (-) groups. Abbreviation: *ALK*: Anaplastic lymphoma kinase; DVT: Deep vein thrombosis; *EGFR*: Epidermal growth factor receptor; PE: Pulmonary embolism; VTE: Venous thromboembolism.

Table 2. Laboratory parameters of patients with VTE

Variables	Study population (*n*=343)	Mutation (+) (*n*=30)	Mutation (-) (n=24)	*P*-value
Hemoglobin (g/dl) (mean±SD)	12.89±1.99	12.9±2.31	12.88±1.58	0.97
White blood cell (/mm^3) (median [min–max])	10600 (4000 – 83333)	10600 (4000 – 83333)	9965 (4460 – 27100)	0.76
Lymphocyte (/mm^3) (mean±SD)	1520 (170 – 4110)	1380 (170 – 4110)	1895 (537 – 4000)	0.01*
Platelet (×10^3) (median [min–max])	264 (119 – 965)	257 (152 – 965)	272 (119 – 553)	0.45
D-dimer (ng/dl) (median [min–max])	1720 (194 – 14990)	2240 (908 – 14990)	930 (194 – 1670)	0.01*
LDH (U/L (median [min–max])	267 (143 – 2298)	297 (143 – 2298)	234 (156 – 1389)	0.09

Note: *Represents a statistically significant difference (P<0.05) between the mutation (+) and mutation (-) groups. Abbreviation: LDH: Lactate dehydrogenase.

In terms of DVT, although a higher rate was observed in the exon 21 group, statistical significance was not reached (P = 0.06). However, a significantly higher VTE rate was observed within the exon 21 subgroup (P = 0.03).

Univariate Cox regression analysis unveiled variables affecting the risk of PE, including the number of metastases (HR: 4.709 [95% CI: 2.255 – 9.834]; P < 0.001) and the presence of *EGFR* exon 21 mutations (HR: 3.085 [95% CI: 1.416 – 6.721]; P = 0.005). Multivariate COX regression analysis identified the number of comorbidities as the only factor with an increased risk of PE (HR: 4.112 [95% CI: 1.923 – 8.793]; P < 0.001).

Similarly, univariate Cox regression analysis identified independent predictors of VTE as the number of metastases (HR: 3.784 [95% CI: 2.198 – 6.515]; P < 0.001) and the presence of *EGFR* exon 21 mutations (HR: 2.386 [95% CI: 1.276 – 4.462]; P = 0.006). In the multivariate analysis, only the number of comorbidities was associated with an increased risk for VTE (HR: 3.462 [95% CI: 1.977 – 6.060]; P < 0.001) (Table 3).

Table 3. Univariate and multivariate Cox regression analysis for the prediction of VTE

Variables	Univariate analysis			Multivariate analysis		
	HR	95% CI	*P*-value	HR	95% CI	*P*-value
Age group (<65 vs. ≥65)	1.423	0.829 – 2.441	0.20			
Gender (female vs. male)	1.281	0.705 – 2.327	0.41			
Comorbidities (no vs. yes)	3.784	2.198 – 6.515	<0.001*	3.462	1.977 – 6.060	<0.001*
TNM Stage (locally advanced vs. advanced)	1.014	0.532 – 1.930	0.96			
Number of metastasis (<2 vs. ≥2)	1.163	0.675 – 2.005	0.58			
EGFR mutation (no mutation vs. mutation at exon 19)	0.564	0.283 – 1.126	0.1			
EGFR mutation (no mutation vs. mutation at exon 21)	2.386	1276 – 4.462	0.006*	1.632	0.855 – 3.116	0.13
ALK translocation (no vs. yes)	0.933	0.421 – 2.071	0.86			
Cancer treatment						
No treatment versus chemotherapy	1.212	0.361 – 4.071	0.75			
No treatment versus targeted therapy	1.254	0.380 – 4.139	0.71			

Note: *Represents a statistically significant difference ($P<0.05$) between the mutation (+) and mutation (-) groups. Abbreviations: *ALK*: Anaplastic lymphoma kinase; *EGFR*: Epidermal growth factor receptor.

4. Discussion

This study shed light on the risk of developing VTE among patients with *EGFR* exon 21-positive LA. Cancer-specific hypercoagulability is influenced by factors such as tumor-derived tissue factor (TF) and mucin. Notably, mucin has been demonstrated to interact with L- and P-selectins through various mechanisms to induce the formation of platelet-rich microthrombi[18]. Studies have revealed that lung cancer cells induce the expression of TF[19-21]. Notably, TF overexpression is regarded as the most important factor in cancer-associated thrombosis. Changes in the regulatory mechanisms of TF expression might contribute to an increased risk of thrombosis in cancer patients[22]. Sato *et al.*[23] demonstrated the role of TF in the pathogenesis of VTE in lung cancer patients through a case study involving Trousseau syndrome. Therefore, it appears that LA-derived TF is responsible for recurrent VTE[23].

A review of the literature suggests that *EGFR* mutations may induce an overexpression of TF in cancer cells[24]. Preclinical investigations have consistently demonstrated *EGFR*'s role in inducing overexpression of TF[24,25]. Given these findings, we hypothesized that *EGFR* mutations could potentially reduce tumor procoagulant activity and TF expression, consequently reducing VTE incidence. The increase in TF could establish a direct correlation between oncogene expression and the risk of thrombosis.

In addition to oncological factors, non-oncological factors also contribute to thromboembolism in cancer patients, such as surgery, immobility, infections, and particularly exposure to cytotoxic agents which may increase the overall risk for VTE significantly[26].

In our study, we investigated the relationship between positive mutations and VTE in patients with LA. Univariate Cox regression analysis revealed that VTE occurred at a significantly higher rate in the *EGFR* exon 21 mutation (+) group compared to the mutation (-) group. These findings suggest that the presence of an *EGFR* exon 21 mutation may increase susceptibility to PE in LA patients.

The previous studies have reported the prevalence of VTE in lung cancer patients to be within the range of 7 – 15%[27,28]. In our study, we found the prevalence of VTE to be 15.7%, which is consistent with these previous findings. However, when considering specific driver gene mutations, the reported prevalence of VTE increases to 23%, a higher percentage than the reported prevalence of 7 – 15% in lung cancer patients[10,29]. Consistent with the literature, our study found a VTE prevalence of 19.6% in patients with driver gene mutations.

The impact of tumor gene mutations on thrombosis risk has been the focus of extensive preclinical and clinical studies. For example, a study involving post-pneumonectomy invasive LA patients (n = 323) indicated that those with *EGFR* gene mutations carried a higher risk of ATE[29]. Conversely, the previous studies have reported conflicting correlations between *EGFR* gene mutations and VTE risk in LA patients[10,11]. In our study, we did not observe statistically significant results regarding VTE in the *EGFR* mutation-positive group.

Wang *et al.* conducted a study investigating the prevalence of VTE in cases with exon 18, 19, 20, 21, 30, and 31 mutations, but they did not find a statistically significant increase[29]. In our study, we specifically examined the rates of VTE in the *EGFR* exon 19 and exon 21 groups and found

a higher rate in the exon 21 group. *EGFR* mutations were identified in 40 – 50% of Asian patients and 10%–15% of Caucasian patients[30]. Consistent with the literature, our study reported an *EGFR* mutation rate of 33.5%.

Furthermore, a meta-analysis of various studies confirmed that *ALK* rearrangements are associated with a higher risk of VTE in NSCLC patients, irrespective of the treatment effects[31]. In contrast, Lee *et al.* did not find a correlation between *ALK* or *EGFR* mutations and VTE risk in Asian patients with NSCLC. However, they did identify a correlation between molecular mutations and clinically diagnosed, although not computed, thorax pulmonary angiography-confirmed PE[32]. Dou F *et al.* reported a correlation between the increased risk of VTE in NSCLC patients and the presence of *ALK* gene mutations[13]. Several previous studies on VTE rates of NSCLC with *ALK* rearrangements either did not report any VTE cases or reported them in less than 5% of the patients[33,34]. Our study did not find a correlation between the presence of *ALK* gene mutations and VTE, which may be attributed to the difficulty in determining actual VTE rates due to underreporting[35].

In cancer patients, several factors contribute to an increased risk of thrombosis, such as gender, age, venous catheter use, prolonged bed rest, chemotherapy with or without adjuvant hormone therapy, surgical interventions, infections, and radiotherapy. VTE rates among cancer patients vary according to clinical factors, with tumor histopathological type and stage being the most significant determinants.

Alexander *et al.* conducted a study that revealed a higher risk of thromboembolism in patients diagnosed with LA compared to squamous cell carcinoma[36]. In our study, all patients had adenocarcinoma, and the risk of VTE was consistent with the literature, at 15.7%.

Studies have demonstrated an increased risk of VTE in older patients with lung cancer or other cancers[5]. Chew *et al.* found that patients under the age of 45 had a higher risk of developing VTE within 1 year after an NSCLC diagnosis[37]. Interestingly, Chew *et al.* also reported a higher risk of VTE in elderly patients[37]. The association between age and the occurrence of VTE in lung cancer remains a topic of debate, and further, research is needed to clarify this relationship.

Laboratory parameters such as low hemoglobin level, leukocytosis, elevated platelet count, and increased C-reactive protein levels have been associated with an increased risk of cancer-related thrombosis in lung cancer[29,38,39]. Kadlec *et al.*[40] observed that lung cancer patients with thromboembolic events had elevated platelet counts at the time of diagnosis, with a platelet count exceeding 330,000, correlating with major thromboembolic events. On the contrary, Demirci *et al.*[41] did not find a significant correlation between vascular events and thrombocytosis in their study of lung cancer patients. Pedersen and Milman[42] analyzed platelet count data from a large primary lung cancer population (1178 patients) and observed a high prevalence of high platelet counts (32%) among these patients. They found that the rate of thromboembolism in patients with normal platelet counts was statistically similar to the rate in patients with thrombocytosis. Consequently, these authors suggested that thrombocytosis in cancer patients should not be considered a predisposing risk factor for thromboembolism[43]. In addition, various experts have found that D-dimer levels can predict DVT in cancer patients[43]. Shiina *et al.* discovered a high frequency of vascular invasion in the high D-dimer group[44]. In our study, we investigated the relationship between laboratory parameters and VTE and found that only a high D-dimer level was identified as a predisposing factor for VTE.

We acknowledge several limitations in our study. First, it is a retrospective and single-center study, which may affect the generalizability. Second, patients with PE, which was detected using computed tomography angiography (CTA) or ventilation-perfusion scintigraphy, were excluded from this study. However, most distal peripheral subsegmental embolisms may not be detectable by CTA alone. To obtain more accurate PE rates, simultaneous review of CTA and ventilation-perfusion scans should be performed in future prospective studies that larger prospective cohorts are needed for further research.

5. Conclusion

Our study revealed a VTE prevalence of 19.4% in mutation-positive advanced-stage LA patients who did not receive prophylactic anticoagulant therapy. It was concluded that *EGFR* exon 21 mutation is an independent risk factor for VTE in LA.

Based on our findings, health-care providers should remain vigilant about VTE development in patients with *EGFR* exon 21 mutation-positive LA. This highlights the importance of screening, prophylaxis, and regular follow-up to detect and manage underlying VTE in this patient population.

Acknowledgments

None.

Funding

None.

Conflict of interest

All authors declare that they have no conflicts of interest.

Author contributions

Conceptualization: All authors
Investigation: All authors
Writing – original draft: Suna Kavurgacı
Writing – review & editing: Suna Kavurgacı, Yasemin Söyler, Ülkü Yılmaz

Ethics approval and consent to participate

The study was approved by the Ethics Committee of Ankara Atatürk Sanatorium Education and Training Hospital with the number 10.10.2022/37, performed in accordance with the Good Clinical Practice guidelines and assent specific to our country. The Declaration of Helsinki and its subsequent revisions were followed.

Consent for publication

This study was of a retrospective nature, and an informed consent form was waived.

Availability of data

The dataset generated during and/or analyzed during the current study is available from the corresponding author on reasonable request.

References

1. Shinagare AB, Okajima Y, Oxnard GR, *et al.*, 2012, Unsuspected pulmonary embolism in lung cancer patients: Comparison of clinical characteristics and outcome with suspected pulmonary embolism. *Lung Cancer*, 78: 161–166.

   https://doi.org/10.1016/j.lungcan.2012.08.007

2. Lee AY, 2005, Management of thrombosis in cancer: Primary prevention and secondary prophylaxis. *Br J Haematol*, 128: 291–302.

   https://doi.org/10.1111/j.1365-2141.2004.05292.x

3. Blom JW, Doggen CJ, Osanto S, *et al.*, 2005, Malignancies, prothrombotic mutations, and the risk of venous thrombosis. *JAMA*, 293: 715–722.

   https://doi.org/10.1001/jama.293.6.715

4. Timp JF, Braekkan SK, Versteeg HH, *et al.*, 2013, Epidemiology of cancer-associated venous thrombosis. *Blood*, 122: 1712–1723.

   https://doi.org/10.1182/blood-2013-04-460121

5. Clagett GP, Reisch JS, 1988, Prevention of venous thromboembolism in general surgical patients. Results of meta-analysis. *Ann Surg*, 208: 227–240.

   https://doi.org/10.1097/00000658-198808000-00016

6. White RH, Zhou H, Romanos PS, 2003, Incidence of symptomatic venous thromboembolism after different elective or urgent surgical procedures. *Thromb Haemost*, 90: 446–455.

   https://doi.org/10.1160/TH03-03-0152

7. Swiniarska J, Zekanowska E, Dancewicz M, *et al.*, 2009, Pneumonectomy due to lung cancer results in a more pronounced activation of coagulation system than lobectomy. *Eur J Cardiothorac Surg*, 36: 1064–1068.

   https://doi.org/10.1016/j.ejcts.2009.04.070

8. Yu J, Li A, Laureano M, *et al.*, 2019, Frequency of arterial thromboembolism in populations with malignancies: A systematic review. *Thromb Res*, 184: 16–23.

   https://doi.org/10.1016/j.thromres.2019.10.004

9. Guan JL, Zhong WZ, An SJ, *et al.*, 2013, KRAS mutation in patients with lung cancer: A predictor for poor prognosis but not for EGFR-TKIs or chemotherapy. *Ann Surg Oncol*, 20: 1381–1388.

   https://doi.org/10.1245/s10434-012-2754-z

10. Corrales-Rodriguez L, Soulières D, Weng X, *et al.*, 2014, Mutations in NSCLC and their link with lung cancer-associated thrombosis: A case-control study. *Thromb Res*, 133: 48–51.

    https://doi.org/10.1016/j.thromres.2013.10.042

11. Verso M, Chiari R, Mosca S, *et al.*, 2015, Incidence of Ct scan-detected pulmonary embolism in patients with oncogene-addicted, advanced lung adenocarcinoma. *Thromb Res*, 136: 924–927.

    https://doi.org/10.1016/j.thromres.2015.09.006

12. Zer A, Moskovitz M, Hwang DM, *et al.*, 2017, ALK-rearranged non-small-cell lung cancer is associated with a high rate of venous thromboembolism. *Clin Lung Cancer*, 18: 156–161.

    https://doi.org/10.1016/j.cllc.2016.10.007

13. Dou F, Zhang Y, Yi J, *et al.*, 2020, Association of ALK rearrangement and risk of venous thromboembolism in patients with non-small cell lung cancer: A prospective cohort study. *Thromb Res*, 186: 36–41.

    https://doi.org/10.1016/j.thromres.2019.12.009

14. Khorana AA, Vadhan-Raj S, Kuderer NM, *et al.*, 2017, Rivaroxaban for preventing venous thromboembolism in high-risk ambulatory patients with cancer: Rationale and design of the CASSINI trial. Rationale and design of the CASSINI trial. *Thromb Haemost*, 117: 2135–2145.

    https://doi.org/10.1160/TH17-03-0171

15. Carrier M, Abou-Nassar K, Mallick R, *et al.*, 2019, Apixaban to prevent venous thromboembolism in patients with cancer. *N Engl J Med*, 380: 711–719.

    https://doi.org/10.1056/NEJMoa1814468

16. Key NS, Khorana AA, Kuderer NM, *et al.*, 2020, Venous thromboembolism prophylaxis and treatment in patients with cancer: ASCO clinical practice guideline update. *J Clin Oncol*, 38: 496–520.

https://doi.org/10.1200/JCO.19.01461

17. Rami-Porta R, Bolejack V, Giroux DJ, *et al.*, 2014, The IASLC lung cancer staging project: The new database to inform the eighth edition of the TNM classification of lung cancer. *J Thorac Oncol*, 9: 1618–1624.

https://doi.org/10.1097/JTO.0000000000000334

18. Varki A, 2007, Trousseau's syndrome: Multiple definitions and multiple mechanisms. *Blood*, 110: 1723–1729.

https://doi.org/10.1182/blood-2006-10-053736

19. Sawada M, Miyake S, Ohdama S, *et al.*, 1999, Expression of tissue factor in non-small-cell lung cancers and its relationship to metastasis. *Br J Cancer*, 79: 472–477.

https://doi.org/10.1038/sj.bjc.6690073

20. Goldin-Lang P, Tran QV, Fichtner I, 2008, Tissue factor expression pattern in human non-small cell lung cancer tissues indicate increased blood thrombogenicity and tumor metastasis. *Oncol Rep*, 20: 123–128.

https://doi.org/10.3892/or.20.1.123

21. Minamiya Y, Matsuzaki I, Sageshima M, *et al.*, 2004, Expression of tissue factor mRNA and invasion of blood vessels by tumor cells in non-small cell lung cancer. *Surg Today*, 34: 1–5.

https://doi.org/10.1007/s00595-003-2643-y

22. Belting M, Ahamed J, Ruf W, 2005, Signaling of the tissue factor coagulation pathway in angiogenesis and cancer. *Arterioscler Thromb Vasc Biol*, 25: 1545–1550.

https://doi.org/10.1161/01.atv.0000171155.05809.bf

23. Sato T, Tsujino I, Ikeda D, *et al.*, 2006, Trousseau's syndrome associated with tissue factor produced by pulmonary adenocarcinoma. *Thorax*, 61: 1009–1010.

https://doi.org/10.1136/thx.2004.031492

24. Rong Y, Belozerov VE, Tucker-Burden C, *et al.*, 2009, Epidermal growth factor receptor and PTEN modulate tissue factor expression in glioblastoma through JunD/activator protein-1 transcriptional activity. *Cancer Res*, 69: 2540–2549.

https://doi.org/10.1158/0008-5472.CAN-08-1547

25. Magnus N, Garnier D, Rak J, 2010, Oncogenic epidermal growth factor receptor up-regulates multiple elements of the tissue factor signaling pathway in human glioma cells. *Blood*, 116: 815–818.

https://doi.org/10.1182/blood-2009-10-250639

26. Gary T, 2014, Cancer related venous thromboembolism-prophylaxis and therapy. *Vasa*, 43: 245–251.

https://doi.org/10.1024/0301-1526/a000359

27. Tagalakis V, Levi D, Agulnik JS, *et al.*, 2007, High risk of deep vein thrombosis in patients with non-small cell lung cancer: A cohort study of 493 patients. *J Thorac Oncol*, 2: 729–734.

https://doi.org/10.1097/JTO.0b013e31811ea275

28. Hicks LK, Cheung MC, Ding K, *et al.*, 2009, Venous thromboembolism and nonsmall cell lung cancer: A pooled analysis of National Cancer Institute of Canada Clinical Trials Group trials. *Cancer*, 115: 5516–5525.

https://doi.org/10.1002/cncr.24596

29. Wang J, Hu B, Li T, *et al.*, 2019, The EGFR-rearranged adenocarcinoma is associated with a high rate of venous thromboembolism. *Ann Transl Med*, 7: 724.

https://doi.org/10.21037/atm.2019.12.24

30. Dearden S, Stevens J, Wu YL, *et al.*, 2013, Mutation incidence and coincidence in non small-cell lung cancer: Meta-analyses by ethnicity and histology (mutMap). *Ann Oncol*, 24: 2371–2376.

https://doi.org/10.1093/annonc/mdt205

31. Qian X, Fu M, Zheng J, *et al.*, 2021, Driver genes associated with the incidence of venous thromboembolism in patients with non-small-Cell lung cancer: A systematic review and meta-analysis. *Front Oncol*, 11: 680191.

https://doi.org/10.3389/fonc.2021.680191

32. Lee YG, Kim I, Lee E, *et al.*, 2014, Risk factors and prognostic impact of venous thromboembolism in Asian patients with non-small cell lung cancer. *Thromb Haemost*, 111: 1112–1120.

https://doi.org/10.1160/TH13-11-0956

33. Shaw AT, Kim DW, Mehra R, *et al.*, 2014, Ceritinib in ALK-rearranged non-small-cell lung cancer. *N Engl J Med*, 370: 1189–1197.

https://doi.org/10.1056/NEJMoa1311107

34. Ou SH, Ahn JS, De Petris L, *et al.*, 2016, Alectinib in crizotinib-refractory ALK-rearranged non-small-cell lung cancer: A phase II global study. *J Clin Oncol*, 34: 661–668.

https://doi.org/10.1200/jco.2015.63.9443

35. Carrier M, Khorana AA, Zwicker JI, *et al.*, 2012, Venous thromboembolism in cancer clinical trials: Recommendation for standardized reporting and analysis. *J Thromb Haemost*, 10: 2599–2601.

https://doi.org/10.1111/jth.12028

36. Alexander M, Kirsa S, Wolfe R, *et al.*, 2014, Thromboembolism in lung cancer-an area of urgent unmet need. *Lung Cancer*, 84: 275–280.

https://doi.org/10.1016/j.lungcan.2014.02.009

37. Chew HK, Davies AM, Wun T, *et al.*, 2008, The incidence of venous thromboembolism among patients with primary

lung cancer. *J Thromb Haemost*, 6: 601–608.

https://doi.org/10.1111/j.1538-7836.2008.02908.x

38. Roselli M, Riondino S, Mariotti S, *et al.*, 2014, Clinical models and biochemical predictors of VTE in lung cancer. *Cancer Metastasis Rev*, 33: 771–789.

https://doi.org/10.1007/s10555-014-9500-x

39. Ay C, Ünal UK, 2016, Epidemiology and risk factors for venous thromboembolism in lung cancer. *Curr Opin Oncol*, 28: 145–149.

https://doi.org/10.1097/CCO.0000000000000262

40. Kadlec J, Skrickova ZM, Merta Z, *et al.*, 2014, The incidence and predictors of thromboembolic events in patients with lung cancer. *ScientificWorldJournal*, 2014: 125706.

https://doi.org/10.1155/2014/125706

41. Demirci NY, Turay UY, Ylmaz A, *et al.*, 2011, Vascular events in lung cancer. *Asian Pac J Cancer Prev*, 12: 2685–2687.

42. Pedersen LM, Milman N, 1996, Prognostic significance of thrombocytosis in patients with primary lung cancer. *Eur Respir J*, 9: 1826–1830.

https://doi.org/10.1183/09031936.96.09091826

43. Fei X, Wang H, Yuan W, *et al.*, 2017, Tissue factor pathway inhibitor-1 is a valuable marker for the prediction of deep venous thrombosis and tumor metastasis in patients with lung cancer. *Biomed Res Int*, 2017: 8983763.

https://doi.org/10.1155/2017/8983763

44. Shiina Y, Nakajima T, Yamamoto T, *et al.*, 2019, The D-dimer level predicts the postoperative prognosis in patients with non-small cell lung cancer. *PLoS One*, 14: e0222050.

https://doi.org/10.1371/journal.pone.0222050

ACCSCIENCE PUBLISHING

Global Translational Medicine

ORIGINAL RESEARCH ARTICLE

A simple, fast, and cost-effective high-performance liquid chromatography-ultraviolet validated method to quantify lacosamide in therapeutic drug monitoring

Ángeles Gloria Rodríguez-Basso[1], María Cecilia Kravetz[2]*, María Sylvia Viola[1], Florencia Ayelén Fernández[2], Nicolás Martín Barrionuevo[2], Damián Consalvo[3], Mariano Núñez[2], and Guillermo Federico Bramuglia[1,4]

[1]Department of Pharmacology, Faculty of Pharmacy and Biochemistry, University of Buenos Aires, Buenos Aires, Argentina

[2]Institute of Pharmacology, Faculty of Medicine, University of Buenos Aires, Buenos Aires, Argentina

[3]Institute of Neurology and Neurosurgery, Sanatorio de Los Arcos, Buenos Aires, Argentina

[4]Fundación Investigar, Buenos Aires, Argentina

Abstract

Lacosamide is a third-generation anticonvulsant used in the treatment of epilepsy. While therapeutic levels for various patient subpopulations are still under investigation to achieve optimal responses, therapeutic drug monitoring has been proven to be useful in improving patient management. To ensure the reliability of results, it is essential to establish a reliable quantitative method. Thus, the aim of this study was to develop and validate a simple and feasible method for quantifying lacosamide in human plasma, with the specific aim of facilitating drug monitoring purposes. A high-performance liquid chromatography method with ultraviolet detection was developed for the quantification of lacosamide in human plasma. Analyte recovery was achieved through ethyl acetate extraction, with propranolol serving as the internal standard. A C18 column and a mobile phase consisting of 10 mM phosphate buffer and acetonitrile (70:30 v/v, pH = 3.5) were employed. Validation parameters included specificity, linearity, repeatability, precision, accuracy, sensitivity, and stability. The method exhibited linearity within the range of 2.5 – 30 μg/ml ($R^2 = 0.997$), with a limit of quantitation of 2.29 μg/ml. The average recovery percentage was 100.2%, and it proved to be accurate, precise, and specific. In plasma samples, the drug content remained stable for 72 h at 4°C, 1 month at −20°C, and 2 years at −80°C. The post-processed sample remained stable for 1 week under all tested conditions. Due to its simplicity, short analysis time, sensitivity, and cost-effectiveness, the proposed analytical method proves to be useful for therapeutic monitoring and pharmacokinetic studies of lacosamide.

Keywords: High-performance liquid chromatography; Lacosamide; Pharmacokinetics

***Corresponding author:**
María Cecilia Kravetz
(mariaceciliakravetz@gmail.com)

Citation: Rodríguez-Basso ÁG, Kravetz MC, Viola MS, *et al.*, 2023, A simple, fast, and cost-effective high-performance liquid chromatography-ultraviolet validated method to quantify lacosamide in therapeutic drug monitoring. *Global Transl Med,* 2(3): 1265.
https://doi.org/10.36922/gtm.1265

Received: July 7, 2023
Accepted: September 5, 2023
Published Online: September 26, 2023

1. Introduction

Lacosamide is a third-generation antiepileptic drug (AED) used to treat epileptic seizures, both as monotherapy and in combination with other AEDs. Its primary mechanism of

action, which justifies its efficacy, involves the modulation of slow sodium channels[1]. Lacosamide is indicated for use in adults, adolescents, and children. Its pharmacokinetics include excellent bioavailability, a linear pharmacokinetic profile, and low plasma protein binding, with 60% hepatic elimination and 40% renal elimination[2].

While some authors have questioned the utility of therapeutic drug monitoring in the general population, citing the perceived predictability of plasma concentration in relation to the dose[3,4], others have documented the benefits of therapeutic drug monitoring. They argue for the necessity of measuring anticonvulsant concentrations to characterize individual pharmacokinetics and optimize patient drug regimens[5,6]. Preclinical studies have indicated the potential for plasma level variations if lacosamide clearance is affected[7]. Clinical evidence also supports the need for dose adjustments in patients co-administered with enzyme inducers or those experiencing impaired hepatic or renal function due to critical illnesses[8]. Furthermore, patients with dynamic physiology (the elderly, children, and pregnant women) present a challenge in establishing a single reference range, which remains a topic of debate in these populations[9].

Some of the reported analytical methods for the determination of lacosamide include ultraviolet spectroscopy (UVS), high-performance liquid chromatography (HPLC) with UV detection (HPLC-UV)[10], thin-layer chromatography (HPTLC), and HPLC-mass spectrometry[11]. However, the existing methods for the determination of lacosamide in human plasma exhibit various limitations, especially in low-resource settings where affordable analytical methods are a key factor for obtaining versatile and reliable results. Challenges associated with these methods include the absence of an internal standard[12,13], the necessity for more costly or unavailable reagents due to supply shortages, and the potential inefficiency of proposed sample treatments. The absence of an internal standard can affect the accuracy and precision of measurements, as well as the reproducibility of the results. The analyte recovery from the matrix is a significant source of variation in the analytical process; thus, it is critical for the success of the method and requires an adequate sample treatment. An unsatisfactory analyte recovery can cause a systematic error in the method, which affects not only accuracy and precision but also sensitivity and selectivity. Furthermore, obtaining inaccurate or imprecise analytical results may have implications for therapeutic drug monitoring, drug dosing recommendations, and patient safety.

These challenges prompted the development of an internal method with a focus on regional accessibility. This work presents the development, optimization, and validation of a simple, fast, cost-effective, reliable, and efficient HPLC-UV method for quantifying lacosamide in human plasma, intended for therapeutic monitoring purposes.

2. Materials and methods

2.1. Critical reagents and solvents

Lacosamide standard (generously donated by local industry [origin: Sigma-Aldrich, Ref. No. SML3059, purity >98%, Saint Luis, Missouri, USA]); propranolol hydrochloride standard (used as an internal standard, purchased from INAME, Control No. 190031, purity 100.2%, Buenos Aires, Argentina); HPLC-grade acetonitrile, HPLC-grade methanol, analytical-grade hydrochloric acid, and ethyl acetate (SINTORGAN, Villa Martelli, Buenos Aires Argentina); MilliQ water; and monobasic potassium phosphate salt (CICARELLI, Buenos Aires, Argentina).

2.2. Equipment

Analytical balance (METTLER TOLEDO, model MS 105), vortex mixer (Scientific Industries, Genie2 G560), magnetic stirrer (Thermo Scientific Cimarec Basic model S194615), ultrasonic bath (TestLab, model TB-010 TA), thermostatic bath (FAC, model Ballus), vacuum filtration system (Millipore), vacuum pump (Pascal, model PC-75), water purifier (Simplicity Millipore), centrifuge (IEC Centra-7R), -80°C freezer (Revco), pH meter (COLE PARMER, model 05669-29), and air compressor (Total Tools, industrial TTAC2506).

2.3. Chromatographic system

The analysis was performed using a THERMO SCIENTIFIC ULTIMATE 3000 HPLC system equipped with an autoinjector, column oven, and a diode array UV detector. A Phenomenex Kinetex C18, 100 A column with dimensions of 150 mm × 4.6 mm and a particle diameter of 2.6 µm was selected as the stationary phase. The mobile phase (MP) consisted of a 70:30 v/v ratio of 10 mM potassium phosphate buffer (KH_2PO_4) and acetonitrile, pH adjusted to 3.5 using hydrochloric acid (HCl). An isocratic elution method was employed with a flow rate of 0.6 ml/min, an injection volume of 20 µL, and detection at a wavelength of 210 nm. Each sample had a total elution time of 10 min.

2.4. Method optimization

The optimized conditions encompassed the following parameters: The choice of the bonded phase (C8, C18), the composition of the mobile phase (organic solvent type and percentage, buffer type and pH), operational parameters such as flow rate, temperature, and wavelength, the nature of the internal standard, and the method for preparing the biological sample (either precipitation or liquid-liquid extraction).

For the system suitability test, chromatographic parameters such as retention time, capacity factor, tailing factor, resolution, and column efficiency were assessed. These parameters were chosen to determine the method's acceptability and were calculated according to the USP guidelines[14], utilizing typical chromatograms as the basis for evaluation.

2.5. Working solutions

Approximately 50 mg of lacosamide reference standard was accurately weighed and placed into a 50 ml volumetric flask. It was then dissolved and brought to volume with MilliQ water, creating a stock solution with a concentration of 1.0 mg/ml solution. Further dilutions were prepared from this stock solution.

In a 100 ml volumetric flask, exactly 50 mg of propranolol was added and brought to volume with acetonitrile. Subsequently, it was further diluted with MilliQ water to obtain a concentration of 50 µg/ml (internal standard solution).

2.6. Samples and controls

Freshly obtained plasma samples were stored at −20°C for subsequent use. A plasma pool was then generated to prepare control solutions with predetermined concentrations of lacosamide, using the stock solution at the concentrations of 2.5 µg/ml, 5 µg/ml, 10 µg/ml, 15 µg/ml, 20 µg/ml, and 30 µg/ml.

To each solution, 200 µL aliquots were taken, and 10 µL of an internal standard was added. The resulting mixture was vortexed for 15 s. Subsequently, 2 mL of ethyl acetate was added as the extraction solvent, followed by 1 min of vortexing and centrifugation at 3500 rpm for 10 min. The resulting organic phase was transferred to a glass tube and subjected to evaporation to dryness within a thermostatic bath set at 37°C , all conducted under an extraction hood. Finally, the dried extract was reconstituted in 200 µL of the mobile phase, and 20 µL of this solution was injected into the chromatographic system.

2.7. Validation

The validation parameters evaluated included specificity, linearity, repeatability, intermediate precision, accuracy, and stability, with adherence to the stipulated international[15,16] and national[17] guidelines. Data analysis was conducted using statistical software R[18].

2.7.1. Specificity

Specificity was evaluated through three tests:

(i) Analysis of plasma interferents: Five plasma samples with varying characteristics, including normal appearance, hemolysis, lipemia, and jaundice, were sourced from different samples. Each sample was processed as a blank to evaluate the presence of endogenous substances that might elute with lacosamide or the internal standard.

(ii) Analysis of forced degradation: Lacosamide solutions, devoid of the internal standard, were subjected to various reactions (oxidation, acid hydrolysis, alkaline hydrolysis, aqueous hydrolysis, and photolytic degradation). The resulting solutions were then used to prepare solutions with known concentration levels.

(iii) Analysis of specificity against other drugs: Considering the possibility of polypharmacy in patients, some commonly used drugs, such as ibuprofen, paracetamol, diclofenac, and clonazepam, among others, were evaluated for specificity.

2.7.2. Linearity

To establish a linear-response range of the instrument within the clinically relevant concentration range (10 – 20 µg/mL), six lacosamide levels (2.5 µg/ml, 5 µg/ml, 10 µg/ml, 15 µg/ml, 20 µg/ml, and 30 µg/ml) were prepared in triplicate, with the addition of the internal standard for all samples. The calibration curve for lacosamide was constructed by plotting the area ratio (lacosamide area/propranolol area) against the lacosamide concentration.

Subsequently, the calculation of correlation coefficient (r) and coefficient of determination (R^2) was performed, followed by a linear regression analysis. This analysis included an assessment of the response factor, an evaluation of the statistical significance of the slope variance (Sb), and a test for proportionality (calculation of the relative zero intercept, calculation of its variance, and calculation of its confidence interval [CI]).

2.7.3. Precision

This parameter was evaluated in two ways:

(i) Repeatability: Six independent lacosamide samples were prepared at a concentration of 10 µg/ml (considered as 100% concentration). The internal standard was added to each sample, and they were analyzed in triplicate. The repeatability of the bioanalytical method was determined by calculating the coefficient of variation (CV%) of the response factors for the six evaluated samples.

(ii) Intermediate precision: Two analysts quantified lacosamide in two aliquots from the same sample on different days. Each analyst used a different instrument and chromatographic column, and the samples were processed following the technique explained earlier. The intermediate precision of the method was determined by calculating the CV% of the lacosamide concentrations obtained in the samples analyzed by the two analysts.

For both precision analyses, a CV% of < 15% was used as the acceptance criterion.

2.7.4. Accuracy

Accuracy was evaluated by calculating the percentage of recovery. Triplicate samples of lacosamide in plasma were prepared at three different concentrations: 5 µg/ml, 10 µg/ml, and 15 µg/ml. These samples were processed according to the described technique and injected in triplicate into the chromatograph.

The percentage of recovery was determined as the ratio between the measured concentration value and the theoretical concentration value. To analyze the results, a Student's *t*-test with a significance level of $P = 0.05$ was employed. Data variability was investigated using the CV% and Cochran's G test. The latter was used to determine whether the concentration level had any influence on the results.

2.7.5. Sensitivity

Sensitivity can be assessed by determining the Limit of Detection (LOD) and the Limit of Quantitation (LOQ). LOD and LOQ were calculated using Equation 1:

$$K \times S0 / b \quad \text{(I)}$$

Where k = 3 for LOD and 10 for LOQ, S0 represents the standard deviation of the y-intercept, and b is the slope of the calibration curve.

2.7.6. Stability

The stability of the analyte of interest was evaluated in three sample stability assays:

(i) Short-term and long-term sample stability: Unprocessed samples were stored under various conditions, including room temperature (for 24 h, 48 h, and 72 h), in the refrigerator at 4°C (for 24 h, 48 h, and 72 h), in a freezer at −20°C (for 24 h, 48 h, 72 h, 7 days, and 30 days), and in a freezer at −80°C (1 week, 1 month, 6 months, 1 year, and 2 years).
(ii) Post-processed sample stability: Samples were processed according to the analytical method and then stored under different conditions, including room temperature, in a refrigerator at 4°C, and in the freezer at −20°C for 24 h, 48 h, 72 h, and 1 week.
(iii) Freeze-thaw stability: Samples were subjected to three freeze-thaw cycles (freezing in a −20°C and -80°C freezer for 24 h each, followed by thawing).

In each of these assays, the obtained lacosamide concentration was compared with the initial (time zero) concentration. Samples were considered stable if their final time concentration remained above 90% of the initial concentration.

2.8. Lacosamide quantification in patients

Lacosamide quantification, utilizing the previously validated HPLC technique as described, was carried out on samples collected from five patients prescribed lacosamide for the treatment of epilepsy. Blood samples were collected during steady-state conditions while undergoing treatment. The first sample was collected before drug intake (trough level), and the second sample was collected 2 h after dosing (peak level). Informed consent was obtained from all patients as part of routine clinical care.

3. Results

3.1. Optimization

The following stationary phases were evaluated: a 150 × 4.6 mm, 2.6 µm Kinetex-Phenomenex C8 column, a 250 × 4.6 mm, 5 µm Thermo C8 column, and a 150 × 4.6 mm, 2.6 µm Kinetex-Phenomenex C18 column. Among these, only the Kinetex-Phenomenex C18 column achieved adequate resolution of both peaks.

The chromatographic conditions employed included a 70:30 ratio of 10 mM phosphate buffer (pH = 3.5) and acetonitrile. This composition facilitated lacosamide elution within 10 min without interferers. The column temperature was set at 30°C; deviations from this temperature resulted in system pressure variations (e.g., increased pressure at 25°C and elution front issues at 40°C). Flow rates of 0.6 mL/min and 0.8 mL/min, except for the working pressure (2440 psi vs. 2880 psi, respectively). Nevertheless, employing a flow rate of 0.6 mL/min proves advantageous in preventing premature aging of a column. In addition, adjusting the pH of the phosphate buffer to 3.0 contributes to stability and minimizes peak broadening compared to higher pH values[19].

Several internal standards, such as aminopyrine, benserazide, acetazolamide, sulfanilamide, caffeine, and propranolol, were examined. While most of them eluted very close to the front peak, propranolol was ultimately selected.

The wavelengths under evaluation were 210 nm, 260 nm, and 290 nm, corresponding to local maxima in the UV absorption spectra. Optimal sensitivity for both molecules was observed at 210 nm.

In the context of sample treatment, various methods were employed. Protein precipitation was tested using perchloric acid at different dilutions (one-third, one-fourth, and one-fifth), in addition to acetonitrile and methanol. However, these preparations led to an underestimation of the true concentration and failed to achieve adequate resolution. Higher concentrations of precipitant resulted in tailing, while lower proportions introduced more plasma interferers. Subsequently, alternative liquid-

liquid extraction solvents, including dichloromethane, cyclohexane, hexane, chloroform, methyl tert-butyl ether, and ethyl acetate, were evaluated. Ethyl acetate was selected due to its ability to provide stable and acceptable recovery percentages for both molecules.

Table 1 presents the results of the system suitability test for the pre-selected parameters, demonstrating that all values fall within acceptable limits. The characteristic chromatogram is depicted in Figure 1, while the UV absorption spectra of lacosamide and propranolol are illustrated in Figure 2.

3.2. Validation

All the results of the validation parameter evaluation are summarized in Table 2.

Table 1. System suitability

Parameter	Acceptance criteria	Results	
		Lacosamide	Propranolol
Theoretical plates (n)	>2000[a]	28845±549	30648±641
Tailing	≤2.0[a]	1.00±0.02	1.12±0.02
Resolution	>2.0[a]	18.96±0.16	
Capacity factor (K')	1 – 20[a]	0.52	1.37
Retention time	<10 min[b]	3.8 min	5.9 min
Repeatability of retention time (CV%)	<1.0[b]	0.05%	0.05%

Notes: [a]By FDA requirement[20]. [b]Establish by work group.

3.2.1. Specificity

When analyzing various types of plasma, including normal, hemolyzed, icteric, and hyperlipidemic plasma (Figure 3), a comparison was made between the non-specific peaks observed and the area of the lowest level of the curve of lacosamide and the internal standard area. In all cases, the non-specific peaks accounted for less than 10% of the total area. Furthermore, the retention times of both analytes did not overlap with those of commonly used drugs, as shown in Figure 4. In addition, forced degradation studies yielded optimal results (Figure 5).

3.2.2. Linearity

The equation of the linear model is as follows:

$$\text{Area ratio} = 2.4069 + 10272.1754 \times \text{lacosamide concentration} \quad \text{(II)}$$

The coefficients R and R^2 were 0.9985 and 0.9970, respectively, in accordance with the obtained linear regression curve.

The t-test for the slope (t exp: 73.4657) resulted in a value higher than the tabulated t-value for n-2 degrees of freedom at a significance level of P = 95% (t [4;0.05: 2.78]). This indicates that the slope is statistically different from zero. The total coefficient of variation of the response factors was <15%.

Conversely, the experimental t-value for the intercept (t exp: 1.0242) was lower than the t (4;0.05) value, and

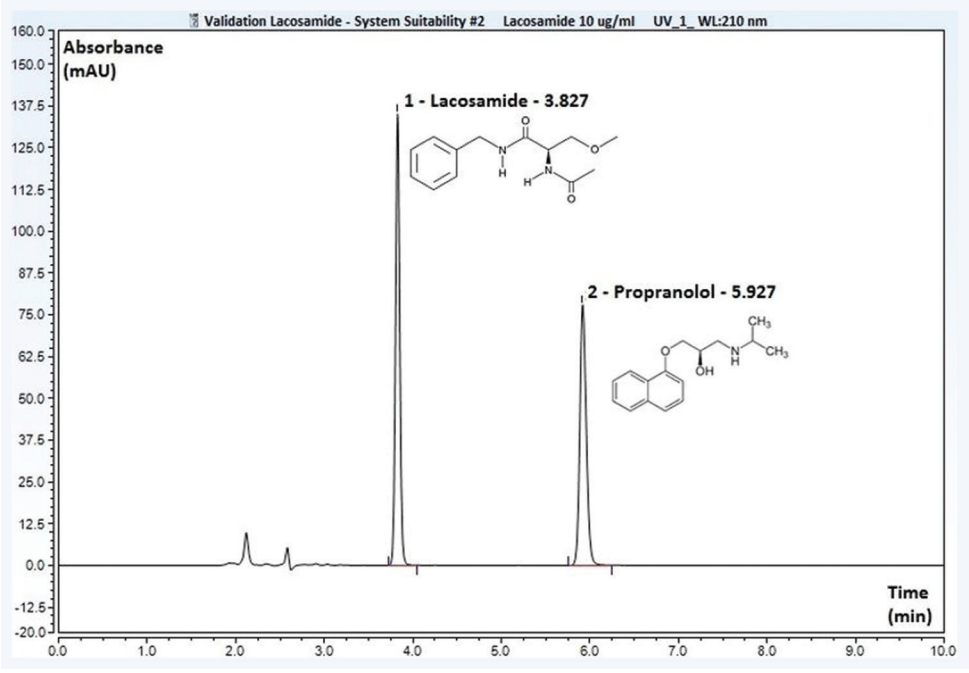

Figure 1. Characteristic chromatogram of lacosamide and propranolol in plasma.

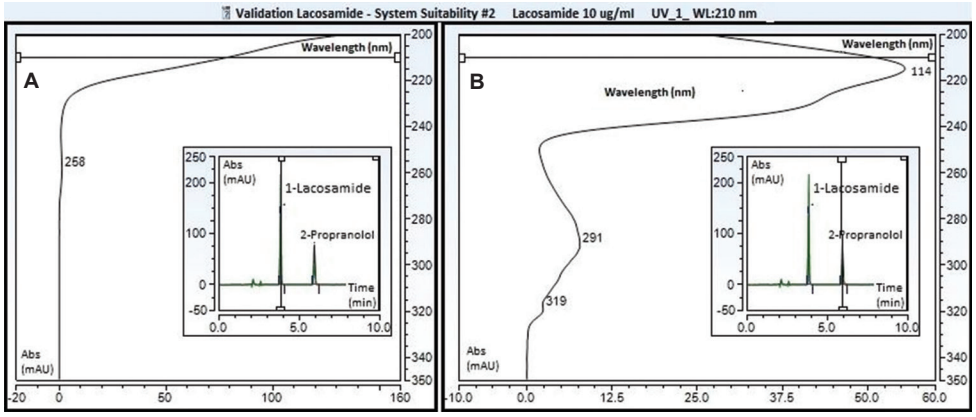

Figure 2. Ultraviolet spectral scanning of lacosamide (A) and propranolol (B).

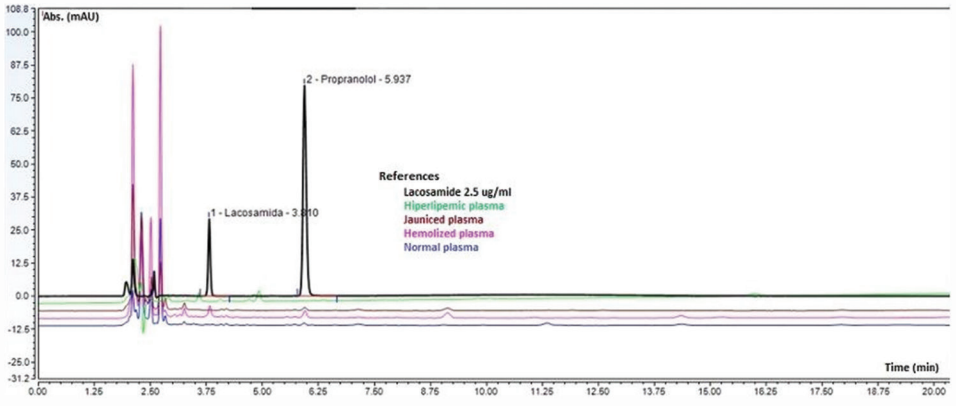

Figure 3. Specificity of different types of human plasmas, with the baselines presented from top to bottom. Lacosamide in water, lipemic plasma, jaundiced plasma, hemolyzed plasma, and normal plasma from different sources was used.

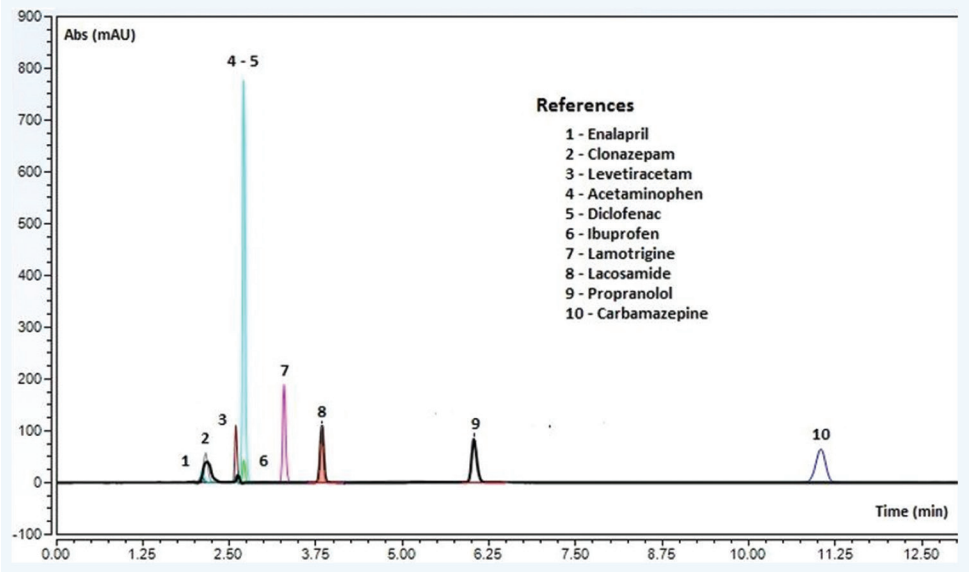

Figure 4. Specificity of ten drugs (1 – 10): enalapril, clonazepam, levetiracetam, acetaminophen, diclofenac, ibuprofen, lamotrigine, lacosamide, propranolol, and carbamazepine.

Table 2. Summary of validation results

Parameters	Tested items		Specifications	Results	
Specificity	Comparison of Rt with and without degradations, using different types of plasmas and other drugs		There were no interference peaks with areas>10% of analyte areas	Accepted	
Repeatability	CV% measuring		<15.00%	6.76%	
Intermediate precision	Date			2018 January 15	2018 January 18
	Analyst			Analyst 1	Analyst 2
	Equipment			Thermo Scientific Ultimate 3000	Shimadzu UFLC
	Column			Phenomenex Kinetex-C18 (4.6×150 mm – 2.6 µ)	YMC-Pack ODS-A (4.6×150 mm-3 µ)
	CV% measuring		<15.00%	12.64%	
	Slope			10272.1754	
Linearity	Y-intercept			2.4069	
	R measuring		Positive correlation >r than tables for df=n-2 and *P*=95%	*R* calculated: 0.9985 *R* tables (4;0,05): 0.811	
	R^2 measuring		>0.98	0.9970	
	Statistical significance of the slope		Response factor	CV% <15.00%	
	Statistical significance of the slope Proportionality test	S_b relat. %	≤2.00%	4.73%	
		Slope CI		1.36%	
		Test *t*: *t* experimental	>*r* from tables to df=n-2 and *P*=95% (*p*<0.05)	Upper limit: 10660.4 Lower limit: 9884.0	
		CI of the y-intercept	Should include 0	T exp: 73.4657 T (4;0,05): 2.78 $P=2 \times 10^{-16}$	
	Proportionality test % average recovery	y-intercept	<2%	Upper limit: 8.9319 Lower limit: - 4.1180	
		Test *t*: *t* experimental	<*t* from tables to df=n-2 and *P*=95% (*P*>0.05)	1.66%	
			100.2%	T exp: 1.0242 T (4;0,05): 2.78 *P*=0.321	
Accuracy	Test *t*: *t* experimental		<*t* from tables to df=n-1 and *P*=95%	T exp: 0.43 T (8;0,05): 2.306	
	Test of equality of variances		G<*t* from tables to α = 0.05% and K concentration and n replicates	G exp: 0.324609 G (9;3;0,05): 0.4775	
	CV%		<15.00%	7.01%	
Sensitivity	Limit of detection Limit of quantification			LOD: 0.69 µg/ml LOQ: 2.29 µg/ml	
Working range	Concentrations within linearity, precision and accuracy are acceptable			2.5 – 30 µg/ml	
Stability	Short and long-term stability		Title≥90% from time 0	Not at room temperature. Stable for 72 h at 4°C, for 1 month at–20°C and for 2 years at–80°C.	
	Stability of the post-processed sample		Title≥90% from time 0	Stable for 1 week at room temperature, at 4°C and at -20°C	
	Stability of freeze and thaw cycles		Title≥90% from time 0	Not stable at -20°C Stable for 2 cycles at -80°C	

Notes: CI: Confidence interval; df: Degrees of freedom; N/A: Not applicable; Rt: Retention time; Sb: Slope variance.

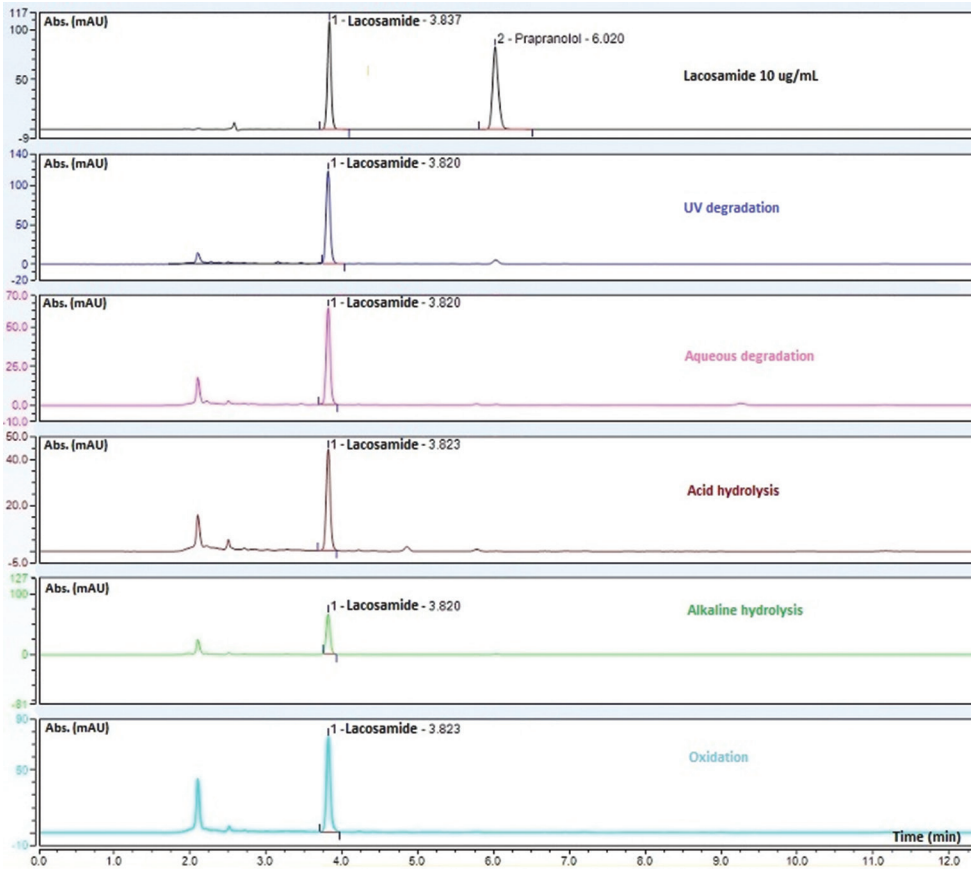

Figure 5. Comparisons of specificity in forced degradation studies.

the CI 95% included the value zero, indicating that the intercept was not statistically different from zero.

3.2.3. Precision

In the evaluation of precision, the methodology performed adequately, with CV% values of 6.76% and 12.64% in the repeatability test and the intermediate precision test, respectively. Both values were lower than the 15.00% limit.

3.2.4. Accuracy

This analysis revealed that the average recovery percentage was 100.2%, along with an experimental *t*-value lower than the tabulated one. In all cases, the CV% remained below 15%, and the variances of the tested concentrations were equivalent, as evidenced by the experimental Cochran's G value being lower than the tabulated one. Therefore, concentration does not significantly influence the variability of the results.

3.2.5. Sensitivity

We achieved 0.69 µg/ml for LOD and 2.29 µg/ml for LOQ.

3.2.6. Stability

The stability study revealed that unprocessed plasma samples containing lacosamide are not stable at room temperature and should be stored under cold conditions. The maximum storage times are summarized in Table 2. When processed using this analytical technique, the samples remain stable for 1 week under all storage conditions. Significant changes in areas are observed in samples subjected to freeze-thaw cycles, but this effect is primarily seen when exposed to −20°C.

3.3. Therapeutic drug monitoring of lacosamide in epileptic patients

The quantification of lacosamide was satisfactorily carried out in five adult patients. A total of 10 blood samples were obtained at steady-state, and lacosamide concentrations were measured using the previously developed and validated HPLC method (Table 3). The lacosamide dose ranged from 200 – 500 mg/day, and the measured plasma levels (troughs and peaks) ranged between 3.6 and 13.8 ug/ml.

Table 3. Summary of patient plasma levels of lacosamide

Subjects	Body mass index (Kg/m^2)	Gender	Response to treatment	Daily dose (mg/day)	Pre- or post-dose	Level (ug/ml)
1.	35.4	Female	Resistant	500	Pre	9.1
					Post	13.5
2.	22.6	Female	Responsive	200	Pre	8.1
					Post	13.8
3.	32.3	Male	Resistant	400	Pre	8.9
					Post	13.4
4.	23.7	Male	Resistant	400	Pre	3.6
					Post	5.4
5.	27.6	Male	Responsive	500	Pre	12.5
					Post	13.6

4. Discussion

Therapeutic drug monitoring services for AEDs remain limited in many countries, both in public and private institutions. Therefore, the development of a simple, reliable, and cost-effective quantitative method could improve accessibility for local laboratories and facilitate therapeutic optimization.

While there are publications on HPLC-mass and UHPLC approaches[21], the use of HPLC-UV is both cost-effective and practical. However, previously published methodologies lacked reproducibility, necessitating the development of a novel approach. Some reported methods involve protein precipitation for deproteinization[10,22,23], but a satisfactory recovery of the analyte within the clinical range was only achieved through solvent extraction.

Propranolol, serving as an internal standard, is an affordable drug widely available for purchase. It has proven to be useful not only for this lacosamide method but also for analyzing other anticonvulsants in our laboratory.

The method presented here demonstrated specificity, as no interferences were found under matrix conditions (normal plasma, hemolyzed plasma, hyperlipemic plasma, etc.) or in the presence of commonly used drugs (diclofenac, ibuprofen, etc.) or other anticonvulsants. This outcome is particularly desirable given the variations in patient treatments and individual circumstances.

The linearity of the method was verified within the concentration range of 2.5 – 30.0 µg/ml for lacosamide, which encompasses the clinically relevant concentration range (10 – 20 µg/mL). In this model, 99.70% of the variation in the area ratio was accounted for by variations in lacosamide concentration. The total coefficient of variation of the response factors met the specifications, and a LOD of 0.69 µg/ml was achieved. This level of sensitivity enables the quantification of lacosamide levels below the reference range, which is crucial in assessing adherence, potential interactions, suspected treatment failure, or subtherapeutic responses resulting from variations in the drug's pharmacokinetics or pharmacodynamics. In addition, the wide range allows the study of lacosamide's pharmacokinetic behavior in treated patients and the assessment of concentration-response variability across diverse populations.

The stability study revealed that the unprocessed sample maintains its integrity for up to 1 month at −20°C or 2 years at −80°C. Once processed, the sample exhibited excellent stability even at room temperature, allowing for reanalysis if necessary. However, it does not withstand more than two cycles of freezing at −80°C (never at −20°C) and subsequent thawing. These findings provide valuable insights for working under good laboratory practice conditions. This involves considering not only sample care but also the well-being of routine patients participating in clinical research.

While it continues to be a topic of discussion, the previous works[5] have suggested that a minimum plasma level (trough level) of 10 ug/ml is required to ensure clinical efficacy. The methodology used in the present study successfully detected clinically useful therapeutic levels. As expected, non-responder patients exhibited blood levels below the therapeutic range. It was also noteworthy that a patient classified as a responder achieved therapeutic effects with lower trough levels than the recommended threshold. Despite the small sample size, which was primarily aimed at assessing the method's utility, these results highlight the importance of establishing blood drug monitoring protocols to optimize lacosamide therapy. Furthermore, this approach will enable a deeper understanding of the prerequisites necessary to ensure its clinical efficacy and its behavior in diverse populations.

Therefore, this analytical methodology is a useful tool with the potential for future adaptation to determine

lacosamide in other biological matrices, such as saliva[24] or urine[25].

5. Conclusion

The proposed HPLC-UV analytical method has demonstrated specificity for the target analyte and has demonstrated adequate accuracy, precision, and linearity within the clinically relevant concentration range. Therefore, it holds value to be used in pharmacokinetic studies and therapeutic drug monitoring of lacosamide due to its simplicity, short analysis duration, appropriate sensitivity, and cost-effectiveness.

Acknowledgments

We would like to thank ARGENOMICS and FUNDACION INVESTIGAR for helping us to afford the equipment qualification. We also thank Dr. Augusto Garcia Vargas, Dr. Emiliana Seminara, and Dr. Patricia Coffey for being involved in patient follow-up.

Funding

This work is part of a research project supported by the University of Buenos Aires, UBACyT 2018–2022 Code: 20020170100734BA.

Conflict of interest

The authors declare they have no competing interests.

Author contributions

Conceptualization: Angeles Gloria Rodriguez Basso, Guillermo Federico Bramuglia
Formal Analysis: Angeles Gloria Rodriguez Basso
Funding Acquisition: Guillermo Federico Bramuglia
Investigation: María Cecilia Kravetz, Damian Consalvo
Methodology: María Cecilia Kravetz
Project administration: Maria Sylvia Viola
Resources: Mariano Núñez
Supervision: Angeles Gloria Rodriguez Basso, Damian Consalvo
Validation: Nicolás Martín Barrionuevo, Florencia Ayelén Fernandez.
Writing – original draft: Angeles Gloria Rodriguez Basso, María Cecilia Kravetz
Writing – review & editing: Maria Sylvia Viola, Florencia Ayelén Fernandez, Guillermo Federico Bramuglia

Ethics approval and consent to participate

The study was approved by IRB "Comité de Ética en Investigación Clínica y Maternidad Suizo Argentina" (ethical approval code: C0004-P00033). This work includes anonymized data from patients who have signed the appropriate informed consent form to participate in the quantification of lacosamide during routine clinical care.

Consent for publication

This work includes anonymized data from patients who have signed the appropriate informed consent form to participate in lacosamide quantification during routine clinical care, as well as authorization to include these data for research and publication as long as anonymity is preserved.

Availability of data

Data used in this work can be made available to the readers by contacting the corresponding author.

References

1. Beydoun A, D'Souza J, Hebert D, *et al*., 2009, Lacosamide: Pharmacology, mechanisms of action and pooled efficacy and safety data in partial-onset seizures. *Expert Rev Neurother*, 9: 33–42.

   https://doi.org/10.1586/14737175.9.1.33

2. EMA European Medicines Agency, 2022, Vimpat Product Monograph, Available from: https://www.ema.europa.eu/en/medicines/human/EPAR/vimpat [Last accessed on 2023 Jan 09].

3. Kawasaki Y, Sendo T, 2016, Monitoring of the blood concentrations of antiepileptic drugs (TDM). *Rinsho Byori*, 64: 1373–1380.

   https://doi.org/10.1002/ana.25641

4. Aícua-Rapún I, André P, Rossetti AO, *et al*., 2020, Therapeutic drug monitoring of newer antiepileptic drugs: A randomized trial for dosage adjustment. *Ann Neurol*, 87: 22–29.

   https://doi.org/10.1002/ana.25641

5. Landmark CJ, Johannessen SI, Patsalos PN, 2020, Therapeutic drug monitoring of antiepileptic drugs: Current status and future prospects. *Expert Opin Drug Metab Toxicol*, 16: 227–238.

   https://doi.org/10.1080/17425255.2020.1724956

6. Czornyj L, Guido PC, Bramuglia G, *et al*., 2018, High incidence of persistent subtherapeutic levels of the most common AEDs in children with epilepsy receiving polytherapy. *Epilepsy Res*, 148: 107–114.

   https://doi.org/10.1016/j.eplepsyres.2018.09.008

7. Kumar B, Modi M, Saikia B, *et al*., 2017, Evaluation of brain pharmacokinetic and neuropharmacodynamic attributes of an antiepileptic drug, lacosamide, in hepatic and renal impairment: Preclinical evidence. *ACS Chem Neurosci*, 8: 1589–1597.

   https://doi.org/10.1021/acschemneuro.7b00084

8. Cawello W, Boekens H, Bonn R, 2012, Absorption, disposition, metabolic fate and elimination of the anti-epileptic drug lacosamide in humans: Mass balance following intravenous and oral administration. *Eur J Drug Metab Pharmacokinet*, 37: 241–248.

https://doi.org/10.1007/s13318-012-0093-x

9. Schultz L, Mahmoud SH, 2020, Is therapeutic drug monitoring of lacosamide needed in patients with seizures and epilepsy? *Eur J Drug Metab Pharmacokinet*, 45: 315–349.

https://doi.org/10.1007/s13318-019-00601-8

10. Greenaway C, Ratnaraj N, Sander JW, *et al.,* 2010, A high-performance liquid chromatography assay to monitor the new antiepileptic drug lacosamide in patients with epilepsy. *Ther Drug Monit*, 32: 448–452.

https://doi.org/10.1097/FTD.0b013e3181dcc5fb

11. Valarmathi R, Banu SF, Akilandeswari S, 2013, A review on new antiepileptic drug-lacosamide and its analytical methods. *Int J Pham Chem Sci*, 2: 181–186.

12. Nazma S, Yasaswini M, Sai Supraja M, *et al.*, 2015, Development and validation of RP-HPLC method for the estimation of lacosamide in bulk and parenteral dosage form. *Int J Res Pharm Chem*, 5: 355–360.

13. Sreenivasulu V, Rao DR, Maheswar U, *et al.*, 2011, Development and validation of a stability-indicating RP-HPLC method for determination of lacosamide. *Res J Pharm Biol Chem Sci*, 2: 1–11.

14. United State Pharmacopeia, 2022, National Formulary 38 (USP 43/2019 NF 38)-General Chapter 621 Chromatography. Available from: https://www.usp.org/sites/default/files/usp/document/harmonization/gen-chapter/harmonization-november-2021-m99380.pdf [Last accessed on 2023 Jan 21].

15. USA Food and Drug Administration (FDA), 2018, Guidance for Industry Bioanalytical Method Validation. Available from: https://www.fda.gov/files/drugs/published/Bioanalytical-Method-Validation-Guidance-for-Industry.pdf [Last accessed on 2022 Jan 03].

16. International Conference on Harmonization: ICH Harmonized Tripartite Guideline, 2021, Q2 (R1) Validation of Analytical Procedures: Text and Metodology, Guidance for Industry. Available from: https://www.fda.gov/regulatory-information/search-fda-guidance-documents/q2r1-validation-analytical-procedures-text-and-methodology-guidance-industry [Last accessed on 2022 Sep 12].

17. Argentina ANMAT, 2013, Disposición 4394/2013 Buenas Prácticas de Laboratorio. https://www.argentina.gob.ar/normativa/nacional/disposici%C3%B3n-4394-2013-217492 [Last accessed on 2022 Sep 12].

18. R Core Team, 2018, R: A Language and Environment for Statistical Computing, R Foundation for Statistical Computing, Vienna, Austria. Available from: https://www.R-project.org/ [Last accessed on 2023 Mar 15].

19. Caballero RR, González RA, Lavaut JA, 1998, Propranolol y sus ésteres: Detección y resolución enantiomérica (Propranolol and its esters: detection and enantiomeric resolution). *Rev Cuba Farm*, 32: 130–139. (Article in Spanish)

20. Dong MH, 2019, HPLC and UHPLC for Practicing Scientists. 2nd ed. Hoboken NY: John Wiley and Sons, Inc.

21. Gonçalves J, Alves G, Bicker J, *et al.,* 2018, Development and full validation of an innovative HPLC-diode array detection technique to simultaneously quantify lacosamide, levetiracetam and zonisamide in human plasma. *Bioanalysis*, 10: 541–557.

https://doi.org/10.4155/bio-2017-0199

22. Kestelyn C, Lastelle M, Higuet N, *et al.*, 2011, A simple HPLC-UV method for the determination of lacosamide in human plasma. *Bioanalysis*, 3: 2515–2522.

https://doi.org/10.4155/bio.11.261

23. Lipecki Y, Haen E, 2022, Simultaneous quantification of 11 antiseizure medications and metabolites in serum for therapeutic drug monitoring using high-performance liquid chromatography with ultraviolet detection: A short communication. *Ther Drug Monit*, 44: 345–350.

https://doi.org/10.1097/FTD.0000000000000908

24. Carona A, Bicker J, Silva R, *et al.*, 2021, HPLC method for the determination of antiepileptic drugs in human saliva and its application in therapeutic drug monitoring. *J Pharm Biomed Anal*, 197: 113961.

https://doi.org/10.1016/j.jpba.2021.113961

25. Mohamed FA, Ali MF, Rageh AH, *et al.*, 2019, Highly sensitive UHPLC-DAD method for simultaneous determination of two synergistically acting antiepileptic drugs; levetiracetam and lacosamide: Application to pharmaceutical tablets and human urine. *Biomed Chromatogr*, 33: e4554.

https://doi.org/10.1002/bmc.4554

ACCSCIENCE PUBLISHING

Global Translational Medicine

ORIGINAL RESEARCH ARTICLE

Immediate onset signatures of autoimmune diseases after vaccination

Darrell O. Ricke*

Department of Research, Molecular BioInsights, Winchester, MA, 01890, USA

Abstract

Severe adverse events, including autoimmune diseases, have been noted in some individuals following vaccination. It is still unknown whether a subset of these autoimmune disease adverse events (ADAE) is triggered by the immunization and is not background chance occurrences. Only a small fraction of adverse events experienced by vaccinees has been reported to the Vaccine Adverse Event Reporting System (VAERS) database. In this study, ADAEs within VAERS are examined. The frequency of autoimmune disease adverse reactions reported immediately following vaccination was compared to the background population adverse event frequency. The frequency of immediate-onset autoimmune diseases, extracted from VAERS, arisen after vaccination was found to exceed the expected background occurrences. Vaccinees who receive a second COVID-19 mRNA vaccination dose 3 weeks after the first dose appear to experience an increased number of ADAE. Furthermore, human papillomavirus (HPV), hepatitis A, and hepatitis B vaccines exhibit distinctive patterns of associations with autoimmune diseases. The potential role of vaccine aluminum adjuvant, included in these vaccines, cannot be ruled out as contributing to ADAE. VAERS data illustrate immediate onset correlations for multiple autoimmune diseases across various vaccines. Autoimmune diseases immediate temporal onset associations that occur following COVID-19 mRNA and adenoviral vaccinations are predicted to occur with similar frequencies for all mRNA and adenoviral vaccines and therapeutics. Taken together, removal of aluminum adjuvants from HPV, hepatitis A, and hepatitis B vaccines, among others, should be considered in the effort to reduce the occurrence of immediate-onset autoimmune diseases.

Keywords: Autoimmune diseases; Vaccines; COVID-19 vaccines; Human papillomavirus vaccines; Hepatitis vaccines; Aluminum adjuvant

***Corresponding author:**
Darrell O. Ricke
(doricke@molecularbioinsights.com)

Citation: Ricke DO, 2023, Immediate onset signatures of autoimmune diseases after vaccination. *Global Transl Med,* 2(3): 1455.
https://doi.org/10.36922/gtm.1455

Received: August 8, 2023
Accepted: September 20, 2023
Published Online: September 29, 2023

1. Introduction

Adverse events following immunization (AEFI) occur with many vaccines. These events encompass adverse events caused by immunization as well as unrelated background occurrences. The likelihood of reporting them as AEFI decreases as the time between immunization and the onset of autoimmune disease increases, creating a time bias in reporting, with a decreasing pattern over time. Following immunization, autoimmune diseases occur at background population frequencies unrelated to the immunization itself. The number of background AEFIs should ideally be proportional to autoimmune disease population frequencies for each vaccine dose administered to vaccinees. This

can be calculated as the background rate multiplied by the number of days examined, with adjustments for reporting bias. The United States Vaccine Adverse Event Reporting System (VAERS) database collects AEFI reports[1], which represent a sample (i.e., subset) of the actual number of adverse events estimated by the underreporting factor (URF). Deviations from background population patterns in the VAERS data serve as indicators of relationships between immunization and the adverse event(s).

Possible associations between autoimmune diseases and immunization have been reported in several studies[2-4]. For example, Guillain-Barré syndrome (GBS) has been linked to influenza vaccination[5-7], narcolepsy to the 2009 H1N1 influenza vaccine[8], and immune thrombocytopenia (ITP) to various vaccinations[9-11]. In addition, multiple autoimmune diseases have been reported following COVID-19 vaccination[12-21]. Some researchers have explored the concept of autoimmune (auto-inflammatory) syndrome induced by adjuvants (ASIA), implicating adjuvants such as aluminum[22] and mercury. Watad *et al.*[23] have provided an overview of thyroid autoimmunity within the ASIA framework. However, it is important to note that other studies have found no significant associations between autoimmune diseases and vaccinations[24-26]. Detecting potential adverse events related to immunization amid a backdrop of background adverse events can lead to observations of both correlation and no correlations. Distinguishing possible adverse events triggered by immunization requires the identification of distinctive signals that set them apart from background adverse events. Possible signals may be overlooked as the number of days considered increases, potentially overshadowing association signals by extending the considered time frame and consequently elevating the expected number of background events.

In this study, VAERS data were examined to assess the relationships between autoimmune disease adverse events (ADAE) and vaccines. Varying frequencies of multiple immediate-onset autoimmune diseases were observed in response to different vaccines. These observed correlation patterns of immediate onset are inconsistent with the notion that these autoimmune diseases are solely background occurrences. Furthermore, an increase in reports of ADAE was observed in association with the second dose of the Pfizer-BioNTech COVID-19 mRNA vaccine (tozinameran, also known as BNT162b2/Comirnaty), occurring 3 weeks after the initial dose. Associations of vaccine platforms with numerous autoimmune diseases are apparent for both mRNA and adenoviral COVID-19 vaccines. When comparing unrelated vaccines, it is predicted that the likelihood of immediate autoimmune disease onset exceeds a certain threshold, particularly in individuals at risk, in proportion to the strength of immune system stimulation (e.g., vaccine reactogenicity[27]). Based on similar ADAE patterns observed for tozinameran (mRNA vaccine), Moderna mRNA-1273 elasomeran (mRNA vaccine), and Janssen Ad26.Cov2.S (adenoviral vaccine), it is predicted that the frequencies of ADAE observed for COVID-19 vaccines will be comparable across all mRNA and adenoviral vaccines and therapeutics in proportion to the level of stimulated immune system response. Understanding the etiology and relationships between ADAE and vaccines can inform strategies for minimizing the risk of ADAE occurrences. These strategies may include: (i) Extending the interval between immunizations within a dose series to at least 4 weeks (or longer), (ii) eliminating aluminum adjuvants and mercury excipients from vaccines, (iii) considering lower-reactogenicity alternatives to mRNA and adenoviral platforms, and so forth.

2. Materials and methods

2.1. VAERS data mining

The VAERS database underwent data mining to identify autoimmune adverse events, including: Acute disseminated encephalomyelitis, alopecia, ankylosing spondylitis, antiphospholipid syndrome, arthritis, autoimmune disorder, autoimmune hemolytic anemia, autoimmune hepatitis, autoimmune thyroiditis, Behcet's syndrome, Bell's palsy, chronic fatigue syndrome, chronic inflammatory demyelinating polyradiculoneuropathy, chronic lymphocytic leukemia, complex regional pain syndrome, Crohn's disease, dermatomyositis, diabetes mellitus, eczema, encephalitis autoimmune, endometriosis, erythema nodosum, giant cell arteritis, glomerulonephritis, granulomatosis with polyangiitis, GBS, Henoch-Schonlein purpura, hidradenitis, hypogammaglobulinaemia, idiopathic pulmonary fibrosis, IgA nephropathy, ITP, juvenile idiopathic fibrosis, Kawasaki's disease, Lichen planus, Lichen sclerosus, Lyme disease, Meniere's disease, Miller Fisher syndrome, mixed connective tissue disease, multiple sclerosis, multiple sclerosis relapse, myasthenia gravis, myositis, narcolepsy, neuromyelitis optica spectrum disorder, neutropenia, optic neuritis, pemphigus, polymyalgia rheumatica, polymyositis, postural orthostatic tachycardia syndrome, psoriasis, psoriatic arthropathy, Raynaud's phenomenon, restless legs syndrome, rheumatoid arthritis, sarcoidosis, scleritis, scleroderma, Sjogren's syndrome, Still's disease, systemic lupus erythematosus, Type 1 diabetes mellitus, Type 2 diabetes mellitus, uveitis, vasculitis, and vitiligo. The downloaded VAERS data include all adverse events reported from 1990 to May 19, 2023. The Ruby program, named vaers_slice2.rb[27,28], was used to tally selected reported vaccine adverse events based on vaccine type and the day of onset. The vaers_slice2.rb program takes a list of one or more adverse events for characterization,

summarizing them from the yearly VAERS Symptoms, Vax, Data files spanning from 1990 to 2023, and NonDomestic. The output generated by vaers_slice2.rb consists of six reports: Summaries categorized by vaccine, annual summaries, summaries based on the age of vaccinees, summaries categorized by day of symptom onset, which is further divided by (i) dose and gender and (ii) vaccine name/type, and two summaries covering additional reported symptoms (selected symptoms and all other symptoms). For tables and figures, adverse events associated with diphtheria, tetanus, and pertussis vaccines are combined under "DTAP/TDAP," influenza vaccines are consolidated as "FLU," hepatitis A and B vaccines are represented as "HEP," human papillomavirus (HPV) vaccines are grouped as "HPV," and pneumococcal vaccines are consolidated as "PNC." Microsoft Excel was used for creating figures.

2.2. AEFI

AEFI can be represented as the sum of two components: Immunization-associated adverse events (if any) and background occurrences of adverse events. These adverse events diminish due to reporting bias as the time since immunization increases. This relationship can be represented mathematically for a group of vaccinated people (P) by considering reporting bias (r_i) for the ith day post-immunization, the vaccine-associated adverse events reported on the ith day post-immunization (v_i), and the background rate of adverse events (b^X) for a single day (Equations I–III).

$$\text{Adverse events}(X) = AE^X = V^X + B^X \quad \text{(I)}$$

$$V^X = \sum_{i=0}^{n\,days} r_i\, v_i^X P \quad \text{(II)}$$

$$B^X = \sum_{i=0}^{n\,days} r_i\, b_i^X P \quad \text{(III)}$$

If immunization does not lead to any autoimmune adverse events (X), this simplifies to Equation IV:

$$\text{Adverse events}(X) = B^X = \sum_{i=0}^{n\,days} r_i b^X P \quad \text{(IV)}$$

The first 24 h following vaccination can be examined to derive the term v_0^X (Equations V and VI):

$$\text{Adverse events}(\text{X within 24 h}) = AE_0^X = r_0(v_0^X + b^X)P \quad \text{(V)}$$

Immunization-associated adverse events (X) become detectable when $v_0^X > 0$ (when the number of adverse events exceeds the background rate within the first 24 h of immunization). By comparing the frequency of reports of common adverse events in the clinical trial(s) to the frequency of VAERS reports, valuable insights into the values of reporting bias (r_i) can be gained.

2.3. VAERS URF estimate

By June 1, 2023, COVID-19 vaccine doses administered included 366,979,906 tozinameran, 232,147,784 elasomeran, and 19,007,537 Ad26.Cov2.S. Considering 898,860 common adverse events reported in VAERS, with an average of 35% (combining averages of 47.4% and 22.8% for fatigue after doses 1 and 2) of vaccinees experiencing headache, fatigue, pyrexia, chills, and/or pain, the estimation of VAERS underreporting is represented in Equation VII and subsequently applied in Equation VIII:

$$UDF_{common\ AEs\%} = \frac{\text{Vaccine doses} * (\text{faction common adverse events})}{\text{VAERS common adverse events}} \quad \text{(VII)}$$

$$UDF_{35\%} = \frac{617{,}135{,}227\ \text{doses} * 0.35}{898{,}860} = 241 \quad \text{(VIII)}$$

3. Results

3.1. VAERS data mining results

Reports from Vaers_slice2.rb were generated for selected autoimmune diseases in VAERS, and Figures 1 and 2 illustrate ADAEs for vaccines with the highest reported cases by day of onset.

The vaccine types associated with the highest number of multiple ADAE reported are summarized in Table S1. Comparisons of the frequency of vaccine-associated ADAE to background rate estimates are found in Table S2. Regarding COVID-19 ADAEs, VAERS includes reports of ADAE for two different types of vaccines: mRNA (elasomeran and tozinameran) and adenoviral (Ad26.Cov2.S). The contributions of ADAE by individual COVID-19 vaccines are illustrated in Table 1. For GBS, Ad26.Cov2.S represents 3.1% of the vaccine doses administered but accounts for 16.2% of the GBS-related adverse events reported — 91 expected based on elasomeran and tozinameran ([657 + 2,200]/0.97 = 91) but 554 GBS ADAEs were reported (Table 1). The initial immunization of COVID-19 mRNA vaccines involved a two-dose series, with 3 weeks (tozinameran) and 4 weeks (elasomeran) between doses. The ratio of autoimmune adverse events when comparing dose 2 to dose 1 for these COVID-19 vaccines is presented in Figure 3.

4. Discussion

Numerous articles have suggested potential associations between immunization and autoimmune diseases[2-21],

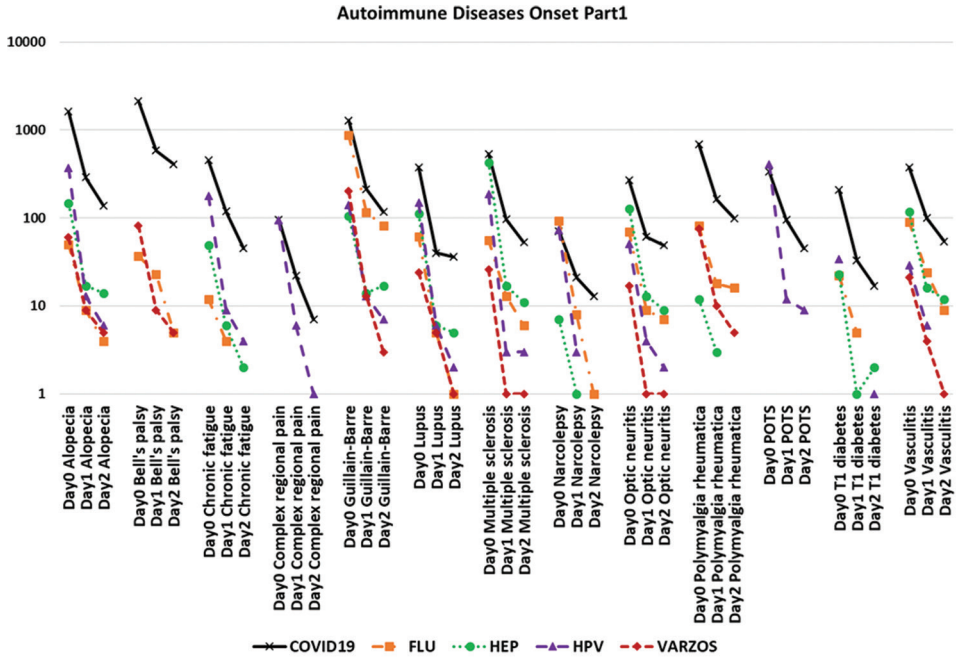

Figure 1. Day of onset of autoimmune diseases after administration of selected vaccines (1 of 2). Vaccine labels: COVID-19: COVID-19 vaccines; FLU: Influenza vaccines; HEP: Hepatitis A and hepatitis B vaccines; HPV: Human papillomavirus; VARZOS: Varicella-zoster vaccines. Autoimmune disease labels: Lupus: Systemic lupus erythematosus; POTS: Postural orthostatic tachycardia syndrome.

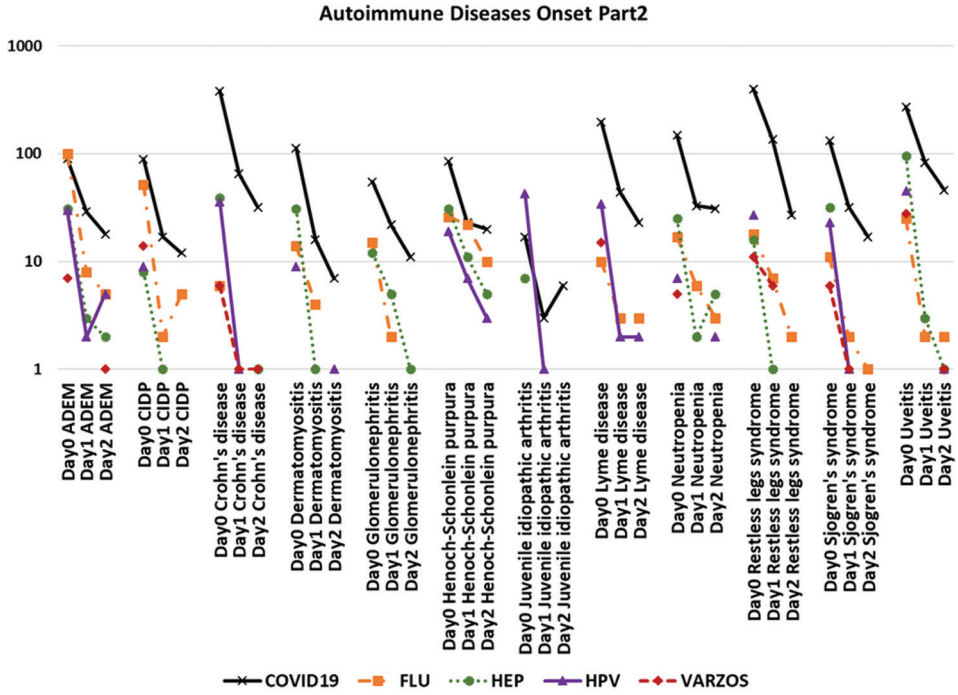

Figure 2. Day of onset of autoimmune diseases after administration of selected vaccines (2 of 2). Vaccine labels: COVID-19: COVID-19 vaccines; FLU: Influenza vaccines; HEP: Hepatitis A and hepatitis B vaccines; HPV: Human papillomavirus; VARZOS: Varicella-zoster vaccines. Autoimmune disease labels: ADEM: Acute disseminated encephalomyelitis; CIDP: Chronic inflammatory demyelinating polyneuropathy.

while other opposing articles contend that no such associations can be detected[24-26]. When considering any immunization, the number of adverse events (AE^X), if there are any vaccine-caused adverse events (V^X) in a

Table 1. Autoimmune adverse events and doses by COVID-19 vaccine. VAERS data include adverse event reports from 1990 to May 19, 2023

Adverse event	COVID-19 Ad26.Cov2.S	COVID-19 elasomeran	COVID-19 tozinameran
Administered doses	19,007,537 (3.1%)	232,147,784 (37.6%)	366,979,906 (59.4%)
Alopecia	220 (5.5%)	1,174 (29.6%)	2,570 (64.8%)
Arthritis	204 (4.9%)	1,277 (30.6%)	2,692 (64.5%)
Bell's palsy	343 (4.7%)	1,981 (27.1%)	4,980 (68.2%)
Guillain-Barré syndrome	554 (16.2%)	657 (19.3%)	2,200 (64.5%)
Immune thrombocytopenia	108 (6.6%)	383 (23.3%)	1,155 (70.2%)
Rheumatoid arthritis	109 (3.2%)	824 (24.4%)	2,443 (72.4%)

Note: The percentages in parentheses represent the proportion of this adverse event by vaccine.

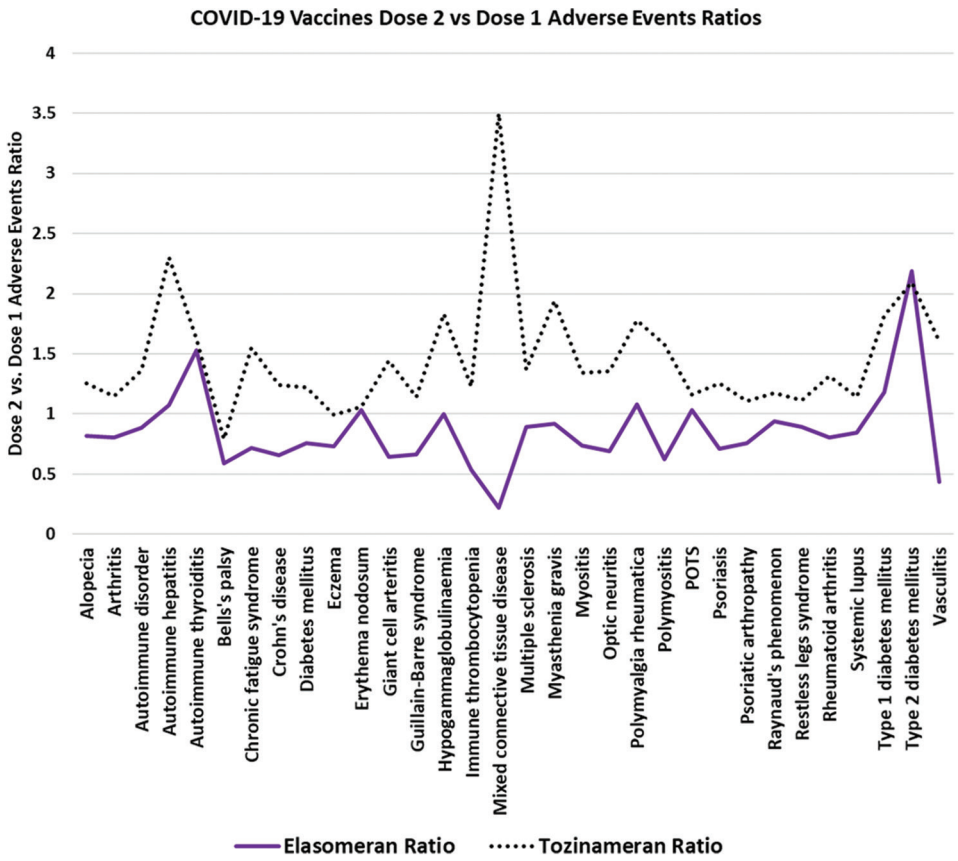

Figure 3. The autoimmune disease adverse event ratios after COVID-19 vaccines dose 2 versus dose 1 administration. Labels of autoimmune diseases: POTS: Postural orthostatic tachycardia syndrome.

population sample, remains constant. However, the sum of background adverse events (B^X) is proportional to the number of days considered. Hence, it is always possible to find no associations by increasing the number of days examined (e.g., by selecting a timespan where $B^X > V^X$ since V^X remains constant while B^X increases with time).

Following immunizations, the occurrence of autoimmune diseases is expected to align with population background rates unrelated to immunization. Any autoimmune diseases resulting from immunization are in addition to these background events. Vaccines with the highest ADAEs in VAERS are summarized in Table S1 and Figures 1 and 2. Following immunization, ADAE reports are anticipated to decrease over time, a phenomenon referred to as reporting bias. Most ADAE reports in VAERS indicate symptom onset within 24 h of immunization (Figures 1 and 2, Table S2).

Table S2 illustrates reporting bias values (r_0) of 1/20 and 1/40; however, based on the frequency of VAERS reports related to common adverse events of COVID-19 vaccines, the r_0 (URF) for these vaccines (Equation VIII) could be closer to 1/241. If r_0 is indeed close to 1/241, then many of the detected COVID-19 ADAEs (Table S1) hold significant.

Primary and secondary humoral immune responses, with the amplification of B-cell antibodies, increase over a period of multiple days (peaking around 7- – 11-day post-immunization). Observed ADAEs (Table S1) that occur within 24 h after immunization cannot be attributed to either primary or secondary humoral immune responses (the immediate timespan is inconsistent with humoral immune responses). Immediate ADAEs are more consistent with the hypothesis of autoimmune disease threshold being exceeded due to immune dysregulation on a rapid timescale post-immunization.

4.1. COVID-19 mRNA and adenoviral vaccines

Most COVID-19 vaccines available on the market are the novel mRNA and adenoviral vaccines, and both of these vaccine platforms have been associated with multiple ADAE (Table 1). For both Ad26.Cov2.S and tozinameran vaccines, the percentage of associated ADAE is higher than the elasomeran vaccine. For instance, for the Ad26.Cov2.S vaccine, GBS accounts for 16.2% of the adverse events but represents only 3.1% of the COVID-19 vaccine doses (Table 1). All three of these COVID-19 vaccines contribute to the combined COVID-19 results reported in Table S1. Of particular note is the high percentage of Bell's palsy occurrence when compared to other vaccines (Table S1). In comparison to widely provided vaccines like influenza and others, COVID-19 immunizations show a broad association with many autoimmune diseases (Table S1). Furthermore, high percentages of these ADAEs are reported within 24 h of immunization (Table S1).

The timing of mRNA vaccine doses appears to be important for ADAE onset (Figure 3). Specifically, the tozinameran mRNA COVID-19 vaccine exhibits a higher number of ADAE reports for 30 out of 32 autoimmune adverse events for dose 2 compared to dose 1, with a ratio >1.0. In 29 of these cases, the ratio >1.1, with Bell's palsy being the only exception (ratio = 0.79) (Figure 3). On the other hand, the elasomeran mRNA COVID-19 vaccine shows seven vaccines with ratios >1.0 and three vaccines >1.1. Notably, the elasomeran vaccine contained 100 micrograms of mRNA, with 4 weeks between the first and second vaccine doses, whereas the tozinameran vaccine contained 30 μg of mRNA, with only 3 weeks between the first and second vaccine doses. The higher ADAE ratios observed for the tozinameran vaccine compared to elasomeran vaccines (Figure 3) suggest that increasing the time between first and second doses for this vaccine to at least 4 weeks or longer would likely decrease the dose 2 to dose 1 ratio, as observed in Figure 3. This extended interval is predicted to help mitigate higher non-specific amplification observed for the tozinameran COVID-19 vaccine when the second dose is administered just 3 weeks after the first dose (Figure 3).

These COVID-19 vaccines appear to induce immediate-onset ADAEs, which are consistent with subsets of at-risk vaccinees exceeding the disease onset thresholds for a broad spectrum of autoimmune diseases (Table S1). Based on the onset data reported in VAERS, the highest risks appear to be immediately post-immunization, especially for at-risk vaccinees. By design, both mRNA and adenoviral vaccine platforms elicit high levels of expression of the SARS-CoV-2 spike protein, which is foreign to the immune systems, effectively stimulating strong immune responses. COVID-19 ADAEs associated with 33 autoimmune diseases/groups are summarized in Table S1. The observed patterns of immediate-onset frequencies, common to all ADAEs (Figures 1 and 2, Table S1), suggest the possibility of unintended immune responses triggering these ADAEs. These frequency patterns are consistent with the hypothesis of bystander or polyclonal activation but not epitope molecular mimicry[2] (as there is insufficient time for adaptive immune responses to vaccine epitopes). Note that Guo *et al.*[15] have considered molecular mimicry, adjuvants, and bystander activation. In examining the etiology of COVID-19 vaccine ADAEs, Table S1 presents data on 33 different autoimmune diseases with immediate onset, indicating an immediate effect rather than a direct result of the expressed spike protein or possible shared epitopes. Differences in age distributions among vaccinees for selected autoimmune diseases are illustrated in Figure 4. The demographic characteristics of individuals experiencing these ADAEs are consistent with the amplification of pre-existing mechanisms, especially for individuals at higher risk of developing these autoimmune diseases. For instance, polymyalgia rheumatica, one of the COVID-19 ADAEs, is predominantly reported in older adults[29] (Figure 4).

4.2. HPV vaccines

The HPV vaccines contain aluminum as an adjuvant[3]. While aluminum has a long history of use in vaccines, it is also associated with neurotoxicity[3,22]. In mice, macrophages have been shown to transport aluminum to lymph nodes, spleen, liver, and brain[30]. Regarding the correlation of HPV vaccines with adverse events, it is noteworthy that temporal onset correlations exist with multiple ADAEs (Table S1). Among these, the ADAEs with

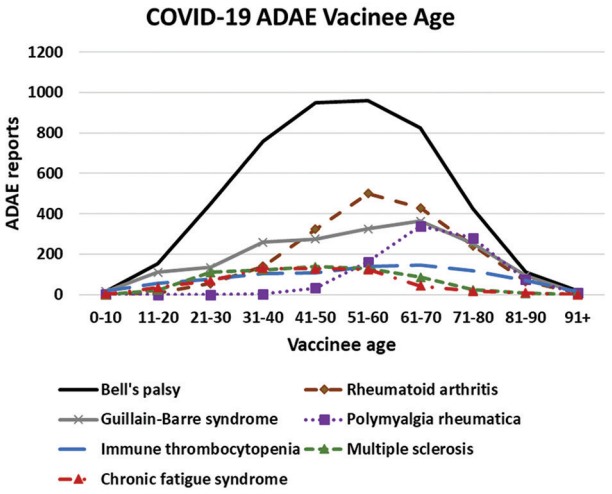

Figure 4. The age of COVID-19 vaccinees experiencing various autoimmune disease adverse events.

the highest descending order of correlations, expressed as a percentage of common adverse events, include postural orthostatic tachycardia syndrome (POTS) (1.91%), alopecia (1.72%), multiple sclerosis (0.87%), chronic fatigue syndrome (0.83%), systemic lupus erythematosus (0.70%), GBS (0.59%), narcolepsy (0.34%), complex regional pain syndrome (0.30%), arthritis (0.30%), optic neuritis (0.24%), rheumatoid arthritis (0.22%), uveitis (0.21%), eczema (0.21%), juvenile idiopathic arthritis (0.20%), Raynaud's phenomenon (0.20%), restless legs syndrome (0.20%), Crohn's disease (0.17%), Type 1 diabetes mellitus (0.16%), autoimmune thyroiditis (0.15%), acute disseminated encephalomyelitis (0.14%), vasculitis (0.14%), Lyme disease (0.13%), and Sjogren's syndrome (0.11%) (Table S1). Furthermore, it is important to highlight that multiple ADAEs manifest with neurological implications. Multiple autoimmune diseases have been reported in case reports following HPV immunization, including POTS[31], systemic lupus erythematous[32], myasthenia gravis[33], complex regional pain syndrome (CRPS)[34], arthritis and rheumatoid arthritis[32], uveitis[35], vasculitis[36], and pseudoneurological syndrome[37]. In addition, antinuclear antibodies were found to be enriched in patients with autoimmune-like symptoms following HPV vaccination[38]. The ADAEs associated with HPV vaccination present as non-random signals higher than the expected background ADAEs (Table S2). Several of these ADAEs, such as POTS, multiple sclerosis, chronic fatigue syndrome, systemic lupus erythematous, GBS, narcolepsy, CRPS, optic neuritis, restless legs syndrome, acute disseminated encephalomyelitis, and myasthenia gravis, are neurological in nature. This raises concerns given that HPV vaccines include the aluminum adjuvant, which is known to be neurotoxic[3,22]. To date, other possible components within HPV vaccine contributing to the etiology of these neurological adverse events have not been identified. It is a clinically testable hypothesis that reducing or eliminating the aluminum adjuvant from HPV vaccines might mitigate or eliminate these ADAEs. The observed ADAEs associated with HPV vaccine exhibit a unique pattern, which does share some similarities with those linked to hepatitis A and B (HEP) vaccines.

4.3. Hepatitis A and B vaccines

Similar to HPV vaccines, HEP vaccines also contain aluminum as an adjuvant[39]. The highest frequencies of ADAEs associated with HEP vaccines, expressed as a percentage of common adverse events, include multiple sclerosis (1.18%), arthritis (0.73%), rheumatoid arthritis (0.43%), alopecia (0.40%), optic neuritis (0.35%), vasculitis (0.32%), systemic lupus erythematosus (0.31%), GBS (0.29%), eczema (0.27%), uveitis (0.27%), chronic fatigue syndrome (0.14%), and more (Table S1). Furthermore, there have been case reports of multiple autoimmune diseases following HPV immunization[40], encompassing conditions such as arthritis and rheumatoid arthritis[41,42], alopecia[43], optic neuritis[44,45], vasculitis[46,47], systemic lupus erythematosus[48], and GBS[49]. In addition, there was a previous report suggesting a potential association between the hepatitis B vaccine and multiple sclerosis[50], although it was subsequently found to have a strong family history of multiple sclerosis, with an overrepresentation of the HLA-DR2 antigen (as reviewed in Pordeus *et al.*[51]). The frequency pattern of ADAEs for HEP vaccines appears different from that of ADAEs for HPV vaccines (Table S1), possibly implicating aluminum[22] in combination with additional factors contributing to the etiologies of ADAEs associated with these vaccines. Similar to HPV vaccines, the presence of multiple sclerosis, optic neuritis, systemic lupus erythematosus, GBS, and chronic fatigue syndrome as ADAEs establishes a set of neurological ADAEs associated with HEP vaccines. Moreover, like HPV vaccines, HEP vaccines also incorporate aluminum as an adjuvant. Therefore, it is plausible that to consider the reduction or elimination of aluminum from HEP vaccines as clinically testable approach to potentially reduce the occurrence of neurological and other ADAEs associated with HEP vaccines.

4.4. Influenza, pneumococcal, and varicella-zoster vaccines

Influenza displays the strongest association with GBS[5-7]. Moreover, GBS appears to be associated with multiple vaccines, including HPV, varicella-zoster, HEP, and others (Tables S1 and S3). The pneumococcal (PNC) vaccine demonstrates significant associations with eczema,

Kawasaki disease, neutropenia, and GBS (Table S1). In the case of influenza, there is a possibility of slight epitope molecular mimicry, which may be more pronounced for specific influenza strain protein(s) included within yearly vaccines. However, for other vaccines, the associations with GBS might align more with the hypothesis of bystander or polyclonal activation, and the likelihood of epitope molecular mimicry appears lower. In addition to the PNC vaccine (0.43%), 6VAX-F (diphtheria and tetanus toxoids and acellular pertussis absorbed + inactivated poliovirus + hepatitis B + Haemophilus B conjugate vaccine) (1.78%), RV (rotavirus vaccine) (0.83%), MENB (meningococcal group B, rDNA absorbed vaccine) (0.69%), and HIBV (*Haemophilus influenzae* Type B vaccine) (0.23%) vaccines exhibit significant temporal onset associations with adverse events related to Kawasaki disease (Table S3). Despite the unknown etiology of Kawasaki disease, the observed associations with multiple vaccines represent unexpected observations. One proposed hypothesis suggests that high-titer antibodies capable of activating mast cells may play a key role in the etiology of Kawasaki disease[52,53]. It is plausible that immunizations for these vaccines may activate mast cells due to the high titers of immunization-stimulated antibodies binding to vaccine antigens. Consequently, therapeutic approaches targeting activated mast cells may hold promise for patients experiencing vaccine-associated Kawasaki disease[52,53].

4.5. Patients with pre-existing autoimmune diseases

Immunosuppressed individuals and those with autoimmune diseases are advised to consult with licensed medical professional regarding suitable vaccine candidates. It is important to note that live-attenuated vaccines are not recommended for patients with autoimmune inflammatory rheumatic diseases, especially those who are immunosuppressed[54]. In the work of Frasca *et al.*[55], there is a debate concerning the necessity of COVID-19 vaccines for individuals with autoimmune diseases as well as for the general population. It is worth highlighting that impaired immunogenicity to COVID-19 vaccines has been reported in individuals with autoimmune systemic diseases[56], although there have been reports of vaccine efficacy in patients with autoimmune hepatitis[57]. In the consideration of candidate treatments, relevant information needs to be provided to ensure that informed consent requirements have been met while carefully weighing the risks against the benefits.

4.6. Study limitations

This study is based on adverse events reported to the VAERS database, which are considered a subset of all adverse events experienced by vaccinees. Any reporting biases or exclusion of reported adverse events would perturb the accuracy of VAERS in representing the immunized populations. By comparing the relative proportions of adverse events with large clinical trial datasets, we can detect possible perturbations in the VAERS dataset.

4.7. Study recommendations

The risks associated with developing autoimmune diseases following vaccinations may be mitigated through the following measures: (i) Evaluating alternative vaccine and therapeutic platforms to either avoid or minimize the use of mRNA and adenoviral platforms, and (ii) increasing the time between mRNA vaccine doses to 4 weeks or longer, and perhaps (iii) removing aluminum adjuvants and mercury excipients from vaccines.

5. Conclusion

Autoimmune diseases appear to be triggered by specific vaccines in some vaccinees (COVID-19 vaccine: alopecia, Bell's palsy, chronic fatigue syndrome, CRPS, GBS, Henoch-Schonlein purpura, ITP, myositis, multiple sclerosis, narcolepsy, optic neuritis, POTS, rheumatoid arthritis, systemic lupus erythematosus, and Type 1 diabetes mellitus. Influenza vaccine: GBS [already known]. HEP vaccine: Alopecia, chronic fatigue syndrome, GBS, multiple sclerosis, optic neuritis, systemic lupus erythematosus, and vasculitis. HPV vaccine: alopecia, chronic fatigue syndrome, CRPS, GBS, multiple sclerosis, narcolepsy, optic neuritis, POTS, and systemic lupus erythematosus. PNC vaccine: GBS, Kawasaki disease, and neutropenia. Vericella-zoster vaccine: Bell's palsy, GBS, and rheumatoid arthritis. Refer to Table S2. The study reveals specific temporal onset correlations of ADAEs for multiple vaccines (Figures 1 and 2, Table S1). Both mRNA and adenoviral COVID-19 vaccine platforms appear to non-specifically increase the occurrence of ADAEs associated with multiple autoimmune diseases (Table S1). Increasing the time between initial COVID-19 mRNA shots to at least 4 weeks is likely to mitigate the observed increase in ADAEs for tozinameran (Figure 3). It is important to note that increased non-specific ADAEs are not observed for all other vaccines. These well-established platforms may offer safer alternatives for COVID-19 vaccination with respect to ADAEs. HEP and HPV vaccines, on the other hand, appear to induce specific patterns of ADAEs, with aluminum being a common adjuvant to both vaccines. The removal of aluminum adjuvants from HPV vaccines, HEP vaccines, and potentially other vaccines may reduce the frequency of ADAEs. Adhering to the principle of informed consent and the disclosure of information, it is advisable to provide ADAE risk notifications for COVID-19, HPV, HEP, and other vaccines.

ADAEs associated with Kawasaki disease have been observed in relation to multiple vaccines (PNC, 6VAX-F, RV, MENB, and HIBV). These observations suggest a potential link between immunization-stimulated antibodies and the activation of mast cells. It concludes by proposing a further investigation into therapeutics targeting mast cell activation for Kawasaki disease patients.

Acknowledgments

None.

Funding

None.

Conflict of interest

The author declares that he/she has no competing interests.

Author contributions

This is a single-authored article.

Ethics approval and consent to participate

Not applicable.

Consent for publication

Not applicable.

Availability of data

The vaers_slice2.rb reports are available here: Ricke D, 2023, "ADAE Post Vaccination", Harvard Dataverse, V1, https://doi.org/10.7910/DVN/EROCQQ.

References

1. VAERS, 2023, Vaccine Adverse Event Reporting System. U.S. Department of Health and Human Services. Available from: https://vaers.hhs.gov/data/datasets.html [Last accessed on 2023 Aug 08].
2. Vadalà M, Poddighe D, Laurino C, *et al*., 2017, Vaccination and autoimmune diseases: Is prevention of adverse health effects on the horizon? *EPMA J*, 8: 295–311.
   https://doi.org/10.1007/s13167-017-0101-y
3. Guimarães LE, Baker B, Perricone C, *et al*., 2015, Vaccines, adjuvants and autoimmunity. *Pharmacol Res*, 100: 190–209.
   https://doi.org/10.1016/j.phrs.2015.08.003
4. Seida I, Seida R, Elsalti A, *et al*., 2023, Vaccines and autoimmunity-from side effects to ASIA syndrome. *Medicina* (*Kaunas*), 59: 364.
   https://doi.org/10.3390/medicina59020364
5. Babazadeh A, Afshar ZM, Javanian M, *et al*., 2019, Influenza vaccination and Guillain-Barré syndrome: Reality or fear. *J Transl Int Med*, 7: 137–142.
   https://doi.org/10.2478/jtim-2019-0028
6. Sencer D, Millar JD, 2006, Reflections on the 1976 swine flu vaccination program. *Emerg Infect Dis J*, 12: 29–33.
   https://doi.org/10.3201/eid1201.051007
7. Vellozzi C, Iqbal S, Broder K, 2014, Guillain-Barré syndrome, influenza, and influenza vaccination: The epidemiologic evidence. *Clin Infect Dis*, 58: 1149–1155.
   https://doi.org/10.1093/cid/ciu005
8. Ahmed SS, Schur PH, MacDonald NE, *et al*., 2014, Narcolepsy, 2009 A(H1N1) pandemic influenza, and pandemic influenza vaccinations: What is known and unknown about the neurological disorder, the role for autoimmunity, and vaccine adjuvants. *J Autoimmun*, 50: 1–11.
   https://doi.org/10.1016/j.jaut.2014.01.033
9. David P, Shoenfeld Y, 2020, ITP following vaccination. *Int J Infect Dis*, 99: 243–244.
   https://doi.org/10.1016/j.ijid.2020.07.085
10. Black C, Kaye JA, Jick H, 2003, MMR vaccine and idiopathic thrombocytopaenic purpura. *Br J Clin Pharmacol*, 55: 107–111.
    https://doi.org/10.1046/j.1365-2125.2003.01790.x
11. Jin CQ, Dong HX, Sun ZX, *et al*., 2013, Acute immune thrombocytopenic purpura as adverse reaction to oral polio vaccine (OPV). *Hum Vaccin Immunother*, 9: 1739–1740.
    https://doi.org/10.4161/hv.24847
12. Chen Y, Xu Z, Wang P, *et al*., 2022, New-onset autoimmune phenomena post-COVID-19 vaccination. *Immunology*, 165: 386–401.
    https://doi.org/10.1111/imm.13443
13. May Lee M, Bertolani M, Pierobon E, *et al*., 2022, Alopecia areata following COVID-19 vaccination: Vaccine-induced autoimmunity? *Int J Dermatol*, 61: 634–635.
    https://doi.org/10.1111/ijd.16113
14. Rossini A, Cassibba S, Perticone F, *et al*., 2023, Increased prevalence of autoimmune thyroid disease after COVID-19: A single-center, prospective study. *Front Endocrinol* (*Lausanne*), 14: 1126683.
    https://doi.org/10.3389/fendo.2023.1126683
15. Guo M, Liu X, Chen X, *et al*., 2023, Insights into new-onset autoimmune diseases after COVID-19 vaccination. *Autoimmun Rev*, 22: 103340.
    https://doi.org/10.1016/j.autrev.2023.103340
16. Ishay Y, Kenig A, Tsemach-Toren T, *et al*., 2021, Autoimmune phenomena following SARS-CoV-2 vaccination. *Int Immunopharmacol*, 99: 107970.

https://doi.org/10.1016/j.intimp.2021.107970

17. Ruggeri RM, Giovanellla L, Campennì A, 2022, SARS-CoV-2 vaccine may trigger thyroid autoimmunity: Real-life experience and review of the literature. *J Endocrinol Invest*, 45: 2283–2289.

https://doi.org/10.1007/s40618-022-01863-x

18. Pujol A, Gómez LA, Gallegos C, *et al*., 2022, Thyroid as a target of adjuvant autoimmunity/inflammatory syndrome due to mRNA-based SARS-CoV2 vaccination: From Graves' disease to silent thyroiditis. *J Endocrinol Invest*, 45: 875–882.

https://doi.org/10.1007/s40618-021-01707-0

19. Elrashdy F, Tambuwala MM, Hassan SS, *et al*., 2021, Autoimmunity roots of the thrombotic events after COVID-19 vaccination. *Autoimmun Rev*, 20: 102941.

https://doi.org/10.1016/j.autrev.2021.102941

20. Rodríguez Y, Rojas M, Beltrán S, *et al*., 2022, Autoimmune and autoinflammatory conditions after COVID-19 vaccination. New case reports and updated literature review. *J Autoimmun*, 132: 102898.

https://doi.org/10.1016/j.jaut.2022.102898

21. Kaulen LD, Doubrovinskaia S, Mooshage C, *et al*., 2022, Neurological autoimmune diseases following vaccinations against SARS-CoV-2: A case series. *Eur J Neurol*, 29: 555–563.

https://doi.org/10.1111/ene.15147

22. Shaw CA, Tomljenovic L, 2013, Aluminum in the central nervous system (CNS): Toxicity in humans and animals, vaccine adjuvants, and autoimmunity. *Immunol Res*, 56: 304–316.

https://doi.org/10.1007/s12026-013-8403-1

23. Watad A, David P, Brown S, *et al*., 2017, Autoimmune/inflammatory syndrome induced by adjuvants and thyroid autoimmunity. *Front Endocrinol* (*Lausanne*), 7: 150.

https://doi.org/10.3389/fendo.2016.00150

24. Willame C, Dodd C, van der Aa L, *et al*., 2021, Incidence rates of autoimmune diseases in European healthcare databases: A contribution of the ADVANCE project. *Drug Saf*, 44: 383–395.

https://doi.org/10.1007/s40264-020-01031-1

25. Willame C, Rosillon D, Zima J, *et al*., 2016, Risk of new onset autoimmune disease in 9-to 25-year-old women exposed to human papillomavirus-16/18 AS04-adjuvanted vaccine in the United Kingdom. *Hum Vaccin Immunother*, 12: 2862–2871.

https://doi.org/10.1080/21645515.2016.1199308

26. Angelo MG, David MP, Zima J, *et al*., 2014, Pooled analysis of large and long-term safety data from the human papillomavirus-16/18-AS04-adjuvanted vaccine clinical trial programme. *Pharmacoepidemiol Drug Saf*, 23: 466–479.

https://doi.org/10.1002/pds.3554

27. Ricke DO, 2022, Etiology model for many vaccination adverse reactions, including SARS-CoV-2 spike vaccines. *AIMS Allergy Immunol*, 6: 200–215.

https://doi.org/10.3934/allergy.2022015

28. Ricke DO, 2023, VAERS-tools. Available from: https://github.com/doricke/vaers-tools [Last accessed on 2023 Aug 08].

29. Michet CJ, Matteson EL, 2008, Polymyalgia rheumatica. *BMJ*, 336: 765–769.

https://doi.org/10.1136/bmj.39514.653588.80

30. Gherardi RK, Authier FJ, 2012, Macrophagic myofasciitis: Characterization and pathophysiology. *Lupus*, 21: 184–189.

https://doi.org/10.1177/0961203311429557

31. Tomljenovic L, Colafrancesco S, Perricone C, *et al*., 2014, Postural orthostatic tachycardia with chronic fatigue after HPV vaccination as part of the "autoimmune/auto-inflammatory syndrome induced by adjuvants": Case report and literature review. *J Investig Med High Impact Case Rep*, 2(1).

https://doi.org/10.1177/2324709614527812

32. Anaya JM, Reyes B, Perdomo-Arciniegas AM, *et al*., 2015, Autoimmune/auto-inflammatory syndrome induced by adjuvants (ASIA) after quadrivalent human papillomavirus vaccination in Colombians: A call for personalised medicine. *Clin Exp Rheumatol*, 33: 545–548.

33. Chung JY, Lee SJ, Shin BS, *et al*., 2018, Myasthenia gravis following human papillomavirus vaccination: A case report. *BMC Neurol*, 18: 222.

https://doi.org/10.1186/s12883-018-1233-y

34. Kinoshita T, Abe RT, Hineno A, *et al*., 2014, Peripheral sympathetic nerve dysfunction in adolescent Japanese girls following immunization with the human papillomavirus vaccine. *Intern Med*, 53: 2185–2200.

https://doi.org/10.2169/internalmedicine.53.3133

35. Kong K, Ding X, Ni Y, 2022, Resolution of Harada disease-like uveitis after quadrivalent human papillomavirus vaccination: A case report. *Hum Vaccin Immunother*, 18: 1–4.

https://doi.org/10.1080/21645515.2021.1953349

36. Gomes SM, Glover M, Malone M, *et al*., 2013, Vasculitis following HPV immunization. *Rheumatology* (*Oxford*), 52: 581–582.

https://doi.org/10.1093/rheumatology/kes168

37. Poddighe D, Castelli L, Marseglia GL, *et al*., 2014, A sudden onset of a pseudo-neurological syndrome after HPV-16/18 AS04-adjuvated vaccine: Might it be an autoimmune/inflammatory syndrome induced by adjuvants (ASIA) presenting as a somatoform disorder? *Immunol Res*, 60: 236–246.

https://doi.org/10.1007/s12026-014-8575-3

38. Mehlsen J, Brinth L, Pors K, *et al*., 2022, Autoimmunity in patients reporting long-term complications after exposure to human papilloma virus vaccination. *J Autoimmun*, 133: 102921.

https://doi.org/10.1016/j.jaut.2022.102921

39. CDC, 2023, Vaccine Excipient Summary. Available from: https://www.cdc.gov/vaccines/pubs/pinkbook/downloads/appendices/b/excipient-table-2.pdf [Last accessed on 2023 Aug 08].

40. Geier DA, Geier MR, 2005, A case-control study of serious autoimmune adverse events following hepatitis B immunization. *Autoimmunity*, 38: 295–301.

https://doi.org/10.1080/08916930500144484

41. Gross K, Combe C, Krüger K, *et al*., 1995, Arthritis after hepatitis B vaccination. Report of three cases. *Scand J Rheumatol*, 24: 50–52.

https://doi.org/10.3109/03009749509095156

42. Rahimi SS, Ostrov BE, Lopez-Pena M, 2021, Inflammatory arthritis following hepatitis B vaccination in an infant. *Case Rep Rheumatol*, 2021: 5598217.

https://doi.org/10.1155/2021/5598217

43. Wise RP, Kiminyo KP, Salive ME, 1997, Hair loss after routine immunizations. *JAMA*, 278: 1176–1178.

https://doi.org/10.1001/jama.1997.03550140068042

44. Erguven M, Guven S, Akyuz U, *et al*., 2009, Optic neuritis following hepatitis B vaccination in a 9-year-old girl. *J Chin Med Assoc*, 72: 594–597.

https://doi.org/10.1016/S1726-4901(09)70435-6

45. Sudarshan S, Huang EH, Lim PL, *et al*., 2012, A case of post-vaccination optic neuritis: Coincidence or causative? *Eye* (*Lond*), 26: 1498.

https://doi.org/10.1038/eye.2012.146

46. Cockwell P, Allen MB, Page R, 1990, Vasculitis related to hepatitis B vaccine. *BMJ*, 301: 1281.

https://doi.org/10.1136/bmj.301.6763.1281-b

47. Awad MH, El-Hawary A, Sawah G, *et al*., 2021, Pan-vasculitis and fulminant hepatitis following routine vaccination at the age of 4 months. *Clin Exp Vaccine Res*, 10: 78–80.

https://doi.org/10.7774/cevr.2021.10.1.78

48. Finielz P, Lam-Kam-Sang LF, Guiserix J, 1998, Systemic lupus erythematosus and thrombocytopenic purpura in two members of the same family following hepatitis B vaccine. *Nephrol Dial Transplant*, 13: 2420–2421.

https://doi.org/10.1093/ndt/13.9.2420

49. Blumenthal D, Prais D, Bron-Harlev E, *et al*., 2004, Possible association of Guillain-Barré syndrome and hepatitis A vaccination. *Pediatr Infect Dis J*, 23: 586–588.

https://doi.org/10.1097/01.inf.0000130941.72712.33

50. Tourbah A, Gout O, Liblau R, *et al*., 1999, Encephalitis after hepatitis B vaccination: Recurrent disseminated encephalitis or MS? *Neurology*, 53: 396–401.

https://doi.org/10.1212/WNL.53.2.396

51. Pordeus V, Szyper-Kravitz M, Levy RA, *et al*., 2008, Infections and autoimmunity: A panorama. *Clin Rev Allergy Immunol*, 34: 283–299.

https://doi.org/10.1007/s12016-007-8048-8

52. Ricke DO, 2021, Two different antibody-dependent enhancement (ADE) risks for SARS-CoV-2 antibodies. *Front Immunol*, 12: 640093.

https://doi.org/10.3389/fimmu.2021.640093

53. Ricke DO, 2021, Etiology scenarios for multisystem inflammatory syndrome in children and adults associated with SARS-CoV-2. *J Integr Pediatr Healthc*, 3: 1–5.

54. Liang Y, Meng FY, Pan HF, *et al*., 2015, A literature review on the patients with autoimmune diseases following vaccination against infections. *Hum Vaccin Immunother*, 11: 2274–2280.

https://doi.org/10.1080/21645515.2015.1009337

55. Frasca L, Ocone G, Palazzo R, 2023, Safety of COVID-19 vaccines in patients with autoimmune diseases, in patients with cardiac issues, and in the healthy population. *Pathogens*, 12: 223.

https://doi.org/10.3390/pathogens12020233

56. Ferri C, Ursini F, Gragnani L, *et al*., 2021, Impaired immunogenicity to COVID-19 vaccines in autoimmune systemic diseases. High prevalence of non-response in different patients' subgroups. *J Autoimmun*, 125: 102744.

https://doi.org/10.1016/j.jaut.2021.102744

57. Efe C, Taşçılar K, Gerussi A, *et al*., 2022, SARS-CoV-2 vaccination and risk of severe COVID-19 outcomes in patients with autoimmune hepatitis. *J Autoimmun*, 132: 102906.

https://doi.org/10.1016/j.jaut.2022.102906

ACCSCIENCE PUBLISHING

Global Translational Medicine

ORIGINAL RESEARCH ARTICLE

Genome-wide analysis identifies non-reference transposable element polymorphisms associated with Parkinson's disease

Hao Wu[1,2], Junfeng Luo[1,2], and Ganqiang Liu[1,2]*

[1]Shenzhen Key Laboratory for Systems Medicine in Inflammatory Diseases, School of Medicine, Shenzhen Campus of Sun Yat-sen University, Shenzhen, Guangdong, 518107, China

[2]Neurobiology Research Center, School of Medicine, Shenzhen Campus of Sun Yat-sen University, Shenzhen, Guangdong, 518107, China

Abstract

Parkinson's disease (PD) is a common neurodegenerative disease that primarily affects the elderly, significantly impacting patients' health and quality of life. While most genetic studies on PD have focused on single nucleotide polymorphisms, the effects of other forms of genomic variation in PD are yet to be fully elucidated. Transposable elements (TEs) are one of the main sources of human genome structural variation, with known associations with many human diseases. However, their potential connection to PD remains unclear. In this study, we investigated non-reference TE polymorphisms in three independent PD cohorts and explored their associations with both PD risk and progression. Our findings revealed that one non-reference TE is associated with the risk of PD, while two TEs are associated with disease progression. Furthermore, through expression quantitative trait locus (eQTL) analysis, we identified 18 *cis* TE-eQTLs in an interaction model and 290 *cis* TE-eQTLs in a non-interaction model. Several non-reference TE polymorphisms are correlated with specific PD-gene expression patterns in *trans*. These results indicate the feasibility of delving into the genetics of PD through the study of complex genomic variations. Advances in genomics research have the potential to deepen our understanding of this disease and pave the way for further translational medicine research in PD.

Keywords: Transposable elements; Parkinson's disease; Genome-wide association studies; Transposable element-expression quantitative trait locus

***Corresponding author:**
Ganqiang Liu
(liugq3@mail.sysu.edu.cn)

Citation: Wu H, Luo J, Liu G, 2023, Genome-wide analysis identifies non-reference transposable element polymorphisms associated with Parkinson's disease. *Global Transl Med*, 2(3): 1583.
https://doi.org/10.36922/gtm.1583

Received: August 11, 2023
Accepted: October 7, 2023
Published Online: October 16, 2023

1. Introduction

Parkinson's disease (PD) is a prevalent neurodegenerative disease, second in incidence only to Alzheimer's disease[1,2]. With the global population aging, the number of PD patients is projected to steadily increase, reaching an estimated 12.9 million worldwide by 2040[3,4]. Over the past few decades, we have gained a deep understanding of the clinical features of PD, including a wide range of motor and non-motor symptoms[5,6]. There are two main pathological features in patients with PD: first, a significant number of dopaminergic neurons in the substantia nigra compacta of the midbrain undergo degeneration and death. Second, there is the appearance of Lewy bodies (LB), which are formed due to the aggregation of α-synuclein[7,8].

The exact cause of PD remains incompletely understood, with a growing body of evidence indicating that several factors, such as genetics, environmental factors, oxidative stress, and aging, contribute to an increased risk of the disease[9]. It is estimated that approximately 15% of PD patients have a family history of the disorder[10]. Furthermore, research has identified around 20 gene mutations associated with familial PD, including genes *SNCA*[11], *PRKN*[12], and *LRRK2*[13]. The interplay of genetic and environmental factors plays a significant role in the development of sporadic PD. Large-scale genome-wide association studies (GWAS) have identified several dozen risk variants that may exert cumulative effects with relatively low impacts[14]. A recent GWAS analysis of PD identified 90 independent autosomal risk signals. However, this analysis only explained 16–36% of heritability associated with PD, implying the existence of additional undiscovered risk variants[15]. To address this gap in knowledge, two potential approaches emerge: the first involves increasing the sample size, while the second entails incorporating other types of variants into GWAS analysis. In a recent GWAS study[16], short tandem repeats (STRs) were reported to be associated with the PD risk, resulting in an increase in the heritability of PD estimate from 26.9% to 28.8%. In addition, another study identified two common X-chromosome variants[17] linked to PD risk. These findings highlight the importance of exploring different types of variants to gain a comprehensive understanding of the genetic architecture underlying PD.

Transposable elements (TEs) are nucleotide sequences widely present in the human genome, varying in length from 100 bp to 10 kb, and capable of independent replication and movement[18]. TEs account for nearly half of the human genome[19] and are categorized into two classes according to their insertion mechanisms: retrotransposons (class 1) and DNA transposons (class 2)[20]. The former is commonly referred to as the "copy-and-paste" mechanism, while the latter is known as the "cut-and-paste" mechanism[18,21]. Retrotransposons consist of two subtypes: long terminal repeat (LTR) retrotransposons and non-long terminal repeat (non-LTR) retrotransposons, depending on the presence of LTR sequences at both sides. Non-LTR retrotransposons include short interspersed nuclear elements (SINEs) and long interspersed nuclear elements (LINEs)[22]. TEs can be classified into two categories based on the ability to independently complete insertion events: autonomous elements and non-autonomous elements. Autonomous TEs can encode the proteins required for insertion events, while non-autonomous TEs rely on proteins encoded by autonomous TEs to complete insertion events[23].

TEs have been recognized for their pivotal roles in shaping genome structure, function, and evolution[24]. Various mechanisms have evolved to suppress uncontrolled TE activity, such as epigenetic silencing mechanisms induced by DNA methylation[25]. In the human genome, most TEs gradually lose their transposition ability due to accumulated mutations during continuous evolution. Only LINE1, SINE-VNTR-Alus (SVA), and Alu elements remain active[26]. The earliest reports of TE insertion causing disease were related to hemophilia A, where LINE1 insertions were discovered in the 14th exon of the *F8* gene in two patients[27]. Recent research has further substantiated the role of TE polymorphisms, demonstrating strong linkage disequilibrium (LD) with GWAS risk signals for specific human diseases[28]. Studies have demonstrated that TE insertions primarily induce deleterious effects through three pathways. First, the integration of novel TEs into exonic regions can disrupt normal gene expression in the human genome. Second, RNA transcribed or proteins translated from TEs may impact host physiological activities. Finally, an increased frequency of ectopic recombination between subfamilies of the same type of TE induces chromosomal rearrangement events[29,30].

Compared to the majority of ancient TEs that remain immobile within the human genome, non-reference TEs are relatively younger and more active. Some studies have suggested that these non-reference TEs exhibit activity in the brain and may contribute to vulnerability to brain disorders[31]. In a recent investigation, several dozen SVA insertion polymorphisms were reported to be linked to PD progression[32] using data from the Parkinson's Progression Markers Initiative (PPMI) cohort. Similarly, another recent study, also utilizing PPMI cohort whole-genome data, revealed a significant correlation between TE polymorphisms and the progression of PD[33]. In this study, we conducted a genome-wide analysis to explore the associations between non-reference TE polymorphisms and the risk and progression of PD based on data from three independent cohorts. In addition, we integrated whole-blood transcriptomic data and investigated the association between TE polymorphisms and gene expression through TE expression quantitative trait loci (TE-eQTL) analysis.

2. Materials and methods

2.1. Study participants and quality control

The study's subjects were sourced from the Parkinson's Progression Markers Initiative (PPMI, https://ppmi-info.org)[34], the PD Biomarker Program (PDBP, https://pdbp.ninds.nih.gov)[35], and the Fox Investigation for New Discovery of Biomarkers (BioFIND, https://biofind.loni.usc.edu)[36]. All data utilized were obtained with proper

authorization from the Accelerating Medicines Partnership in PD (AMP-PD) databases (v2.5 release, https://amp-pd.org) upon signing the AMP-PD Data Use Agreement. The Institutional Review Board of the School of Medicine, Sun Yat-sen University, approved the current analysis.

To reduce genetic heterogeneity, participants of Hispanic or Latino heritage were excluded, and only subjects from the Caucasian population were included in subsequent analyses. The majority of subjects initially recruited in the PPMI, PDBP, and BioIFND cohorts had PD, although it is possible that some subjects may have received different neurodegenerative disease diagnoses during the follow-up period. For the PD cases, we included only those who were initially diagnosed with PD at baseline and remained exclusively affected by PD throughout the follow-up period. Regarding healthy controls, we included subjects who did not exhibit any neurodegenerative diseases at both baseline and during the follow-up period. After quality control (QC), a total of 1,931 PD patients and healthy controls were included in further analysis (Table 1). All of them had whole-genome sequencing (WGS) data, and 1,709 of them also had whole-blood transcriptome sequencing (total RNA-seq) data from the baseline visit. Detailed information about the QC processes for WGS and RNA-seq can be found in Section S1.

The clinical information used in this study includes sex, age of onset, education level, race, cohort, and PD diagnosis information, as well as Montreal Cognitive Assessment (MoCA) score, Hoehn-Yahr staging scale (HY), and MDS Unified Parkinson Disease Rating Scale (MDS-UPDRS) (Table 1). Notably, patients with PD in the PDBP and PPMI cohorts had longitudinal visits with several follow-up visits.

2.2. TEs discovery and annotation

The WGS CRAM files of 1,931 subjects were generated through the alignment of sequencing reads to the human reference genome GRCH38DH using the BWA-MEM (version 0.7.15)[37], following the GATK (version 4.0)[38] best practices workflow[39]. TEs were called using the Mobile Element Locator Tool (MELT, version 2.2.2)[40], which was specifically designed for detecting TEs in Illumina platform-based WGS data. The reliability of the MELT has been validated in projects such as the 1000 Genomes Project (1KGP)[41] and the NyuWa Genome Project[42]. Post-discovery QC was performed using vcftools (version 0.1.16)[43] and PLINK (version 1.90b6.22)[44]. In this study, each TE was assigned a unique ID based on its chromosome position information and TE type, following the ID format: chr_pos_ALU/LINE1/SVA. A detailed description of TE discovery and QC is shown in the Sections S2 and S3.

The insertion frequency of TEs was calculated using vcftools[43] after QC. The lengths of TEs were extracted from the VCF file using vcftools. The Variant Effect Predictor (VEP, version 109)[45], developed and maintained by Ensembl for annotating genomic variation regions, provides comprehensive information on the functional impact of genetic variants. The positions of TEs (GRCH38DH) were extracted from the VCF file using vcftools and were used as input for VEP of the Ensembl website (https://asia.ensembl.org/info/docs/tools/vep/index.html) to obtain the annotation results.

Table 1. Clinical characteristics of subjects in the PDBP, PPMI, and BioFIND cohorts at baseline

Group	PDBP		PPMI		BioFIND	
	PD	HC	PD	HC	PD	HC
Sample size	748	444	390	190	92	67
Age at baseline (mean years [SD])	64.7 (11.02)	62.5 (8.96)	61.9 (9.55)	60.9 (10.34)	67.7 (6.22)	66.3 (7.64)
Male (N, %)	477 (73.8%)	197 (45.4%)	253 (74.9%)	125 (67.4%)	59 (64.1%)	36 (65.7%)
Hoehn and Yahr (mean [SD])	1.28 (1.09)	NA	1.56 (0.50)	NA	1.93 (0.59)	NA
MDS-UPDRS Part I (mean [SD])	7.62 (5.67)	NA	5.63 (4.30)	NA	9.43 (6.09)	NA
MDS-UPDRS Part II (mean [SD])	6.90 (7.73)	NA	5.96 (4.28)	NA	11.04 (6.36)	NA
MDS-UPDRS Part III (mean [SD])	16.15 (14.97)	NA	20.99 (8.90)	NA	28.26 (14.39)	NA
MDS-UPDRS Part IV (mean [SD])	1.30 (2.94)	NA	NA[a]	NA	3.17 (2.89)	NA
MoCA (mean [SD])	25.70 (3.25)	NA	27.16 (2.28)	NA	26.90 (2.51)	NA

Legends: Hoehn and Yahr stage: The Hoehn and Yahr stage is a common scale to describe the progression of motor symptoms in PD;
MDS-UPDRS: MDS-Sponsored Revision of the UPDRS is a comprehensive scale for assessing Parkinson's disease motor and non-motor symptoms.
MDS-UPDRS includes four parts: Part I: Non-motor experiences of daily living; Part II: Motor experiences of daily living; Part III: Motor examination;
Part IV: Motor complications; MOCA: Montreal Cognitive Assessment, an assessment scale for rapid screening for mild cognitive impairment.
[a]The baseline MDS-UPDRS Part IV: scores were not available for the patients from the PPMI cohort in this study.
Abbreviations: HC: Health control; NA: Not available; PD: Parkinson's disease; SD: Standard deviation.

We used two different conservation scores, PhastCons[46] and Phylop[47], to assess the conservation of TE insertion regions. The UCSC Genome Browser (https://genome.ucsc.edu/) provides genome conservation score annotations, namely, PhastCons100way and Phylop100way. These scores are derived from multi-sequence alignments of the human genome with 99 different species using PhastCons and PhyloP, respectively. The conservation score of a specific region in the human genome is calculated based on PhastCons100way and PhyloP100way[48]. In this study, regions with PhyloP scores >0.76 or PhastCons scores >0.2 were considered highly conserved, while the remaining regions were categorized as non-conserved regions, as described in Qiao *et al.*[49].

2.3. LD between TEs and SNPs

The AMP-PD database employed the GATK best practices workflow and the GATK joint genotyping model[38] to generate SNP genotype data in the transformed PLINK binary format. Our original TE VCF file was converted into the PLINK binary format, followed by integrating SNP genotype data and TE data from corresponding subjects. The LD between each TE and its associated SNPs within 1 Mb window size was calculated using PLINK. The 90 independent PD risk variants were obtained from the GWAS study conducted by Nalls *et al.*[15].

2.4. Reproducibility of TEs in the 1KGP and gnomAD database

The reproducibility of this study was evaluated by examining whether the 500 bp window upstream and downstream of the identified TE regions contained the same type of TE as annotated in the 1KGP[41] and Genome Aggregation Database (gnomAD) databases[50]. The public TE annotation data from the 1KGP (dbVar: nstd144) and the structural variation annotation data from gnomAD (dbVar: nstd166) were downloaded from the dbVar database (https://www.ncbi.nlm.nih.gov/dbvar/). The Bedtools (version 2.26.0)[51] intersect function was used with a window parameter set to 500 bp to determine whether the TE insertions belong to the same TE insertion category.

2.5. TE Genome-wide Association Study

TE Genome-Wide Association Study (TE-GWAS) was performed using the logistic regression function in R software to investigate the genetic association between TE insertion and the risk of PD. In consideration of the uniqueness of TE insertions, TE genotypes in this study were classified as having a TE insertion event (coded as "1") or no TE insertion event (coded as "0"). This classification included both heterozygous (0/1) and homozygous (1/1) TE insertions at specific genomic regions as TE insertion events. Principal component analysis (PCA) of TEs was performed using PLINK, with principal component numbers calculated using the EIGENSOFT package (version 7.2.1)[52]. The significant PC1 was used as a covariate to correct for population structure. Finally, PC1, sex, age, and cohort information were included as covariates in the logistic regression model for TE-GWAS analysis. The original *P*-values were corrected using the false discovery rate (FDR), with an FDR <0.05 set as the significance threshold. A detailed description of the QC process before TE-GWAS analysis is shown in Section S4.

2.6. TE- linear mixed model

We used a linear mixed model (LMM) to investigate the correlation between TE polymorphisms and the progression of PD. Nine years of clinical follow-up data from the PPMI cohort and 5 years of clinical follow-up data from the PDBP cohort were combined. The analysis included six different clinical scales: MoCA score, MDS-UPDRS score (Part I to Part IV), and Hoehn-Yahr staging scale. Details of the QC of the clinical scale are presented in Section S5.

To construct the TE-LMM model, we used the lmer function from the lme4 package (version 1.1-34)[53]. The model included fixed effects such as PC1, sex, age, study name, and interaction between TE and years in the study in each model. In addition, education level was incorporated as a fixed effect in the MoCA score model and the MDS-UPDRS Part I score model. Individual subjects were included as random terms in each of the six LMM models. The original *P*-values of the TE-LMM model were calculated using the lmertest package (version 3.1-3)[54] based on the Satterthwaite algorithm and subsequently corrected using the FDR approach.

2.7. Transcriptome data processing and TE-eQTL mapping

The peripheral blood transcriptome (total RNA-seq) dataset was available for the subjects in the PPMI, PDBP, and BioIFND cohorts. Subjects with both total RNA-seq and WGS were retained for analysis. We used the quality-controlled and normalized gene expression transcripts per million (TPM) data for subsequent TE-eQTL analysis. The TPM data were generated from the transcriptome's raw FASTQ files using the Salmon workflow, which is based on the genome annotation file Gencode.v29 (https://www.gencodegenes.org/). We evaluated the association between TE polymorphism and gene expression following the TE expression quantitative trait locus (TE-eQTL) analysis workflow proposed by Wang *et al.*[55]. TE polymorphisms were classified as no TE insertion (coded as "0") or TE insertion as ("1"), similar to the TE-GWAS study. Due to the significantly longer length of TE sequences compared

to SNPs (Figure 1C), the *cis*-TE-eQTL region was expanded from the typical 1 Mb range used in SNP QTL studies to a 10 Mb range.

We performed TE-eQTL analysis using the Matrix eQTL (version 2.3)[56] tool in R software. To investigate whether TE polymorphisms and gene expression associations were affected by disease status, we performed both interaction and non-interaction TE-eQTL analyses, respectively. For interaction-TE-eQTL analysis, we used the "modelLINEAR_CROSS" function in Matrix eQTL, with PC1, sex, age, RNA integrity number (RIN), and cohort included as covariates, and disease status as the interaction term. For non-interaction-TE-eQTL analysis, we utilized the "modelLINEAR" function in Matrix eQTL, with PC1, sex, age, RIN, cohort, and disease status included as covariates.

2.8. Statistical analysis

All statistical analyses in this study were performed using the R v4.1.0 (http://CRAN.R-project.org/).

3. Results

3.1. Identification of TEs and quality assessment

We analyzed WGS data from three independent cohorts, encompassing a total of 1,931 subjects, to investigate the non-reference TE insertion status of each subject. Following rigorous QC procedures, 25,805 high-confidence TE insertion events were identified, including 19,119 ALU, 4,454 LINE1, and 2,232 SVA.We found that ALU exhibited the highest number of insertions, followed by SVA, while LINE1 had the lowest count (Figure 1A), aligning with the known distribution of different TE types within the human genome[57]. Our analysis of TE insertion frequency (Figure 1B) corroborated previous studies, with approximately 57.7% of TEs classified as Singletons. In addition, our observations concurred with existing literature, revealing that LINE1 sequences were the longest (median length of 1,094 bp), followed by SVA (median length of 691 bp), and ALU, which had the

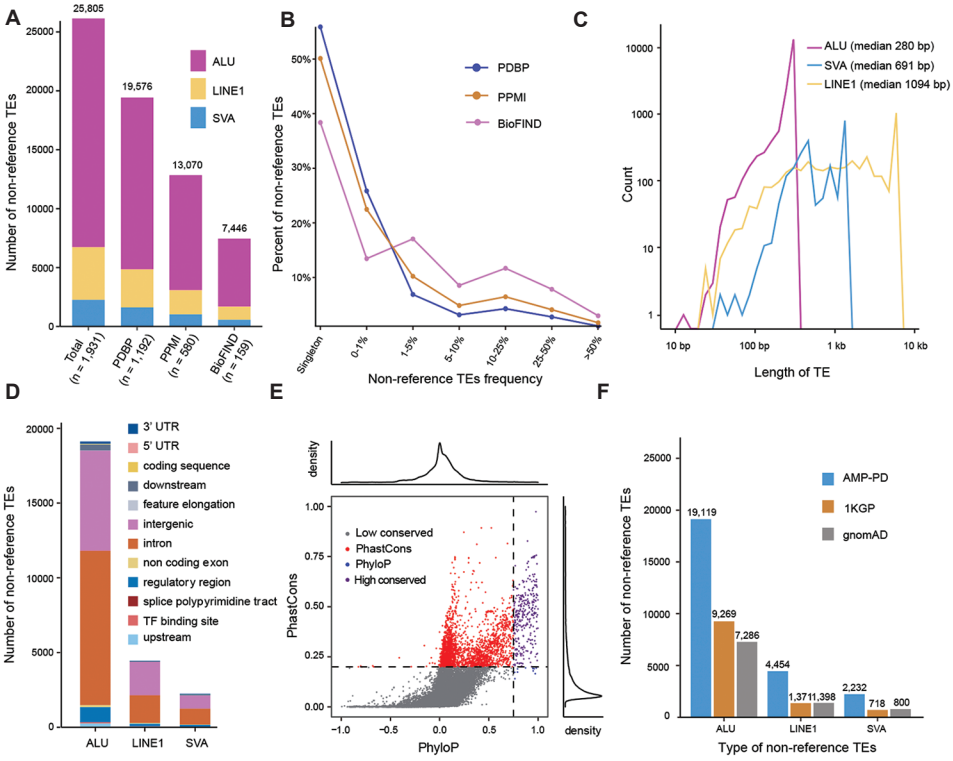

Figure 1. Characteristics of identified non-reference TEs. (A) The numbers of TEs detected in three independent PD cohorts (PPMI, PDBP, and BioFIND), differentiated by their respective types of TEs. (B) Frequency distribution of different types of TE insertions. The X-axis shows the frequency of TE insertions within the genome, while the Y-axis shows the proportion of TEs with different insertion frequencies among all TEs. (C) The length distribution of different types of TEs. The X-axis shows the length of the TE after the $\log_{10}$ transformation, while the Y-axis shows the number of TEs after the $\log_{10}$ transformation. (D) Results of the annotation for different types of TEs within the human genome. (E) Conservation scores of TEs across the genome. The X-axis shows the PhyloP score of the TE insertion area, while the y-axis shows the PhastCons score of the TE insertion area. The isodensity map visually demonstrates the distribution range of TEs, with most TE insertion regions belonging to unconserved regions. (F) Verification of different types of TE using data from the 1KGP and the gnomAD databases.
Abbreviations: TE: Transposable element; PD: Parkinson's disease; PPMI: Parkinson's Progression Markers Initiative.

shortest sequences (median length of 280 bp, Figure 1C). The annotation of TE insertion sites was also consistent with expectations (Figure 1D): approximately 51.3% of TE insertion sites were located within intergenic regions, while approximately 38.0% were located in the intronic areas. This observation confirms the propensity of TE insertions to occur predominantly in the regions of the genome with minimal or negligible impact on genomic structure and function, favoring the retention of TEs within the genome.

TE insertions are prone to preferentially occur in non-coding regions, where they do not significantly disrupt normal genomic structure and function, indicating a higher likelihood of these regions being non-conserved. To evaluate the conservation status of TE insertion sites, we used two conservation scoring tools and found that highly conserved TE insertion sites accounted for a mere 0.033% of all TE insertion events (25,805 TEs). In comparison, non-conserved TE insertion sites accounted for 87.3% of all TE insertion sites (Figure 1E). We also measured the repeatability of our TE calling by comparing it to data from the 1KGP and Genome Aggregation Database (gnomAD) databases. Our detected TEs showed high reproducibility with these existing 1KGP and gnomAD data (Figure 1F): out of the 19,119 ALU detected, 9,269 and 7,286 were validated in the 1KGP and the gnomAD databases, respectively; among the 4,454 LINE1 detected, 1,371 and 1,398 were confirmed in the 1KGP and the gnomAD databases, respectively; regarding the 2,232 SVA detected, 718 and 800 were validated in the 1KGP and the gnomAD databases, respectively. In total, 11,358 (44.0%) and 9,484 (36.8%) out of the 25,805 TEs were validated in the 1KGP and the gnomAD databases, respectively.

3.2. The associations of TEs with the risk and the progression of PD

To investigate the genetic association between TEs and PD, we performed a TE-GWAS. Following rigorous quality control (QC), we retained 1,910 samples and identified 2,867 high-quality TEs suitable for TE-GWAS analysis. The dataset included 689 healthy controls and 1,221 PD patients (Figure S1). During our analysis, we identified a significant TE insertion site, labeled as chr1_246429040_ALU (Figure 2A, $P = 8.73 \times 10^{-6}$, FDR = 0.024, effect size $\beta = -0.44$), which exhibited a significant association with PD onset. This finding suggests that subjects carrying this TE insertion have a lower risk of developing PD. The TE-GWAS inflation factor λ was calculated as 1.058, indicating the reliability of the overall results (Figure S2) and their independence from confounding factors. To further explore potential genetic associations, we conducted an LD analysis of SNPs within the 500 kb region upstream and downstream of the TE risk locus chr1_246429040_ALU. This analysis aimed to determine whether this TE risk locus exhibited strong LD ($r^2 > 0.8$) with known PD risk SNPs. The TE LD analysis revealed no significant PD risk SNP signals in this TE locus region, indicating that this TE insertion site represents an independently discovered PD risk locus (Figure S3).

There were 691 PD cases with longitudinal visits, and 2,111 TE loci were used (Table S1) to examine potential differences in disease progression over time among subjects with TE genotypes. We constructed TE-LMM models for six clinical indicators separately, and our analysis revealed that chr8_114592257_ALU carriers (Figure 2B) exhibited a faster progression in the Hoehn and Yahr stage compared to non-carriers ($P = 1.87 \times 10^{-5}$). In addition, patients carrying chr13_81793576_SVA (Figure 2C) on chromosome 13 q31.1 demonstrated a more rapid progression in MDS-UPDRS Part I scores than non-carriers ($P = 2.47 \times 10^{-6}$).

3.3. Effects of TEs on gene expression

After undergoing QC processing, a total of 1,709 subjects from three cohorts were included in the TE-expression quantitative trait loci (TE-eQTL) analysis. This cohort consisted of 611 healthy controls and 1,098 patients with PD. A total of 2,867 TEs and 28,644 genes were used to investigate the associations between TEs and genes. In our investigation, we identified a total of 18 *cis* TE-eQTLs (27 TE-gene pairs) in the interaction model and 290 *cis* TE-eQTLs (800 TE-gene pairs) in the non-interaction model. Notably, we observed that ALU contributed significantly to the identified TE-eQTLs, a finding consistent with previous reports[58]. Quantile–quantile analysis demonstrated the observed distribution of *P*-values for outliers in the TE-eQTL analysis, demonstrating the reliability of interaction-TE-eQTL (Figure S4A) and non-interaction-TE-eQTL analyses (Figure S4D). We also assessed the distribution of effect size (β) for different types of TEs-eGene (eGene: A gene with a TE-eQTL) in both interaction (Figure S4B) and non-interaction modes (Figure S4E). Our findings revealed that TE insertions were linked to reduced gene expression levels in both models. Furthermore, we investigated the types of genes linked to TE polymorphisms and found that only a minority of these genes corresponded to protein-coding genes. Instead, they primarily comprised pseudogenes and non-coding RNAs (Figure S4C and S4F).

To explore the signaling pathways or functions associated with genes regulated by *cis*-TE-eQTL loci in normal cellular physiology, we performed Gene Ontology (GO) enrichment analysis on the significant eGenes identified through the TE-eQTL analysis. This

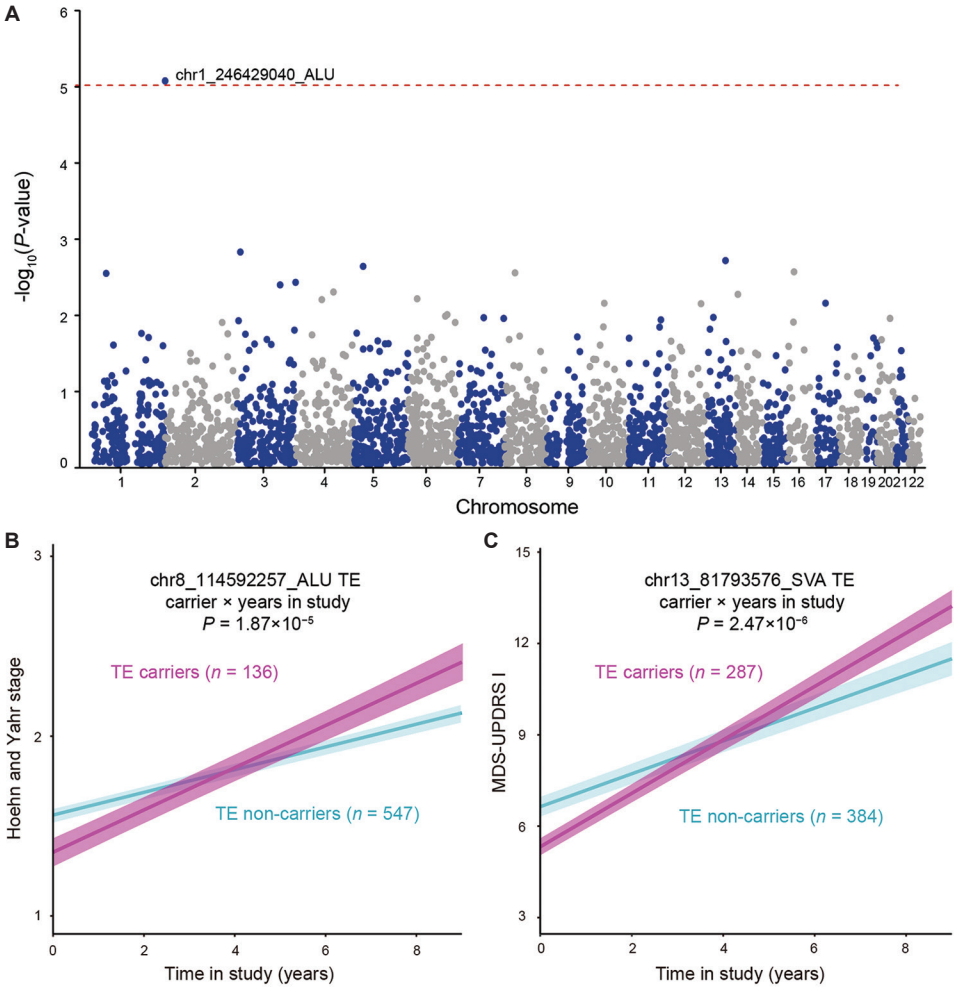

Figure 2. Association analysis identified the associations of TEs with the risk and the progression of PD. (A) Manhattan plot of TE-GWAS obtained from the logistic regression model, comparing PD cases (n = 1,221) with healthy controls (n = 689). Each data point on the plot represents a TE. The Y-axis shows the original P-values after the -$\log_{10}$ transformation of each TE association; the X-axis shows the sequential position of TEs by chromosome (not real scale). The dashed red line corresponds to the significance threshold (FDR-adjusted P-value lower than 5%). (B) Adjusted mean Hoehn and Yahr stage across time predicted by the TE-LMM model for PD cases with chr8_114592257_ALU carriers (magenta line) and non-carriers (light-blue line). (C) Adjusted mean MDS-UPDRS I score across time predicted by the TE-LMM model for PD cases with chr13_81793576_SVA carriers (magenta line) and non-carriers (light-blue line). Shaded ribbons indicate the standard error of the mean.

Abbreviations: TE-LMM: Transposable element-linear mixed model; TE: Transposable element; PD: Parkinson's disease; TE-GWAS: TE Genome-Wide Association Study.

analysis revealed that the 26 genes (27 TE–gene pairs) affected by interaction-TE-eQTL *cis* loci were related to the formation of immunoglobulin complexes and were involved in the recognition of immunoglobulin receptor binding (Figure S5A). The 624 eGenes (800 TE–gene pairs) affected by non-interaction-TE-eQTL *cis* loci were more prominently involved in antigen receptor-mediated signaling pathways, RNA methylation modification, MHC protein complex formation, and endoplasmic reticulum composition (Figure S5B). These findings suggest the existence of specific TE-eQTLs in PD patients, with these TE-eQTLs having a broader impact on RNA methylation levels and a more pronounced involvement in immune-related signaling pathways.

We conducted further investigations to determine whether TE polymorphisms have an impact on the expression of known PD risk genes. Due to the intricate nature of TEs, our analysis focused exclusively on those TEs located on the same chromosome as known PD risk genes[15]. Our findings revealed distinct associations between the expression of three PD risk genes and *trans* TE (*trans* TE-eQTL loci). Among them, an SVA insertion (chr1_111353551_SVA), located upstream of the *GBA* gene at approximately 43 Mb on chromosome 1, was associated

with increased *GBA* expression (Figure 3A, $P = 1.66 \times 10^{-7}$). Similarly, an ALU insertion (chr4_159704892_ALU), located downstream of the PD risk gene *GAMK2D* at approximately 46 Mb on chromosome 4, exhibited a significant association with increased *GAMK2D* expression (Figure 3B, $P = 5.03 \times 10^{-6}$). In addition, a LINE1 insertion (chr6_13190783_LINE1), located downstream of the PD risk gene *RPS12* at approximately 119 Mb on chromosome 6, was linked to elevated *RPS12* expression (Figure 3C, $P = 4.62 \times 10^{-6}$). Interestingly, in contrast to the prevailing trend observed in most *cis* TE-eQTL loci, which are associated with the downregulation of gene expression, these three long-distance TE insertion events were linked to the upregulation of gene expression.

4. Discussion

TEs occupy nearly half of the human genome, yet TE polymorphisms have been overlooked in many disease GWAS studies. In this pilot study, we investigated the genetic association between TE polymorphisms and both the onset and progression of PD by integrating data from nearly 2,000 subjects. Our analysis led to the identification of a TE locus linked to PD onset (Figure 2A) and two TE loci associated with PD progression (Figure 2B and C). Notably, the TE locus associated with PD risk, chr1_246429040_ALU, is located near the *SMYD3* gene, which encodes a histone methyltransferase. *SMYD3* gene plays a pivotal role in epigenetic mechanisms. While numerous studies have consistently demonstrated a significant association between the *SMYD3* gene and tumor progression[59], emerging evidence suggests a correlation between this gene and endothelial senescence[60]. Given the age-related association of PD, it is worth further exploring whether epigenetic regulation of the *SMYD3* gene in the brain is linked to neuronal death. Furthermore, the PD progression associated locus chr8_114592257_ALU is positioned at 1.1 Mb downstream of *CSMD3*, which is predominantly expressed in developing cortical neurons. The absence of *CSMD3* expression is related to abnormal synaptic formation and neurodevelopmental disorders, ultimately resulting in developmental delay[61]. Current evidence suggests that TE-derived sequences regulate gene expression by both maintaining and shaping 3D genome architecture[62]. Further studies involving epigenomics data, such as ATAC-seq, 4C, Hi-C, and ChIP-seq, may aid in elucidating the causal effects of TEs on the development of PD.

To date, the association between the immune system and PD has been supported by multiple lines of evidence[63], with immune cell dysfunction playing a key role in the development of PD[64]. Our interaction *cis*-TE-eQTL analysis revealed that eGenes were enriched in immune-related signaling pathways, suggesting that TE polymorphisms may be linked to abnormal gene expression in the immune system. We propose that elucidating how TE polymorphisms affect immune dysregulation in PD pathogenesis could not only deepen our understanding of the disease but also facilitate the development of novel therapy strategies.

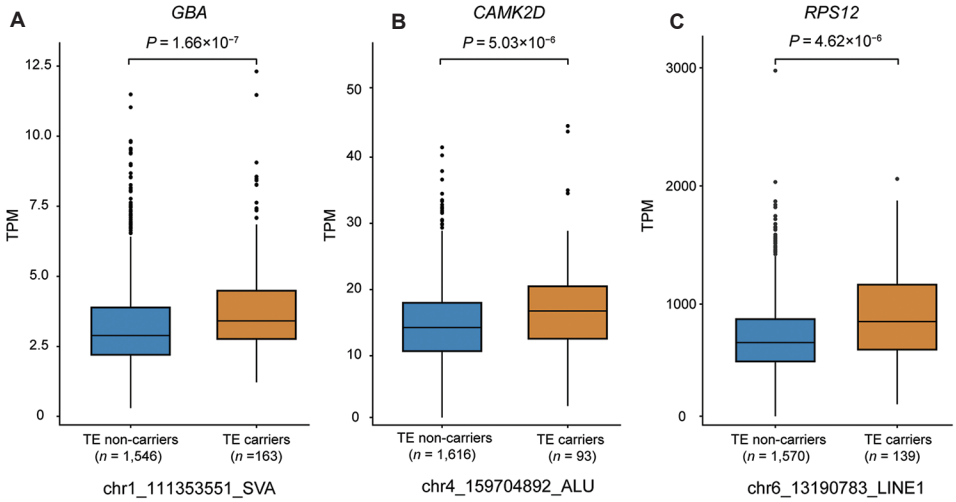

Figure 3. TE polymorphisms link to the expression alternation of PD risk genes. In non-interaction TE-eQTL analysis: (A) the expression of *GBA* was significantly upregulated in carriers of chr1_111353551_SVA compared to non-carriers; (B) the expression of *GAMK2D* was significantly upregulated in carriers of chr4_159704892_ALU compared to non-carriers; (C) the expression of *RPS12* was significantly upregulated in carriers of chr6_13190783_LINE1 compared to non-carriers. The lines within the boxes represent the median value, while the upper and lower ends of the boxes represent the interquartile range.

Abbreviation: TPM: transcripts per million; TE: Transposable element; PD: Parkinson's disease; TE-eQTL: Transposable element-expression quantitative trait locus.

We also observed that long-distance TE polymorphism events were significantly linked to the upregulation of several known PD risk genes, such as *GBA*, *CAMK2D*, and *RPS12* (Figure 3). Functional studies have indicated that *GBA* mutations disrupt the normal structure and function of glucocerebrosidase, leading to the aggregation of alpha-synuclein and mitochondrial dysfunction, ultimately exacerbating the progression of PD[65,66]. While *CAMK2D* and *RPS12* are loci that have been confirmed to be associated with the risk of PD in GWAS studies, there remains a lack of relevant functional studies[15]. These findings suggest that further exploration of the connection between TE polymorphisms and PD-related genes is warranted.

Our study has several limitations. First, the identification of TE insertions based on short-read sequencing data often results in fewer detections than those obtained through third-generation long-read sequencing data. This leads to incomplete and less accurate coverage of TE polymorphism information across the entire genome[58]. Moreover, while typical SNP-based GWAS analyze millions of SNP genotypes and hundreds of thousands of samples, our TE-GWAS study includes only around two thousand samples. As a result, the coverage of genome-wide variations, the power to identify associated loci, and the ability to detect rare variants in TE-GWAS analysis are comparatively weaker than those of classical GWAS. Third, our discoveries of TE risk loci and the effects of TE-eQTLs were based solely on individuals of European ancestry, and it is essential to assess populations of diverse ancestry. Finally, it should be noted that our TE-eQTLs analysis was based on peripheral blood transcriptome data. Further investigation is required to determine whether these associations extend to the brain or not.

5. Conclusion

Our study explored the association between TE polymorphisms and the risk of PD, highlighting the necessity of incorporating other complex genomic variations in GWAS. In addition, we integrated omics data to explore the potential associations between TE polymorphisms and gene expression, including risk genes related to PD. While it is challenging to fully elucidate and establish causative links between TE polymorphisms and the onset and progression of PD based on current evidence and data sources, we propose that the advent of multi-omics big data and platforms for PD research, such as the Global Parkinson's Genetics Program (GP2)[67], will provide additional insights into the connections between TE polymorphisms and PD. This could pave the way from genetics to translational medicine for PD.

Acknowledgments

Data used in the preparation of this article were obtained from the Accelerating Medicines Partnership® (AMP®) PD (AMP PD) Knowledge Platform. For up-to-date information on the study, visit https://www.amp-pd.org. For each individual cohort, acknowledgments are listed in the supplementary file.

Funding

This study is supported by the Shenzhen Fundamental Research Program (JCYJ20190807161601692), National Natural Science Foundation of China (32270701), the Fundamental Research Funds for the Central Universities, Sun Yat-sen (22ykqb07), Young Talent Recruitment Project of Guangdong (2019QN01Y139), and Shenzhen Key Laboratory for Systems Medicine in Inflammatory Diseases (ZDSYS20220606100803007).

Conflict of interest

All authors report no relevant financial or other conflicts of interest in relation to this study.

Author contributions

Conceptualization: Ganqiang Liu, Hao Wu
Formal analysis: Hao Wu
Investigation: Hao Wu
Methodology: Hao Wu, Junfeng Luo
Writing – original draft: Hao Wu
Writing – review & editing: Ganqiang Liu

Ethics approval and consent to participate

All data utilized were authorized for download from the Accelerating Medicines Partnership in PD (AMP-PD) databases (v2.5 release, https://amp-pd.org) on signing the AMP-PD Data Use Agreement.

Consent for publication

Not applicable.

Availability of data

The WGS, RNA-seq, genotypes, and clinical data used in this study were downloaded from the AMP-PD database (https://amp-pd.org/). AMP-PD database was collaboratively established by the National Institutes of Health (NIH), multiple biopharmaceutical and life science companies, and other organizations. The AMP-PD database aims to identify and validate diagnostic, prognostic, and progression biomarkers for Parkinson's disease by conducting in-depth molecular characterization and longitudinal clinical analysis of patient samples.

References

1. Emamzadeh FN, Surguchov A, 2018, Parkinson's disease: Biomarkers, treatment, and risk factors. *Front Neurosci*, 12: 612.

   https://doi.org/10.3389/fnins.2018.00612

2. de Lau LM, Breteler MMB, 2006, Epidemiology of Parkinson's disease. *Lancet Neurol*, 5: 525–535.

   https://doi.org/10.1016/S1474-4422(06)70471-9

3. GBD 2016 Neurology Collaborators, 2019, Global, regional, and national burden of neurological disorders, 1990-2016: A systematic analysis for the Global Burden of Disease Study 2016. *Lancet Neurol*, 18: 459–480.

   https://doi.org/10.1016/S1474-4422(18)30499-X

4. Dorsey ER, Bloem BR, 2018, The Parkinson pandemic-a call to action. *JAMA Neurol*, 75: 9–10.

   https://doi.org/10.1001/jamaneurol.2017.3299

5. Armstrong MJ, Okun MS, 2020, Diagnosis and treatment of Parkinson disease: A review. *JAMA*, 323: 548–560.

   https://doi.org/10.1001/jama.2019.22360

6. Schapira AHV, Chaudhuri KR, Jenner P, 2017, Non-motor features of Parkinson disease. *Nat Rev Neurosci*, 18: 435–450.

   https://doi.org/10.1038/nrn.2017.62

7. Dickson DW, Braak H, Duda JE, *et al.*, 2009, Neuropathological assessment of Parkinson's disease: Refining the diagnostic criteria. *Lancet Neurol*, 8: 1150–1157.

   https://doi.org/10.1016/S1474-4422(09)70238-8

8. Obeso JA, Stamelou M, Goetz CG, *et al.*, 2017, Past, present, and future of Parkinson's disease: A special essay on the 200th Anniversary of the Shaking Palsy. *Mov Disord*, 32: 1264–1310.

   https://doi.org/10.1002/mds.27115

9. Poewe W, Seppi K, Tanner CM, *et al.*, 2017, Parkinson disease. *Nat Rev Dis Primers*, 3: 17013.

   https://doi.org/10.1038/nrdp.2017.13

10. Deng H, Wang P, Jankovic J, 2018, The genetics of Parkinson disease. *Ageing Res Rev*, 42: 72–85.

    https://doi.org/10.1016/j.arr.2017.12.007

11. Polymeropoulos MH, Lavedan C, Leroy E, *et al.*, 1997, Mutation in the alpha-synuclein gene identified in families with Parkinson's disease. *Science*, 276: 2045–2047.

    https://doi.org/10.1126/science.276.5321.2045

12. Kitada T, Asakawa S, Hattori N, *et al.*, 1998, Mutations in the parkin gene cause autosomal recessive juvenile parkinsonism. *Nature*, 392: 605–608.

    https://doi.org/10.1038/33416

13. Zimprich A, Biskup S, Leitner P, *et al.*, 2004, Mutations in LRRK2 cause autosomal-dominant parkinsonism with pleomorphic pathology. *Neuron*, 44: 601–607.

    https://doi.org/10.1016/j.neuron.2004.11.005

14. Fernandez-Santiago R, Sharma M, 2022, What have we learned from genome-wide association studies (GWAS) in Parkinson's disease? *Ageing Res Rev*, 79: 101648.

    https://doi.org/10.1016/j.arr.2022.101648

15. Nalls MA, Blauwendraat C, Vallerga CL, *et al.*, 2019, Identification of novel risk loci, causal insights, and heritable risk for Parkinson's disease: A meta-analysis of genome-wide association studies. *Lancet Neurol*, 18: 1091–1102.

    https://doi.org/10.1016/S1474-4422(19)30320-5

16. Bustos BI, Billingsley K, Blauwendraat C, *et al.*, 2023, Genome-wide contribution of common short-tandem repeats to Parkinson's disease genetic risk. *Brain*, 146: 65–74.

    https://doi.org/10.1093/brain/awac301

17. Le Guen Y, Napolioni V, Belloy ME, *et al.*, 2021, Common X-chromosome variants are associated with Parkinson disease risk. *Ann Neurol*, 90: 22–34.

    https://doi.org/10.1002/ana.26051

18. Burns KH, Boeke JD, 2012, Human transposon tectonics. *Cell*, 149: 740–752.

    https://doi.org/10.1016/j.cell.2012.04.019

19. Nurk S, Koren S, Rhie A, *et al.*, 2022, The complete sequence of a human genome. *Science*, 376: 44–53.

    https://doi.org/10.1126/science.abj6987

20. Bourque G, Burns KH, Gehring M, *et al.*, 2018, Ten things you should know about transposable elements. *Genome Biol*, 19: 199.

    https://doi.org/10.1186/s13059-018-1577-z

21. Finnegan DJ, 1989, Eukaryotic transposable elements and genome evolution. *Trends Genet*, 5: 103–107.

    https://doi.org/10.1016/0168-9525(89)90039-5

22. Wicker T, Sabot F, Hua-Van A, *et al.*, 2007, A unified classification system for eukaryotic transposable elements. *Nat Rev Genet*, 8: 973–982.

    https://doi.org/10.1038/nrg2165

23. Wells JN, Feschotte C, 2020, A field guide to eukaryotic transposable elements. *Annu Rev Genet*, 54: 539–561.

    https://doi.org/10.1146/annurev-genet-040620-022145

24. Chuong EB, Elde NC, Feschotte C, 2017, Regulatory activities of transposable elements: From conflicts to benefits. *Nat Rev Genet*, 18: 71–86.

    https://doi.org/10.1038/nrg.2016.139

25. Hoyt SJ, Storer JM, Hartley GA, *et al.*, 2022, From telomere to telomere: The transcriptional and epigenetic state of human repeat elements. *Science*, 376: eabk3112.

https://doi.org/10.1126/science.abk3112

26. Mills RE, Bennett EA, Iskow RC, *et al.*, 2007, Which transposable elements are active in the human genome? *Trends Genet*, 23: 183–191.

https://doi.org/10.1016/j.tig.2007.02.006

27. Kazazian HH Jr., Wong C, Youssoufian H, *et al.*, 1988, Haemophilia A resulting from *de novo* insertion of L1 sequences represents a novel mechanism for mutation in man. *Nature*, 332: 164–166.

https://doi.org/10.1038/332164a0

28. Payer LM, Steranka JP, Yang WR, *et al.*, 2017, Structural variants caused by Alu insertions are associated with risks for many human diseases. *Proc Natl Acad Sci U S A*, 114: E3984–E3992.

https://doi.org/10.1073/pnas.1704117114

29. Payer LM, Burns KH, 2019, Transposable elements in human genetic disease. *Nat Rev Genet*, 20: 760–772.

https://doi.org/10.1038/s41576-019-0165-8

30. Burns KH, 2020, Our conflict with transposable elements and its implications for human disease. *Annu Rev Pathol*, 15: 51–70.

https://doi.org/10.1146/annurev-pathmechdis-012419-032633

31. Ahmadi A, De Toma I, Vilor-Tejedor N, *et al.*, 2020, Transposable elements in brain health and disease. *Ageing Res Rev*, 64: 101153.

https://doi.org/10.1016/j.arr.2020.101153

32. Pfaff AL, Bubb VJ, Quinn JP, *et al.*, 2021, Reference SVA insertion polymorphisms are associated with Parkinson's disease progression and differential gene expression. *NPJ Parkinsons Dis*, 7: 44.

https://doi.org/10.1038/s41531-021-00189-4

33. Koks S, Pfaff AL, Singleton LM, *et al.*, 2022, Non-reference genome transposable elements (TEs) have a significant impact on the progression of the Parkinson's disease. *Exp Biol Med*, 247: 1680–1690.

https://doi.org/10.1177/15353702221117147

34. Parkinson Progression Marker Initiative, 2011, The Parkinson progression marker initiative (PPMI). *Prog Neurobiol*, 95: 629–635.

https://doi.org/10.1016/j.pneurobio.2011.09.005

35. Rosenthal LS, Drake D, Alcalay RN, *et al.*, 2016, The NINDS Parkinson's disease biomarkers program. *Mov Disord*, 31: 915–923.

https://doi.org/10.1002/mds.26438

36. Kang UJ, Goldman JG, Alcalay RN, *et al.*, 2016, The BioFIND study: Characteristics of a clinically typical Parkinson's disease biomarker cohort. *Mov Disord*, 31: 924–932.

https://doi.org/10.1002/mds.26613

37. Li H, Durbin R, 2009, Fast and accurate short read alignment with Burrows-Wheeler transform. *Bioinformatics*, 25: 1754–1760.

https://doi.org/10.1093/bioinformatics/btp324

38. DePristo MA, Banks E, Poplin R, *et al.*, 2011, A framework for variation discovery and genotyping using next-generation DNA sequencing data. *Nat Genet*, 43: 491–498.

https://doi.org/10.1038/ng.806

39. Regier AA, Farjoun Y, Larson DE, *et al.*, 2018, Functional equivalence of genome sequencing analysis pipelines enables harmonized variant calling across human genetics projects. *Nat Commun*, 9: 4038.

https://doi.org/10.1038/s41467-018-06159-4

40. Gardner EJ, Lam VK, Harris DN, *et al.*, 2017, The mobile element locator tool (MELT): Population-scale mobile element discovery and biology. *Genome Res*, 27: 1916–1929.

https://doi.org/10.1101/gr.218032.116

41. Sudmant PH, Rausch T, Gardner EJ, *et al.*, 2015, An integrated map of structural variation in 2,504 human genomes. *Nature*, 526: 75–81.

https://doi.org/10.1038/nature15394

42. Niu Y, Teng X, Zhou H, *et al.*, 2022, Characterizing mobile element insertions in 5675 genomes. *Nucleic Acids Res*, 50: 2493–2508.

https://doi.org/10.1093/nar/gkac128

43. Danecek P, Auton A, Abecasis G, *et al.*, 2011, The variant call format and VCFtools. *Bioinformatics*, 27: 2156–2158.

https://doi.org/10.1093/bioinformatics/btr330

44. Purcell S, Neale B, Todd-Brown K, *et al.*, 2007, PLINK: A tool set for whole-genome association and population-based linkage analyses. *Am J Hum Genet*, 81: 559–575.

https://doi.org/10.1086/519795

45. McLaren W, Gil L, Hunt SE, *et al.*, 2016, The ensembl variant effect predictor. *Genome Biol*, 17: 122.

https://doi.org/10.1186/s13059-016-0974-4

46. Hubisz MJ, Pollard KS, Siepel A, 2011, PHAST and RPHAST: Phylogenetic analysis with space/time models. *Brief Bioinform*, 12: 41–51.

https://doi.org/10.1093/bib/bbq072

47. Pollard KS, Hubisz MJ, Rosenbloom KR, *et al.*, 2010, Detection of nonneutral substitution rates on mammalian phylogenies. *Genome Res*, 20: 110–121.

https://doi.org/10.1101/gr.097857.109

48. Navarro Gonzalez J, Zweig AS, Speir ML, *et al.*, 2021, The UCSC genome browser database: 2021 update. *Nucleic Acids Res*, 49: D1046–D1057.

https://doi.org/10.1093/nar/gkaa1070

49. Qiao Y, Ren C, Huang S, *et al.*, 2020, High-resolution annotation of the mouse preimplantation embryo transcriptome using long-read sequencing. *Nat Commun*, 11: 2653.

https://doi.org/10.1038/s41467-020-16444-w

50. Karczewski KJ, Francioli LC, Tiao G, *et al.*, 2020, The mutational constraint spectrum quantified from variation in 141,456 humans. *Nature*, 581: 434–443.

https://doi.org/10.1038/s41586-020-2308-7

51. Quinlan AR, Hall IM, 2010, BEDTools: A flexible suite of utilities for comparing genomic features. *Bioinformatics*, 26: 841–842.

https://doi.org/10.1093/bioinformatics/btq033

52. Price AL, Patterson NJ, Plenge RM, *et al.*, 2006, Principal components analysis corrects for stratification in genome-wide association studies. *Nat Genet*, 38: 904–909.

https://doi.org/10.1038/ng1847

53. Bates D, Mächler M, Bolker B, *et al.*, 2015, Fitting linear mixed-effects models using lme4. *J Stat Softw*, 67: 1–48.

https://doi.org/10.18637/jss.v067.i01

54. Kuznetsova A, Brockhoff PB, Christensen RHB, 2017, lmerTest Package: Tests in linear mixed effects models. *J Stat Softw*, 82: 1–26.

https://doi.org/10.18637/jss.v082.i13

55. Wang L, Rishishwar L, Marino-Ramirez L, *et al.*, 2017, Human population-specific gene expression and transcriptional network modification with polymorphic transposable elements. *Nucleic Acids Res*, 45: 2318–2328.

https://doi.org/10.1093/nar/gkw1286

56. Shabalin AA, 2012, Matrix eQTL: Ultra fast eQTL analysis via large matrix operations. *Bioinformatics*, 28: 1353–1358.

https://doi.org/10.1093/bioinformatics/bts163

57. Lander ES, Linton LM, Birren B, *et al.*, 2001, Initial sequencing and analysis of the human genome. *Nature*, 409: 860–921.

https://doi.org/10.1038/35057062

58. Vialle RA, de Paiva Lopes K, Bennett DA, *et al.*, 2022, Integrating whole-genome sequencing with multi-omic data reveals the impact of structural variants on gene regulation in the human brain. *Nat Neurosci*, 25: 504–514.

https://doi.org/10.1038/s41593-022-01031-7

59. Bernard BJ, Nigam N, Burkitt K, *et al.*, 2021, SMYD3: A regulator of epigenetic and signaling pathways in cancer. *Clin Epigenetics*, 13: 45.

https://doi.org/10.1186/s13148-021-01021-9

60. Yang D, Wei G, Long F, *et al.*, 2020, Histone methyltransferase Smyd3 is a new regulator for vascular senescence. *Aging Cell*, 19: e13212.

https://doi.org/10.1111/acel.13212

61. Song W, Li Q, Wang T, *et al.*, 2022, Putative complement control protein CSMD3 dysfunction impairs synaptogenesis and induces neurodevelopmental disorders. *Brain Behav Immun*, 102: 237–250.

https://doi.org/10.1016/j.bbi.2022.02.027

62. Lawson HA, Liang Y, Wang T, 2023, Transposable elements in mammalian chromatin organization. *Nat Rev Genet*, 24: 712–723.

https://doi.org/10.1038/s41576-023-00609-6

63. Tan EK, Chao YX, West A, *et al.*, 2020, Parkinson disease and the immune system - associations, mechanisms and therapeutics. *Nat Rev Neurol*, 16: 303–318.

https://doi.org/10.1038/s41582-020-0344-4

64. Tansey MG, Wallings RL, Houser MC, *et al.*, 2022, Inflammation and immune dysfunction in Parkinson disease. *Nat Rev Immunol*, 22: 657–673.

https://doi.org/10.1038/s41577-022-00684-6

65. Ryan E, Seehra G, Sharma P, *et al.*, 2019, GBA1-associated parkinsonism: New insights and therapeutic opportunities. *Curr Opin Neurol*, 32: 589–596.

https://doi.org/10.1097/WCO.0000000000000715

66. Liu G, Boot B, Locascio JJ, *et al.*, 2016, Specifically neuropathic Gaucher's mutations accelerate cognitive decline in Parkinson's. *Ann Neurol*, 80: 674–685.

https://doi.org/10.1002/ana.24781

67. Lange LM, Avenali M, Ellis M, *et al.*, 2023, Elucidating causative gene variants in hereditary Parkinson's disease in the Global Parkinson's Genetics Program (GP2). *NPJ Parkinsons Dis*, 9: 100.

https://doi.org/10.1038/s41531-023-00526-9

Our Journals

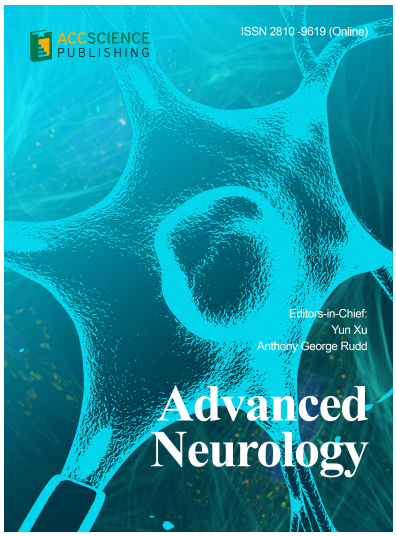

Advanced Neurology is a peer-reviewed and open-access journal that aims to publish and disseminate novel research in the breadth of neurology and neuroscience. The journal aims to advance our understanding in the nervous system and provide a platform to neuroscientists and physicians to showcase their findings in original fundamental and clinical research as well as to present new ideas that highlight the changes in the neurological clinical practice.

Advanced Neurology covers subject areas, including but not limited to the following:

- Neurological disorders
- Neurodegenerative disease
- Cerebrovascular disease
- Epilepsy and movement disorders
- Neuroimmune disease
- Neurological infections
- Muscle disease
- Molecular and cellular neuroscience
- Systems neuroscience
- Cognitive neuroscience
- Computational modeling of nervous system

Gene & Protein in Disease publishes rigorously peer-reviewed and high quality original articles and authoritative reviews that focus on the latest development in multidisciplinary areas in biology and biomedicine, with an emphasis on gene and protein research. The journal has worldwide authorship, and a broad scope in basic and translational biomedical research of genetics, biochemistry, biophysics, oncology, immunology, cell biology, molecular biology, developmental biology, microbiology, neuroscience, stem cell, protein science, structural biology, regenerative medicine and translational medicine.

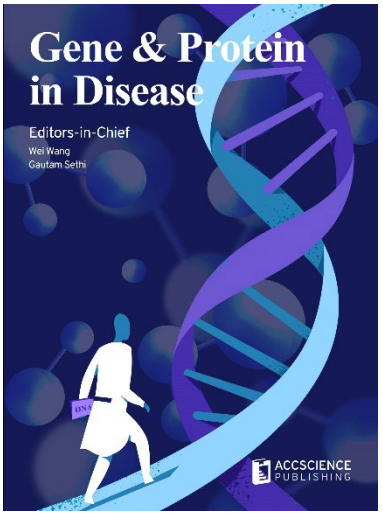

Start a new journal

Write to us via email if you are interested to start a new journal with AccScience Publishing. Please attach your CV, professional profile page and a brief pitch proposal in your email. We shall inform you of our decision whether we are interested to collaborate in starting a new journal.

Contact: info@accscience.com

https://accscience.com/journal/GTM

Contact
www.accscience.com
8 Burn Road, #15-03 Trivex, Singapore 369977
Email: editorial@accscience.com
Phone: +65 8182 1586